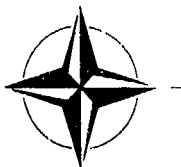


(12)

AD A 1 25324

SACLANTCEN Conference Proceedings No. 32 PART 2



SACLANTCEN

Conference Proceedings No. 32

PART 2

Pages 13-1 to end

SACLANT ASW
RESEARCH CENTRE

UNDERWATER AMBIENT NOISE

Proceedings of a conference held at SACLANTCEN
on 11-14 May 1982

VOL. II UNCLASSIFIED PAPERS

Organized by

RONALD A. WAGSTAFF and OREST Z. BLUY

15 JUNE 1982

DTIC
ELECTE
MAR 0 1 1983
S E

DTIC FILE COPY

NORTH
ATLANTIC
TREATY
ORGANIZATION

LA SPEZIA, ITALY

This document is unclassified. The information it contains is published subject to the conditions of the legend printed on the inside cover. Short quotations from it may be made in other publications if credit is given to the author(s). Except for working copies for research purposes or for use in official NATO publications, reproduction requires the authorization of the Director of SACLANTCEN.

This document has been approved
for public release and sale; its
distribution is unlimited.

83 03 04 001

SACLANTCEN
CONFERENCE PROCEEDINGS NO. 32

NORTH ATLANTIC TREATY ORGANIZATION
SACLANT ASW Research Centre
Viale San Bartolomeo 400, I-19026 San Bartolomeo (SP), Italy.

tel. national 0187 560940
international + 39 187 560940
telex: 271148 SACENT I

UNDERWATER AMBIENT NOISE

Proceedings of a Conference held at SACLANTCEN
on 11-14 May 1982

VOL. II UNCLASSIFIED PAPERS
(Part 2: Pages 13-1 to end)

Organized by
Ronald A. Wagstaff and Orest Z. Bluy

15 June 1982



Accession For	
NTIS GRA&I	<input checked="checked" type="checkbox"/>
DTIC TAB	<input type="checkbox"/>
Unannounced	<input type="checkbox"/>
Justification	
By _____	
Date _____	
Accession Code	
Number	
Dist _____	
A	

This document has been prepared from text and illustrations provided by each author. The opinions expressed are those of the authors and are not necessarily those of the SACLANT ASW Research Centre.

↓
TABLE OF CONTENTS →

	<u>Pages</u>
Introduction	1
Summary	3
 1 <u>BACKGROUND</u>	
Role of propagation in ambient noise by D. Ross	a) 1-1 to 1-18
 2 <u>MECHANISMS</u>	
Acoustic source characteristics of merchant ships by J.C. Heine	b) 2-1 to 2-16
Flow-noise interference in measurements of infrasonic ambient noise by M. Strasberg	c) 3-1 to 3-12
 3 <u>LOW-FREQUENCY PHENOMENA</u>	
Low-frequency seismic and hydroacoustic noise measurements in a fjord by E. Sevaldsen	d) 4-1 to 4-25
Seismic and hydroacoustic sensing of infrasonic noise in coastal waters by B. Schmalfeldt and D. Rauch	e) 5-1 to 5-12
 4 <u>MEASUREMENTS AND MEASUREMENT TECHNIQUES</u>	
Le programme Ulysse by J. Roy	f) 6-1 to 6-17
Arctic ambient noise statistical measurement results and their implications to sonar performance improvements by R.F. Dwyer (presented by A.H. Nuttall)	g) 7-1 to 7-10
Acoustic ambient noise in the Barents Sea by O. Grenness	h) 8-1 to 8-9
Depth dependence of directionality of ambient noise in the North Pacific: experimental data and equipment design by R.C. Tyce	i) 9-1 to 9-16

Table of Contents (Cont'd)Pages

Ambient noise levels in the northeast
Pacific ocean as measured by aircraft-dropped
sonobuoys
by R.H. Bourke et al

j) 10-1 to 10-13

5 PROCESSING TECHNIQUES - -

A real-time system for towed-array calibration
and performance analysis, or how to get 50 dB
sidelobes from a towed array
by J.L. Berrou, O.Z. Bluy & R.A. Wagstaff

k) 11-1 to 11-14

Notes on the interpretation of ambient
noise statistics
by R.C. Cavanagh

l) 12-1 to 12-10

→ A method of estimating the influence of ship's
noise on ambient noise measurements,
by H. Bendig

m) 13-1 to 13-12

→ Optimal detection and tracking of acoustical
noise sources in a time-varying environment,
by H. Van Asselt

n) 14-1 to 14-11

→ Influence of background-noise spatial
coherence on high-resolution passive
method
by G. Bienvenu and L. Kopp

o) 15-1 to 15-10

→ Performance of three averaging methods for
various distributions
by A.H. Nuttall

p) 16-1 to 16-13

→ Is power averaging the best estimator for
undersea acoustic data?
by R.A. Wagstaff and J.L. Berrou

q) 17-1 to 17-16

6 MODELLING: DEVELOPMENT AND USE

→ A parametric examination of some properties
of the low-frequency ambient-noise field
by I.A. Fraser

r) 18-1 to 18-14

Table of Contents (Cont'd)Pages

✓ Detection models and target-information processing,
by J.W. Bond

s) 19-1 to 19-14

✓ The prediction of temporal statistics of directional ambient shipping noise
by M. Groen

t) 20-1 to 20-17

✓ Site and frequency dependence of ambient noise in the north eastern Pacific Ocean;
by J.H. Wilson

u) 21-1 to 21-12

7 ACOUSTIC PROPAGATION EFFECTS

✓ Site dependence of wind-dominated ambient noise in shallow water,
by S.N. Wolf and F. Ingenito

v) 22-1 to 22-9

✓ Effects of topographic blockage and ocean boundaries on low-frequency noise fields
by A. Anderson and R. Martin
(presented by S. Marshall)

w) 23-1 to 23-16

✓ The seamount as a noise barrier.
by H. Medwin et al

x) 24-1 to 24-11

A METHOD OF ESTIMATING THE INFLUENCE OF SHIP'S NOISE
ON AMBIENT NOISE MEASUREMENTS

by

Horst Bendig
Fried. Krupp GmbH
Krupp Atlas-Elektronik Bremen
D2800 Bremen, West GermanyABSTRACT

Ambient noise measurements are often adversely affected by noise from passing ships. Here, a method is presented which allows the estimation of this influence. The method is especially suitable for shallow water applications. It is based on mode interference. The broad-band ship-generated noise is transmitted to the measuring sensor by modes. Because of the interference of these modes, the spectrogram of the noise exhibits interference patterns. Disturbance of ambient noise measurements occurs whenever interference patterns appear in the spectrogram. The degree of the disturbing effect is specified by a mode interference modulation factor which is defined here. In addition, the number of ships and their distance from the measurement sensor can be estimated from the interference patterns. Measurement results are shown which have been evaluated with this method.

1. INTRODUCTION

Ambient noise measurements are often disturbed by noise from passing ships. This is especially the case in sea areas which carry a large amount of shipping, such as the North Sea and the Baltic.

The aim of this investigation is to identify the disturbances and to estimate the degree of disturbance. Level observations alone are not adequate for solving this problem. In the sea areas mentioned above, which are shallow-water areas, the ambient noise level itself fluctuates considerably [1, 2], so that it is difficult to distinguish between fluctuations in ambient noise level and changes in disturbance level. For this reason, the disturbance is to be characterised in a different way. A method of doing this is presented here. The method is based on mode propagation.

The structure of this paper is as follows: In Chapter 2, some basic matters are discussed. In Chapter 3, the mode interference modulation factor is defined. Chapter 4 deals with the estimation of the number of disturbance sources and their distance from the measurement point. In Chapter 5, measurement results are discussed. Finally, Chapter 6 gives conclusions.

2. BASICS

The acoustic energy emitted by the disturbing ship is carried to the measurement point with the aid of normal modes. This is a well-known fact (e. g. [3], [4], [5]). Because of the mode propagation, the spectrograms (defined in [6], for example) of the measured underwater sound contain interference patterns [7, 8].

The spectrogram is the power P versus frequency f and measurement time t . According to this, the function for the spectrogram can be written as $P(t, f)$. In cases where motion is involved, the time may be replaced by the distance.

An example of a measured interference pattern is shown in the lower part of Fig. 1; the distance is plotted against the frequency. The degree of blackness corresponds to the acoustic intensity. The associated measurement situation is sketched in the upper part of the illustration. If the disturbing source of noise is moving away from the measurement point at constant speed, the modulation of the power in each narrow analysis band (e.g. at frequency F_0) is harmonic.

Because of its orderly structure, this interference pattern is easily distinguished from the ambient noise, and is therefore very suitable for the detection of disturbance sources. This is substantiated by Fig. 2. This illustration shows a longer spectrogram. Here, a frequency band from 0 to 450 Hz is shown. The ordinate scale is not in distance units like the scale in Fig. 1; instead, it is in time units (the usual procedure in spectrograms). The spectrogram contains an interference pattern of a passing ship. Shortly after the starting instant $t = 0$ of the spectrogram recording, the measured noise had not yet been affected by the ship which would later cause disturbance. No mode interference pattern is apparent yet in this period of time. The pattern does not begin until later; it then becomes more and more pronounced as the distance between the disturbance source and the measurement point becomes smaller. After the closest point of approach (CPA) has been reached, the pattern becomes fainter again.

The clear distinction between spectrogram regions with and without a mode interference pattern, as illustrated in Fig. 2, causes us to make the following statement: whenever interference patterns are present in the spectrogram, it should always be assumed that a source of disturbance is present. The degree of disturbance is to be described by a modulation factor, which is referred to here as the "mode interference modulation factor".

In addition to the degree of acoustic disturbance of the ambient noise measurement, a rough estimate of the number of disturbance sources and their distance from the measurement point is often of interest. Mode interference offers possibilities for this. A glance at the spectrogram in Fig. 2 will verify this. The interference lines which characterise the fan-like structure of the interference pattern have different gradients. At a given frequency, the absolute value of the gradient of the interference lines increases with the distance between the source and the receiver. This fact forms the basis of the distance estimate.

Let us mention the following boundary conditions for the method proposed here for estimating the influence of disturbance sources on the ambient noise measurement.

The sound propagation channel must be such as to ensure that mode propagation can take place. This is so in shallow water areas especially. The disturbance source should radiate acoustic energy over a wide band of frequencies. This condition is fulfilled for the broad-band cavitation and flow noise produced by moving ships. Here, the frequency band from a few tens of Hz to about 500 Hz is investigated. The underwater sound is to be measured omnidirectionally.

3. DETERMINATION OF THE MODE INTERFERENCE MODULATION FACTOR

The mode interference modulation factor is intended to describe the degree of modulation of a periodogram component. It is thus a measure of the measured time-dependent variation of the power in the narrow analysis bands. To be able to compute the degree of modulation formally, we make the following assumptions. We assume that each periodogram component can be described approximately by a stochastic process $Z(t)$:

$$Z(t) = X(t) \cdot A(t) \quad (3.1)$$

Equation (3.1) is valid for a fixed frequency. The frequency is suppressed in the notation. According to the function for the power $P(t, f)$ in the spectrogram, our function $Z(t)$ approximates the power $P(t, f = \text{const.})$ at constant frequency.

The product process $Z(t)$ is to consist of a carrier process $X(t)$ and a modulation process $A(t)$, which are both assumed to be stationary.

We shall assume that the carrier process and the modulation process are independent of each other. We shall also assume that short-time power spectra computed one after another are likewise independent of each other.

In the harmonic modulation, the modulation factor is defined as the quotient of the amplitude and mean value; the amplitude is $\sqrt{2}$ times the standard deviation σ .

We shall adopt this definition and describe the mode interference modulation factor M of a periodogram component by:

$$M = \sqrt{2} \cdot \sigma_A / \mu_A \quad (3.2)$$

where σ_A is the standard deviation of the modulation process and μ_A is its mean value.

Since the product process only (and not the modulation process) is measurable, the quotient σ_A/μ_A cannot be determined directly. For this reason, the modulation process will be described by the obtainable relative standard deviations of the product process $Z(t)$ and of the carrier process $X(t)$. We obtain the following:

$$M = \sqrt{2 \cdot \frac{\left(\frac{\sigma_z}{\mu_z}\right)^2 - \left(\frac{\sigma_x}{\mu_x}\right)^2}{1 + \left(\frac{\sigma_x}{\mu_x}\right)^2}} \quad (3.3)$$

We now go over to the discrete case, since discrete periodograms are computed in practice, e. g. with the aid of the fast Fourier Transform. The modulation factor is thus computed for discrete frequency values f_i only. We also assume that, for estimating the modulation factor, only time-intervals of duration T are used in the spectrogram. The position of an interval with respect to time is assigned to the discrete instant t_j . The modulation factor will therefore be symbolised by $M_T(t_j, f_i)$. Averaging in the frequency direction over K modulation factors of adjacent spectrogram-components gives the mean mode interference modulation factor for the instant t_j :

$$\bar{M}_T(t_j) = \frac{1}{K} \sum_{i=1}^{L+K-1} M_T(t_j, f_i) \quad (3.4)$$

where $f_i = i \cdot \Delta f$ and Δf is the frequency resolution cell of the discrete periodogram. During the ambient noise measurement, this mean value \bar{M}_T is continually updated. Depending on the magnitude of \bar{M}_T , a decision is then made as to whether the disturbance is too great or is still acceptable.

To estimate the modulation factor in accordance with equation (3.3), we need not only the relative standard deviation $\hat{\sigma}_z/\hat{\mu}_z$ (which can be estimated directly from the spectrogram) but also the relative standard deviation $\hat{\sigma}_x/\hat{\mu}_x$ for the carrier process. (In the following, estimated values are indicated by a "hat", $\hat{}$.) This quotient is generally not known. The required quotient $\hat{\sigma}_x/\hat{\mu}_x$ is a constant and can be computed after a special procedure has been applied. This procedure is called "normalisation" [9]. This normalisation is applied to each individual periodogram of the spectrogram before determination of the modulation factor.

To summarise, the expected value of the power density in the neighbourhood of the individual frequency points f_i of the original periodogram is estimated first. Next, the values of the original periodogram are divided by the estimated expected values. An effect of this normalisation is, for example, that broad-band pink noise turns into white noise (more or less).

Furthermore - and this is important for us - in the unmodulated case all moments for the components of the normalised periodogram can be stated, and thus also the required values μ_x and σ_x of our carrier process.

We expect the mean modulation factor \bar{M}_T for an unmodulated spectrogram to be around zero. In this case especially, it is clear that estimated relative standard deviations $\hat{\sigma}_z / \hat{\mu}_z$ of individual periodogram-components may be smaller than the calculated quotient σ_x / μ_x of the carrier process. The modulation factor according to equation (3.3) would become imaginary. However, this result is not meaningful. For this reason, equation (3.3) is modified somewhat:

$$\hat{M} = \text{sign} \left\{ \left(\frac{\hat{\sigma}_z}{\hat{\mu}_z} \right)^2 - \left(\frac{\sigma_x}{\mu_x} \right)^2 \right\} \cdot \sqrt{2 \cdot \frac{\left| \left(\frac{\hat{\sigma}_z}{\hat{\mu}_z} \right)^2 - \left(\frac{\sigma_x}{\mu_x} \right)^2 \right|}{1 + \left(\frac{\sigma_x}{\mu_x} \right)^2}} \quad (3.5)$$

in equation (3.5), the radical expression is now unsigned. The sign has been moved to a place in front of the root, and is determined by the operation "sign{•}". The following applies:

$$\text{sign} \{ c \} = \begin{cases} 1, & c > 0 \\ 0, & c = 0 \\ -1, & c < 0 \end{cases} \quad (3.6)$$

According to equation (3.5), the estimate may yield negative modulation factors. This is unimportant as only the mean value of the modulation factor must be zero or positive.

4. ESTIMATION OF THE NUMBER OF SHIPS AND THEIR DISTANCE

By means of the interference patterns in the spectrogram, it is possible to estimate the number of disturbing ships and to make a rough estimate of the distance. However, this requires the spectrogram to be available in a form which will allow visual evaluation, e. g. as a display on a grey-shade recorder or on a TV screen.

If the ambient noise measurement is being disturbed by more than one ship, the corresponding interference patterns are superimposed on one another. In the spectrogram, this superimposition is clearly recognisable, especially for the practised eye. An example is shown in Fig. 3. There, two principal sources of disturbance are involved. The superimposition is clearly visible in the time interval from 15:10 to 15:17.

The interference pattern in Fig. 2 had shown that the pattern depends on distance. The magnitude of the gradient of the "interference lines" is propor-

tional to the distance between the disturbance source and the measurement point. This fact is used to make a passive estimate of distance. In addition to the modulation factor, we thus also obtain an important parameter for situation assessment in ambient noise measurement.

The method described here works with relatively simple aids. It requires that the sources of disturbance are approximately on a collision course with respect to the measurement point. Since this requirement is only more or less fulfilled in practice, the estimate can only produce rough values for the distance.

Fig. 4 summarises the main steps in the evaluation. In addition to the measured interference pattern, results from the model calculation are required: for the evaluation frequency F_0 , we require the interference wavelength IWL (also called the "horizontal interaction distance") Λ of the mode pair which is dominant in the measured interference pattern. Secondly, the frequency-dependent changes of the IWL, $\partial\Lambda/\partial f$, must be determined. These tasks can be performed by computer programs such as those described in [10] or [11] or by much simpler procedures [12].

Two things must be determined from the measured spectrogram - firstly, the number k of interference wavelengths passed through per unit time by the disturbing ship (k does not have to be an integer), and secondly the gradient of the interference lines.

The expression $k \cdot \Lambda/T$ represents the speed of approach or departure, v . The distance can be estimated from the determined values according to the following formula:

$$r \approx v \cdot \left[\Lambda \cdot \frac{1}{\frac{\partial \Lambda}{\partial f}} \cdot \frac{\partial t}{\partial f} \right]_{f=F_0} \quad (4.1)$$

In this formula, the interference line gradient $\partial t/\partial f$ is the most important parameter. The other parameters act as scaling factors to some extent.

It is immediately apparent that k can be estimated with sufficient reliability if and only if the interference maxima along the line $f = F_0$ are equidistant. However, this is so only if the speed of approach or departure of the disturbance source (relative to the measurement point) is constant within the evaluation time T .

5. DISCUSSION OF THE MEASUREMENT RESULTS

The evaluation results of many experiments at sea show that the proposed method for estimating the influence of disturbance noise is practicable.

The measured data come from North Sea areas with a water depth of about 43 m. The measurements were performed in the spring of two successive years. An omnidirectional hydrophone was used to receive the sound.

The mean mode interference modulation factor \bar{M}_T was evaluated in the frequency band from 50 Hz to 450 Hz. The duration T of the evaluation interval was fixed at 128 sec. The normalisation produced a computed value of 1.054 for σ_x/μ_x .

All evaluations gave similar results, so we can restrict ourselves here to a discussion of a few examples. In Figs. 5, 6 and 7, the modulation factor \bar{M}_T is plotted against time. The shaded area symmetrical to the modulation factor \bar{M}_T indicates the standard deviation of the $K = 401$ individual modulation-factors. A new estimation of the modulation factor was carried out every 20 sec, so there is an overlap of 108 periodograms.

The modulation factor \bar{M}_T in Fig. 5 shows the typical variation with time as a ship passes by: at the beginning of the experiment, the disturbing ship is far away and the modulation factor is small. As the distance between the ship and the measurement point decreases, the modulation increases. After the ship has passed the closest point of approach (CPA), the modulation decreases again. The drop in the modulation factor in the region of the CPA is due to the particular form of the interference pattern in this region. A glance at the spectrogram in Fig. 2 which refers to this experiment will make this clear.

At the beginning and end of the experiment, the modulation factor in Fig. 5 stays at a value of about 0.2. However, the passing ship did not have any disturbing influence here. Reduction of the modulation factor to zero was prevented here by slight disturbances of a non-definable type. These disturbances can be recognised in the original plot of the spectrogram. (Owing to the copying process, the grey shades are unfortunately not reproduced very well, so that it is no longer possible to see all of the details in the reproduced spectrograms.)

If sources of disturbance are present, the model is an appropriate one. This has been shown by the measurement results. It has not yet been possible to carry out the test for the case in which disturbance sources are absent, since there were always slight disturbances in the sea areas at all available measurement times.

The noise for Fig. 5 had been measured with a hydrophone situated about 1.5 m above the bottom. Fig. 6 shows an example from a measurement 5 m below the surface of the water. Here too, a ship passed by. The principal difference between the two examples is to be found in the time period after the instant of CPA: the decrease in the modulation factor with time is much steeper in Fig. 6.

Whereas in Fig. 5 the increase and decrease of the modulation factor before and after the CPA are roughly symmetrical, the variation in Fig. 6 is very asymmetrical. This effect was found generally. It is probably due to a strong screening effect produced by the wakes of the ships.

Fig. 7 shows the modulation factor \bar{M}_T as two sources of disturbance pass by. In the first 25 minutes of the experiment, the first disturbance source is dominant, and then the second one is dominant. A corresponding excerpt of the spectrogram for the time period from 10 minutes to 15 minutes after the start of the experiment is shown in Fig. 3.

No representative results can be offered for the distance estimate since the accuracy of the results depends to a very large extent on the amount of practice which the estimator has had - especially in the case of complicated interference patterns. We want to show, by means of an example, that the evaluation method works successfully.

We shall evaluate a part of the experiment which gave the spectra shown in Fig. 2. For this experiment, the model calculation gives an interference wavelength $\Lambda_{1,2} \approx 780$ m and a gradient $\partial \Lambda_{1,2} / \partial f \approx 3.55$ m / Hz, determined at an evaluation frequency $F_0 = 200$ Hz. In the spectrogram, the number of interference wavelengths which have been passed through in 5 minutes is estimated as 3.9. Because the pattern is very complicated, a "ten point divider" is required for this. With the aid of this instrument, the equidistant interference-maxima can be found quickly. The distances estimated after the $\partial t / \partial f$ evaluation are listed for various times in Table I.

TIME SINCE START OF EXPERIMENT (minutes)	ESTIMATED DISTANCE (nautical miles)	DISTANCE MEASURED BY RADAR (nautical miles)
9	3.4	3.55
10	3.0	3.25
11	2.6	2.95
12	2.4	2.55
13	2.1	2.25
14	1.8	1.8
15	1.5	1.5

TABLE I: EXAMPLE OF DISTANCE ESTIMATION

For the sake of comparison, the radar measurements are also listed here. They are not normally available during application of the proposed method. Their purpose here is to act as reference values. The comparison shows that the estimate gives acceptable values.

6. CONCLUSIONS

A method was to be developed with which the influence of disturbing ship's noise on the ambient noise measurement could be estimated. This objective has been achieved by the defining of a mode interference modulation factor. The theoretical model selected for this can be used in practice. This has been demonstrated with the aid of measurement results.

The additional information gained from mode interference, namely information about the distance of the disturbance sources, extends the basis for situation assessment during ambient noise measurement.

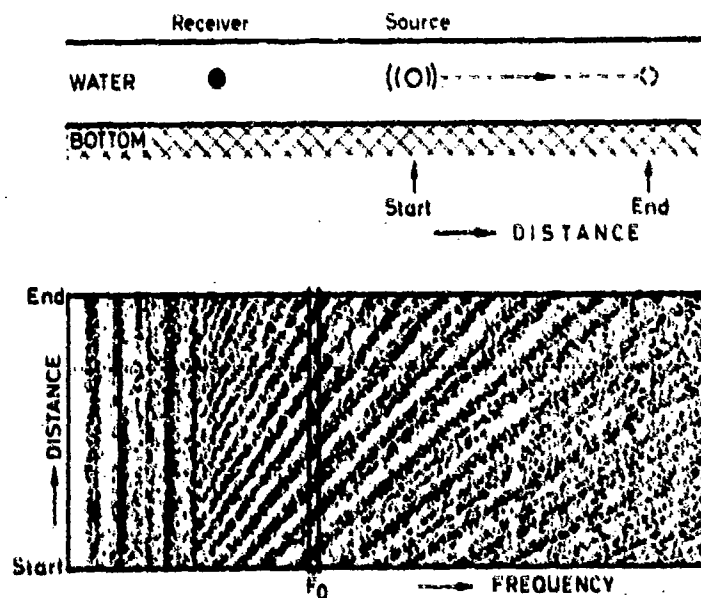
The mode interference modulation factor offers the possibility of automating the monitoring of the measurement process; the idea is to use a threshold decision.

In the evaluation of the mode interference modulation factor carried out so far, all periodogram components within a specified frequency band have been taken into account. However, it may be better to evaluate only some of the periodogram components within a specified frequency band, namely those with the largest modulation factors. In this way, frequency bands involving poor propagation behaviour would be excluded from the evaluation process. This would lead to an improvement in the estimation result.

REFERENCES

- [1] R.S. Urick, Principles of Underwater Sound, McGraw-Hill, New York, 1975, Ch. 7, pp. 181 - 210
- [2] P. Wille, "Noise Sources in the Ocean (Part I)", SACLANTCEN Conf. Proc. No.17, Oct. 1975, pp 2-1 - 2-20
- [3] C. B. Officer, Introduction to the Theory of Sound Transmission, McGraw-Hill, New York, 1958
- [4] I. Tolstoy and C.S. Clay, Ocean Acoustics: Theory and Experiment in Underwater, McGraw-Hill, New York, 1966
- [5] I. Tolstoy, Wave Propagation, McGraw-Hill, New York, 1973
- [6] R.A. Altes, "Detection, estimation, and classification with spectrograms", J. Acoust. Soc. Am., Vol. 67, No 4, April 1980, pp. 1232 - 1246
- [7] D.E. Weston and K.S. Stevens, "Interference of wide-band sound in shallow water", Journal of Sound and Vibration, Vol. 21, No. 1, 1972, pp. 57 - 64

- [8] G. Kracht. Der Einfluß von Modeninterferenzen auf das Spektrogramm von Schiffsgeräuschen, Krupp Atlas-Elektronik, Bericht BL 5100, Bremen, 1974
- [9] G. Hermstrüwer, Statistische Verteilungen und Detektion eines periodischen Zeitsignals im weißen gauß'schen Rauschen für normalisierte Periodogramme, Krupp Atlas-Elektronik, Bericht BL 5526, Bremen, 1976
- [10] A.V. Newmann and F. Ingenito, A normal mode computer program for calculating sound propagation in shallow water with an arbitrary velocity profile, Naval Research Laboratory Memorandum Report 2381, Washington, 1972
- [11] J.F. Miller and F. Ingenito, Normal mode FORTRAN programs for calculating sound propagation in the ocean, Naval Research Laboratory Memorandum Report 3071, Washington, 1975
- [12] H. Bendig, Simulationsrechnungen zum Thema Modeninterferenz im Flachwasser, Krupp Atlas-Elektronik, Bericht BL 5528, Bremen, 1976



MEASUREMENT OF INTERFERENCE PATTERN

FIG. 1

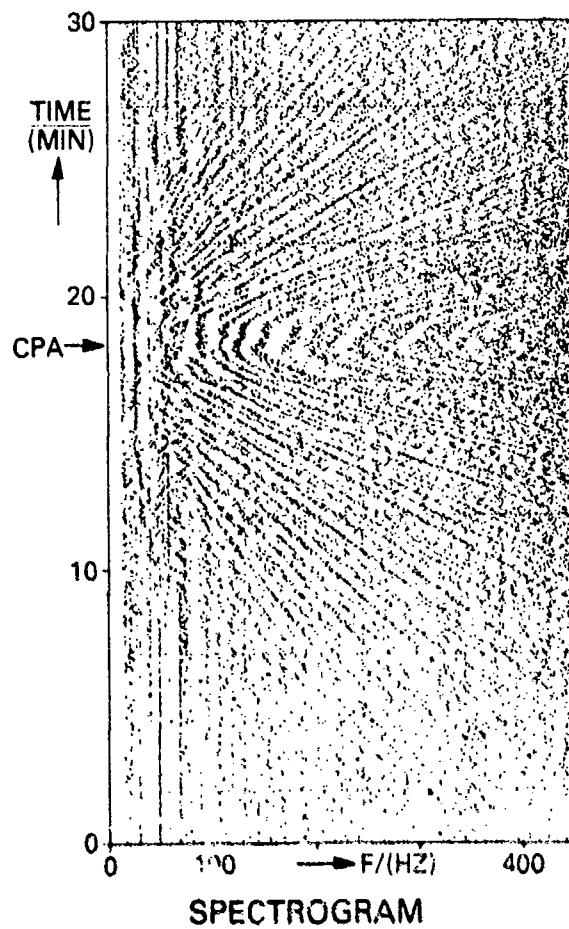


FIG. 2

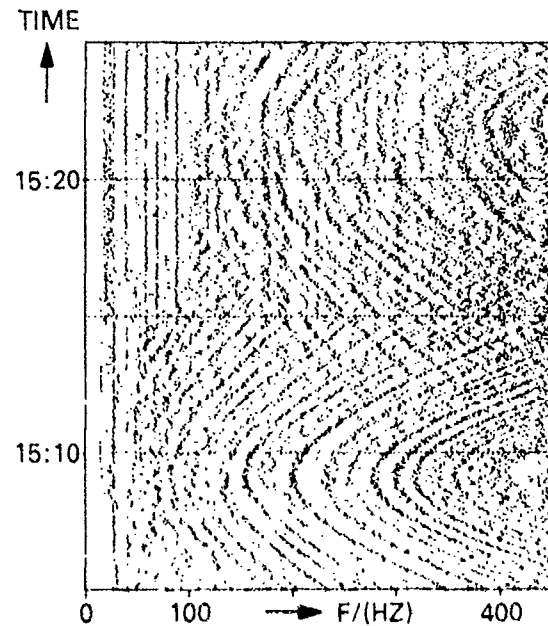
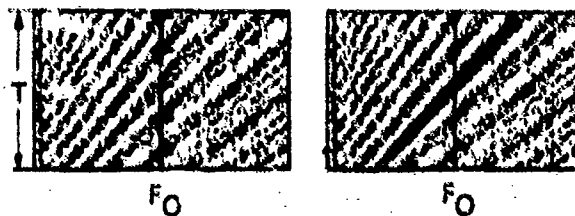


FIG. 3

MODEL CALCULATIONS:

- $\Lambda(f)$
- $\partial \Lambda(f) / \partial f$

MEASUREMENT:



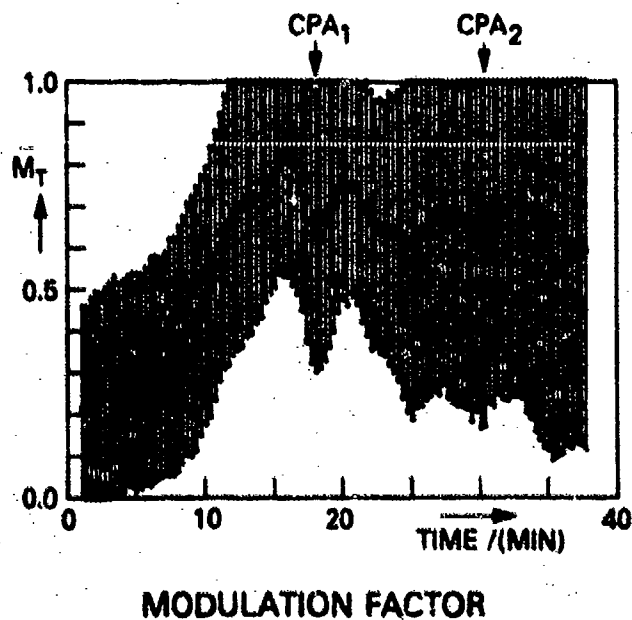
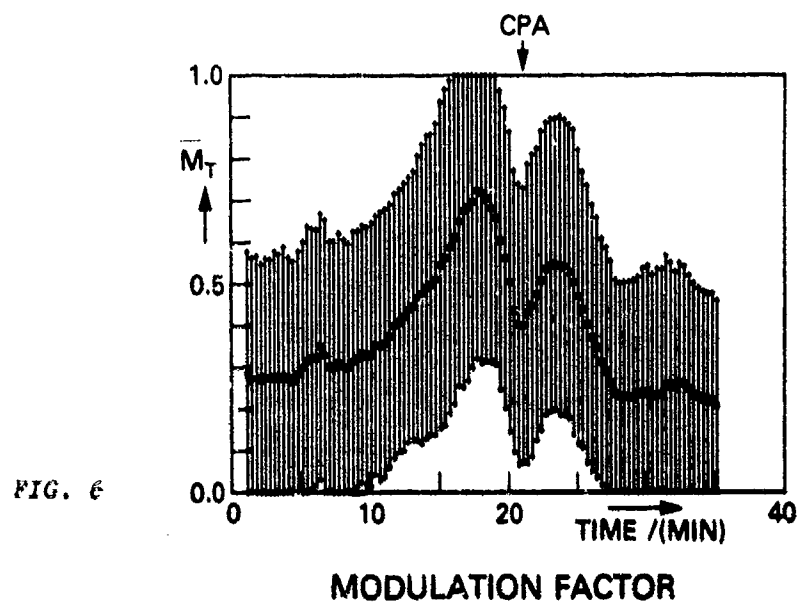
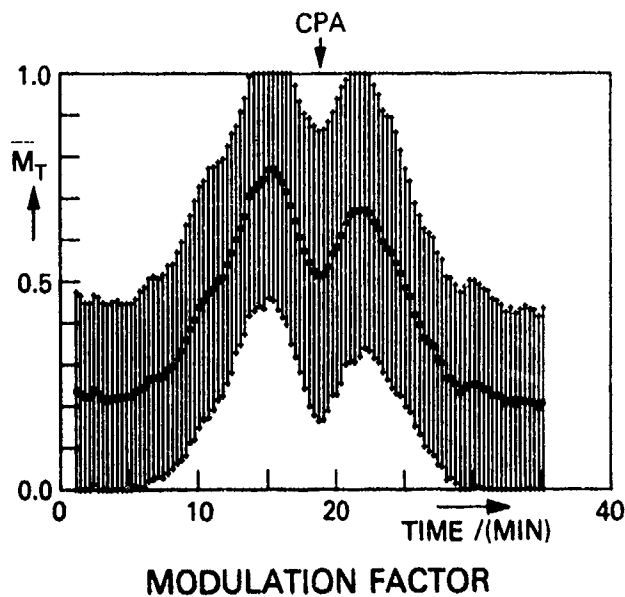
$$v \approx \frac{k \cdot \Lambda}{T}$$

$$\partial t / \partial f$$

$$r \approx v \cdot \begin{bmatrix} 1 & \partial t \\ \Lambda & \partial \Lambda \\ \partial f & \partial f \end{bmatrix} \quad f = F_0$$

FIG. 4

ESTIMATING THE DISTANCE



OPTIMAL DETECTION AND TRACKING OF ACOUSTICAL NOISE SOURCES
IN A TIME-VARYING ENVIRONMENT

by

Hendrik Van Asselt
SACLANT ASW Research Centre
La Spezia, Italy

ABSTRACT

A dynamical detector estimator is derived for nonlinear nongaussian signal processes based on Bucy's representation theorem which is the fundamental result in stochastic filtering. A quantized version of two-dimensional conditional probability density functions is generated for bearing and bearing-rate as well as for frequency and frequency-rate. Results of the analysis of real data for bearing and bearing rate are presented and discussed using optimal nonlinear filtering techniques.

INTRODUCTION

Target detection and tracking from passive sensors is a nonlinear estimation problem and has practical significance. This paper discusses this problem and presents an analysis of real target data measured in shallow water.

The present state of the art makes it feasible to develop detection and estimation algorithms in discrete time, since nonlinear processing algorithms based on Bayes law are developed in discrete time.

In this paper we have restricted ourselves to hardware that is available today, which means that the closeness of approximations to optimality depends largely on the dimensionality of the signal processes.

We have divided our system into two parts, bearing and frequency estimators, which each turn out to be two-dimensional dynamical processes having nonlinear system functions and linear observation functions. Because of the lower dimensionality of bearing and frequency, when the state spaces are decoupled, one can use a more accurate approximation to optimality than for the coupled state/space representation if one thinks in terms of the number of computations required and of the real-time implementation.

For bearing and frequency estimation we are able to generate quantized versions of two-dimensional conditional probability density functions and represent these as a set of point masses on a moving mesh. A detailed discussion is given in <1>.

Our motivation for this type of data-processing scheme is that the nature of most signals relating to passive sonar detection and tracking are multidimensional signal processes and are commonly dynamical, nonlinear, and nongaussian and, further, may have time-varying statistics. "Classical" signal-processing schemes based on the stationary steady-state filtering theory therefore often give undesired performance, especially in cases of low signal-to-noise ratios.

1 SYSTEMS CONSIDERATIONS

Kalman filtering is often applied for designing suboptimal nonlinear estimators. The procedure is that the models are linearized and then the linear theory is applied. This is one of the simplest methods of deriving suboptimal data-processing schemes for nonlinear dynamical signal processes. Often, however, these techniques lead to undesirable performance, as we will illustrate in a simple example.

Figure 1 compares a recursive realization of the kalman filter with the discrete Bayes-Law estimator for the case of truncated gaussian densities. The a-priori conditional probability density function is indicated by \hat{p}_{n-1} having a variance $\hat{P}_{n-1} = 0.6$. The probability density function of the observations Z_n has a variance $R_n = 1.2$ and the system noise has a probability density function m and variance $Q_n = 0.696$.

If we calculate the a posteriori conditional probability density function, then both the kalman estimator and the Bayes-Law estimator provide almost the same output variance: $\hat{P}_B = 0.6$ and $P_k = 0.62$. The difference results from the fact that Bayes Law computes on the real truncated gaussian densities whereas the kalman filter assumes non-truncated densities.

Figure 2 makes the same comparison. Consider now \hat{p}_{n-1} ; the real a-priori conditional probability density function is nongaussian, whereas the kalman filter assumes it is gaussian, both having the same variance. Also the real probability density function Z of the input data is nongaussian and again the kalman filter assumes it is gaussian.

Comparing the results of this example we note that a kalman filter severely underestimates the conditional a-posteriori variance. As a consequence it will also severely underestimate the filter gain matrix. This causes too little information to be extracted from the measurements, leading frequently to divergence. This, of course, is not to blame the kalman filter, it is a result of its wrong application.

1.1 Implementation of a Bayes-Law System

Figure 3 shows the configuration of a Bayes-Law system. The input is obtained from a line array of 20 hydrophones approximately 2 m apart. This is followed by a conventional beamformer in order to sample the noise field passively. The beam-axes are 1° apart and the beamwidth is 5° at the 3 dB level.

All the beams do not necessarily carry the same levels of energy and the energy levels per beam fluctuate within a range of approximately 10 dB.

Along the array we observe the signal, which is "more or less" coherent. We cannot specify a measure of coherence, because it is not a constant. After beamforming we could observe this as presented in Fig. 4. The shaded zone shows the collection of 2000 beamformer output samples, where we have eliminated time dependence. If this shadowed zone were to collapse to a broken line we would receive a fully coherent signal; so a measure of noncoherence is indicated by the width of the shaded area. Note also that the noise field is nonhomogeneous.

Given these sample functions we then evaluate the likelihood function in order to generate a probabilistic structure in space.

In Fig. 3 these observations are indicated as $Z[h(\xi), G(\xi)]$, where $h(\xi)$ is the input function and $G(\xi)$ the array gain in a given direction. We then continue by two-dimensionally convolving the probabilistic structure described above with the product of the probability density function $m[y, f(\xi), r]$ describing the target trajectory noise and the a-priori conditional probability density function $\hat{D}_{n-1}(\xi)$ (see also Ch. 4 of <2>, especially pp 43-59).

We have m modelled as a gaussian density function, the arguments y (and dummy ξ) describing the target-motion variables in state/space (bearing, bearing rate and frequency, frequency rate) and the target-motion model represented by $f(\xi)$, where r is the average manoeuvring time. During the detection phase the target motion is modelled as a linear trajectory in cartesian coordinates having random accelerations (the constant-speed model). During the tracking phase we use a constant-acceleration model in order to allow target manoeuvring. This can be achieved by changing the autocorrelation time.

After we have generated the conditional probability density function, it is simple to compute mean values and variances, as is indicated in Fig. 3. Figure 5 presents the estimated variances of a) bearing and b) bearing-rate and shows the potential of the nonlinear optimal estimator.

Figure 6 shows a typical example, where the dynamics behave reasonably stationary. We cut the density function into two halves along the correlation axis in order to study its transient during the detection phase (Fig. 4). At the start, t_0 , we have no information, which is represented by a uniform initial probability density $\hat{D}(t_0)$. Then at intervals of 2 seconds we update the estimated density $\hat{D}(\cdot)$, e.g. t_1 refers to 10 seconds processing time. We stop the detection phase after t_R , which is where the detector has reached the steady-state solution. Table 1 presents the detector performance numerically, with reference to the highest level, which is at 91° and zero degrees per second. After the detection phase the autocorrelation time of the target accelerations is increased so that the transient is observed from detection to tracking phase. Figure 7 shows a sequence of pictures showing both transients. Figure 8 is another example, in which the estimators have been left in the detection mode so as to show the detectors capability of handling dynamical processes (a relative fast ship moving through a fixed set of beams).

A sequence of 2000 sequentially estimated conditional probability densities has been filmed to show in more detail the systems dynamics. This pictorial display demonstrates why techniques based on stationary steady-state filtering theory cannot work properly. This is because often averaging time is too long with respect to the non-stationarity of the underlying signal-process <3>.

2 DETECTOR DERIVATION

The stochastic differential equation representing a diffusion process is:

$$dx_t = f(x_t, t)dt + \sigma(x_t, t)du_t, \quad (\text{Eq. 1})$$

where x_t , u_t and $f(x_t, t)$ are n -dimensional vectors

and $\sigma(x_t, t)$ is an $n \times n$ matrix.

Assume that a solution exists and is unique and that the domain of the solution will be the bounded time interval $[a, b]$. The process $\{u_t\} = \{(u_{1,t}, u_{2,t}, \dots, u_{n,t})^T\}$ defines the vector of n independent Brownian motions. The components of $f(x_t, t)$ and $\sigma(x_t, t)$ are continuous in t and Lipschitz-continuous in x_t .

For the m -dimensional observation process we use the differential equations

$$dz_t = h(x_t, t)dt + \gamma(t)dv_t \quad \text{signal present} \quad (\text{Eq. 2})$$

$$dz_t = \gamma(t)dv_t \quad \text{signal absent}$$

where dx_t is defined in Eq. 1,

$$\begin{aligned} x(a) &= c, \\ z(a) &= 0, \end{aligned} \quad (\text{Eq. 3})$$

v_t is an m -dimensional Brownian motion, independent of u_t .

Then, following <4>, consider

$$dx_t = f(x_t, t)dt + \sigma(x_t, t)du_t \quad (\text{Eq. 4})$$

$$dz_t = [f(x_t, t) + \sigma(z_t, t) \gamma(z_t, t)]dt + \sigma(z_t, t)dv_t, \quad (\text{Eq. 5})$$

where $t \in [a, b]$ $x(a) = z(a)$

f, γ are n -vectors and σ is an $n \times n$ matrix

f, σ and γ are measurable in both arguments

$$\int_a^b |\gamma(x_t, t)|^2 dt < \infty \quad \text{w.p.1}$$

$|\gamma(x_t, t)| < \gamma_0(|x_t|)$; γ_0 being a nondecreasing function of a real variable.

Then the measures m_x and m_z induced on the space of all continuous functions in $\mathbb{R}^n, C[a,b]$ by the processes $\{x_t\}$ and $\{z_t\}$ are mutually absolute continuous. The Radon-Nikodym derivative dm_x/dm_z is then given by

$$\frac{dm_x}{dm_z} = \exp \left[\int_a^b Y^T(x_s, s) dv_s - \frac{1}{2} \int_a^b |Y(x_s, s)|^2 ds \right] \quad (\text{Eq. 6})$$

The nonlinear detection and estimation problem is described <2> by:

$$dx_t = f(x_t, t)dt + \sigma(x_t, t)du_t \quad (\text{Eq. 7})$$

$$dz_t = h(t)x_t dt + y(t)dv_t \quad (\text{Eq. 8})$$

The conditional mean for this estimation problem is given by

$$E[x_t | z_r; a \leq r \leq t] = \hat{x}_t = \frac{E_{mx}[\Omega_t x_t]}{E_{mx}[\Omega_t]} \quad (\text{Eq. 9})$$

The expectation symbol E_{mx} defines integration with respect to the function space measure m_x generated by solving Eq. 7 and

$$\Omega_t = \Omega_t(x_r, z_r; a \leq t \leq r) = \exp \left[\int_a^t x_r^T h_r^T [Y_r^T Y_r]^{-1} dz_r - \frac{1}{2} \int_a^t x_r^T h_r^T [Y_r^T Y_r]^{-1} h_r x_r dr \right]$$

Recalling the detection problem of Eq. 2 and defining the process $\{P_t\}$ as

$$P_t = \lambda E_{mx}[\Omega_t],$$

which satisfies the stochastic differential equation

$$dP_t = \lambda_t^T h_t^T [Y_t^T Y_t]^{-1} dz_t - \frac{1}{2} \lambda_t^T h_t^T [Y_t^T Y_t]^{-1} h_t \lambda_t dt, \quad (\text{Eq. 10})$$

where λ_t is given by Eq. 9.

This can be proved because $E_{mx}[\Omega_t]$ is positive and finite w.p. 1; therefore P_t is well defined. If we apply the stochastic differential rule to $\lambda_t^T E_{mx}[\Omega_t]$ we obtain

$$\begin{aligned} dP_t &= \frac{E_{mx}[x_t^T h_t^T [Y_t^T Y_t]^{-1} \Omega_t] dz_t}{E_{mx}[\Omega_t]} + \\ &- \frac{1}{2} \frac{E_{mx}[x_t^T h_t^T [Y_t^T Y_t]^{-1} h_t x_t \Omega_t]}{(E_{mx}[\Omega_t])^2} \end{aligned}$$

and we find the likelihood function

$$dP_t = \hat{x}_t^T h_t^T [y_t^T y_t]^{-1} dz_t + \\ - \frac{1}{2} \hat{x}_t^T h_t^T [y_t^T y_t]^{-1} h_t \hat{x}_t dt$$

This concludes our detection process for a diffusion process in white noise.

CONCLUSIONS

A dynamical detector/estimator is presented for nonlinear nongaussian signal processors. We have shown the performance of the bearing/bearing rate estimator where the input was real data.

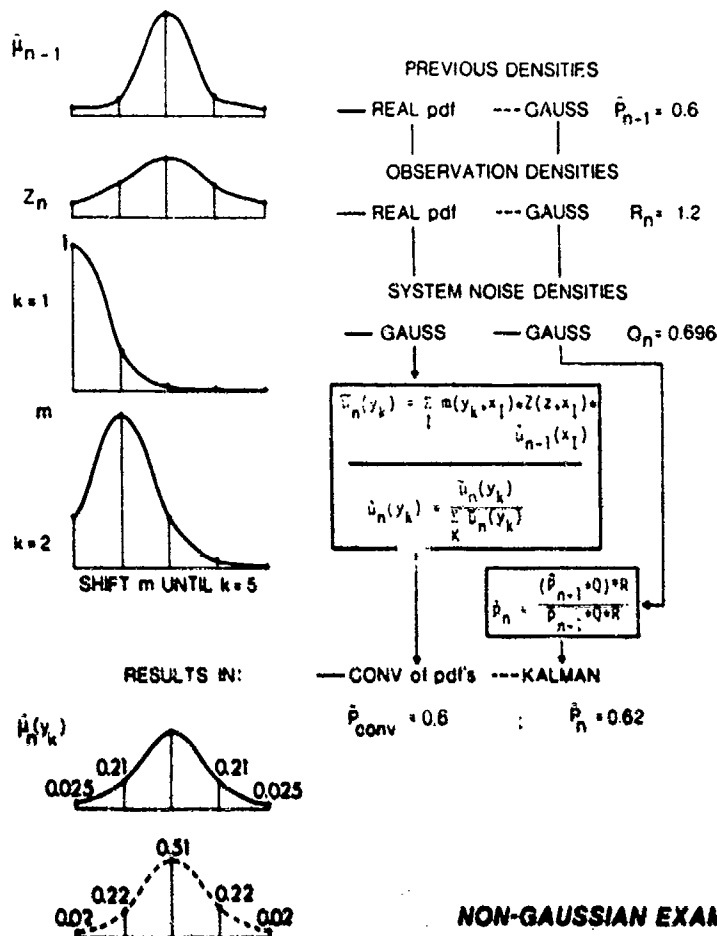
REFERENCES

1. BUCY, R.S. and SENNE, K.D. Digital synthesis of non-linear filters, Automatica, 7, 1981: 287-298.
2. BUCY, J. Filtering for stochastic processes with applications to guidance. New York, N.Y., Interscience publishers, John Wiley and Sons, 1968.
3. UMAPATH Reddy V., EGARDT, B. and KAILATH, T. Optimized lattice form adaptive line enhancer for a sinusoidal signal in broadband noise, IEEE Transactions, Acoustics, Speech and Signal Processing, 29, 1981: 702-710.
4. GIRSANOV, I.V. On transforming a certain class of stochastic processes by absolutely continuous substitution of measures, 1960.

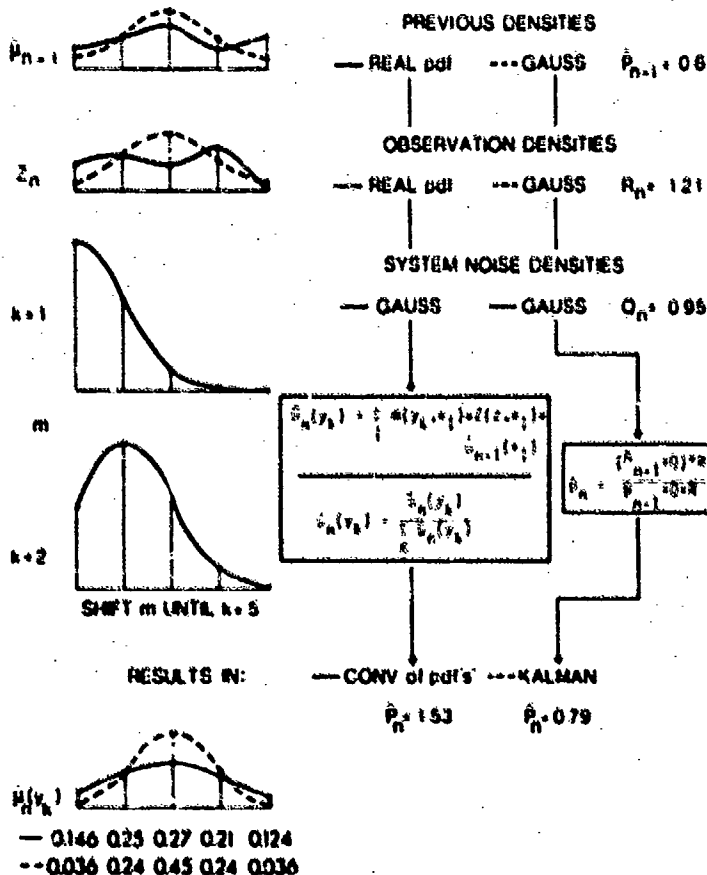
ADDITIONAL BIBLIOGRAPHY

- ITO, K. Lectures on stochastic processes. Tata Institute for Fundamental Research, 1961.
- STRATONOVICH, R.L. A new representation for stochastic integrals (English translation). SIAM Journal on Control and Optimization, 4, 1966: 362-371.
- SOSULIN, STRATONOVICH. Optimum detection of a diffusion process in white noise (English translation). Radio Engineering and Electronic Physics, 10, 1965: 704-714.
- KALMAN, R.E. and BUCY, R.S. New results in linear filtering theory. Journal Basic Engineering (ASME TRANS), 83, 1961: 95-108.

**TRUNCATED GAUSSIAN EXAMPLE
FOR LINEAR SCALAR SYSTEM**



NON-GAUSSIAN EXAMPLE FOR LINEAR SCALAR SYSTEM



SYSTEM CONFIGURATION

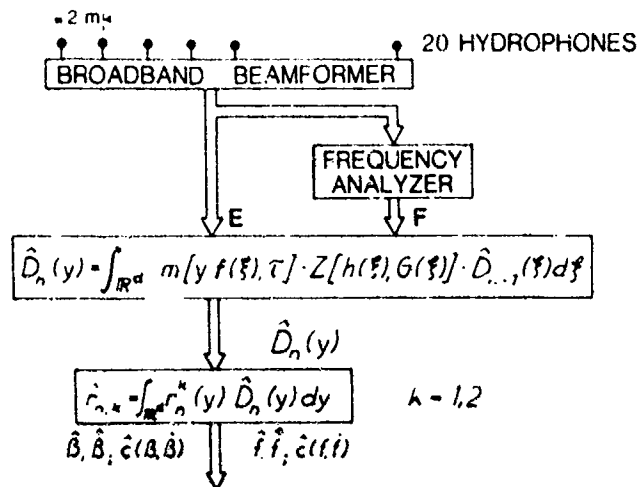


FIG. 3

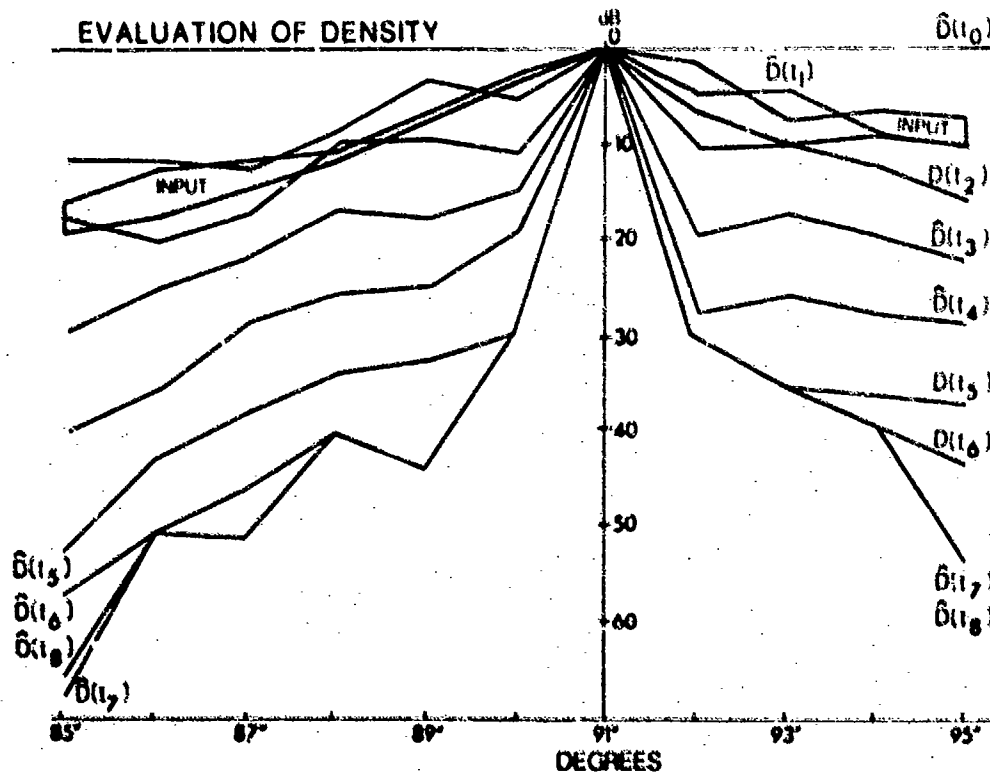


FIG. 4

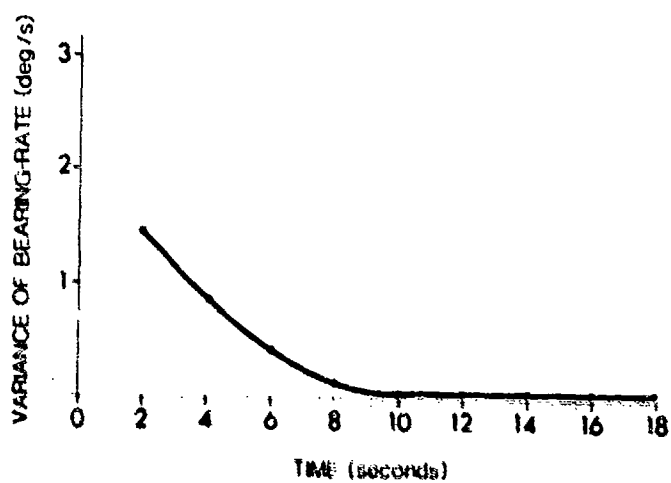
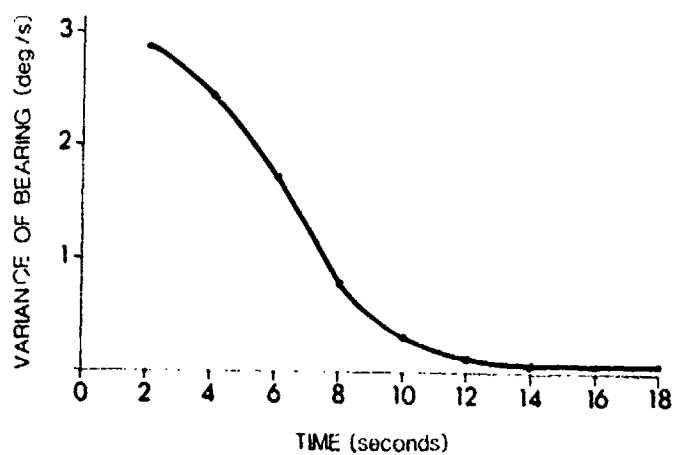


FIG. 5

QUANTIZED CONDITIONAL PROBABILITY DENSITY FUNCTION

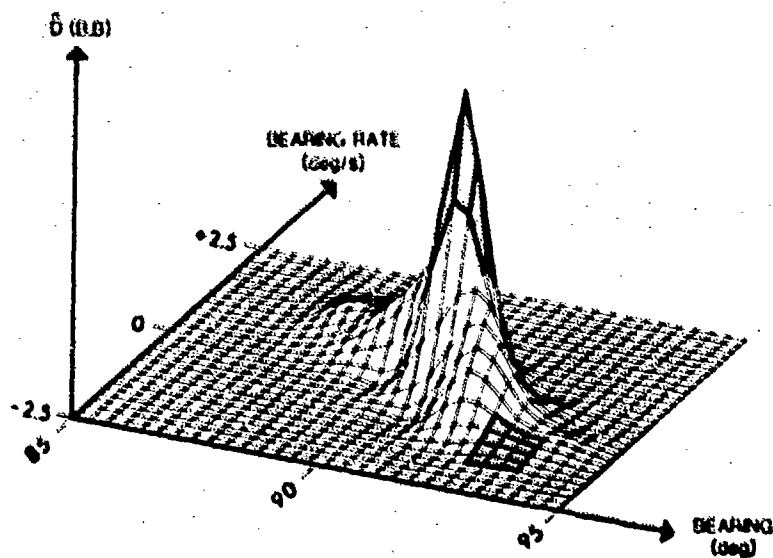


FIG. 6

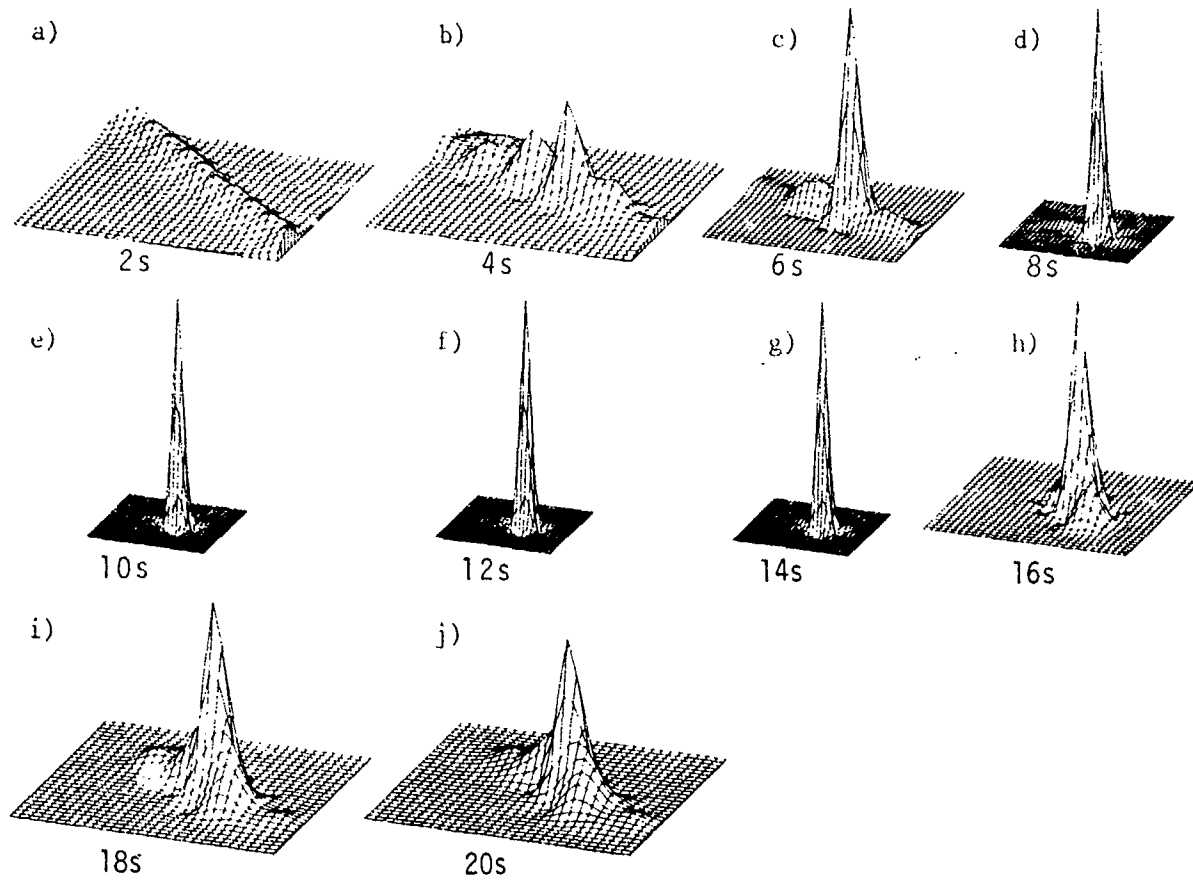


FIG. 7

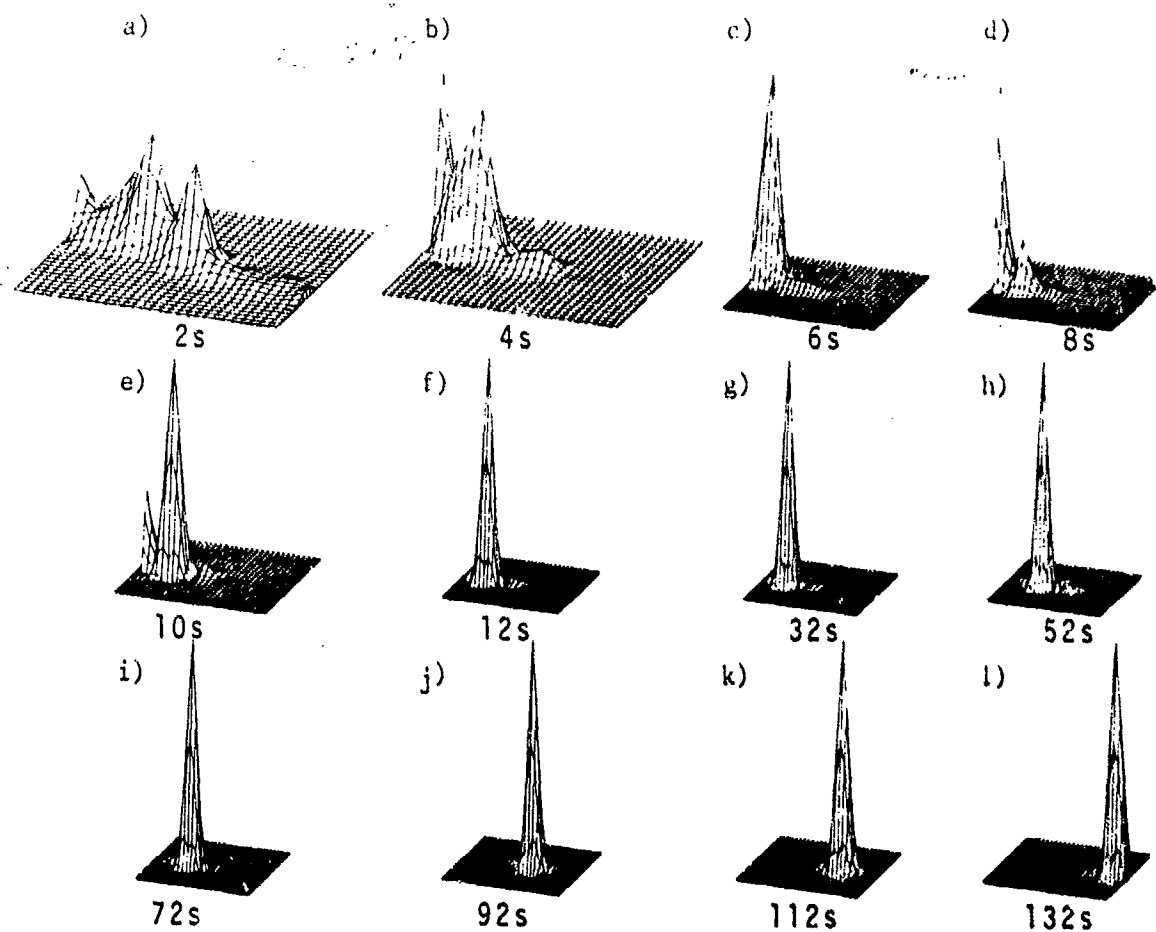


FIG. 8

QUANTIZED CONDITIONAL PROBABILITY DENSITY FUNCTION NUMERICAL VALUES

-106	-131	-134	-147	-164	-194	-203	-220	-302	-∞	-∞	2.5
-81	-98	-70	-106	-127	-130	-138	-179	-187	-281	-∞	2
-75	-73	-69	-65	-65	-97	-115	-115	-122	-171	-281	1.5
-74	-48	-62	-37	-61	-33	-80	-102	-96	-106	-151	1
-66	-58	-51	-42	-33	-29	-33	-66	-77	-84	-85	0.5
-94	-89	-78	-73	-62	-32	0	-47	-65	-63	-72	0
-107	-98	-90	-83	-74	-63	-33	-29	-36	-45	-53	-0.5
-172	-137	-128	-119	-117	-94	-65	-32	-50	-39	-55	-1
-302	-201	-151	-136	-135	-122	-112	-94	-65	-67	-71	-1.5
-∞	-303	-216	-201	-84	-165	-157	-145	-121	-100	-72	-2
-∞	-∞	-333	-240	-234	-225	-194	-175	-162	-150	-134	-2.5
85	86	87	88	89	90	91	92	93	94	95	$\frac{B}{B}$

← SPATIAL BINS (degrees) →

VALUES IN dB

↑ RATE BINS (degrees / s) ↓

TABLE 1

INFLUENCE OF BACKGROUND NOISE SPATIAL COHERENCE
ON HIGH RESOLUTION PASSIVE METHOD

by

Georges BIENVENU and Laurent KOPP
THOMSON-CSF, ASM Division, BP 53, 06801 CAGNES-sur-MER Cedex, FRANCEABSTRACT

New signal processing methods for passive listening have appeared recently : they are called "high resolution" methods because they have theoretically a better resolving power than conventional or adaptive beamforming. But they need additional knowledge on background noise structure, and particularly on ambient noise for low frequency. These methods are based on the estimation of the spectral density matrix of the signal received on the array and on the utilization of its eigenvectors and eigenvalues. This matrix contains the background noise spectral density matrix for which a good parametrized model is needed. Performances estimated by simulations show on one hand the interest of high resolution methods compared to conventional methods, and on the other hand their sensitivity to the background noise model which is used.

1 - INTRODUCTION

One of the main functions of an underwater passive listening system is the determination of the number of sources present in the medium, as well as their characteristic parameters. For that, one uses noises radiated by the sources which are received on the sensors of an array. The basic function is array processing which is traditionally carried out by conventional beamforming. Effort towards performance improvement has led first to adaptive array processing. It provides a gain which is limited by the signal to noise ratio of the sources. Recently, studies have been done on new methods which are more powerful [1-2-3] : they are called high resolution methods. But they need an additional hypothesis on the medium.

Adaptive array processing, as conventional beamforming, needs hypothesis only on the sources : they are point like, perfectly spatially coherent, and the wavefront shape from a source is a known function of the source position (the transfer function of the sensors is also supposed known). Let $\vec{r}(t)$ be the vector representing the signal received on the K sensors of the array. The correlation matrix of the received signal is :

$$C(\tau) = E[\vec{r}(t) \vec{r}^+(t+\tau)] \quad (1)$$

where $E()$ denotes expectation and \vec{r}^+ is the conjugate transpose of \vec{r} . With

the above hypotheses, the spectral density matrix, which is the Fourier transform of $C(\tau)$, of a source alone is equal to :

$$\Gamma(f) = \gamma(f) \vec{D}(f) \vec{D}^+(f) \quad (2)$$

where $\gamma(f)$ is the spectral density of the received signal and $\vec{D}(f)$ the source position vector, composed of the transfer functions between the source and each sensor, normalized by the transfer function between the source and a reference point of the array. This matrix is rank one, which is characteristic of its perfect spatial coherence.

The additional hypothesis needed by the high resolution methods concerns the spatial coherence of the background noise. In general, background noise is supposed to be statistically independent between the sensors [1] or suppressed [2]. High resolution methods have better performances than those of adaptive array processing thanks to that hypothesis. They suppose also that the noise field can be resolved : the number N of sources is less than the number K of sensors. The spectral density matrix of the received signals is equal to (sources and background noise are statistically independent) :

$$\Gamma(f) = \Gamma_B(f) + \Gamma_S(f) = \sigma(f) I + \sum_{i=1}^N \gamma_i(f) \vec{D}_i(f) \vec{D}_i^+(f) \quad (3)$$

$\Gamma_B(f)$ and $\Gamma_S(f)$ are respectively the spectral density matrices of the background noise and of the sources, I is the spatial coherence matrix of the background noise which is the identity matrix and $\sigma(f)$ its spectral density, $\vec{D}_i(f)$ and $\gamma_i(f)$ are respectively the position vector and the spectral density of the i th source.

2 - HIGH RESOLUTION METHOD PRINCIPLES.

High resolution methods are based on eigenvalue-eigenvector decomposition of the spectral density matrix $\Gamma(f)$. An eigenvector $\vec{V}(f)$ and its corresponding eigenvalue $\lambda(f)$, are defined by the relation :

$$\Gamma(f) \vec{V}(f) = \sigma(f) \vec{V}(f) + \sum_{i=1}^N \gamma_i(f) \vec{D}_i(f) [\vec{D}_i^+(f) \vec{V}(f)] = \lambda(f) \vec{V}(f) \quad (4)$$

It can be shown that $\Gamma(f)$ has :

- a) N eigenvectors $\vec{V}_i(f)$ ($i \in [1, N]$) that are the eigenvectors of the sources alone matrix $\Gamma_S(f)$ corresponding to the N non-zero eigenvalues $\lambda_{si}(f)$ of $\Gamma_S(f)$ the rank of which is equal to N ; the corresponding eigenvalues are equal to : $\lambda_i(f) = \lambda_{si}(f) + \sigma(f)$; these N eigenvectors are an orthogonal basis of the N dimensional source subspace spanned by the N position vectors $\vec{D}_i(f)$ of the sources ; then :

$$\sum_{i=1}^N \gamma_i(f) \vec{D}_i(f) \vec{D}_i^+(f) = \sum_{i=1}^N \lambda_{si}(f) \vec{V}_i(f) \vec{V}_i^+(f) \quad (5)$$

- b) $(K-N)$ eigenvectors $\vec{V}_i(f)$ orthogonal to the preceding ones and therefore to each position vector $\vec{D}_i(f)$:

$$\vec{V}_j^+(f) \vec{D}_1(f) = 0 \quad (6)$$

They are a basis of the (K-N) dimensional subspace orthogonal to the source subspace. The corresponding (K-N) eigenvalues are all equal to $\sigma(f)$, and therefore smaller than the previous ones.

From the above analysis, it is deduced that :

- a) The number K of sensors minus the number of minimum and equal eigenvalues gives the number of sources.
- b) The position of the sources can be determined by using :
 - either the source subspace and relation (5) as proposed in [1] or [2]
 - or the orthogonal subspace as proposed in [3] : as the eigenvectors of this subspace are orthogonal to each source position vector, if $\vec{D}(f, \vec{\theta})$ is a position vector according to the wavefront shape of the model (including propagation and array) and corresponding to a source the position of which is denoted by $\vec{\theta}$, the scalar products : $\vec{V}_j^+(f) \vec{D}(f, \vec{\theta})$ are equal to zero for each value of $\vec{\theta}$ corresponding to the position of a source in the medium. For stability and ambiguity reasons [3], the orthogonal subspace method uses the function :

$$G(f, \vec{\theta}) = \sum_{j=1}^{K-N} |\vec{V}_j^+(f) \vec{D}(f, \vec{\theta})|^2 \quad (7)$$

It is that separation into two subspaces, one which contains the sources, the source subspace, and the other which contains the background noise only, the orthogonal subspace, which gives to high resolution methods their main property : their asymptotic (infinite observation time) resolving power is infinite, that is to say two sources can be resolved even if they are very close together and very weak ; it is no longer limited by the input signal to noise ratio $\gamma_1(f)/\sigma(f)$ as it is for adaptive array processing.

The above properties are valid only for an infinite observation time. In practice, the observation time is limited and only an estimation $\hat{r}(f)$ of $r(f)$ is available. Therefore, only estimation of the source parameters can be obtained. The minimum eigenvalues of $\hat{r}(f)$ are not exactly equal but show a spread that depends upon the observation time. Thus the determination of the number of sources is an actual detection test with detection and false alarm probabilities : it must be noticed that this detection test of the number of sources does not need the wavefront shape knowledge.

Eigenvectors are also estimates of the actual ones and only estimates of the source positions are obtained. In particular, orthogonal subspace eigenvectors are not exactly orthogonal to the source position vectors and $G(f, \vec{\theta})$ (relation (7)) exhibits minimum instead of zeroes. Fig. 1 shows an example obtained by simulation. Receiving array is linear, composed of 12 equispaced sensors. There are two sources at infinity in the medium with bearings 0° and -5.3° and spatially incoherent background noise. Sources are in the same plane as array. The figure shows versus bearing the output spectral density of adaptive array processing γ_A and the inverse of $G(f, \vec{\theta})$, which exhibits spikes at the source position instead of minimum. The spectral

density matrix is estimated by :

$$\hat{\Gamma}(f) = \frac{1}{P} \sum_{i=1}^P \vec{X}_i(f) \vec{X}_i^+(f) \quad (8)$$

where $\vec{X}_i(f)$ is the discrete Fourier transform of the vector signal $\vec{r}(t)$ computed on a time duration equal to T . When the parameter P , that is to say the observation time, increases, the adaptive array response remains about the same while the response of $G(f, \theta)$ is improved : the spikes become more narrow.

The physical limitations to the asymptotically infinite resolving power of high resolution methods are given by the imperfect knowledge and the fluctuations of the background noise spatial coherence and of the source wavefront shape. Influence of the background noise spatial coherence is examined now.

3 - INFLUENCE OF BACKGROUND NOISE SPATIAL COHERENCE [4]

In fact, at sea, the background noise has not a spatial coherence matrix equal to an identity matrix. It is composed of several components : the sea noise, generated by the wind at the surface, the flow noise, generated along the array, and the traffic noise at the low frequencies. Generally, the electronic noise of the hydrophone channels is negligible.

So in the general case, the spectral density matrix of the background noise can be written :

$$\Gamma_B(f) = \sigma(f) J(f) \quad (9)$$

where $\sigma(f)$ is the spectral density and $J(f)$ the spatial coherence matrix of the background noise.

In that case, the properties of the eigenvectors and eigenvalues of the spectral density matrix stated in the preceding section, are no more valid. For example, in order to illustrate the phenomenon, the very simple case where the background noise is reduced to surface noise only [5] can be considered. The cross-spectral density between two sensors distant of d is equal to :

$$\gamma_d(f) = \sigma(f) \frac{2^m m!}{(2\pi f d/c)^m} J_m(2\pi f d/c) \quad (10)$$

where c is the sound velocity in the sea, $J_m()$ the Bessel function of order m , and m a modelling parameter.

The signals received on a linear array of 12 equally spaced sensors have been simulated. Bearing only is considered. Table 1 shows the eigenvalues obtained for a noise field composed of background noise only with a parameter m equal to zero, and for a length l between two adjacent sensors equal to 0.3 or 0.7 wavelength. If the spatial coherence matrix of the background noise was an identity matrix according to the hypothesis, all the eigen-

values would be equal : Table 1 shows significant differences

$\lambda=0.3\lambda$	2.45	2.26	1.34	1.29	1.13	1.10	1.05	1.00	0.32	0.05	0.004	2.10^{-4}
$\lambda=0.7\lambda$	2.67	2.22	1.38	1.11	0.76	0.61	0.53	0.55	0.54	0.53	0.52	0.52

Table 1 : Eigenvalues of spatially correlated background noise

Fig. 2 presents the diagram versus bearing θ of the eigenvector corresponding to the maximum eigenvalue of the spectral density matrix estimate $\hat{\Gamma}(f)$. The noise field is composed of background noise and of one source with bearing 5.4° and signal to noise ratio : -15 dB. The length between two adjacent sensors is half a wavelength. In this case, the eigenvector $\vec{V}_M(f)$ corresponding to the maximum eigenvalue of the theoretical spectral density matrix $\Gamma(f)$ is equal to the source direction vector. Therefore, its diagram defined by :

$$D(\theta) = |\vec{D}^+(f, \theta) \vec{V}_M(f)|^2$$

is equal to the classical beamforming diagram. Three diagrams are drawn on Fig. 2 : they are obtained for background noise the spatial coherence parameter m of which is equal to 0.5, 0.2 and 0.8. For 0.5 the spatial coherence matrix of the background noise is equal to the identity matrix according to the hypothesis. The diagram is effectively good for $m=0.5$. Diagrams show weak differences for $m=0.2$ and a completely different shape for $m=0.8$.

Fig. 3 presents results obtained with the same noise field as for Fig. 2, but for the orthogonal subspace method : expression (7). $G^-(f, \theta)$ is drawn instead of $G(f, \theta)$ as in Fig. 1, in order to see spikes instead of minimum. The diagrams $G^-(f, \theta)$ has been drawn for the same background noise spatial coherence parameters as before. The best result is obtained for $m=0.5$, that is to say when the spatial coherence of the actual background noise is equal to the spatial coherence of the model.

Fig. 4 presents results obtained also with the orthogonal subspace method. The noise field is composed of background noise and of two sources with bearings : 0° and 4° , and signal to noise ratio : -10 dB. Three diagrams $G^-(f, \theta)$ are drawn versus bearing θ for the same background noise spatial coherence parameters : 0.5, 0.2 and 0.8. There also the best result is obtained for $m=0.5$.

The few results given in that section show clearly that the background noise spatial coherence has to be known as exactly as possible.

4 - ADAPTIVITY TO BACKGROUND NOISE SPATIAL COHERENCE.

When the background noise spatial coherence matrix is not equal to the identity matrix :

$$\Gamma_B(f) = \sigma(f) J(f)$$

it can be shown [4] that if $J(f)$ is known, the problem can be solved. As $J(f)$ is hermitian, positive definite, it is possible to define a matrix $C(f)$

such that :

$$C(f) J(f) C^+(f) = I \quad (11)$$

Therefore, the spectral density matrix $\Gamma(f)$ transformed by $C(f)$ is equal to :

$$\Gamma_c(f) = C(f) \Gamma(f) C^+(f) = \sigma(f) C(f) J(f) C^+(f) + \sum_{i=1}^N \gamma_i(f) C(f) \vec{D}_i(f) \vec{D}_i^+(f) C^+(f) \quad (12)$$

As : $C(f) \vec{D}_i(f)$ is a vector, which can be written $\vec{D}_{ci}(f)$, the transformed matrix $\Gamma_c(f)$ is equal to :

$$\Gamma_c(f) = \sigma(f) I + \sum_{i=1}^N \gamma_i(f) \vec{D}_{ci}(f) \vec{D}_{ci}^+(f) \quad (13)$$

Therefore, the background noise has been spatially whitened, and the eigenvectors and the eigenvalues of the transformed spectral density matrix $\Gamma_c(f)$ have the properties stated in the theory (section 2). Of course, to recover the source positions, a transformed source position vector model $\vec{D}_c(\vec{\theta}, f)$ must be used, in expression (7) in particular :

$$\vec{D}_c(\vec{\theta}, f) = C(f) \vec{D}(\vec{\theta}, f) \quad (14)$$

So, the problem is solved when $J(f)$ is known.

In fact, it has been shown [6] that it is not necessary to know exactly the spatial coherence matrix of the background noise : it is only necessary that it may be modalized as a function of unknown parameters. In this case, the background noise spectral density matrix model can be written :

$$\Gamma_B(f, \vec{m}) = \sigma(f) J(f, \vec{m}) \quad (15)$$

where $\sigma(f)$ is unknown and \vec{m} represents the unknown parameter.

Let $C(f, \vec{m})$ be the matrix such that :

$$C(f, \vec{m}) J(f, \vec{m}) C^+(f, \vec{m}) = I \quad (16)$$

Let \vec{m}_0 be the parameter values of the actual background noise. If the eigenvalues of the transformed received signal spectral density matrix :

$$\Gamma_c(f, \vec{m}) = C(f, \vec{m}) \Gamma(f) C^+(f, \vec{m}) \quad (17)$$

are computed versus \vec{m} , when \vec{m} is equal to \vec{m}_0 , $(K-N)$ eigenvalues become equal and the other N are greater. In practice, of course, only an estimation $\hat{\Gamma}(f)$ of $\Gamma(f)$ is available. If the eigenvalues diagram of the matrix :

$$\hat{\Gamma}_c(f, \vec{m}) = C(f, \vec{m}) \hat{\Gamma}(f) C^+(f, \vec{m}) \quad (18)$$

is drawn versus \vec{m} , when \vec{m} is near \vec{m}_0 , a focusing spot is observed which is as much sharp as the estimate $\hat{\Gamma}(f)$ is better. The value of \vec{m} corresponding to that focusing spot gives estimates of the background noise parameter \vec{m}_0 and of the number of sources together. Eigenvectors and eigenvalues corresponding to that value of \vec{m} are used for source parameters estimation.

In order to show the ability of the method, simulations have been conducted, using the same array and noise field as in the preceding section: the background noise spatial coherence model (expression (10)) has one unknown parameter : m . The noise field is composed of two sources with bearings : 0° and 4° , and signal to noise ratio : -10 dB (as for Fig. 4), and the background noise spatial coherence parameter is equal to 0.5. Fig. 5 presents the plots versus m of the eigenvalues of the theoretical spectral density matrix (a), and of the matrix $\hat{\Gamma}(f)$ estimated with $P = 80$ (expression (8)) (b), and $P=400$ (c) (P is the number of instantaneous spectra integrated to estimate $\hat{\Gamma}(f)$). The focusing spot happens for $m=0.5$: it becomes sharper when P , that is to say the observation time, is increasing. The two higher eigenvalues which indicate the presence of the two sources are clearly seen.

This eigenvalue diagram is therefore an interesting mean to estimate the background noise spatial coherence parameters.

5 - CONCLUSION

The interest of high resolution methods is clearly demonstrated by their asymptotical performances. But in order to be used in practice, it is absolutely necessary to have a good parametrized model for the spatial coherence of the background noise and in particular of the ambient noise.

REFERENCES

- [1] W.S. LIGETT "Passive sonar : fitting model to multiple time series". Proceed. NATO ASI on Signal Processing, Aug. 1972, Loughborough (U.K) p 327-345
- [2] H. MERMOZ "Imagerie, corrélation et modèles" Annales des Télécommunications, Janv. Fév. 1976, t. 31, n° 1-2, p. 17-36
- [3] G. BIENVENU, L. KOPP "Principe de la goniométrie passive adaptative" Proceed. 7th Colloque GRETSI, Nice (France) 28 mai-2 juin 1979, p. 106/106/10
- [4] G. BIENVENU "Influence of the spatial coherence of the background noise on high resolution passive methods" Proceed. ICASSP-79, Washington D.C April 1979, p. 306-309
- [5] E.M. ARASE, T. ARASE "Correlation of ambient sea noise" JASA vol 40, n° 1, July 1966, p 205-210
- [6] G. BIENVENU, L. KOPP "Adaptivity to background noise spatial coherence for high resolution methods" Proceed. ICASSP-80, Denver, Co. April 1980 p 307-310

This presentation stems from researchs supported by Direction des Recherches Etudes et Techniques, Paris (France).

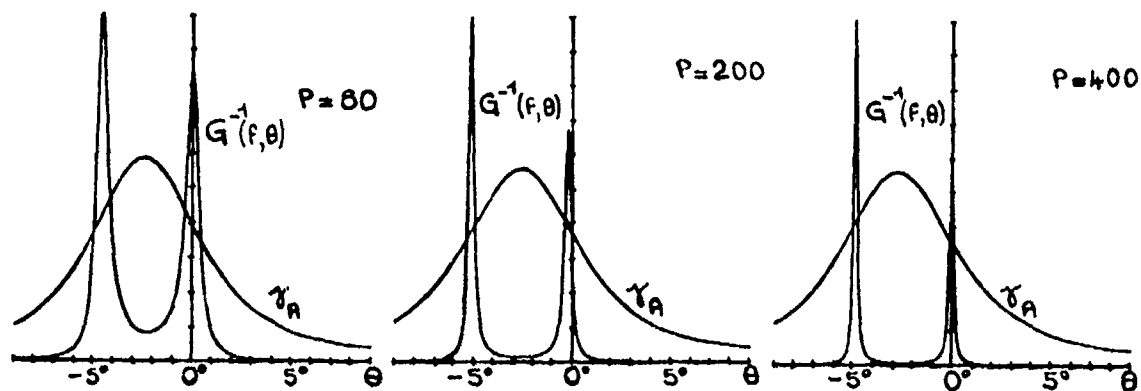


FIG. 1 ADAPTIVE ARRAY OUTPUT POWER γ_A AND INVERSE ORTHOGONAL SUBSPACE HIGH RESOLUTION METHOD RESPONSE $G^{-1}(f, \theta)$ VERSUS BEARING θ , FOR SPATIALLY INCOHERENT BACKGROUND NOISE AND TWO SOURCES WITH BEARINGS: 0° AND -5.3° , AND SIGNAL TO NOISE RATIO: 0 dB

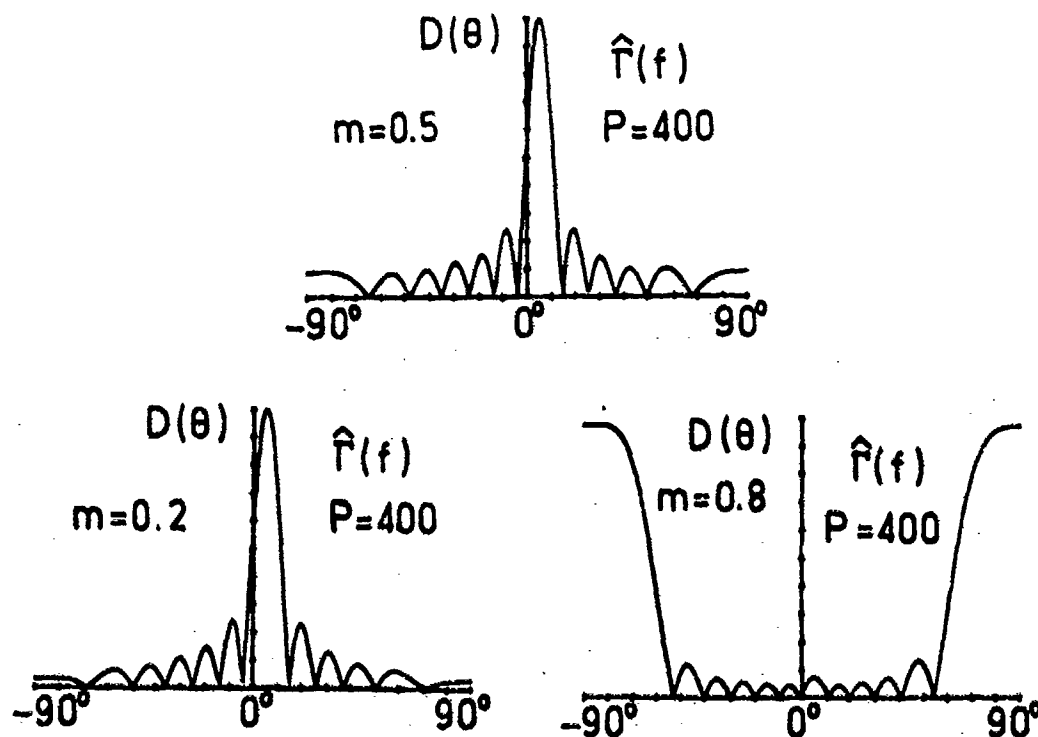


FIG. 2 MAXIMUM EIGENVECTOR DIAGRAMS VERSUS BEARING θ FOR SPATIALLY COHERENT BACKGROUND NOISE WITH SPATIAL COHERENCE PARAMETER m AND ONE SOURCE WITH BEARING: 5.4° , AND SIGNAL TO NOISE RATIO: -15 dB. For $m = 0.5$, background noise is spatially incoherent.

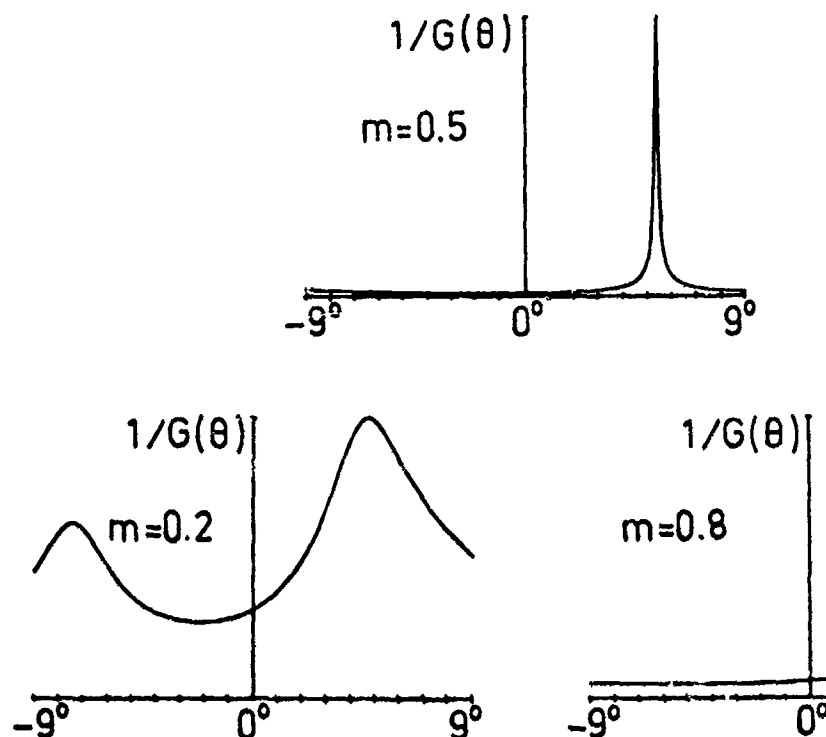


FIG. 3 INVERSE OF ORTHOGONAL SUBSPACE HIGH RESOLUTION METHOD RESPONSE $G^{-1}(f, \theta)$ VERSUS BEARING θ FOR THE SAME NOISE FIELD AS IN FIG. 2.

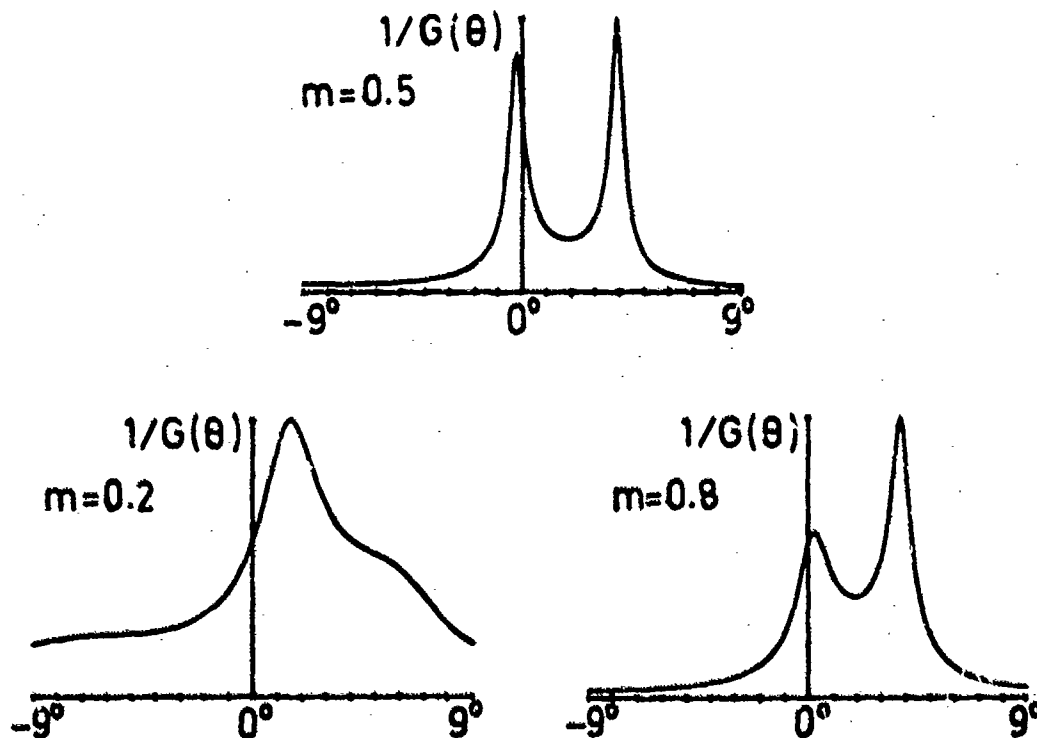


FIG. 4 INVERSE OF ORTHOGONAL SUBSPACE HIGH RESOLUTION METHOD RESPONSE $G^{-1}(f, \theta)$ VERSUS BEARING θ FOR THE SAME BACKGROUND NOISE AS IN FIG. 2 AND TWO SOURCES WITH BEARINGS: 0° AND 4° , AND SIGNAL TO NOISE RATIO: -10 dB.

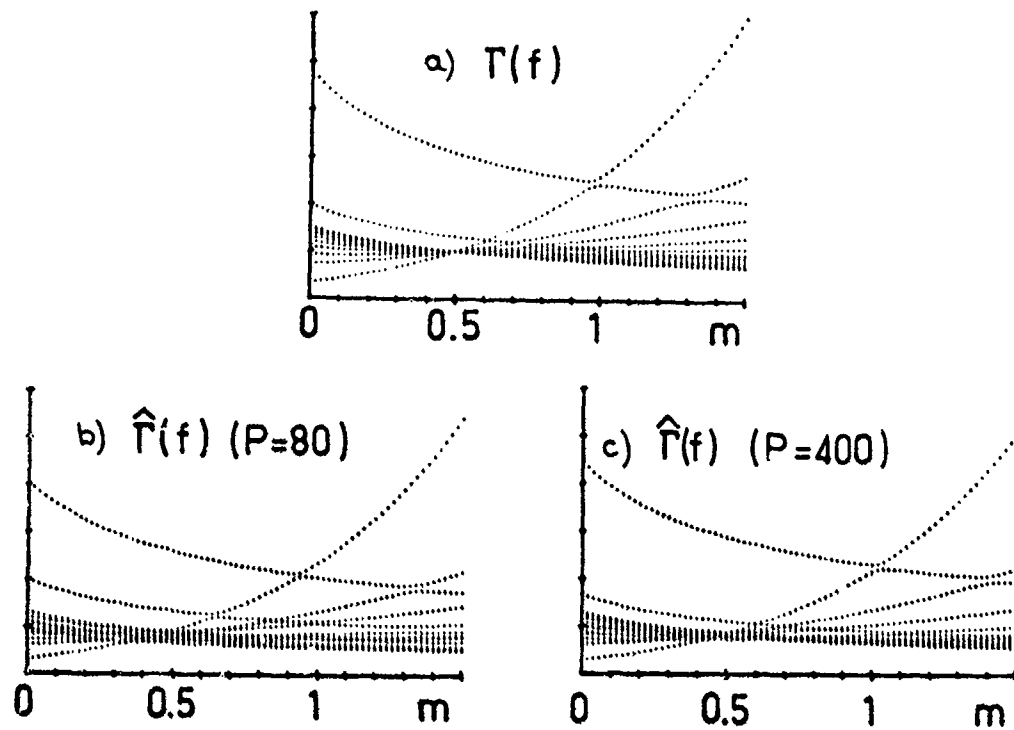


FIG. 5 EIGENVALUE DIAGRAMS FOR THE SAME NOISE FIELD AS IN FIG. 4 FOR THE THEORETICAL SPECTRAL DENSITY MATRIX: a), AND FOR THE SPECTRAL DENSITY MATRIX ESTIMATE FOR TWO VALUES OF THE OBSERVATION TIME (proportional to P): b) and c).

PERFORMANCE OF THREE AVERAGING METHODS,
FOR VARIOUS DISTRIBUTIONS

by

Albert H. Nuttall
Naval Underwater Systems Center
New London, CT 06320 USA

ABSTRACT

The performance of three averaging methods, namely the sample median, the sample arithmetic mean, and the sample geometric mean, are analyzed in terms of their bias, variance, and mean square error. The bias and variance are numerically evaluated for various parent distributions and plotted versus the number, N , of data points employed in the sample statistics. Also, the limiting behaviors, as N increases without limit, are derived. It is found that the best averaging method is very dependent upon the distribution of the data, with the sample median being favored for data with occasional large out-liers.

INTRODUCTION

Estimation of average properties, such as the average power in a particular angular sector and/or frequency bin is often accomplished by taking N independent measurements of such data and calculating a simple arithmetic average. However, when the desired process is subject to random fade-outs or occasional large out-liers, this sample arithmetic mean (SAM) is severely perturbed, and alternative averaging methods should be considered. Two possible candidates are the sample median (SM) and the sample geometric mean (SGM); these nonlinear processors of the available data have the potential of suppressing the deleterious effects mentioned above. Here we investigate* the performance of all three of these averaging methods in terms of the number, N , of independent data points employed in the pertinent average, and the parent distribution of the data. A wide variety of distributions are considered, some with parameters which allow for significantly different character and shapes of the governing probability functions.

*The basic analysis, derivations, and programs are given in Ref. 1.

DEFINITIONS

We have available N statistically-independent identically-distributed samples (random variables) x_1, x_2, \dots, x_N from some parent population with cumulative distribution function $P(u) = \text{Prob}\{x < u\}$ and probability density function, PDF, $p(u) = P'(u)$. The SAM of the available measurements is

$$a(N) = \frac{1}{N} (x_1 + x_2 + \dots + x_N); \quad (1)$$

the SMD is

$$q(N) = \text{middle value of } \{x_1, x_2, \dots, x_N\}, \text{ for } N \text{ odd}; \quad (2)$$

and the SGM is (for non-negative random variables)

$$g(N) = (x_1 x_2 \dots x_N)^{1/N} = \exp \left(\frac{\ln(x_1) + \dots + \ln(x_N)}{N} \right)$$

$$= B^{\left(\frac{1}{A} \frac{A \log_B(x_1) + \dots + A \log_B(x_N)}{N} \right)} \quad \text{for any base } B > 0 \text{ and scaling } A. \quad (3)$$

The last form in (3) for base $B = 10$ goes under the name of dB averaging.

As N tends to infinity, the sample quantities above tend to definite (non-random) limits. In particular, as $N \rightarrow \infty$,

$$a(N) \rightarrow \text{arithmetic mean} = \int du \, u \, p(u);$$

$$q(N) \rightarrow \text{median} = u_{1/2}, \text{ where } P(u_{1/2}) = \frac{1}{2};$$

$$g(N) \rightarrow \text{geometric mean} = \exp \left(\int du \, \ln(u) \, p(u) \right); \quad (4)$$

where we drop the prefix 'sample' for these deterministic quantities. The last result in (4) follows from the exponential form of the SGM in (3). If the $1/2$ in the median definition is replaced by r , we have for $q(N)$ the sample quantile of order r (Ref. 2, page 181).

The three limiting quantities in (4) will generally not be equal. For example, for an exponential parent PDF

$$p(u) = \frac{1}{m} \exp\left(-\frac{u}{m}\right) \text{ for } u > 0, \quad (5)$$

we have

$$\begin{aligned} \text{arithmetic mean} &= m; \\ \text{median} &= m \ln(2) = m .693; \\ \text{geometric mean} &= me^{-\frac{1}{2}} = m .562. \end{aligned} \quad (6)$$

Thus we define the bias of each of the sample statistics (1)-(3) as the difference between their mean value and their asymptotic value:

$$\begin{aligned} \text{bias \{SAM\}} &= \overline{a(N)} - \text{arithmetic mean}; \\ \text{bias \{SMD\}} &= \overline{q(N)} - \text{median}; \\ \text{bias \{SGM\}} &= \overline{g(N)} - \text{geometric mean}. \end{aligned} \quad (7)$$

By virtue of this definition, all three biases will tend to zero as $N \rightarrow \infty$; that is, all three estimators, (1)-(3), are asymptotically unbiased, each with respect to its desired value as given by (4), respectively.

It is then convenient to define a normalized bias, NB, for each sample statistic as

$$NB(N) = N \frac{\text{bias}}{\sigma}, \quad (8)$$

where σ is the standard deviation of parent PDF $p(u)$. The scale factor of N leads to a non-zero value of the normalized bias for large N , while the scale factor of σ is convenient in that it eliminates the dependence of the normalized bias on the absolute scale of the input data. For large N , (8) yields

$$\text{bias} \sim \sigma \frac{NB(\infty)}{N} \text{ as } N \rightarrow \infty; \quad (9)$$

thus $NB(\infty)$ is an important measure of quality of the particular sample statistic under consideration.

The variances of sample statistics (1)-(3) are defined as

$$\begin{aligned} \text{var\{SAM\}} &= \overline{a^2(N)} - \frac{2}{a(N)}; \\ \text{var\{SMD\}} &= \overline{q^2(N)} - \frac{2}{q(N)}; \\ \text{var\{SGM\}} &= \overline{g^2(N)} - \frac{2}{g(N)}. \end{aligned} \quad (10)$$

Again, since these quantities tend to zero for large N , it is more convenient to define a normalized variance, NV , as

$$NV(N) = N \frac{\text{variance}}{\sigma^2} . \quad (11)$$

Then we can state that

$$\text{variance} \sim \sigma^2 \frac{NV(\infty)}{N} \text{ as } N \rightarrow \infty; \quad (12)$$

thus $NV(\infty)$ is also an important measure of the quality of a particular sample statistic.

We present results here for $NB(N)$ and $NV(N)$, along with their asymptotic values at $N = \infty$, for a variety of parent distributions $P(u)$. Additional results for the sample quantile with $r = .75$ and $.9$, and for the PDF, cumulative distribution function, characteristic function, cumulants, and moments of the various sample statistics are available in Ref. 1.

RESULTS

The first case we consider is the Gaussian PDF with arithmetic mean m and variance σ^2 . Since this random variable can go negative, the SGM is undefined. The SAM and SMD are unbiased for all N ; thus $NB(N) = 0$ for all N , for this example. Results for the normalized variance are presented in Fig. 1 for the number of samples, N , between 1 and 51, for both the SAM and the SMD. The normalized variance for the SMD is computed only at odd values of N , indicated by an X, and straight lines drawn between these points for ease of association of values. It is seen that the variance of the SMD is always greater than that for the SAM, the limiting value, $NV(\infty)$, being $\pi/2$ for the SMD; see also Ref. 2, page 369. Observe that the parameters m and σ of this PDF have dropped out of this normalized plot.

It is worth pointing out here, and for similar results to follow, that although the curve for the SMD increases with N , that does not mean that the variance increases with N ; rather, the normalizing factor of N in definition (11) causes this behavior. The actual (unnormalized) variance decreases monotonically with N , eventually being of order $1/N$.

For a Rayleigh random variable, the results for the normalized bias are given in Fig. 2. The SAM is unbiased for all N , whereas the SGM and SMD are, of course, only asymptotically unbiased. The limiting values, $NB(\infty)$, for both of these latter sample statistics are given by analytically complicated expressions and are not repeated here, for the sake of brevity; they are indicated numerically by horizontal lines at the right edge of the figure. The corresponding results for the normalized variance are given in Fig. 3. They indicate that whereas the SGM has about the same stability as the SAM, the variance for the SMD is about 65% greater.

For an exponential PUF (as given by (5)), the normalized bias and variance results are presented in Figs. 4 and 5 respectively. The biases of the SGM and SMD are comparable, but we observe that the variance for the SGM is twice as small as that for the SAM and the SMD.

For a log-normal PDF, ^{*}

$$p(u) = \frac{1}{\sigma_y u \sqrt{2\pi}} \exp \left[-\frac{(\ln(u) - m_y)^2}{2\sigma_y^2} \right] \quad \text{for } u > 0, \quad (13)$$

the NB(N) and NV(N) results are independent of location parameter m_y , but they do depend on spread factor σ_y . This may be anticipated by plotting the PDF (13) for various values of σ_y and observing that the shape changes as σ_y does. Since NB(N) and NV(N) depend upon the shape of the PDF (rather than upon absolute location and scale), results will depend on the particular value of σ_y selected. An example of NB(N) and NV(N) for $\sigma_y = 1$ is presented in Figs. 6 and 7. Now we observe that the variance of the SMD is 3 times better, and that of the SGM 4.6 times better, than for the SAM, at least for larger values of N. However, as $\sigma_y \rightarrow 0$, the log-normal PDF in (13) approaches a Gaussian PDF about the point $u = \exp(m_y)$, and the behaviors would revert back to Fig. 1 then.

The next example is the Rice PDF; physically, this corresponds to the squared-envelope of the sum* of a sine wave and a centered narrowband Gaussian noise process. That is, the PDF is

$$p(u) = \frac{1}{2\sigma_1^2} \exp \left(-\frac{u + A^2}{2\sigma_1^2} \right) I_0 \left(\frac{A \sqrt{u}}{\sigma_1} \right) \quad \text{for } u > 0, \quad (14)$$

where A is the sine wave amplitude and σ_1 is the noise standard deviation. Once again, the shape of the PDF depends on a parameter, namely A/σ_1 . Results for $A/\sigma_1 = 1$ are given in Figs. 8 and 9. The SMD has 14% greater variance than the SAM, but the SGM has about 60% of the SAM variance. As $A/\sigma_1 \rightarrow 0$, the exponential PDF results are obtained, whereas as $A/\sigma_1 \rightarrow \infty$, the Gaussian case is realized. Thus (14) represents a transition case between these extremes.

The last example we consider here is an exponential PDF with out-liers. That is, each sample or measurement $\{x_k\}$ in (1)-(3) is given by

$$x_k = x_a + x_b, \quad (15)$$

where x_a has an exponential PDF,

$$p_a(u) = \frac{1}{m_a} \exp \left(-\frac{u}{m_a} \right) \quad \text{for } u > 0, \quad (16)$$

*If each of the observed random variables x_1, x_2, \dots, x_N in (1)-(3) is obtained by first summing up the envelope-squared outputs of M narrowband filters, as for example in diversity reception, the PDF in (14) is replaced by the Q_M distribution. Results for this case are available in Ref. 1, but are not given here, for sake of brevity.

and disturbance x_b is a random variable which is zero most of the time, but occasionally takes on a large value (out-lier) L . That is, its PDF is

$$p_b(u) = (1 - Q) \delta(u) + Q \delta(u - L), \quad (17)$$

where Q is the probability of an out-lier. Then the parent PDF of observation (sample) x_k is the convolution of (16) and (17):

$$p(u) = \frac{1 - Q}{m_a} \exp\left(-\frac{u}{m_a}\right) U(u) + \frac{Q}{m_a} \exp\left(-\frac{u - L}{m_a}\right) U(u - L), \quad (18)$$

where unit step

$$U(t) = \begin{cases} 1 & \text{for } t > 0 \\ 0 & \text{for } t < 0 \end{cases}. \quad (19)$$

The important parameter now is L/m_a , which obviously affects the shape of PDF (18).

Now however, before we get into the detailed bias and variance results, another consideration is of paramount importance. Our sample statistics, (1)-(3), will no longer extract (estimate) the arithmetic mean, median, and geometric mean, respectively, of the (disturbance-free) exponential PDF (16), but perforce, the corresponding statistics of the measurement PDF (18). If, however, we are really interested in the parameters of (16), then we must inquire into the quantitative disturbance caused by the out-liers described in (17). Here we merely cite the results for one numerical case; additional results are given in Ref. 1.

For probability $Q = .05$, and out-lier value $L/m_a = 6$, we find that the ratio of arithmetic means, for (18) with respect to (16), is 1.3. The corresponding ratio of medians is only 1.08, whereas the ratio of geometric means is 1.13. Thus the SMD and SGM are more resistant to the presence of infrequent out-liers, insofar as their effects on the particular parameters of median and geometric mean.

The results for the normalized bias and variance are given in Figs. 10 and 11. The variances of the SMD and SGM are again smaller than that for the SAM. The bias of the SMD and SGM are comparable.

If we define a mean-square error as the average value of the squared difference between a sample statistic s and a desired parameter d_a of the disturbance-free PDF, we can develop it as follows:

$$\begin{aligned} \text{MSE} &= \overline{(s - d_a)^2} = \overline{(s - \bar{s} + \bar{s} - d_a)^2} \\ &= \overline{(s - \bar{s})^2} + (\bar{s} - d_a)^2. \end{aligned} \quad (20)$$

But the first term is the variance of the sample statistic, and the second term can be expressed as

$$\bar{S} - d_a = (\bar{S} - d) + (d - d_a) = \text{bias} + \text{deflection in desired parameter}, \quad (21)$$

where d is the modified value of the desired parameter d_a , due to the disturbance. Thus

$$\text{MSE} = \text{variance} + (\text{bias} + \text{deflection})^2. \quad (22)$$

Now the bias and variance are $O(N^{-1})$ for large N , whereas the deflection of the desired parameter does not decay with N at all; in fact, it is independent of N . Thus the considerations above, whether for the ratio of arithmetic means or medians or geometric means, are very important, since they dominate the magnitude of the mean-square error for very many samples available.

DISCUSSION

The ability of the SMD and SGM to suppress deleterious effects due to occasional large interferences is very pronounced for some probability density functions. Not only is the deflection of the desired parameter (arithmetic mean or median or geometric mean) decreased, but the bias and variance of the estimate can be markedly reduced in some cases. The exact amounts depend on the magnitude and frequency of the interference.

Another possible approach to alleviate the effects of additive large outliers is to subject the available samples x_1, x_2, \dots, x_N to a nonlinear transformation such as saturation, in order to suppress the large contributions, prior to evaluating the SAM or SGM or SMD. Knowledge of relative levels (such as L/m_a for the above example) would be required for optimal adjustment of the saturation level, but performance could be markedly improved. The nonlinear transformation would reduce the deflection, while the averaging of N samples would reduce the bias and variance. This possibility has not yet been pursued.

REFERENCES

1. A. H. Nuttall, "Statistics of Sample Median, Quantile, Geometric Mean, and Arithmetic Mean, for Various Distributions," Technical Report 6689, Naval Underwater Systems Center, New London, CT USA.
2. H. Cramer, Mathematical Methods of Statistics, Princeton University Press, Princeton, N.J., 1961.

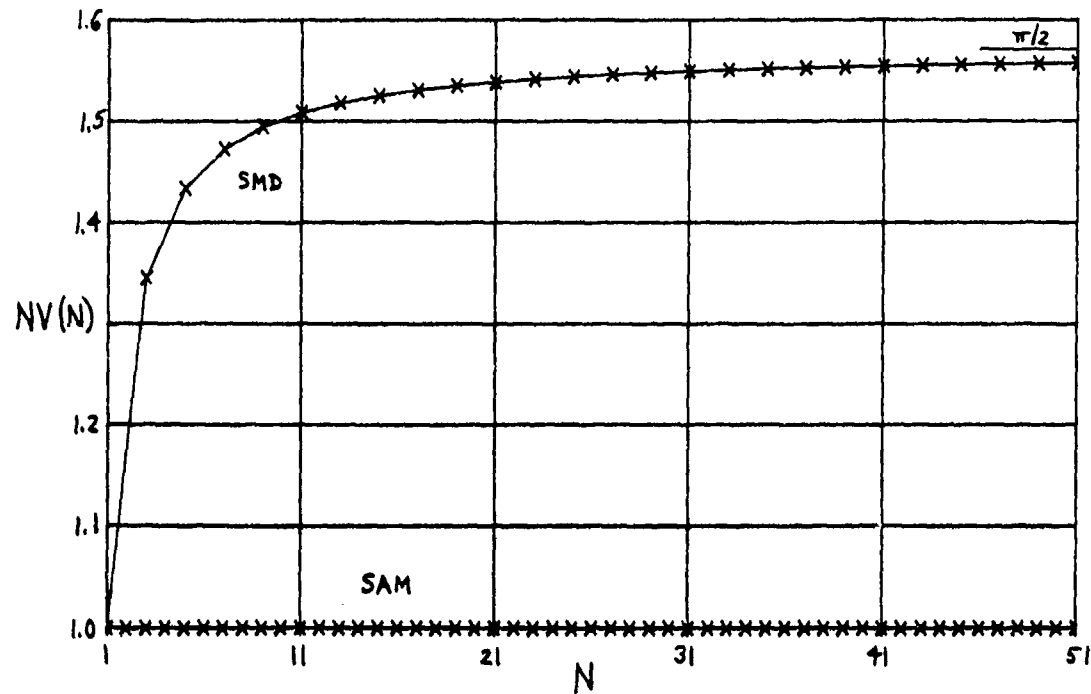


FIG. 1 NORMALIZED VARIANCE; GAUSSIAN PDF

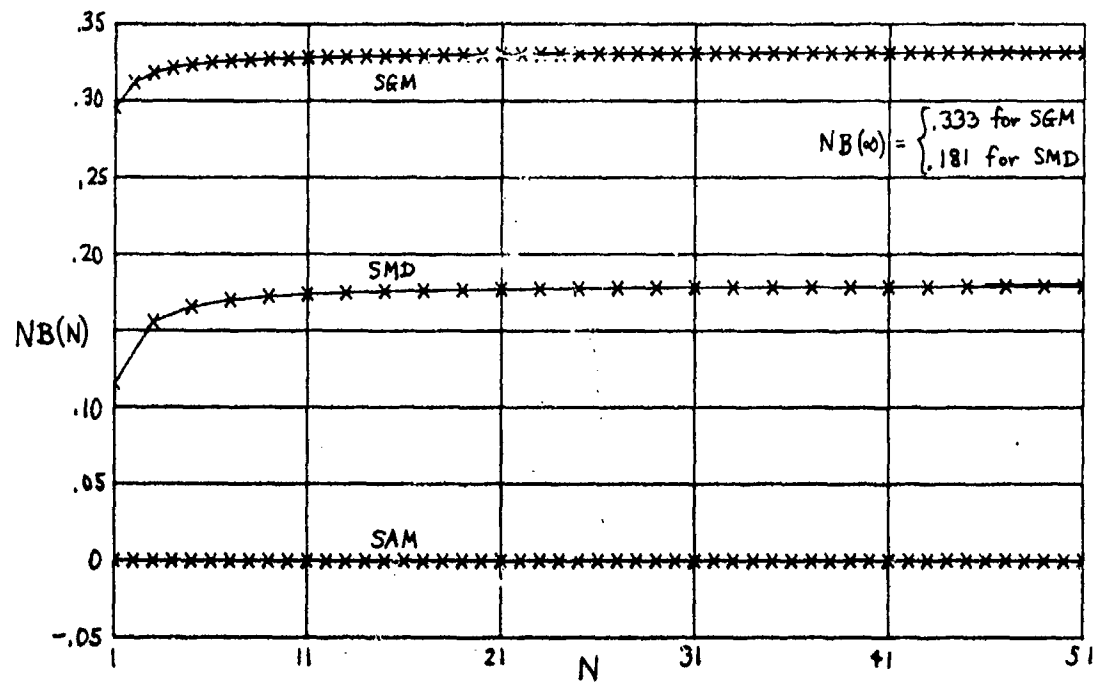


FIG. 2 NORMALIZE BIAS; RAYLEIGH PDF

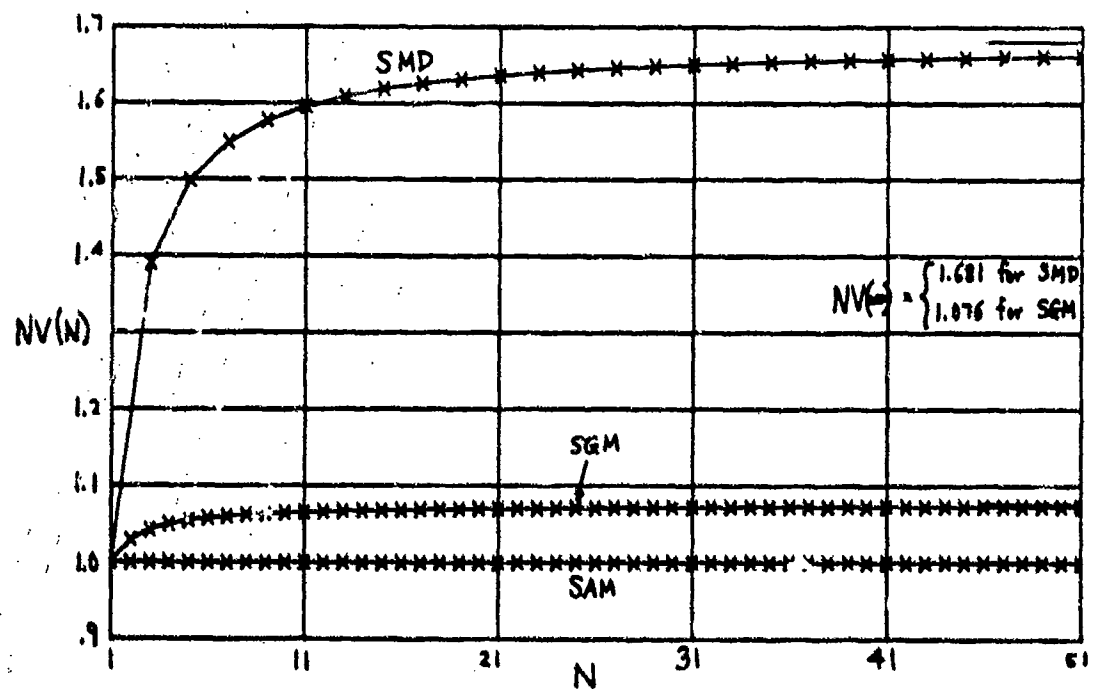


FIG. 3 NORMALIZED VARIANCE; RAYLEIGH PDF

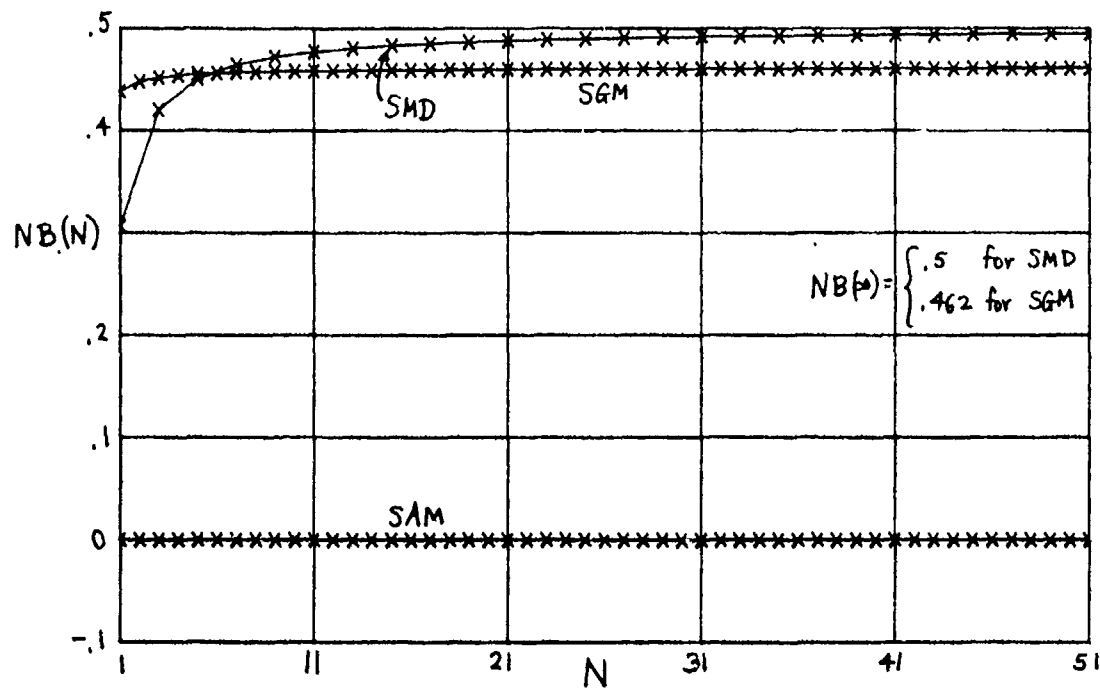


FIG. 4 NORMALIZED BIAS; EXPONENTIAL PDF

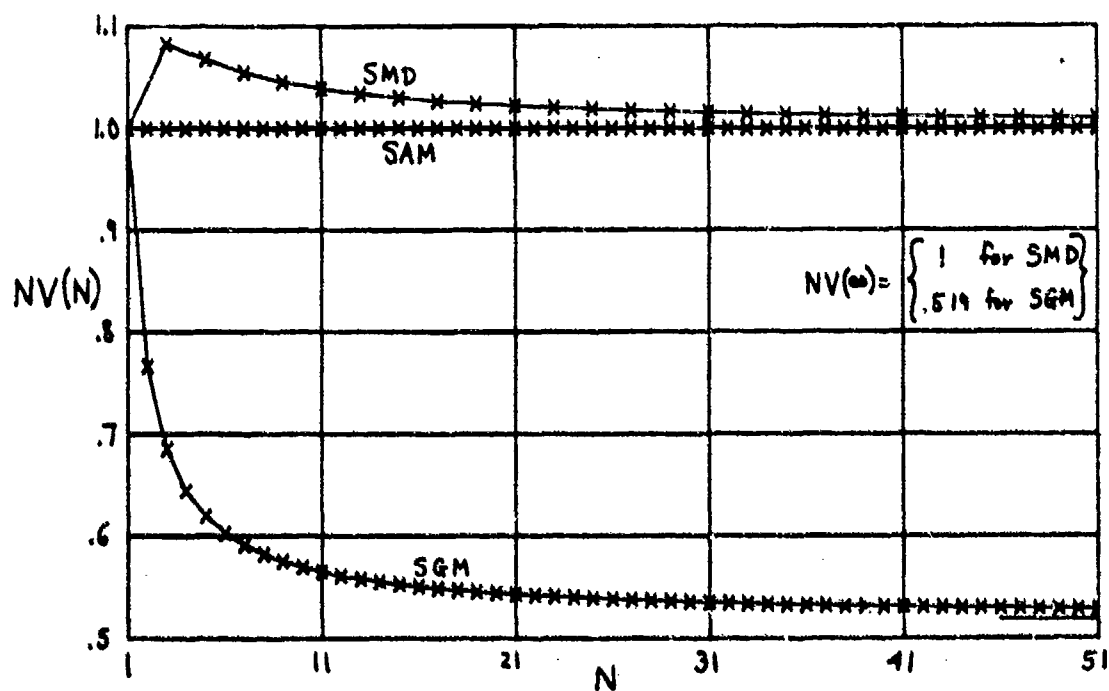


FIG. 5 NORMALIZED VARIANCE; EXPONENTIAL PDF

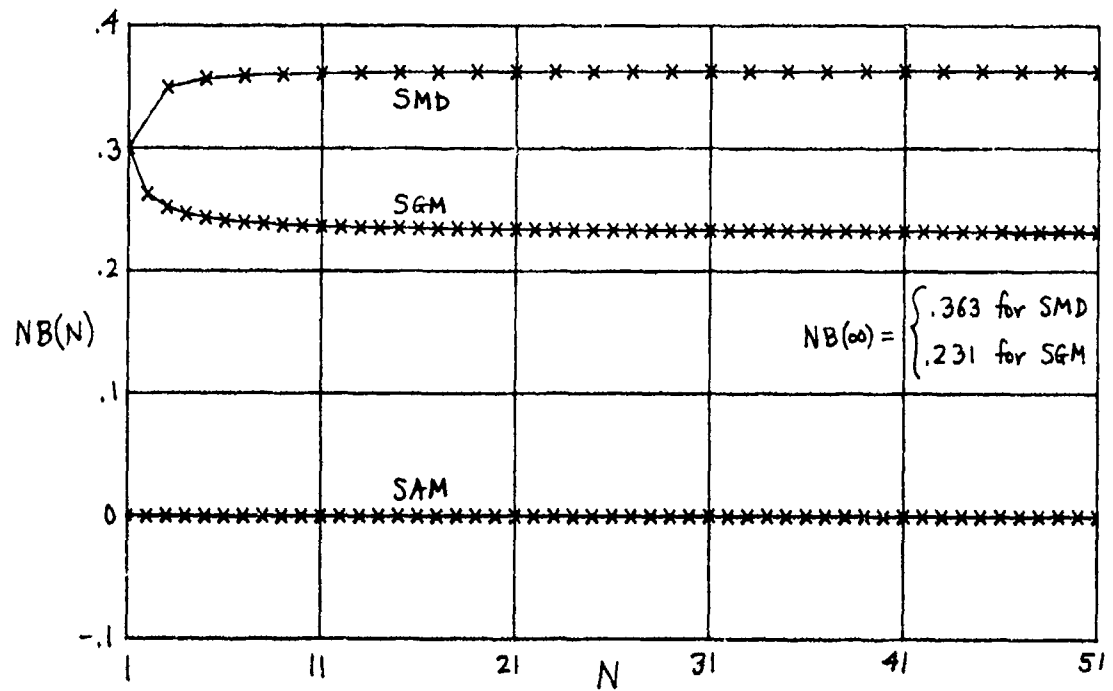


FIG. 6 NORMALIZED BIAS; LOG-NORMAL PDF ($\sigma_y = 1$)

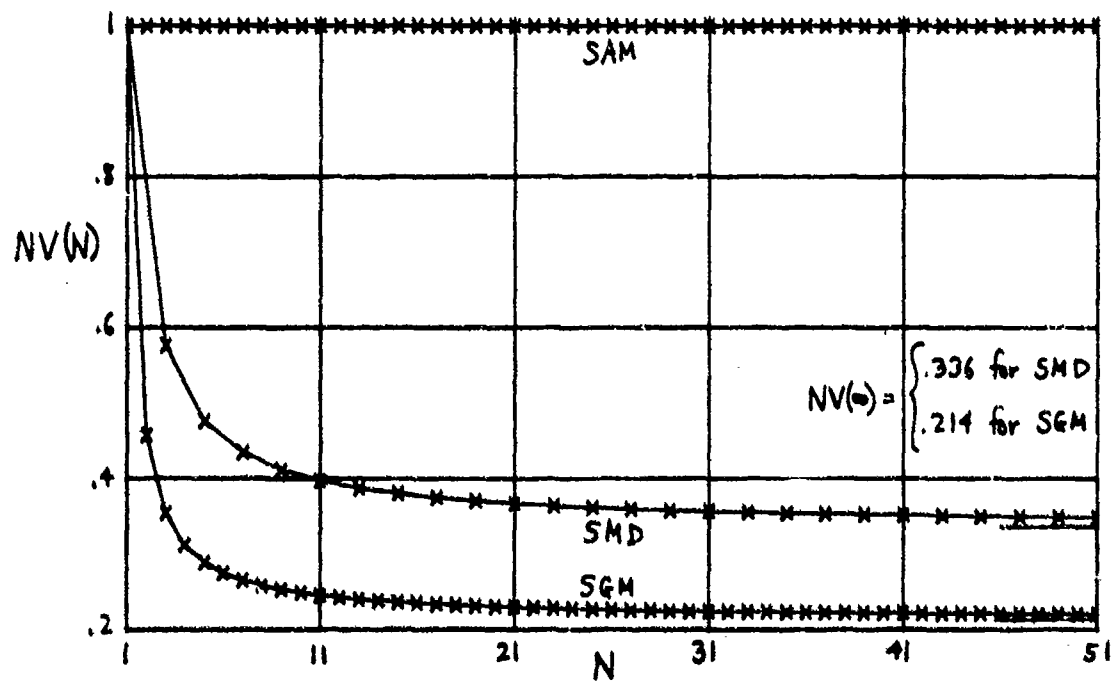
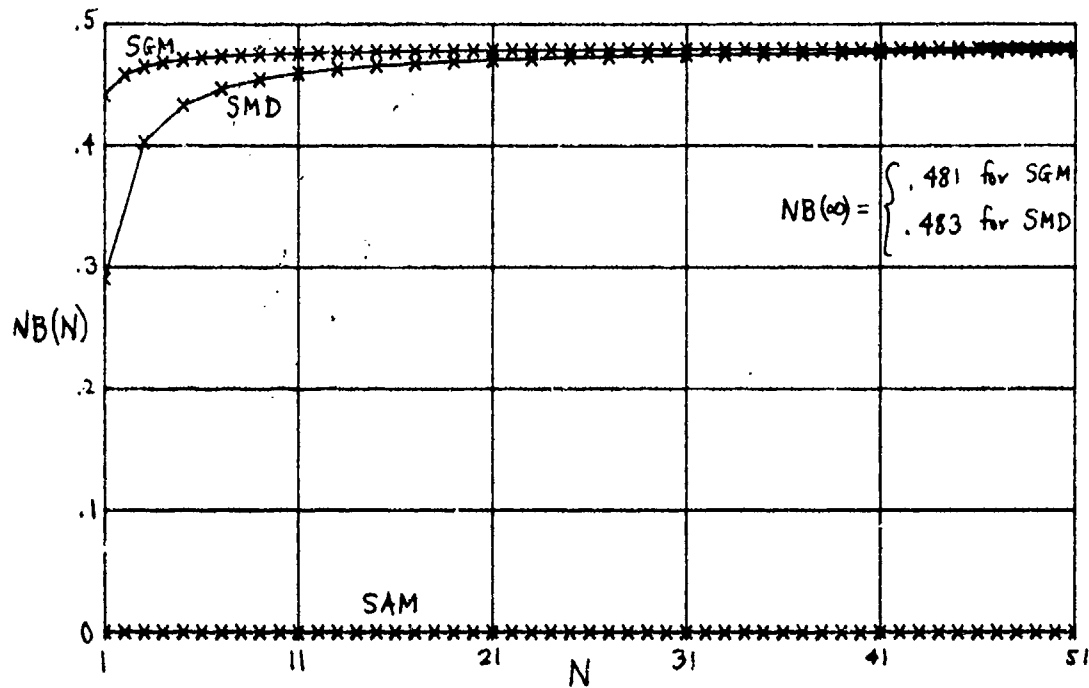
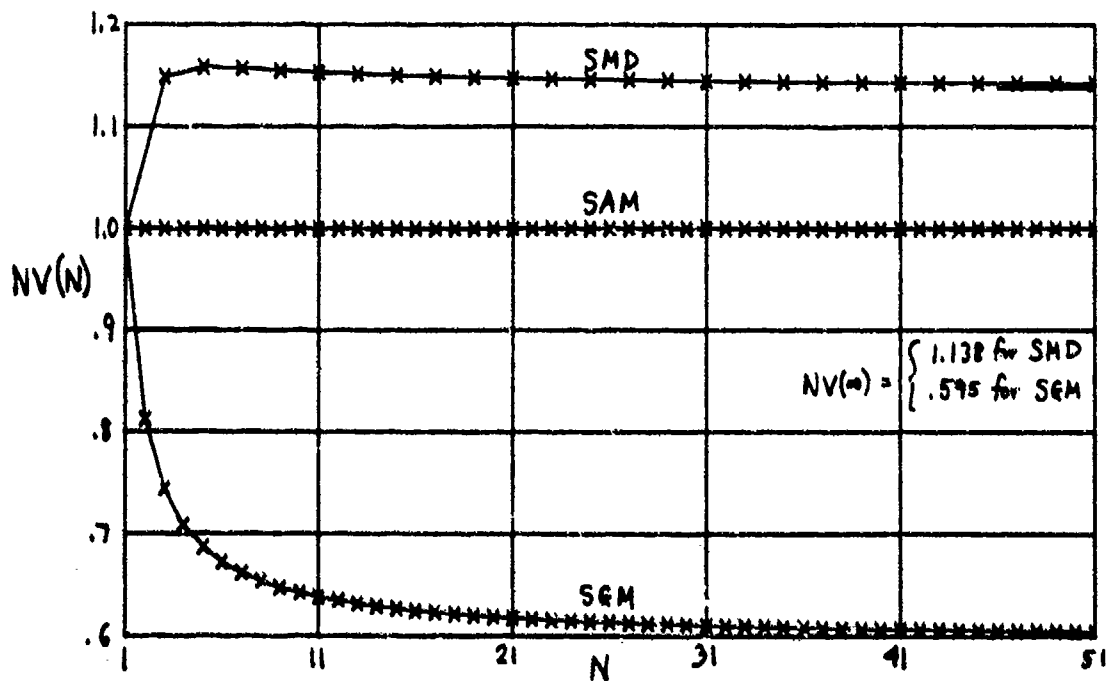


FIG. 7 NORMALIZED VARIANCE; LOG-NORMAL PDF ($\sigma_y = 1$)

FIG. 8 NORMALIZED BIAS; RICE PDF ($A/\sigma_1 = 1$)FIG. 9 NORMALIZED VARIANCE; RICE PDF ($A/\sigma_1 = 1$)

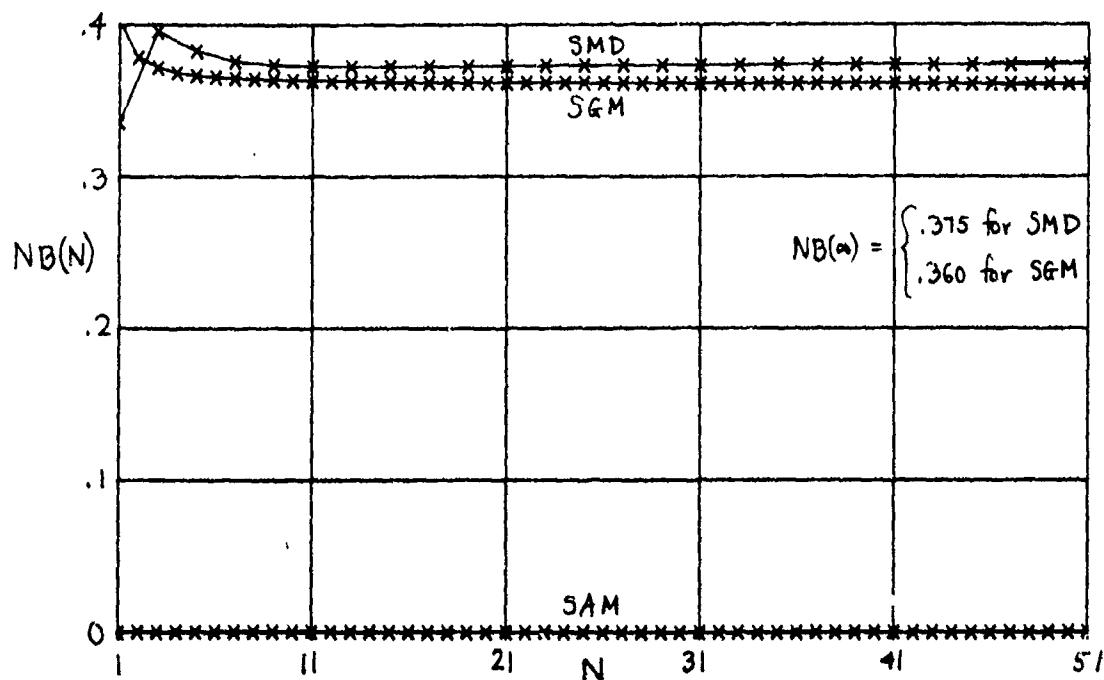


FIG. 10 NORMALIZED BIAS; EXPONENTIAL PDF WITH OUT-LIERS ($\frac{L}{m_a} = 6$, $Q = .05$)

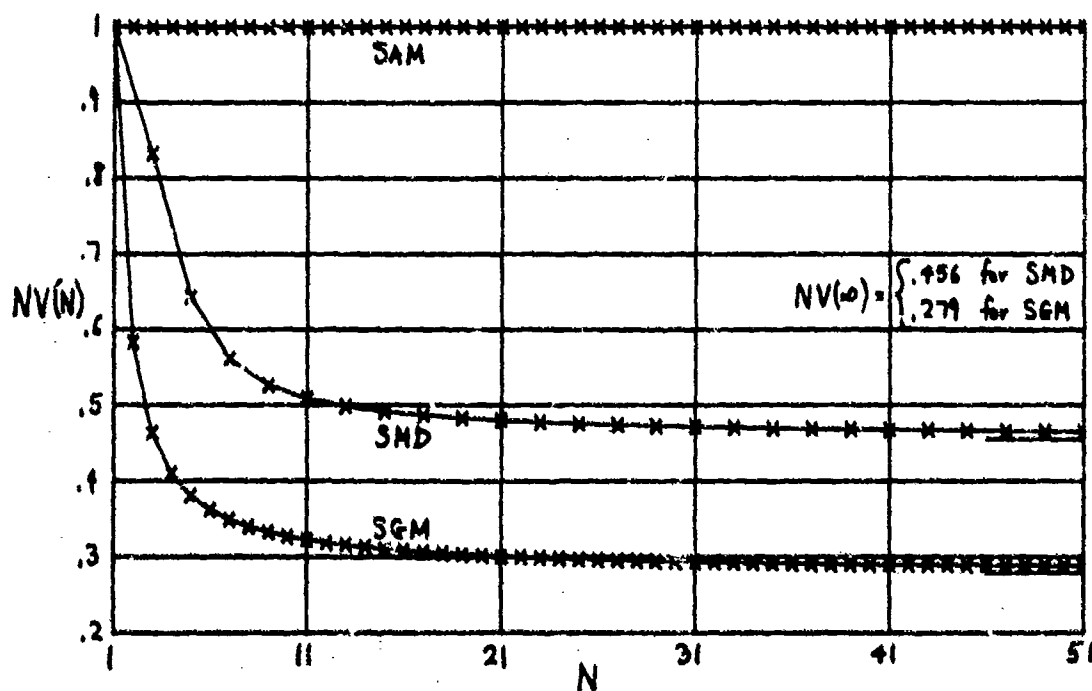


FIG. 11 NORMALIZED VARIANCE; EXPONENTIAL PDF WITH OUT-LIERS ($\frac{L}{m_a} = 6$, $Q = .05$)

IS POWER AVERAGING THE BEST ESTIMATOR
FOR UNDERSEA ACOUSTIC DATA?

By

R.A. Wagstaff and J.L. Berrou
SACLANT ASW Research Centre
La Spezia, Italy

ABSTRACT

The power average is the statistic which is commonly used in all types of acoustic data processing. It is an excellent estimator for "well behaved" Gaussian distributions when the central or average value is desired. However, when there are "outliers" and errors or when the distributions are not Gaussian there are other statistics which are better estimators. In the case of ambient noise, the distributions are seldom Gaussian or free from "outliers" and errors. For this case the median and the geometric mean power level (dB average) are less sensitive to interference in the environment and to some of the minor system faults and are more powerful statistics.

INTRODUCTION

It is not a simple task to measure the undersea ambient noise and to process and report the results with a high level of confidence. The measurement itself is plagued with many potential hazards. The equipment is seldom in perfect condition and the noise environment is usually not cooperative. Nearby ships, seismic exploration, and countless other interferences have ruined many hours of otherwise good data. The measurement system has its own problems which increase the difficulty of achieving good results. Hydrophones can go bad as well as can the electronic components in amplifiers, preamplifiers, and filters which condition the acoustic signals. If the system is a towed array there is the additional problem of towship noise. In some cases, the noise from the towship is considerably more than the ambient which is to be measured.

Past experience in the measurement of ambient noise in many different areas, with different environmental conditions and noise source distributions, and with different measurement systems indicates that ambient noise data are generally not Gaussian distributed. The distributions tend more toward the shape of a log-normal or Rayleigh distribution. The distribution function in levels has a longer tail on the low noise level end than on the high noise level end. Most of the usual

interferences, however, are distributed more toward the high-level end. This is intuitively obvious, since an interference of low level noise cannot reasonably interfere with the measurement.

The average power level is a commonly used statistic in ambient noise data processing. Because of the extremely high level of the interference, the average power level can be dominated even when the interference constitutes a relatively small percentage of the data. If a "persistent background" noise is desired from the measurement, the average power will not provide it. This is also true if trying to detect a target during times of high level noise interference, which is illustrated by the time series in Fig. 1. Two explosions were received from seismic prospecting during the measurement period. Three statistics have been calculated: the average power level, the decibel average (dB AVG), and the median level (MEDIAN). In this case, the average power level, being biased upward about 5 dB, is not a good estimator for what might be considered representative of the data. The other two seem reasonable. A target line would be masked if the averaging period contained one or more of these transient noise "spikes".

The selection of a best statistic is based on a very simple concept: for a source to interfere it must be of relatively high level. A lower level source does not interfere. The ideal statistic, then, is one which discriminates against high levels. This would not be the average power level. The average power can easily be captured and biased upward as in Fig. 1 when the high level interference constitutes a small percentage of the data. However, it is this statistic which is most commonly used in ambient noise processing. The geometric mean power level (dB average) and median levels, on the other hand, are relatively insensitive to interferences which constitute a small percentage of the data. A simple example illustrates this point. Consider a set of 50 observations. Let 45 be of 60 dB level and 5 of 100 dB level. The average power level of the 50 samples is about 90 dB. The dB average is 64 dB and the median is 60 dB. The differences between these latter two and the average power level are about 26 and 30 dB. If it is accepted that the five samples of 100 dB are a result of interference, then the dB average and median are better statistics than the average power level. These statistics have the obvious advantage that they give very good estimates without the need for deleting suspect data. This is important for automatic data processing. The advantage of course, decreases as the percentage of the contaminated data increases. Some examples will be given from measured data which illustrate the "power" of these two statistics for ambient noise measurement. The same concepts apply to other processes in acoustic measurement and signal processing. It will be left as a challenge to the reader to discover in which phases of analysis this simple concept can be applied to his situation.

RESULTS

During one ambient noise measurement exercise with the towed array, interference from seismic prospecting was received during the entire measurements. The range to the source was not known, only the azimuth. The level of the interference at the array was about 95 dB at 480 Hz. The

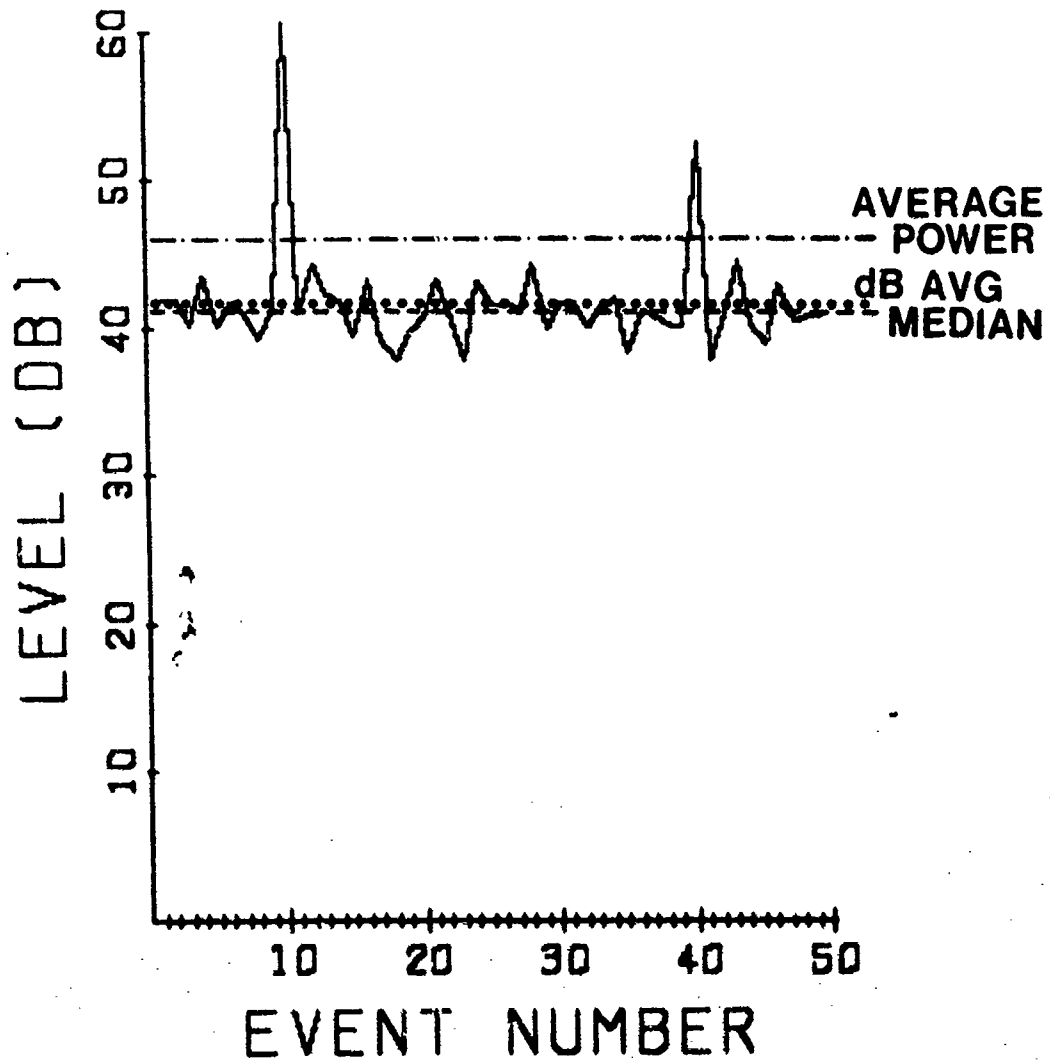


FIG. 1 EXAMPLE OF POWER AVERAGE LEVEL, DECIBEL AVERAGE, AND MEDIAN FOR A 50 POINT TIME SERIES OF ACOUSTIC NOISE DATA CONTAINING TWO SEISMIC PROSPECTING EVENTS

repetition rate was between 9 and 12 seconds and each explosion lasted about 2 seconds. The 480 Hz ambient noise without the interference was approximately 66 dB. The effects of these explosive sources on the data processing are illustrated in Fig. 2. There are three curves in each plot of Fig. 2. The dashed curves at the top are the average power levels for 50 spectral estimates. The next two curves are the for the median (solid) and the dB average (dashed) for the same 50 data points.

The explosions cause an interference pattern across the array in the hydrophone noise power average (top dashed curve). The mean level decreases about 5 dB across the array and has oscillations with an amplitude of about one decibel. Such effects could cause problems to many types of signal processing. The curves of the median (solid curve) and dB average (bottom dashed curve) register considerably different behavior. The median has about a 1.5 dB slope across the array with very little evidence of oscillations and the dB average is flat with no oscillations.

The reasons the median and the dB average give such excellent results are the following. The data points with the explosions are all above the median level. About half of them might have been below the median if there had been no explosions. Therefore, the median level is shifted in the ordering of the data by an amount equal to about half the number of explosions. If 4 explosions were received in the 50 samples the shift would be about two numbers but not more than four. The resulting change in the level of the median would be small and possibly none at all. As the number of occurrences increases in proportion to the total data, the affect on the median increases. The same is true for the dB average. However, the discrimination capability of the dB average, in addition, is affected by the relative magnitude of the difference between the good data and the interference. Estimates of the beam noise level and the noise field horizontal directionality could be made from the median and dB average beam noise levels; it could not be done from the average power levels without being biased by the explosions. The results in the beam noise plot Fig 2b indicate the explosion, near beam number 13, which dominates the curve for the average power levels (top dashed line), but is not evident in the curves for the dB average and median. The discrimination level of the latter two is approximately 34 dB against the explosion.

Figure 3 illustrates the three different statistics on data from two other time periods. In each case the data base consists of sets of 50 beam noise spectral estimates. Figure 3a is for 1460 Hz when interference was being received from a source which was believed to be of biological origin, possibly snapping shrimp. The plot of average beam power levels shows the obvious effects of the interference. Judging from the other two curves (median and dB average) in the same plot, the average power level has been biased up by as much as 15 dB. The curves for the median (solid) and dB average (lower dashed curve) appear unaffected, with the anisotropy due to shipping noise being clearly evident.

The data for Fig. 3b were obtained when a different type of biological source was nearby. The noises received on the array sounded like carpenters hammering on a roof. The sources of the noise were most likely carpenter fish (Sperm whale). The average power levels (top dashed curve) are again "captured", being biased upward as much as 17 dB, while the

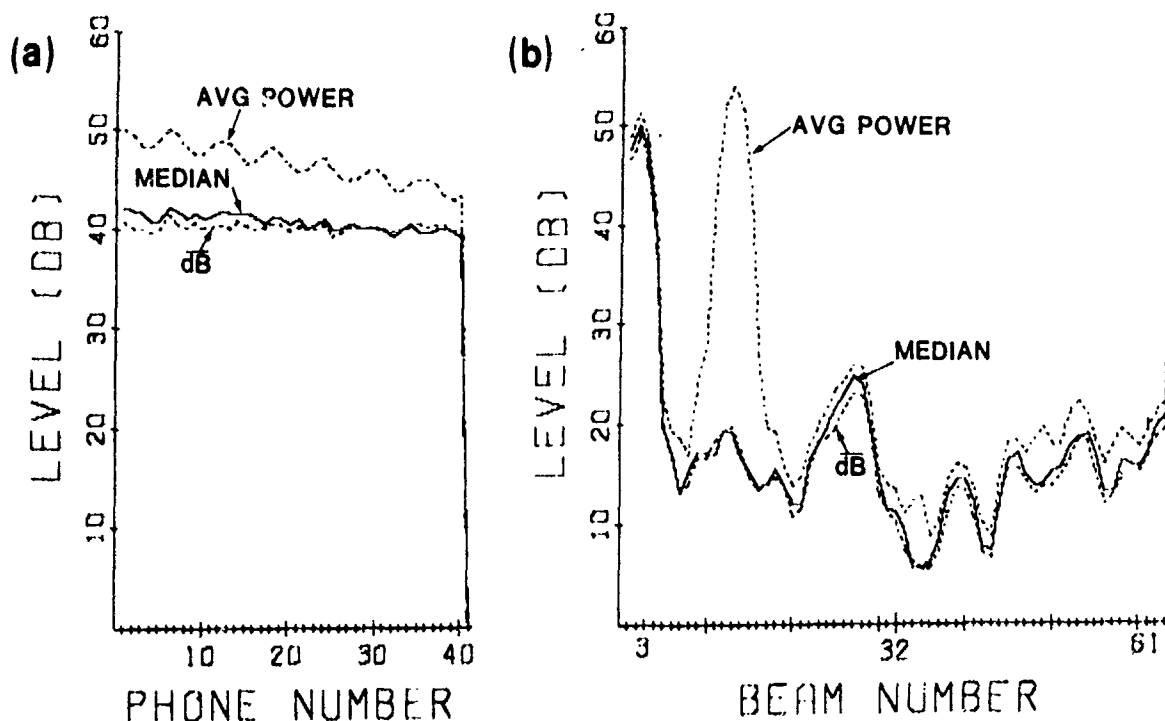
RESULTS DURING SEISMIC PROSPECTING

FIG. 2 NOISE LEVEL VERSUS HYDROPHONE NUMBER PLOT (2a) AND BEAM NOISE LEVEL VERSUS BEAM NUMBER PLOT (2b) FOR A PERIOD WHEN NOISE FROM SEISMIC PROSPECTING WAS BEING RECEIVED. POWER AVERAGE (top dashed curve), MEDIAN (solid curve), AND dB AVERAGE (bottom dashed curve)

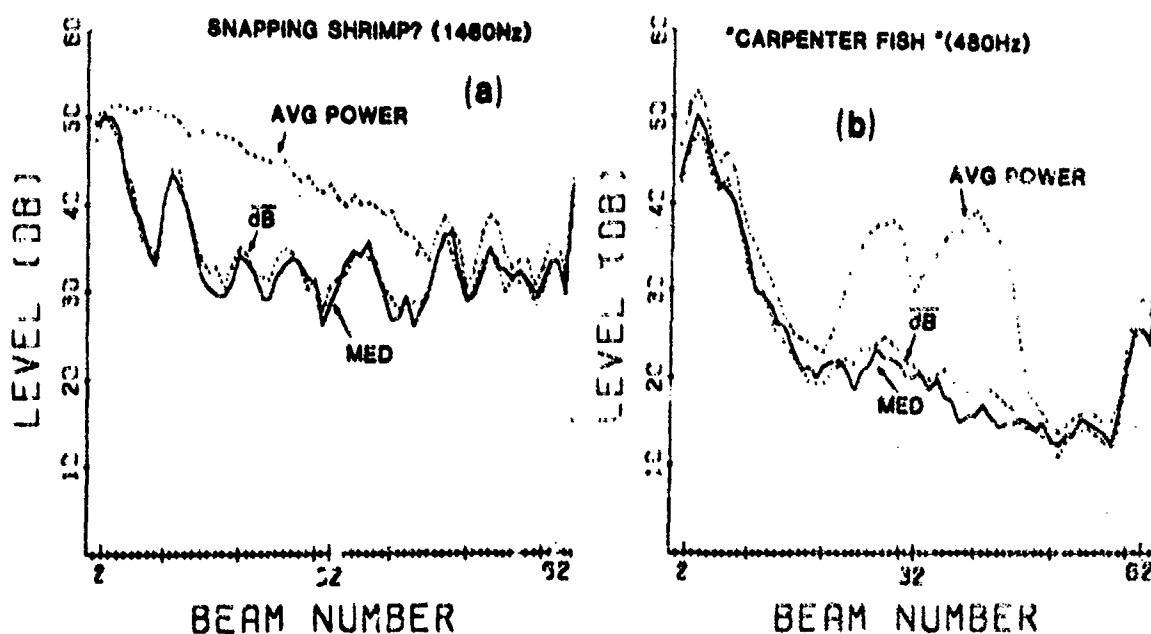
BIOLOGICAL NOISES

FIG. 3 NOISE LEVEL VERSUS BEAM NUMBER FOR TIMES OF NOISE INTERFERENCE FROM (2a) SNAPPING SHRIMP, AND (2b) CARPENTER FISH (Sperm whale). POWER AVERAGE (dashed curve), AND dB AVERAGE (bottom dashed curve)

curves for the medians and dB averages do not register any significant effects. Hence, in both sets of data in Fig. 3 the background shipping noise could be measured by the median and the dB average during the periods of interference, while it could not be measured with the power average. This might also have been true if instead the objective was to detect a target. The gain against the interference is the level differences between the power average and the other two statistics. The potential improvement is substantial.

The previous examples demonstrate that the median and the dB average can effectively discriminate against high level transient sources in the environment. Unfortunately, the environment is not the only source of bad data. The measurement system can also be a problem. Most of the present systems contain many components and are highly sophisticated. As the number of components increases, the probability of experiencing a mechanical or electronic failure also increases. In fact, past experience indicates there is always a defect in the measurement system. It is a challenge to minimize the deleterious effects of the defect and produce high quality results.

The median and the dB average can also be used to improve the data quality for some types of system faults. Consider, for example, the two plots in Fig. 4. The plot on the left is a strip chart recording of a hydrophone output from a towed array during a time of acoustic measurements. Noise "spikes" of about 18 dB above the background occur about every 10 seconds. The spikes are believed to be caused by the relative motion of the hydrophone in its fasteners. The affect the transient noise spikes in Fig. 4a have on data quality is illustrated in the beam noise plot of Fig. 4b. The beams from 22 to 42 are steered into real space and receive acoustic energy on their main lobes. The beams outside this range correspond to phase shifts greater than for endfire beams. They are virtual beams and receive acoustic energy only through the sidelobes which extend into acoustic space (see reference 1 for more detail). When the sidelobes are good the levels of these virtual beams are measures of the self noise of the system. For the case in Fig. 4b the sidelobes were in the neighborhood of 40 dB down at the time of this measurement but were masked by the "system" noises in Fig. 4a.

The self noise resulting from the noises illustrated in Fig. 4a are given by the levels of the virtual beams. Relative to the plot, the self noise is about 38 dB for the power average and about 28 dB for the dB average. The median is a few decibels below the dB average. These results indicate that for the power average the self noise of the system is about 4 to 6 dB below the acoustic levels on the beams. The lowest average power beam levels would most certainly be contaminated by the hydrophone noise spikes. The median and dB average beam levels, on the other hand, have a greater safety range. The differences between the acoustic and virtual beams is generally in excess of 12 dB for these latter two statistics.

The dB average and median can be used in the spatial domain as effectively as in the time domain. For example, consider the problem of estimating the omnidirectional level and horizontal directionality of the ambient noise from the beam outputs of a towed-line array. There are two major problems which must be solved to do this. The first is that the line array has an

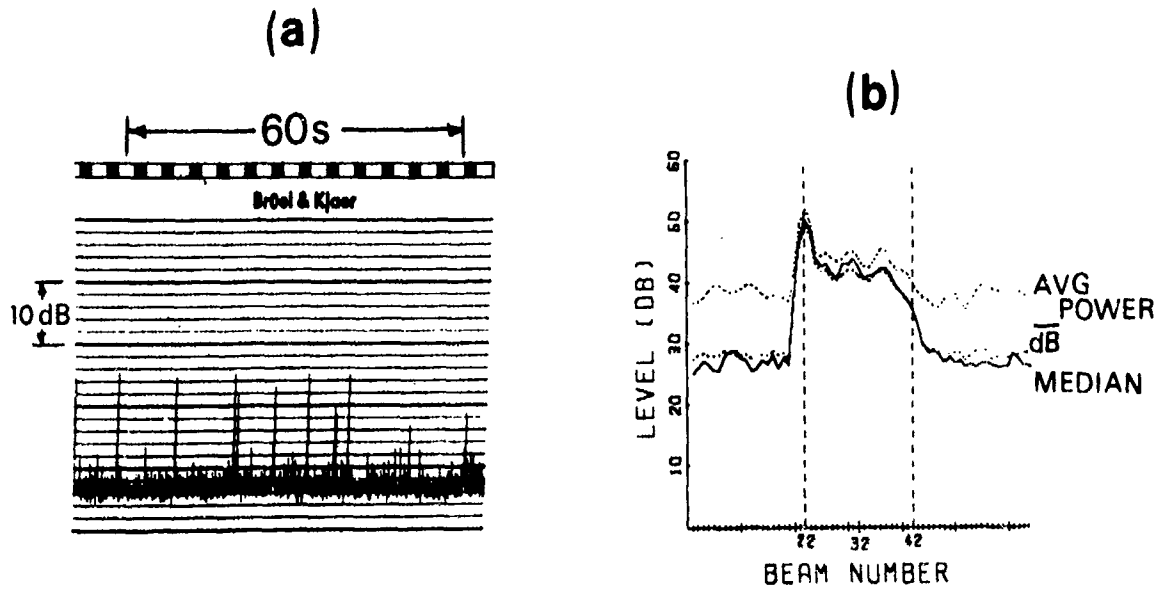
MECHANICAL NOISE

FIG. 4 STRIP-CHART RECORDING OF NOISES ON ONE HYDROPHONE CHANNEL (4a) AND THE EFFECTS ON THE BEAMFORMED OUTPUT (4b). POWER AVERAGE (top dashed curve), MEDIAN (solid curve), AND dB AVERAGE (bottom dashed curve)

inherent left-right ambiguity which must be resolved. This requires that measurements be made on different array headings. Unfortunately, the noise-field changes over the time required to do this. Hence, an exact solution is generally impossible. The second problem is caused by the towship. The noise received from it interferes with the measurement of the ambient. It can be as much as 30 dB above the ambient for the entire set of measurements.

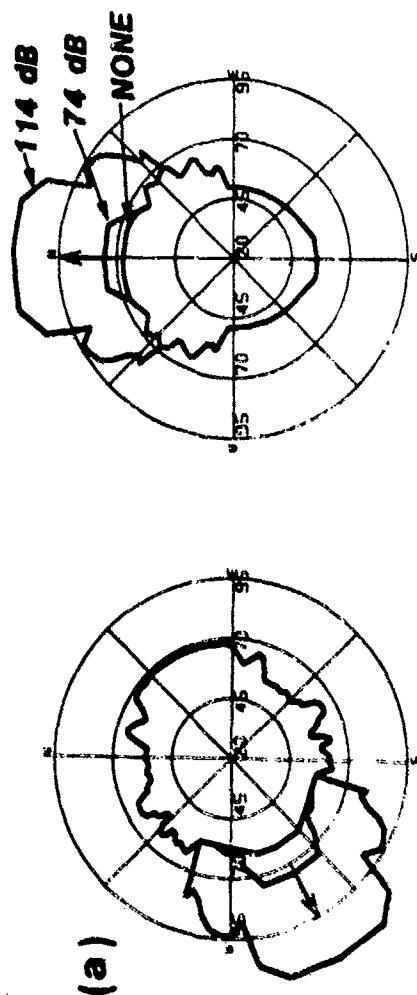
The capability of the dB average and the median to discriminate against the high level transient noise can also be used to discriminate against the towship noise. When the measurements are performed on different array headings, the towship noise appears on a different true azimuth each measurement period. This constitutes a spatial transient. Hence, the transient discrimination capability of the median and the dB average can be utilized to discriminate against the towship in the estimation of the horizontal directionality of the noise field. Furthermore, the ambiguities in the beam noise measurements will be resolved in the same way. The true azimuth of a fixed source is not transient. The ambiguous azimuth, however, will vary with the array heading and this constitutes a spatial transient. It will, therefore, be discriminated against by the median and the dB average performed in the spatial domain. When the source does not remain on a fixed azimuth for the entire set of measurements, all true and ambiguous azimuths will be spatial transients. The median and dB averages will arrive at values which will be between the extremes. They will be good estimators of the noise field most of the time. The omnidirectional level can then be obtained by integrating the horizontal directionality pattern. Because of the discrimination capability of the median and the dB average, the omnidirectional level of the ambient noise can be estimated exceptionally well in the presence of masking by the towship and other high level moving or transient sources.

The spatial discrimination capability of the median and the dB average can be illustrated by estimating the horizontal directionality and omnidirectional level of the ambient noise for various levels of interference from the towship. This was done for simulated measurements in the Alboran Sea south of the shipping lane. The shipping surveillance data, obtained during the actual measurements were used in the RANDI II noise model <2> and the positions dead-reckoned from one measurement period to another. The measurements were made each hour for nine hours on nine array headings which were incremented 80 deg. each hour. Noise was added to the beams normally contaminated by the towship and the measurement was simulated again. This was done for towship noise levels received at the array equal to 74 dB and again for 114 dB. This latter level was about 40 dB above the ambient and 70 dB above the lowest beam noise levels (10 kt of wind at 480 Hz). The algorithm in reference 3 was used to obtain estimates of the horizontal directionality and the omnidirectional level of the ambient noise from the beam noise data for each level of towship noise contamination. This algorithm utilizes the dB average in the deconvolution of the beam data by an iterative approach and either the dB average or the median in space to resolve the ambiguities and discriminate against the towship.

Example polar plots of the beam data for three of the nine headings are given in Fig. 5a. Only a few of the forward beams are affected by the

TOWSHIP NOISE

BEAM RESPONSE DATA



NO TOWSHIP NOISE

HORIZONTAL DIRECTIONALITY

74 dB TOWSHIP NOISE

HORIZONTAL DIRECTIONALITY

114 dB TOWSHIP NOISE

HORIZONTAL DIRECTIONALITY

--- IDEAL
...dB AVG
— MEDIAN

(b)

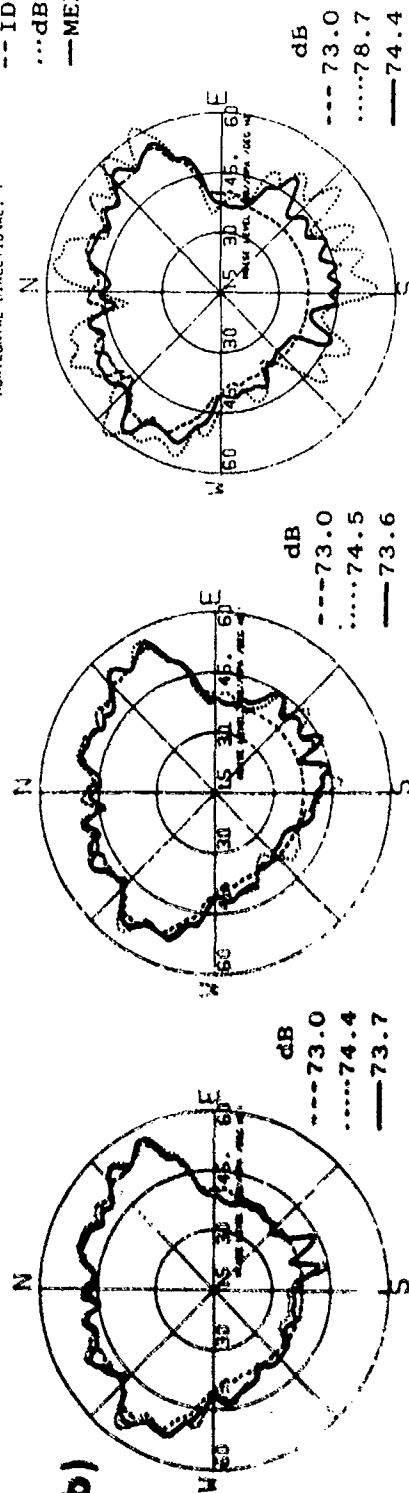


FIG. 5 TYPICAL SIMULATED BEAM NOISE POLAR PLOTS FOR VARIOUS LEVELS OF TOWSHIP NOISE (5a) AND THE RESULTING HORIZONTAL DIRECTIONALITY PATTERNS OBTAINED DIRECTLY FROM THE NOISE MODEL (IDEAL), BY dB AVERAGING, AND BY USING THE MEDIAN BEAM LEVELS (5b)

towship noise as is evident by the superposition of the beam noise plots for the cases of no towship noise, 74 dB towship noise, and 114 dB towship noise. The sidelobes have been reduced sufficiently to eliminate the system as a source of degraded results in order to concentrate only on the discrimination capabilities of the dB average and the median.

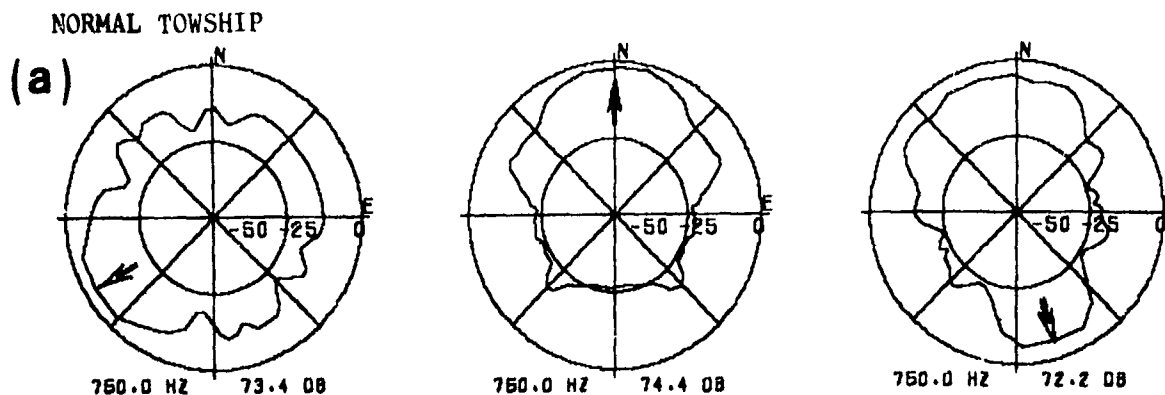
The directionality estimates and the corresponding omnidirectional levels are given in Fig. 5b. The dashed curve in each plot was obtained directly from the model. It is the unambiguous estimate (ideal) of the time averaged and spatially smoothed noise field. It is not degraded by the towship noise or the ambiguities of the array. It is the quantity that the algorithm <3> is attempting to estimate. The solid curve in each plot is the estimated directionality pattern using the median. The dotted curve corresponds to the dB average processing. The plots from left to right are for no noise from the towship, 74 dB, and 114 dB from the towship. The omni-directional levels corresponding to each pattern are also included beside each plot.

In each of the three cases illustrated in Fig. 5b the median estimate agrees well with the ideal pattern except in the 90 deg. sector south of southeast. In this region the estimated levels are biased up by about 7 dB. The azimuthal extent of this region increases with the level of the contamination. The omnidirectional level of the median estimate is biased up about 1.4 dB when the contamination is 41 dB above the ambient. This is rather impressive suppression of the contamination. The dB average does not perform as well but still gives impressive results. The omnidirectional levels of the dB average estimates are biased up about 5 dB for the 114 dB contamination and 1.5 dB for 74 dB contamination. The excellent agreement between the patterns, especially for the first two plots of Fig. 5b, indicates that the dB average and the median are very effective in resolving the ambiguities and estimating the omnidirectional levels and the directionalities. The last two plots indicate that these statistics are also very good at discriminating against spatial transients, in this case the towship.

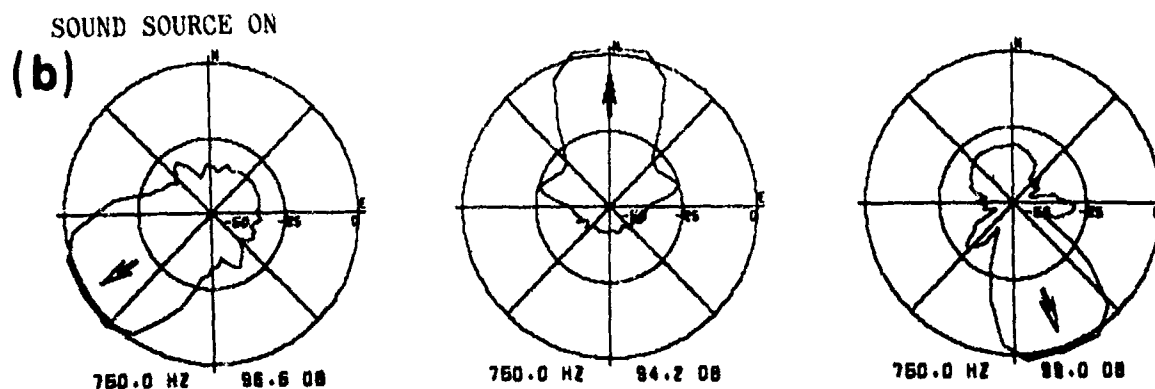
There is always a question of the validity of modeled results. The previous results are supported by measurements of a similar nature obtained in the Alboran Sea. The level of the towship noise was increased by switching on the active rudder of the towship. This increases the noise received from the towship by up to 30 dB. The exact amount depends on frequency. It is negligible at 100 Hz and 30 dB at 1000 Hz. Ambient noise measurements were made on nine different headings. Data were acquired on each heading with the active rudder off and another set with it on. The data were processed as two separate nine-sided polygons, one with the active rudder noise and one without.

Figure 6 illustrates the results for 750 Hz. The top row of plots are beam noise measured during three of the nine legs. The effective omnidirectional level was about 73 dB. The noise from the towship exceeds the ambient beam noise from 5 to 20 dB depending on array orientation. The second row of plots are for the same orientations but the active rudder is switched on. In these cases the noise from the towship exceeds the beam noise from the ambient by 30 to 40 dB. The omnidirectional levels were about 96 dB, 23 dB higher than without active rudder. The active rudder

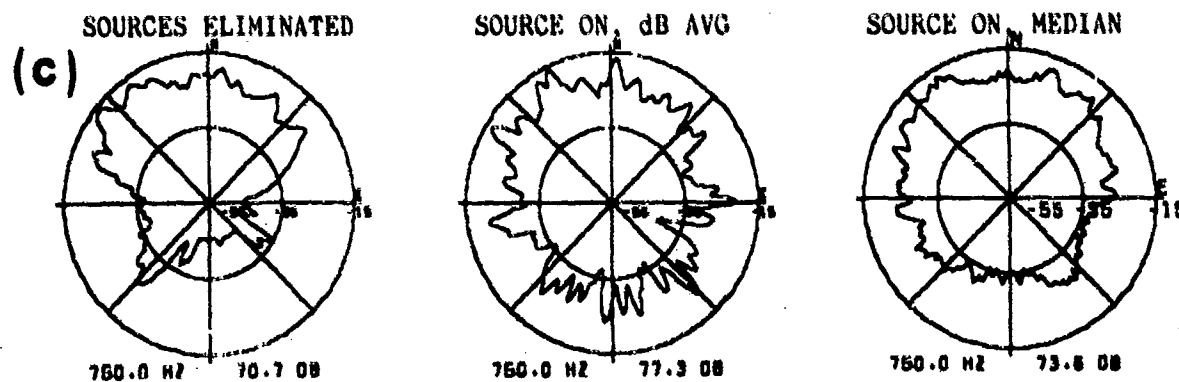
BEAM NOISE



NOISE LEVEL (DB//MPA^{mm2}/HZ)
PLOT LEVELS ARE RELATIVE TO OMNI LEVELS



HORIZONTAL DIRECTIONALITY



NOISE LEVEL (DB//MPA^{mm2}/HZ DEG)
PLOT LEVELS ARE RELATIVE TO OMNI LEVELS

FIG. 6 MEASURED BEAM NOISE POLAR PLOTS SHOWING NORMAL TOWNSHIP NOISE INTERFERENCE (6a), INTERFERENCE WHEN A HIGH LEVEL SOURCE IS OFF (left column) AND WHEN IT IS ON (center and right column) (6b) AND THE RESULTING HORIZONTAL DIRECTIONALITY PATTERNS OBTAINED BY dB AVERAGING AND THE MEDIAN (6c)

measurements for each leg were immediately preceeding or following the measurements without the active rudder on.

The final row of plots are the ambient noise directionality estimates from the beam noise data for 9 legs. The pattern on the left-hand side was obtained from the data sets without the active rudder and the beams containing the towship noise were eliminated from the processing. Hence, this pattern is completely free of contamination by the towship. It will be used to judge the effectiveness of the dB average and the median in discriminating against the towship noise. The omnidirectional level, printed below the plot, is 70.7 dB. The center plot is the directionality estimate from the active rudder data when dB averaging is used. The omnidirectional level is biased up 7 dB and the low levels in the southern half space have not been well reproduced. The results for the median in the third plot are much better. The omnidirectional level is biased up only 3 dB and the low levels have been reproduced much better. The median is clearly a more effective discrimination than the dB average.

The lowest levels achieved by the dB average and the median are not as low as when the active rudder is not used and the towship noise is eliminated in the processing. The main reason this is so is that the sidelobes of the array were not sufficiently suppressed during the measurements. The differences between the active rudder noise and the lowest beams were about 46 dB (96-50). This level of sidelobe suppression was not always achieved during the measurements.

As an example of discrimination in both the temporal and spatial domains consider the ambient noise horizontal directionality results which were obtained by a towed array at one site in the northeast Atlantic. During most of the measurement periods interference was being received every 9 to 11 seconds at levels in excess of 30 dB above the normal beam levels. The hydrophone time series data in Fig. 1 and the hydrophone and beam noise plots in Fig. 2 are from the same measurement time period but for different frequencies. The difficulty of estimating the ambient from the beam data was increased by a sea state of about $\frac{1}{2}$. In such a case, the towship noise is the dominant source, not considering the seismic prospecting noise. It is much easier to estimate the ambient at higher sea states when the towship noise is a smaller part of the total and less discrimination is required.

This case is one in which there was interference in the time domain and spatial domain. The time domain interference consisted of explosive sources being received about every 9 to 12 seconds from an azimuth of approximately 333° . The spatial domain interference consisted of the towship on the forward beams. These two sources dominated the measurements. The seismic prospecting noises were discriminated against in the time domain by using the median beam outputs and the towship noise was discriminated against by using the dB average in the spatial domain. The resulting directionality patterns for 500 to 1500 Hz are included in Fig. 7. These patterns do not show evidence of either the seismic prospecting noise or the towship noise. They are obviously dominated by distant shipping. The two peaks in the northeast quadrant are along azimuths to a Port (72°) and a shipping lane (52°). Without having employed the median and/or dB average in both spatial and temporal domains, it is unlikely that such excellent results could have been achieved.

HORIZONTAL DIRECTIONALITY

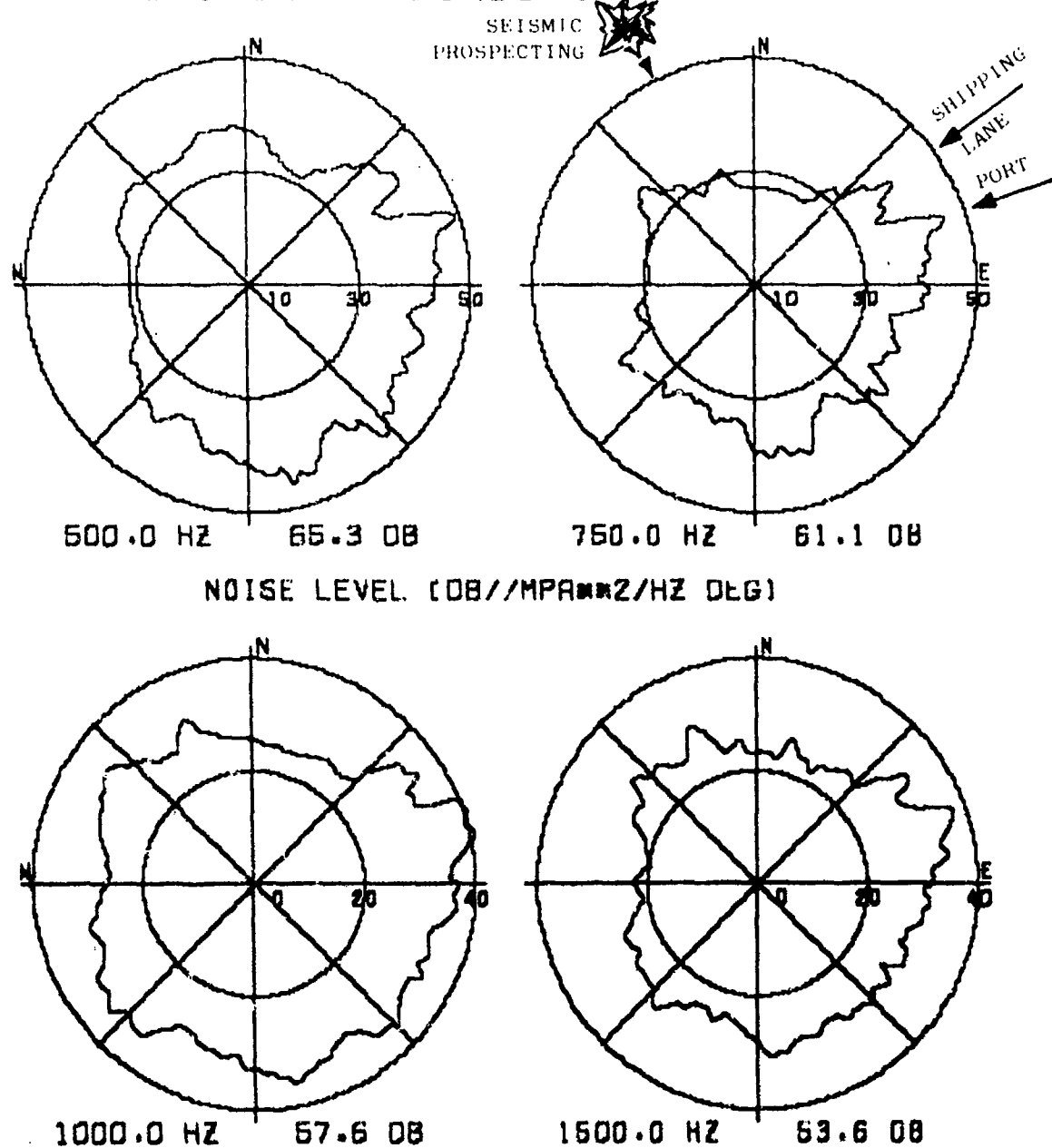


FIG. 7 EXAMPLE OF AMBIENT NOISE HORIZONTAL DIRECTIONALITY PATTERNS OBTAINED IN THE PRESENCE OF A VERY NOISY TOWNSHIP AND SEISMIC PROSPECTING (about 333°)

In general the towed array has a variable geometry. As it is towed along it snakes through the water. The deviation from linearity often increases with increasing sea state and wind conditions. One of the effects of this on the acoustic performance is a degradation in the beamforming capability of the system. One measure of this degradation is the deviation of the measured beamwidth from theoretical. Figure 8a illustrates the effective beam response of a towed array system to the noise from a source on the towship. The arrival angle was about 6 deg. from forward endfire. The results for the three statistics indicate the wiggling of the array over the 13 minute time period required to collect the data has had no adverse effects. All three statistics produce beam responses near theoretical. This is not the case near broadside where the effects of the wiggling are maximum. The bottom reflected arrival for the same time period was received 70 deg. from forward endfire. The results in Fig. 8b indicate that the effective beam response obtained by all three statistics has increased. The theoretical half-power beamwidth should be about 2.15 beam spacings. It is 2.4 for the median, 2.66 for the dB average and 2.95 for the power average. Hence, the median and the dB average have, in effect, "straightened" the array compared to the results for power averaging. The median, however, is the best statistic for this case.

CONCLUSION

It has been shown by example that the power average is not always the best estimator for underwater acoustic data. The median and the dB average are very effective in eliminating or discriminating against some of the sources of data degradation in the environment and in the data measurement and processing systems and give improved result over the power average. Tradition is probably the main reason the power average has been used so extensively by the underwater acousticians. If the power average is not vital to the processing technique the dB average, median, or some other statistic may provide significant improvement in the results. This has been the experience of the authors in the measurement and analysis of towed array data. The technique is sufficiently general that it could be applied to other situations, such as detection or signal processing, with similar results.

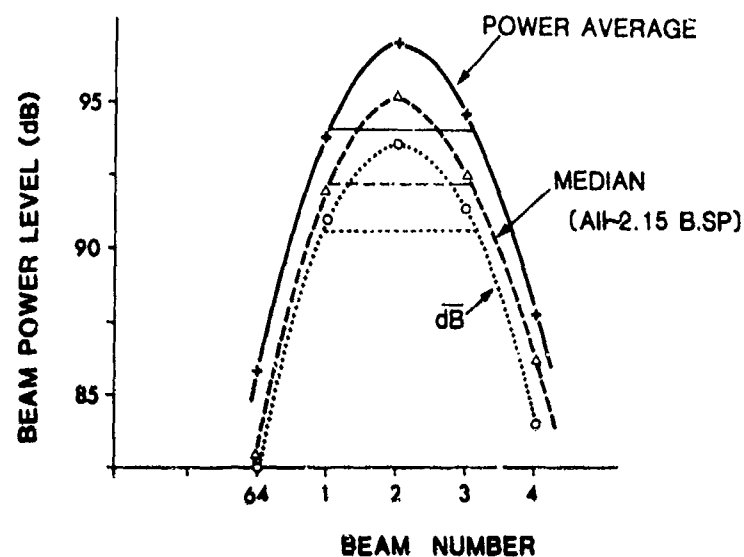
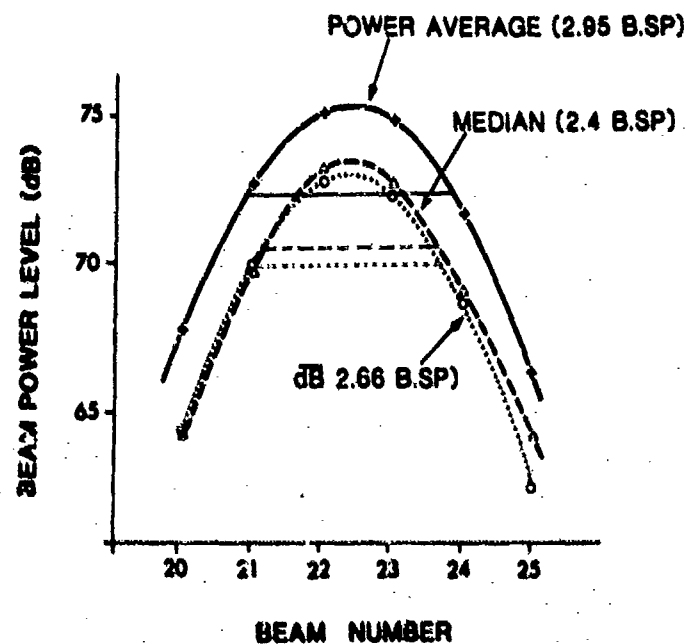
(a) DIRECT ARRIVAL FROM TOWSHIP (~6°)**(b) BOTTOM REFLECTED NOISE FROM TOWSHIP (~70°)**

FIG. 8 BEAM RESPONSE TO A SOURCE (a) 6 DEG. FROM FORWARD ENDFIRE AND (b) 70 DEG. FROM FORWARD ENDFIRE

REFERENCES

1. Berrou, J.L. and Wagstaff, R.A. "Virtual beams from an FFT beamformer and their use to assess the quality of a towed-array system", Proceedings of the IEEE ICASSP 82 conference in Paris, May 82.
2. Hamson, R.M. and Wagstaff, R.A. "RANDI II - An ambient noise model that includes coherent hydrophone summation for sonar systems in shallow, intermediate, and deep water". Presented at and published in the proceedings of the Ambient Noise Conference at SACLANTCEN, May 82.
3. Wagstaff, R.A. "Iterative techniques for ambient-noise horizontal directionality estimation from towed line-array data", J. Acoust. Soc. Am. 63, 1978, 863-869.

A PARAMETRIC EXAMINATION OF SOME PROPERTIES OF THE LOW-FREQUENCY AMBIENT-NOISE FIELD

by

I. A. Fraser

Defence Research Establishment Atlantic
Canadian Department of National Defence
Dartmouth, Nova Scotia, Canada

ABSTRACT

Models for ship-generated ambient noise vary considerably in the detail required of their input data on sources and the environment. This paper describes a model that predicts ambient-noise levels and cumulative distribution functions for Poisson-distributed shipping. Representing statistically both the locations and source levels of the ships serves to minimize the input requirements. It then proves relatively easy to study parametrically the sensitivity of the predictions to propagation conditions, shipping densities, source-level distributions, and array directivity. The model is also well-matched to the limited environmental information often available for sea trials. Predictions will be compared with experimental data to illustrate the utility of the model.

1 INTRODUCTION

Many acoustic sea trials collect ambient-noise data in the frequency range of 10 to 250 Hz where ship-radiated noise is the dominant source mechanism. However, a very considerable effort is then required if enough information on the ship sources and on environmental effects is to be collected to permit the ambient-noise field to be modelled deterministically. Time and resources are very seldom available to do this. Then we must rely on statistical estimates of source levels and locations of ships, and upon transmission-loss model predictions, to provide the necessary input data for the ambient-noise model.

It is essential to have a thorough understanding of the limitations of the predictive capability of such models. How dependent is each aspect of the statistical prediction upon each of the input parameters? How much confidence can be placed in the model if environmental or shipping conditions change? Are all of the major influences on ambient-noise statistics accounted for correctly in the model? It is hoped that this paper and the ambient-noise model FLAN described herein will make significant progress towards answering these questions.

The model is similar to a few others¹⁻³ in that it divides the ocean into arbitrary areas within which transmission loss to a sensor is constant. The number of

ships in each of the areas is assumed to be a random variable (abbreviated rv) governed by Poisson statistics. Based on these assumptions and statistically distributed source levels (SL), we can estimate the zeroth and first order ambient noise statistics, i.e. mean, standard deviation (sd), and (cumulative) distribution function (cdf), where the cdf $F(x)$ is related to the probability density function (pdf) $f(y)$ by the following expression:

$$F(x) = \int_{-\infty}^x f(y) dy.$$

FLAN differs from the other models¹⁻³ to some extent in its ease of specifying input parameter values. It also uses a different procedure for specifying the areas governed by each independent Poisson distribution, and for convolving the contribution of each area to the total noise field.

A set of predictions is made in Section 3 to illustrate the influence of each adjustable parameter upon the noise statistics. To indicate that the model, using plausible input values, is able to reproduce experimental data, some of the examples are compared with data collected by DREA during sea trials. Section 4 briefly describes the influence of horizontal directivity of an array of sensors upon the ambient-noise statistics. A summary of points covered and the main conclusions that stem from this study appear in Section 5.

2 THE MODEL

2.1 ASSUMPTIONS

In the FLAN model for ship-generated ambient noise, the emphasis is on making the input specification as simple as possible. In deference to this aim several assumptions are made. These assumptions are more easily visualized if reference is made to the map in Fig. 1, on which are defined some of the model parameters. The principal assumptions are as follows:

- (1) the ocean area of interest can be divided into a number of subareas, each with constant mean transmission loss to the receiving hydrophone;
- (2) transmission loss (TL), or more specifically, transmission efficiency (TE) defined by $TE = 10^{-(TL/10)}$, is independent of azimuth within a specified sector (in this paper 360° will be assumed for simplicity);
- (3) points (1) and (2) above suggest that the subareas should be annular in shape, as illustrated in Fig. 1, with the sensor or array located at their center;
- (4) the density of shipping (number per unit area Q) is constant between arbitrary minimum and maximum range limits, R_{min} and R_{max} .

- (5) the number of ships in a given annulus is an rv n_h drawn from a Poisson distribution, with a mean ship count of b_h in the h -th annulus;
- (6) each contributing class of ships is distributed uniformly throughout the area of interest so that the composite source-level distribution will prevail everywhere;
- (7) transmission loss will normally be assumed to increase as $20 \log R$ up to transition range R_0 and as $10 \log R$ thereafter, with an additional attenuation proportional to range and specified by a coefficient α (there is also provision for using TL calculated with a ray-trace model);
- (8) virtually any source-level distribution can be mocked up by combining m relatively narrow distributions of arbitrary mean source level and weighting factor;
- (9) the statistical predictions are representative of an ensemble average over a large number of statistically independent data samples.

2.2 MODEL DEVELOPMENT

The FLAN model is called upon principally to relate ship and environmental information to cumulative distribution functions of ambient-noise level. Therefore convolution of the density functions of input parameters will be expected to play an important role in the calculation. The USI model¹ uses ingenious techniques to avoid traditional convolution formulations. However, in the present case computational efficiency is not of primary concern. Rather, the emphasis is on minimizing the number of user-input parameters and easing the burden of specifying their values.

The discussion will first focus on the model development. Numerical procedures will be described in Section 2.3.

The method of dividing the ocean into annuli, each with constant transmission efficiency, was illustrated in Fig. 1. The model development proceeds from this point as shown schematically in Fig. 2. Four factors must be taken into account: the sources, the ocean medium for conducting the sound, the hydrophone sensor or array, and the data-analysis procedures.

The source power for each ship is an rv y drawn from the same density $f(y)$, as implied by Fig. 2. The selection of a form for the source-power pdf is governed by two requirements: (1) that its characteristic function be easily evaluated, and (2) that it be easily transformed into the log domain to facilitate comparison with published source-level distributions. Perhaps the simplest pdf to fulfill these conditions is the gamma density. In order to fit the great variety of possible SL density-function widths and shapes, it is necessary to provide for a weighted sum of gamma densities with different median values. The source-power pdf then has the following form:

$$f(y) = W_m \frac{c^{p+1}}{p!} y^p e^{-cy},$$

where in the present use p is arbitrarily chosen as 2, W_m is the weight for the m -th SL density, and

$$c = 3 \frac{\exp(-SL_{om}/g)}{TE_h}.$$

Here SL_{om} is the most probable value of the m -th source-level density and $g = 10 \log e = 4.343$.

As noted previously, the number of ships in each annulus, n_h , is also an rv (Poisson-distributed) with parameter b_h , the mean number of ships in the annulus. Since each annulus has the same width Δr , b_h is proportional to the radius r_h . The medium modifies each noise source by the factor TE_h , so that the total noise power from annulus h becomes

$$x_h = \sum_{k=1}^{n_h} TE_h y_k.$$

The sensor provides to the processor an incoherent noise sum over all annuli:

$$z = \sum_{h=1}^H x_h.$$

Rather than convolving the pdfs of the rvs x_h to determine that of z , it is desirable to obtain and multiply together the characteristic functions (cf)s for the rvs in order to determine the ambient-noise power distribution. The process of summing the noise contributions from the various annuli is a "generalized Poisson process" as described by Papoulis (Ref. 4, page 576). The cf for x is then given by:

$$\Phi_{x_h}(\omega) = e^{b_h[\Phi_y(\omega TE_h) - 1]},$$

invoking the following property of cfs

$$\Phi_x = \Phi_y(\omega d),$$

where $x = yd$. The cf for z is

$$\Phi_z(\omega) = \prod_{h=1}^H \Phi_{x_h}(\omega),$$

and for y it is

$$\Phi_y(\omega TE_h) = \sum_{m=1}^M W_m \frac{(1 + j\omega TE_h/c)^3}{[1 + (\omega TE_h/c)^2]^3}.$$

2.3 NUMERICAL PROCEDURES

The inversion of $\Phi_z(\omega)$ to form $f(z)$ is accomplished by a discrete Fourier transform (DFT) using a procedure devised by Bird⁵ and implemented at DREA by Walker⁶. Bird has shown that the DFT can be readily performed provided that the input densities are zero above an arbitrary limit Y . He then deduces appropriate values for Y , and for J , the number of terms in the finite approximation to the DFT for the general case.

Walker obtains⁶

$$F(z) = \frac{z}{Y} \sum_{l=-\infty}^{\infty} \Phi_z\left(\frac{2\pi l}{Y}\right) \text{sinc}\left(\frac{\pi l z}{Y}\right) e^{-j\pi l z/Y} \quad (1)$$

for $z < Y$, where $\text{sinc}(z) = \sin(z)/z$. (It is assumed that $f(z) = 0$ if $z > Y$.) In Eqn. (1)

$$\Phi_z\left(\frac{2\pi l}{Y}\right) = \Phi_z(\omega).$$

In the case of a Poisson density it is necessary to truncate the probability density function (pdf) at a value Y to fulfill the above-mentioned condition. (In FLAN, Y was chosen to be equal to the mean noise level plus 15 dB.) Furthermore, the infinite sum over l in Eqn. (1) can not be accomplished in practice. Bird provides arguments suggesting that a practical rule for truncation is to determine J , the maximum value of l , from the following expression:

$$\frac{|\Phi_z(2\pi l/Y)|}{2\pi l} < 10^{-6}.$$

The expression used to evaluate $F(z)$ in FLAN is Walker's Eqn. (A10):

$$F(z) = \frac{z}{Y} + 2 \sum_{l=1}^J \text{Re} \left[\frac{\Phi_z(2\pi l/Y)}{j2\pi l} (1 - e^{-j2\pi l z/Y}) \right].$$

3 ANALYSIS PROCEDURES AND PREDICTIONS

3.1 INPUT PARAMETERS

The program FLAN was run for a variety of plausible input-value combinations to test their influence upon the cdf, mean and standard deviation. The input variables are listed in Table 1.

TABLE 1. Input parameters for noise model FLAN

Q	Density of shipping (number/km ²)
R _{min}	Minimum analysis range (km)
R _{max}	Maximum analysis range (km)
N	Mean total number of ships (if specified, governs maximum analysis range)
	Transmission-loss range dependence (generated externally by an acoustical model or defined by the following parameters:
R _c	- crossover range (from spherical to cylindrical spreading loss)
α	- attenuation coefficient (dB/km)
Δr	Width of annulus (usually about 2 km)
	Source-level data:
M	- number of density functions
SL _{om}	- most probable source level of each density function
W _m	- weighting factor for each density function.

3.2 PREDICTIONS--DEEP WATER

First we shall examine the dependence of the statistics upon shipping density, with other factors held constant at typical values, and transmission loss assumed to increase linearly with range. Four cdfs covering the range of light to heavy shipping densities are shown in Fig. 3. Several points can be made with respect to these cdfs:

- (1) the median noise level is approximately proportional to $10 \log(\text{shipping density})$: as the density of shipping rises, so does the mean ambient noise power;
- (2) the slopes of the cdfs (related to the sd) increase with decreasing shipping density Q: fewer ships provide less chance of averaging out the differences in source level, transmission loss and ship numbers;

- (3) the cdf is nearly log normal over 2 to 3 standard deviations, at least for the higher values of Q . In a small fraction of the samples and at short ranges a very few ships may be exposed to significantly different propagation conditions, such as the nearest convergence zone, or the direct-path region at a range less than R_0 . This causes the curves to break near the 90th percentile. Since the source levels for all ships are drawn from the same pdf, all the cdfs of ambient noise will tend towards the same value at the high-noise limit.

Several examples showing this break in the cdf are provided in Fig. 4 for two types of propagation: on the left for convergence zones, and on the right for a smoothly increasing dependence of TL upon range. The variation of cdf shape with changing R_{\min} points to nearby ships as the source of the curvature.

In deep water the mean and standard deviation of the noise field appear to depend most strongly upon the mean number of ships N . This dependence is examined with the aid of FLAN predictions in Fig. 5. The mean ship population contributing to the noise field is governed principally by Q , the shipping density, and by the upper range limit R_{\max} . All other model parameters are held constant at representative values. It is clear that the major influence on sd is the value of N . For example, a change in ship density Q from 1.0 to 0.2 ships/ 10^4 km² is seen to change sd by only 0.25 dB, provided that a corresponding change is made in R_{\max} to hold N constant. It is interesting to note that the ambient-noise sd curves in Fig. 5 follow a trend similar to the sd of total ship count, where the latter is assumed to obey Poisson statistics.

A major concern in ambient-noise studies is the difficulty of specifying source-level distributions with any degree of confidence. The influence of several plausible source-level pdfs upon the sd of ambient-noise level is displayed in Fig. 6. The curves relating ambient noise sd to source-level sd were calculated for a single source-level pdf shape, namely that of Case 2 in the upper left corner of the diagram. Larger standard deviations are obtained by stretching the pdf to cover a larger range of source levels. The three source-level pdfs illustrated (Cases 1 to 3) were chosen to assess the effect of extreme changes in the density function shape upon the sd of ambient noise. The results for a Q of 1 ship/ 10^4 km² and a source-level sd of 9 dB are indicated by crosses. In all cases tested, quite drastic changes in shape or in sd of the source-level pdfs were necessary in order to produce even modest changes in the ambient-noise sd.

Next we present a cursory examination of the effect of transmission-loss trends upon the statistics of interest. Several plausible deep-water range dependencies of TL are illustrated in Fig. 7. Two curves, labeled Labrador Sea and Mid-Atlantic were generated by a ray-trace program for specific ocean areas. The other three curves reflect various combinations of R_0 and α . Predictions of cdf shape have been derived for the four lowest curves in Fig. 7 and are displayed in Fig. 8. (The Labrador Sea case will be deferred to Fig. 9.) The variations in shape and slope of the cdfs are seen to be quite weak, considering the large variations in R_0 and in α . When α is greatest, the influence of the many distant ships is diminished relative to those nearby. This increases the ambient-noise variability, i.e. steepens the cdf

slope. The effect is evident in Fig. 8. Little dependence of the cdf on R_0 is observed, however, except above the 90th percentile. For the convergence-zone propagation (mid-Atlantic TL profile), both the slope of TL and of the cdf are most closely aligned with the geometric cases for which $\alpha = 0.01$ dB/km.

Referring again to Fig. 7, we observe a large offset between TL in the Labrador Sea and that typical of the mid-Atlantic. If all other factors are assumed equal, then we would expect the mean ambient-noise level to be many decibels higher in the Labrador Sea environment. The cdf predictions for the two locations are represented by the top and bottom curves for equal densities of 1 ship/ 10^4 km² in Fig. 9. The sd of 1.55 dB for the lowest curve is quite typical of measurements near Bermuda⁷. However, DREA data (represented by dots in Fig. 9) collected in the Labrador Sea imply a much lower ambient-noise level and steeper cdf slope than that represented by the top curve. The good fit provided by the middle curve was obtained simply by reducing the shipping density by a factor of 5, and the ocean-basin size by 30%. Both changes are quite plausible. How much the source-level densities differ in practice, and how significant are different shipping and fishing patterns is, of course, much more difficult to assess.

3.3 PREDICTIONS--SHALLOW WATER

The shallow-water acoustical environment requires some changes in scale to be made to input parameters of the FLAN model. Transmission loss at short ranges tends to be less than in deep water, but often is subject to a relatively large attenuation as range increases. These differences in TL can be accommodated by reducing R_0 and increasing α , relative to their deep-water values. (DREA has been cataloging much of Canada's eastern shallow-water area in terms of these parameters.)

It is also anticipated that R_{\max} should be much smaller in the confined continental shelf areas than in the deep ocean basins. A value of $R_{\max} = 200$ km was chosen for this study.

Source levels of fishing vessels generally are somewhat smaller than those for merchant ships. However, during fishing operations their radiated noise levels can be extremely high and quite variable.

The preceding factors all tend to increase the slope of cdfs relative to their typical deep-water values. A comparison of two cases for which data are available is made in Fig. 10. The shallow-water data were obtained by DREA in an area characterized by heavy shipping; the deep water data were obtained off Canada's east coast. Historical shipping densities were used in the model predictions, together with the source level density function illustrated as Case 2 in Fig. 6. R_{\max} took on values of 750 km and 200 km for, respectively, the deep and shallow-water cases. The only parameter adjusted to provide the model fits shown in Fig. 10 were the mean values of the two source-level pdfs. The main factor contributing to the steepness of the shallow-water cdf is the elimination of contributions normally made by the many ships beyond 200 km range in deep-water areas.

The effect of variations in attenuation coefficient, α , upon the cdf is displayed in Fig. 11. Since α at low frequencies can be an order of magnitude greater in shallow water than in deep, its effect upon the cdf can be significant. As in the deep-water case (Fig. 8), the cdf becomes steeper as α increases. A low-noise limit must be reached, however, as the shipping noise drops to zero, leaving only wind-generated noise in its stead.

4 ARRAY DIRECTIVITY

The directional sensitivity (directivity) of an array of sensors can significantly influence the low-frequency ambient-noise statistics. For example, a narrow horizontal beam will reduce the number of contributing ships from an isotropic shipping distribution by the ratio of beamwidth to 360° (or 180° in the case of a line array). Not only is the mean noise power reduced by this factor, but the cdf slope, and consequently the sd, are increased by an amount that can be assessed by reference to Figs. 3 and 5, which show the influence of mean ship count upon cdf shape and upon sd, respectively. The effect of sidelobe structure requires special attention, and will not be addressed in this paper.

5 SUMMARY AND CONCLUSIONS

A parametric ambient-noise model FLAN has been developed to assess the impact of variations in ship source levels and numbers, of transmission loss, and of sensor directivity upon the first-order statistics of ambient noise at low frequencies. A special effort has been made to minimize the number of input parameters and the effort required to specify their values, possibly at the expense of generality. This was done (1) to match the model's input requirements to the many experimental situations where little is known about the ships contributing to the noise field and the prevailing sound-transmission conditions, and (2) to make it easy to vary each parameter in a systematic manner to assess its impact upon the statistics of ambient noise.

The principal conclusions reached in the study are:

- (1) a wide variety of experimental data can be fit by such a model,
- (2) good model fits to experimental cdfs do not imply an unambiguous set of input-parameter values,
- (3) under many conditions the cdf of ambient noise is predicted to be log normal over two to four standard deviations,
- (4) the sd of ambient noise is principally dependent upon the number of ships contributing to the noise field,
- (5) in the case of directional arrays the number of ships contributing strongly to the noise field is diminished, so that the sd tends to become larger.

- (6) the sd of ambient noise is weakly dependent upon the source-level pdf of contributing ships, upon R_{min} , and upon R_o ,
- (7) the shape of the cdf (as opposed to its slope) draws away from log-normal behavior as R_{min} and Q decrease, and as α increases,
- (8) shallow-water cdfs tend to be much steeper in slope than those for deep water, primarily because of the smaller region over which ships can contribute to ambient noise.

Extensions of the model to include explicitly the effect of shipping lanes, convoys, azimuthal dependence of transmission loss, and TL fluctuations can be envisaged, in order to increase its ability to cope with realistic environments. The cost of such improvements will be additional complexity in the input specification.

6 REFERENCES

1. R.L. Jeanette, E.L. Sander, L.E. Pitts, "The USI noise model, Version 1", Underwater Systems Inc. Report Nos. USI-APL-R-8 and 9 (April 1977); as described in "Review of models of beam-noise statistics", Science Applications Inc. Report No. SAI-78-896-W/A (Nov. 1977).
2. B.J. McCabe, "Ambient noise effects in the modeling of detection by a field of sensors", Daniel H. Wagner, Assoc. Report, Paoli, Pa. (5 Nov. 1976).
3. M. Moll, R.M. Zeskind, F.J.M. Sullivan, "Statistical measures of ambient noise: algorithms, program, and predictions", Bolt Beranek and Newman Report No. 3390, Arlington, Va. (11 June 1977).
4. A. Papoulis, Probability, Random Variables, and Stochastic Processes (McGraw-Hill, New York, 1965).
5. J.S. Bird, "Calculating detection probabilities for radar and sonar systems that employ non-coherent integration", IEEE Trans. Aerosp. Electron. Syst., accepted for publication.
6. R.S. Walker, "The detection performance of FFT processors for narrowband signals", DREA Technical Memorandum 82/A, Dartmouth (Feb, 1982).
7. A.J. Perrone, "Deep-ocean ambient-noise spectra in the northwest Atlantic", J. Acoust. Soc. Amer. 46, 762 (1969).

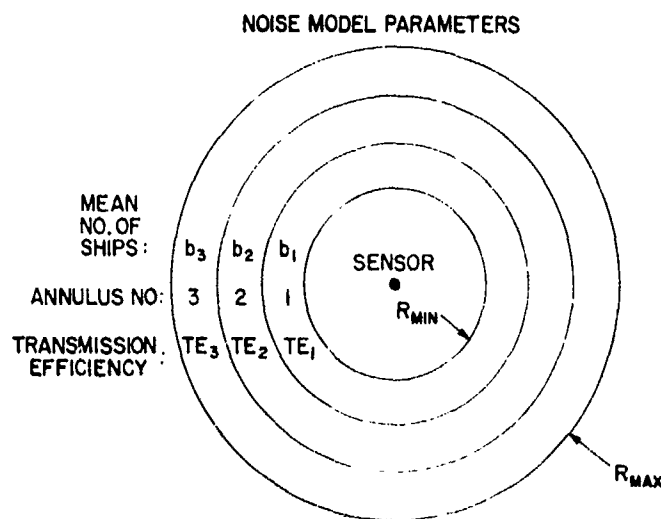


FIG. 1

MAP OF OCEAN AREA DEFINING NOISE-MODEL PARAMETERS

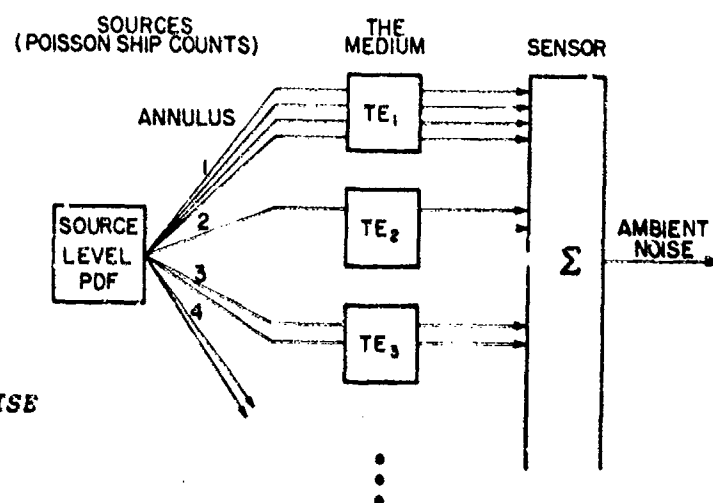


FIG. 2

SCHEMATIC DIAGRAM OF PLAN NOISE MODEL

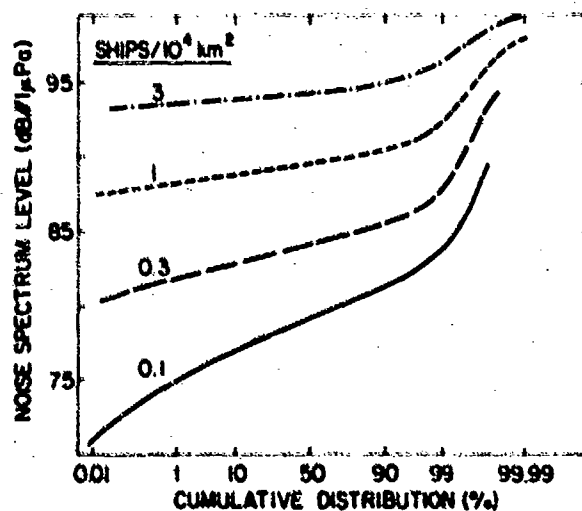


FIG. 3

EFFECT OF SHIPPING DENSITY UPON THE CUMULATIVE DISTRIBUTION FUNCTION OF AMBIENT NOISE

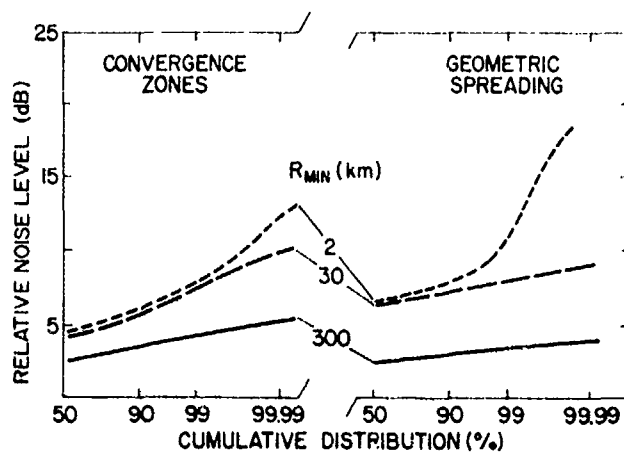


FIG. 4

EFFECT OF MINIMUM CUTOFF RANGE
UPON CUMULATIVE DISTRIBUTIONS
IN TWO OCEAN ENVIRONMENTS

FIG. 5

EFFECT OF MEAN SHIP POPULATIONS
UPON THE AMBIENT-NOISE STANDARD
DEVIATION

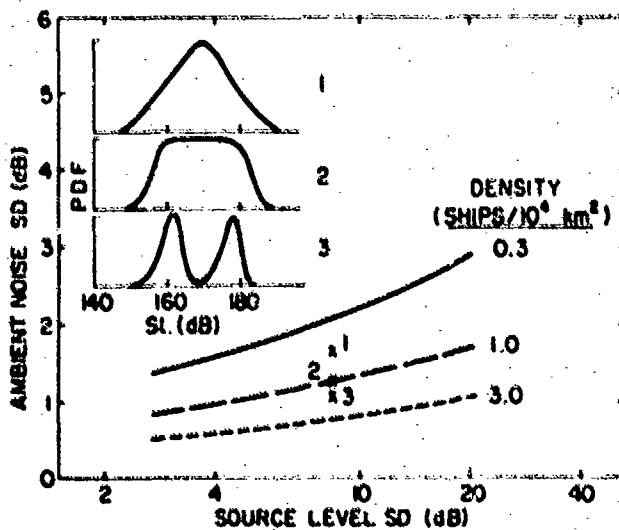
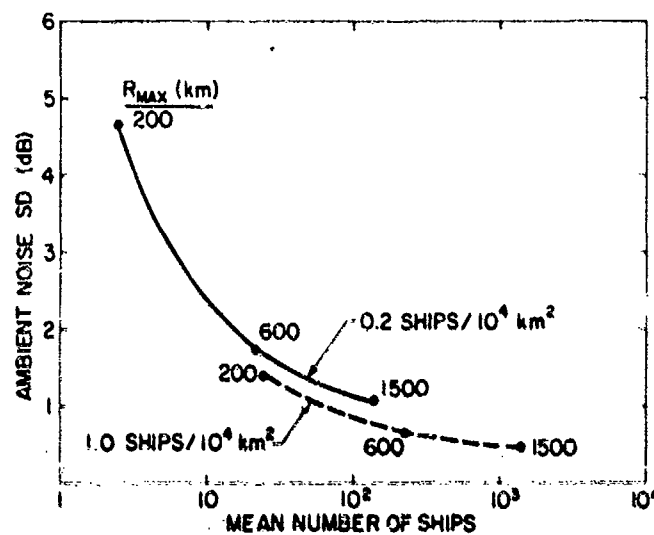


FIG. 6

EFFECT OF SOURCE-LEVEL PROBABILITY
DENSITY FUNCTION UPON THE AMBIENT-
NOISE STANDARD DEVIATION

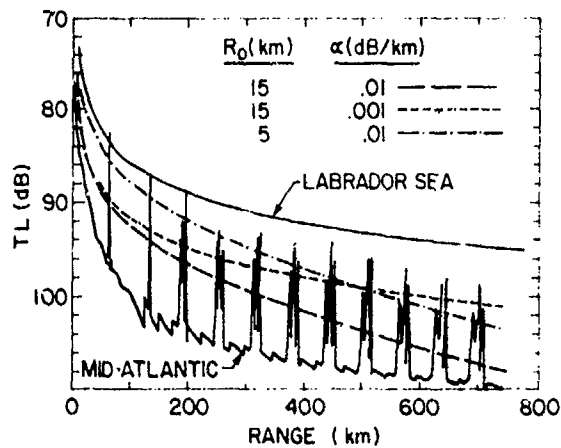


FIG. 7
SOME TYPICAL TRANSMISSION-LOSS
RANGE DEPENDENCES

FIG. 8
CUMULATIVE DISTRIBUTION FUNCTIONS
ASSOCIATED WITH THE TRANSMISSION-
LOSS CURVES OF FIG. 7

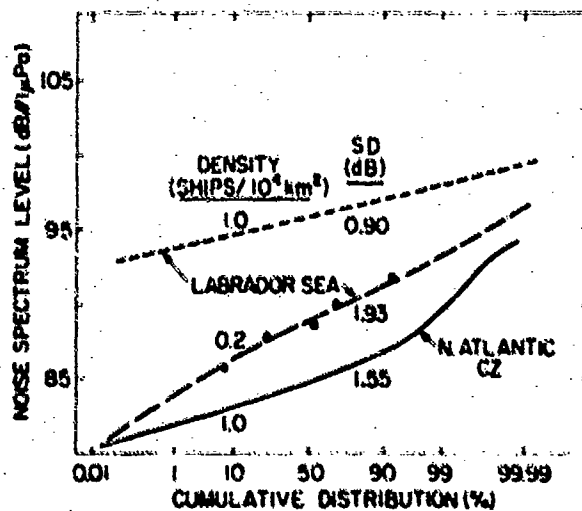
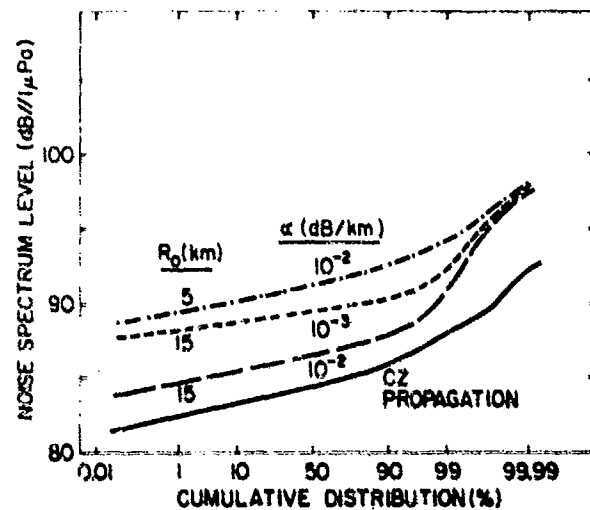


FIG. 9
COMPARISON OF CUMULATIVE DISTRI-
BUTION FUNCTIONS FOR THE LABRADOR
SEA AND AN OCEAN AREA FURTHER
SOUTH

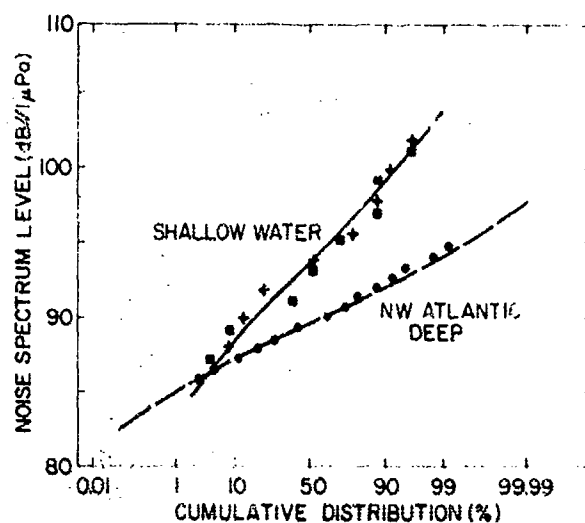
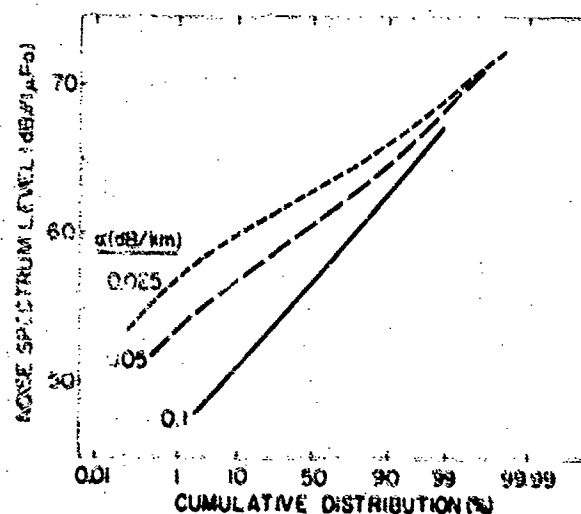


FIG. 10

COMPARISON OF SHALLOW WATER AND DEEP WATER CUMULATIVE DISTRIBUTION FUNCTIONS, WITH SYMBOLS REFERRING TO DREA EXPERIMENTAL DATA

FIG. 11

EFFECT OF ATTENUATION COEFFICIENT UPON THE CUMULATIVE DISTRIBUTION FUNCTION IN A SHALLOW WATER AREA



DETECTION MODELS AND TARGET INFORMATION PROCESSING

by

Dr. James W. Bond
 Naval Ocean Systems Center
 San Diego, Ca., USA

ABSTRACT

The passive sonar equation leads in a natural manner to sensor detection performance contours. Useful information can be extracted from observed fractional holding time on non-cooperative targets by use of these contours. The derived information could aid in multiple sensor contact data association and the localization and tracking of poorly held targets. Target source level and sensor processor recognition differential need not be input to the prediction model to prioritize candidate contact data associations. A surprising example shows that use of predictions to estimate the range to initially detected targets is not likely to work. An idealized but reasonable example shows that the probability of a target remaining undetected at further ranges and first detected at a given range can be independent of the range of the target from the sensor. The theory of stochastic differential equations applied to tracking a target may alleviate the difficulty. The paper closes with recommendations for the development of model capabilities to provide more useful outputs for information processing.

INTRODUCTION

Detection models for passive acoustic sensors have been used for operational research, sensor trade-off studies, and planning sensor deployments. Detection models have been little used for real-time information processing. The purpose of this paper is to describe several applications of models to real-time information processing. The use of detection models to aid in contact data association and target localization and tracking will be investigated.

To provide a context for the discussion, postulate a processing center designed to handle non-cooperative targets through the reduction and analysis of passive acoustic sensor data. The target data consists of detections of signals, whose frequency, bearing relative to the sensor, and signal level relative to ambient noise are measured. The environmental data consists of directional ambient noise and clutter levels estimated within the processing center as well as externally provided data to the center.

Targets held consistently by several sensors pose no intrinsic information handling problems while targets held infrequently pose very difficult

handling problems. For infrequently held targets, detection models appear useful in two ways: (1) to extract meaning from detections and non-detections and (2) to supplement measurement data on a target with predicted data. Applications using models in each of these ways will be discussed.

In section one an operationally observable measure, fractional holding time, is defined. Previous results obtained by the author comparing operational fractional holding time with predicted seasonal detection performance contours are briefly reviewed. These operations analysis results provide, in particular, a characterization of the variability of fractional holding time. The variability of the observable is especially important because it provides the basis for an assessment of the operational usefulness of detection performance predictions.

In section two, a general approach to using detection models to aid in contact data association is identified. The model is used to refine geographic consistency algorithms now commonly used for data association by accounting for the probabilities of observing given fractional holding times conditioned on the association. The predictions required need not use an input value of target source level, thus avoiding the often very difficult problem of estimating this parameter.

In section three the use of detection models for single sensor localization is first discussed. The inference of target range from fractional holding time is investigated. An example indicates that a most likely range for an initial contact need not exist. A more general approach to target tracking appears to be required. The use of stochastic differential equations seems to offer some chance of overcoming these difficulties with the added advantage that use can be made of sensor non-holding information (so-called negative information) as well as better use of sensor holding information (positive information).

Section four contains a brief discussion of the directions that passive acoustic sonar modeling might take to better aid in information processing. It is suggested that the predictions should more fully utilize measurement data available in the processing center and should aim to predict additional observable features of detected signals.

1 SINGLE SENSOR DETECTION PREDICTIONS

The basis for passive acoustic sensor detection performance predictions is the passive sonar equation (in decibels)

$$SE_t = SL - RD - PI + e_t, t \geq 0. \quad (1)$$

From the viewpoint of the user of the predictions, source level (SL) summarizes the relevant target characteristics, while recognition differential (RD) summarizes the relevant signal processor characteristics. The performance index (PI) is a function of range, seasonal, and directional dependent transmission loss (TL), season and directional dependent ambient noise (AN), and directional dependent array gain (AG) in the following manner:

$$PI = TL + AN - AG .$$

The performance index therefore summarizes all of the non-target and non-processor relevant properties of the environment and sensor whose performance is being predicted. Signal excess SE_t varies as a function of time t .

One possible representation of the stochastic behavior of SE_t is the λ - σ jump model which is a simple step function of time. The family of step functions are conditioned by assuming

- (1) ε_t is normally distributed with zero mean and variance σ^2
- (2) ε_s and ε_t are different with probability $1 - \exp[-\lambda(s-t)]$ and equal with probability $\exp[-\lambda(s-t)]$, $\lambda > 0$, $s > t$.

These criteria define a commonly used stochastic process for SE_t which has a normal distribution with variance σ^2 and an exponential autocorrelation function with a relaxation time constant of $1/\lambda$.

A natural manner to summarize expected performance over a period of time T is to predict the probability p that the instantaneous signal excess SE_t is non-negative. For example, if the expected value of signal excess were zero, then SE_t would be expected to be non-negative half of the time and p would be $\frac{1}{2}$. Furthermore, it is assumed that the operational measure of holding performance, the fraction of time that contact is held, fractional holding time (FHT) is an unbiased statistical estimate of p . Values of FHT will therefore be the observables which will be compared to predicted values of p .

From (1) it follows that

$$\begin{aligned} p &= \text{Prob}\{SE_t \geq 0\} = \text{Prob}\{\varepsilon_t \geq PI - SL + RD\} \\ &= 1 - \Phi\left(\frac{PI - SL + RD}{\sigma}\right) \end{aligned}$$

with

$$\Phi(x) = \int_{-\infty}^x \frac{1}{\sqrt{2\pi}} \exp[-\frac{1}{2}y^2] dy . \quad (2)$$

Another formulation of equation (2) is

$$\Phi^{-1}(1 - p) = (PI - SL + RD)/\sigma . \quad (3)$$

Equation (3) exhibits $\Phi^{-1}(1 - p)$ as linearly related to PI with the slope of the line inversely proportional to the standard deviation σ of signal excess and with intercept $(SL - RD)/\sigma$.

The observable to be compared with the predictions is fractional holding time, FHT, defined as a sum of holding intervals of a particular target acoustic source over the sum of opportunity time in a region bounded by two PI contours $1\frac{1}{2}$ dB apart as illustrated in Figure 1. The FHT for such a

region will be compared with the probability p for the average value of the two PI values. The expected variability of the observable FHT is a function of the true probability of non-negative SE_t in the PI bin and the total target opportunity time T in the bin. Let $f(t) = 1$ if the source is detected and 0 if a source is not detected by the sensor. Then, from $FHT =$

$1/T \int_0^T f(t) dt$ and the fact that $\epsilon_t, t \geq 0$ is a zero mean λ - σ stationary process it follows

$$E[FHT] = p \quad (4)$$

$$VAR[FHT] = 2p(1 - p)[(e^{-\lambda T} - 1 + \lambda T)/(\lambda T)^2] \quad (5)$$

The term involving λT converges very rapidly to $1/\lambda T$ as $\lambda T \rightarrow \infty$ and therefore equation (5) simplifies to

$$Var[FHT] \approx 2p(1 - p) 1/\lambda T \quad (6)$$

The variation in SE induced by target position changes and target source level changes as well as sound propagation and ambient noise variation can be estimated by regression of FHT against PI . For this regression each observation $\phi^{-1}(1-FHT)$ should be weighted according to its expected variance. The formulas used for the results presented in this paper are derived from equation (6) by use of the first two terms of the Taylor expression of ϕ^{-1} evaluated at $1 - p$ and resulted in

$$Var \phi^{-1}(1-FHT) \approx \left[\dot{\phi}(x) \right]^{-2} Var FHT = (2\pi) e^{x^2} Var[FHT] \quad (7)$$

where $1 - p = \phi(x)$ and $x = E[FHT]$ using known properties of ϕ .

Data was pooled for several targets with no a priori assumptions as to source level or recognition differential. The standard deviation of signal excess was also assumed to be unknown but dependent on season but independent of target. Figure 2 presents an example of the regression results obtained. Data is presented for seven targets deployed during the winter season. The left scale is in terms of the transformed variable $\phi^{-1}(1-FHT)$ and the right-hand scale is natural. The overall σ results obtained are summarized in Table 1. The noteworthy implication of these results is that summer estimates of σ are from 4 to 7 db higher than winter estimates. This result lends credibility to the estimates because greater variability would be expected during the summer than the winter due to propagation effects. The fact that propagation paths are more sharply focused during the summer would lead to greater variation of received signal level as a function of target position.

The variability in signal excess implied by the values of σ in Table 1 exceeds that estimated due to statistical variability by equation (7). Some of this increased variability is induced by the use of fixed transmission loss estimates as a function of angle for each sensor and season and the use of an average direction dependent ambient noise for each sensor.

TABLE 1. EXAMPLE OF σ ESTIMATES OBTAINED FROM A REGRESSION ANALYSIS OF FHT ON REAL TARGETS.

	Summer Season	Winter Season
SENSOR 1		*
Number of Targets	5	7
Degrees of Freedom	26	41
Point Estimate of σ	17.1	10.2
90% Fiducial Bounds of σ	12.3 27.9	8.2 13.6
SENSOR 2		
Number of Targets	4	7
Degrees of Freedom	29	14
Point Estimate of σ	10.1	5.9
90% Fiducial Bounds of σ	8.1 13.5	4.4 8.7

*Case presented in Figure 2.

Figure 3 shows an example of the variability observed for a nominal case, not the best case nor the worst case. The solid lines are 90% confidence bounds on the regression line and the dotted lines are 90% confidence bounds on the observations. In this example, even though the regression line is estimated with reasonable confidence, the variability of the observations is around 7 dB. Predictions which use real-time estimates of transmission should reduce this loss or ambient noise variability. However, at this time an analysis to assess the variability of observed fractional holding time relative to real-time predictions has not been undertaken to the author's knowledge.

The operational analysis results imply two conclusions relative to the use of models for real-time information processing:

- (1) predictions for real-time use should be based on real-time data; and
- (2) although regression analysis can estimate σ and SL-RD for a large data base, these estimates will normally not be available for real-time applications.

2 USE OF PREDICTIONS FOR CONTACT DATA ASSOCIATION

The fundamental problem in data association is to calculate the probability that a given set of observations occurs. The calculation can be factored into the calculation of two probabilities:

- (1) the probability that the observed line characteristics, e.g., frequency, bandwidth, stability, would be associated with the acoustic sources of a single target; and
- (2) the probability that the available operator heuristic information would have been generated if they were on the same target.

If detections are associated for different sensors, then an additional factor becomes important:

- (3) the probability of the observed detections occurring on specific bearings for some sensors and not occurring on specific bearings for other sensors for each target acoustic source.

There appears to be a real possibility of exploiting detection models to improve the estimation of the third factor and little possibility of their use in the estimation of the other factors. Therefore, we focus our attention on the two sensor contact association problem. It is convenient to introduce the following notation to aid in a concise formulation of the problem:

The observations consist of fractional holding times $FHT_i(f_j)$ for a specified opportunity time T , for sensors $i = 1, 2, \dots, M$, and acoustic sources with nominal frequencies f_1, f_2, \dots, f_N .

The sensor indices $i = 1$ and 2 are chosen so that the contact association consists of $FHT_1(f_j)$ and $FHT_2(f_k)$.

The $FHT_i(f_j)$ are all supposed to be appropriately calculated, i.e., the holding time on a sensor i for target source with frequency f_j has been on a single target. (The reader will note that it would be straightforward to extend the results presented to the case when these single sensor, single source associations had been made correctly with probability P_{ij} over the opportunity time T .)

To interpret the observed fractional holding times it is necessary to associate PI values to them. A value of T of 24 hours or larger appears to be reasonable. To associate a PI value to an observed FHT define an opportunity region as in Figure 4 compatible over time with the bearing information observed on the sources f_j and f_k for sensors 1 and 2, respectively, during the opportunity interval T . Such a region would have lengths on the order of $2VT$ where V is the average speed-of-advance of the target. View the region defined in log R coordinates and take the centroid (or a point approximating it) as the position for which PI predictions are compared with the observed FHT.

The PI predictions for the centroid should be as accurate as possible and therefore should be real-time predictions using sensor measured directional ambient noise and the best available sound velocity depth profiles for transmission loss predictions.

Equation (3) exhibits the probability of detection p as a function of PI, with parameters σ , RD, and SL. The value of σ can be empirically estimated by sensor based on an analysis of historical data. The value of RD can be updated in real time from the outputs of passive acoustic sensors through the use of an automatic detection algorithm to calibrate operator responses. A priori estimates of SL are generally not available, so a posteriori estimates will be used. Toward this end, view p as a function of SL. Suppose that the opportunity time T is long enough and the target maneuvers such that the average value of SL observed by the sensors during the opportunity time T is independent of sensor. Then equation (3) implies that for sensors 1, 2, ..., M the probabilities $p_1(SL)$, $p_2(SL)$, ..., $p_M(SL)$ are derivable from the sensor PI values PI_1 , PI_2 , ..., PI_M for the centroid of the opportunity region as a function of a single unknown SL.

A natural measure of consistency between $p_i(SL)$ and FHT for a given acoustic source and the M sensor's is the weighted mean-square error $E(SL)$ defined by

$$E(SL) = \sum_{i=1}^M (FHT_i - p_i(SL))^2 / (\text{Var}[FHT_i] + \text{Var}[p_i(SL)]) . \quad (8)$$

The smaller $E(SL)$ can be made the more consistent are the observations. Furthermore, the value of SL which minimizes $E(SL)$ provides the a posteriori estimate of SL as previously mentioned.

The value of $\text{Var}[FHT]$ used in equation (8) can be determined using equation (5) with the value of λ estimated empirically from an analysis of historical operational data. (Such an analysis is now in progress at NOSC by the author.)

The value of $\text{Var}[p]$ can be estimated by differential approximation (refer to Figure 5). It follows that

$$\Delta p \approx \phi \left(\frac{SE}{\sigma} \right) \frac{\Delta PI}{\sigma} , \quad (9)$$

where $SE = -PI + SL - RD$ and σ is the standard deviation of signal excess

with $\phi(x) = \frac{e^{-x^2/2}}{\sqrt{2\pi}}$ by the fundamental theorem of calculus. Assume the value

of Δp to match the observed holding time as a function of time is uniformly distributed. It then follows that

$$\text{Var}[p] = \frac{1}{3} \Delta p^2 . \quad (10)$$

The desired approximation for $\text{Var}[p]$ is obtained by substitution of (9) into (10).

The inclusion of the variances in equation (8) appears to be important. It helps ensure correct behavior of (8) for small p when $FHT = 0$. This is because it can be shown that

$$p/(\text{Var}[FHT] + \text{Var}[p]) \rightarrow \text{constant as } p \rightarrow 0.$$

The expression in (8) could clearly be used to rank different associations for the same M sensors. It is not so clear how to compare $E(SL)$ values when the sensors used for the calculations differ. An alternative approach to the calculation of consistency, albeit more complicated, would be to calculate the probability of the observations for an optimum choice of SL . For this approach the random variable

$$(FHT - p(SL)) / \sqrt{\text{Var}[FHT] + \text{Var}[p]}$$

is assumed to be normally distributed with unit variance. Then the probability of observing Y satisfying $|Y - p(SL)| \leq |FHT - p(SL)|$ is given by

$$1 - 2\phi(-|FHT - p(SL)| / \sqrt{\text{Var}[FHT] + \text{Var}[p]}) \quad (11)$$

and the probability of the observations FHT_1, \dots, FHT_M is given by

$$P(SL) = \sum_{i=1}^M (1 - 2\phi(-|FHT_i - p_i(SL)| / \sqrt{\text{Var}[FHT_i] + \text{Var}[p_i(SL)]})) \quad (12)$$

for a choice of SL leading to the normal distributions of the random variables. This choice of SL is assumed to be given by the value which maximizes $P(SL)$.

For either approach, it is suggested that SL be estimated iteratively. A good first choice would be a sensor for which the data association was most straightforward, as long as it was not held all the time. The initial choice for SL can then be obtained by solving equation (3) for SL when the observed fractional holding time is substituted for p .

The value of $E(SL)$ or $P(SL)$ thus obtained would be used in the ranking of contact data associations. The estimates of SL would of themselves be of great value since target source level of a non-cooperative target is not observable using the usual non-calibrated sensors in an incompletely characterized environment. The method provides a recursive procedure for estimating SL for all acoustic sources of all targets being tracked.

At the present time this methodology is being investigated by studying the SL estimates obtained from processing of historical data associated to operational targets with known source level.

3 USE OF PREDICTIONS FOR TARGET LOCALIZATION AND TRACKING

Another important potential use of models is to provide range estimates when cross-fixes are not available as illustrated in Figure 6. Due to uncertainties in the predictions and the expected variability in fractional holding time it appears unlikely that range estimates obtained from comparing predicted probabilities as a function of range with observed holding time would provide useful information when cross-fixes are available during the time frame T associated with the fractional holding time observation. It is natural then to consider the case when an isolated detection has occurred by a single sensor.

Suppose that a sensor first detects a target. Figure 7 summarizes the performance of the sensor. Suppose further that the target is moving toward the sensor so that it moves through regions of poorer coverage toward regions of better coverage. Then the probability of being first detected p in region K is the product of the probability of detection for region K and the probability of non-detection for the regions $1, 2, \dots, k-1$, i.e.,

$$P_k = p_k(1-p_{k-1})(1-p_{k-2}) \dots (1-p_1). \quad (13)$$

Several examples indicated that P_k tended to vary slowly with K . A fellow worker at NOSC, Stefen Hui, found the following important example:

Let

$$p_k = p_1 / (1 - (k-1)p_1) \quad (14)$$

with $p_1 \leq 1/N$ to assure that the p_k as defined satisfy $0 \leq p_k < 1$. Then $p_1 = P_1 = P_2 = \dots = P_N$.

To see that this is the case, proceed by mathematical induction. $P_1 = p_1$. Suppose $P_k = p_1$. Then,

$$\begin{aligned} P_{k+1} &= p_{k+1}(1-p_k) \dots (1-p_1) \\ &= \frac{p_{k+1}}{p_k} (1-p_k) P_k, \end{aligned}$$

and it suffices to verify that $p_{k+1}(1-p_k)/p_k = 1$.

Using (14) it follows that

$$\frac{p_{k+1}}{p_k} (1-p_k) = \frac{1-(k-1)p_1}{1-kp_1} \left(1 - \frac{p_1}{1-(k-1)p_1} \right) = 1 \quad (15)$$

by cancellation after placing the second factor under a common denominator. Furthermore, whenever (15) holds, i.e., whenever $p_{k+1} = p_k / (1-p_k)$, it follows

that $P_{k+1} = P_k$. For example, if $p_k = 1/n$, then $p_{k+1} = \frac{1}{n} \cdot \frac{n}{n-1} = \frac{1}{n-1}$.

The example is not farfetched and suggests that in practice it will be difficult to estimate range from predicted probabilities of detection for a sensor. Indeed, the example shows that for a target of known track (radial toward sensor) and known probabilities of detection for the sensor as a function of range, but unknown time of opportunity for the sensor, there need be no range information associated with an initial detection event. To try to overcome this difficulty, the past history of the target needs to be considered, i.e., the use of the model for tracking rather than localization should be considered.

The contact data association calculation suggests that SL estimates may not be necessary for the tracking application. The ocean could be partitioned into regions with some boundaries associated for the sensors holding and others defined from environmental considerations. For each region a calculation of the probability of observing the given FHT; for sensors $i = 1, 2, \dots, M$ could be made and the calculation of $P(SL)$ defined by equation (12) made as described in Section 2. The target track could be assumed to have random course/speed changes. The suggested technical approach would then attempt to apply the theory of stochastic differential equations to the problem.

Stochastic differential equations have been successfully used for modeling target motion and to represent a more general approach than Kalman filtering (reference 1). The interesting observation, I believe, is that a model using stochastic differential equations might provide a vehicle for using negative information as well as positive information. Here, using negative information simply means using the information that a sensor did not gain contact on a target.

Consider a charged particle moving through a field of charge particles of the same and of opposite charge. The particle is attracted by charges of opposite polarity and repelled by charges of like polarity. Furthermore, while moving through the field the particle experiences random external forces which tend to perturb its track.

Suppose the charged particle is the target. The like charged particles are non-detecting sensors whose repulsion forces are described by the predicted probability of non-detection as a function of the range and bearing of the target from the sensor. The oppositely charged particles are detecting sensors whose attraction force is also described by predicted probabilities of detection. The random forces are other factors leading to course and speed changes of the target. The analogy breaks down because of bearing information which requires that the target be along given bearings at given times. The problem is worth pursuing and it is our intent to study the problem in the future.

The goal of using stochastic differential equations with model inputs to allow use of negative information as well as better use of holding information is not to obtain extremely accurate localization information but to provide information useful for planning the allocation of mobile sensors or re-processing of data recorded in real time.

4 THE NATURE OF PREDICTIONS DESIRED FOR INFORMATION PROCESSING

Performance predictions to be used in information processing can always be based on measured or recently measured ambient noise and clutter.

When a detection has occurred, signal-to-noise estimates are available as a function of time during detection periods. Autocorrelation could be performed on the received signal during these periods. It might be possible to glean multi-path data from the resulting ambiguity surfaces.

It is rare that predictions for a sensor not holding contact will be required unless some other sensor is holding contact. For the case when the sensors and targets are all in a homogeneous environment, it seems reasonable to try to use what was observed by the detecting sensor to generate better predictions for the non-detecting sensor. To my knowledge, such conditional predictions have not been investigated.

It is my feeling that high operational payoff might result if modeling emphasis shifted from predictions based on historical or synoptic data to predictions based on information derivable from directional noise measurements for the sensor and related available measurements for sensors whose outputs can be spectrum analyzed or coherently processed.

The durations of holding and non-holding intervals, signal-to-noise ratios during holding, bearing behavior, all may contain useful clues concerning propagation and hence target range or the probability that detections occur or do not occur on several sensors simultaneously or near simultaneously. The prediction of observables more general than probabilities of detection should be the direction that future acoustic modeling takes if it is to be a major tool in information processing of passive acoustic sensor data.

REFERENCES

- (1) Modeling Target Motion Using Second-Order, Non-Linear, Stochastic Differential Equations, Interim Memorandums, Daniel H. Wagner, Associates, April 1980, Dr. Thomas Corwin and D. P. Kierstead.

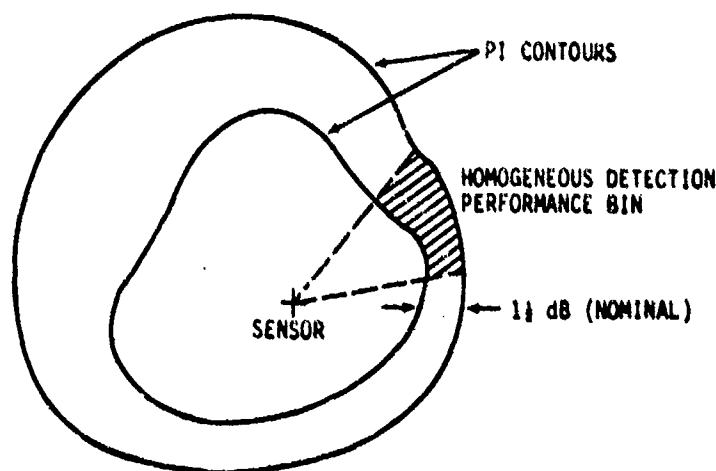


FIG. 1 TYPICAL HOMOGENEOUS DETECTION PERFORMANCE BIN

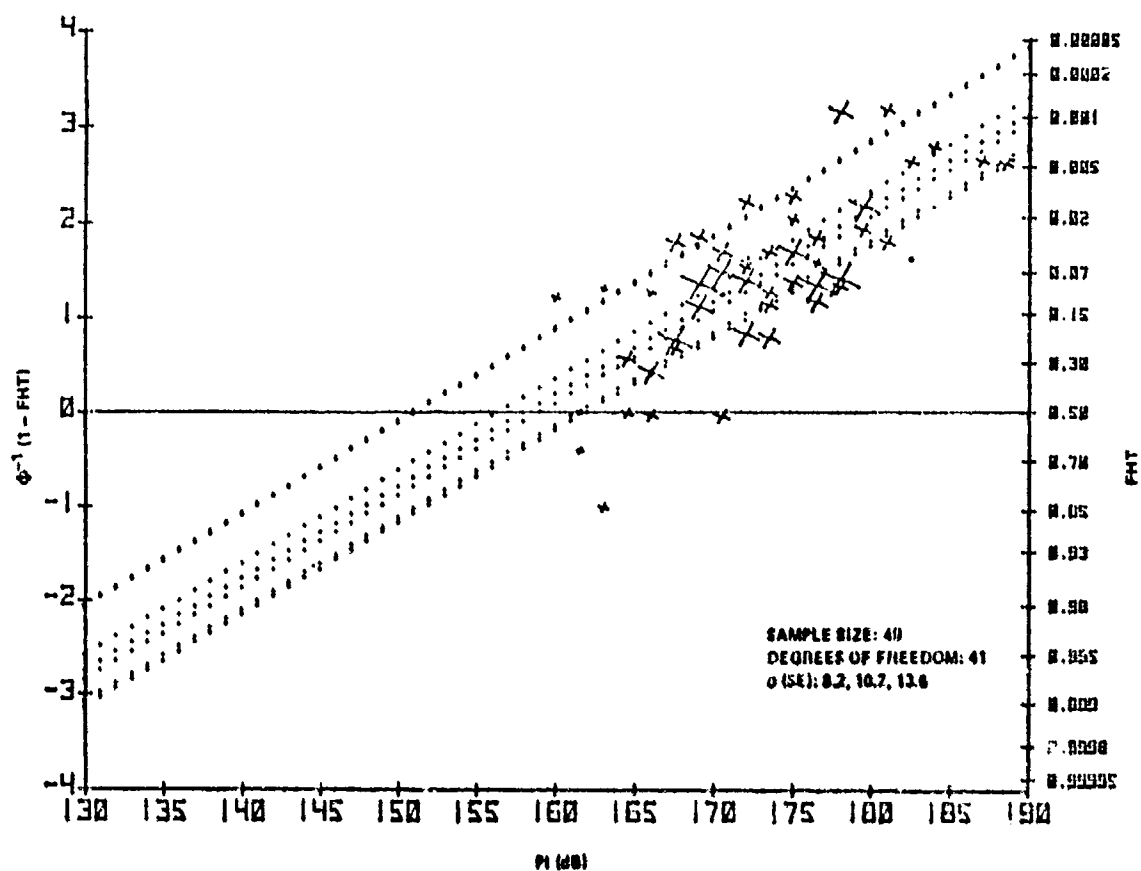


FIG. 2 POOLED TARGET REGRESSION SUMMARY PLOT DURING THE WINTER SEASON

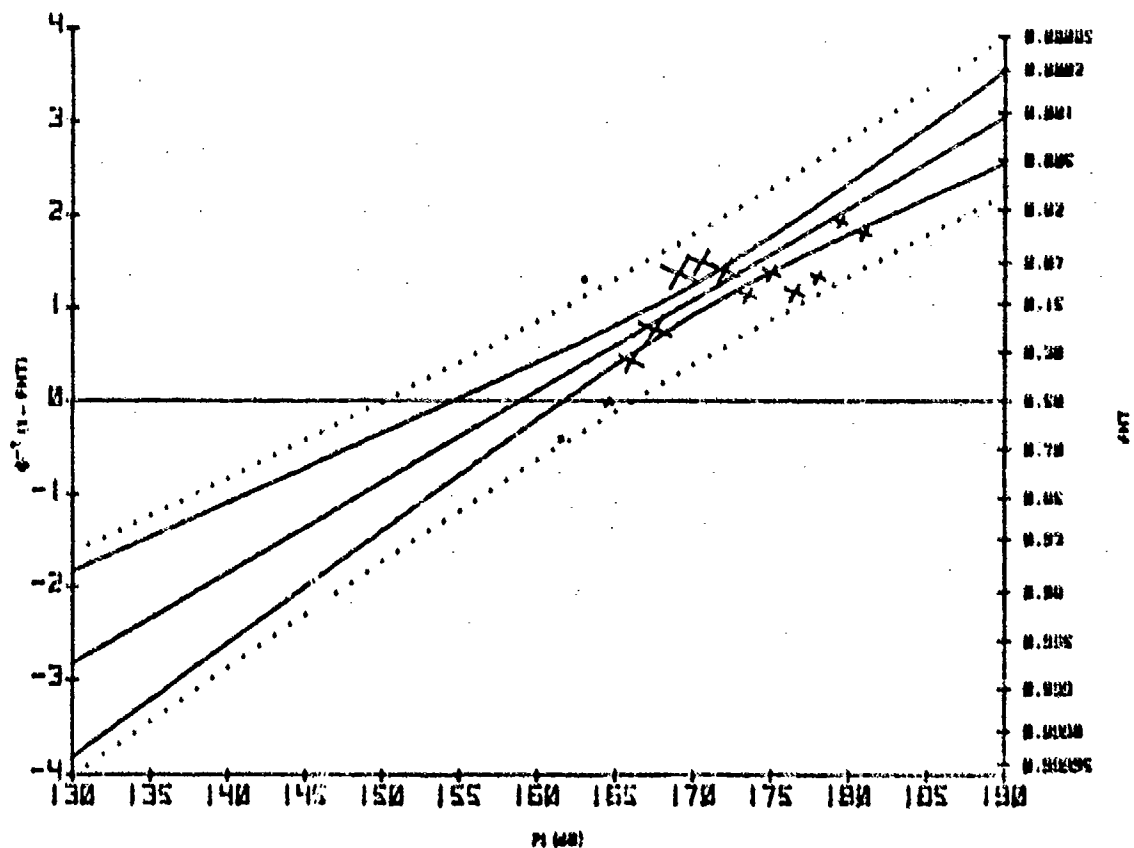


FIG. 3 POOLED REGRESSION RESULTS FOR DURING THE WINTER SEASON

OPPORTUNITY REGION
FOR TARGET CONDITIONED
ON ASSOCIATION OF
DETECTIONS DURING TIME T

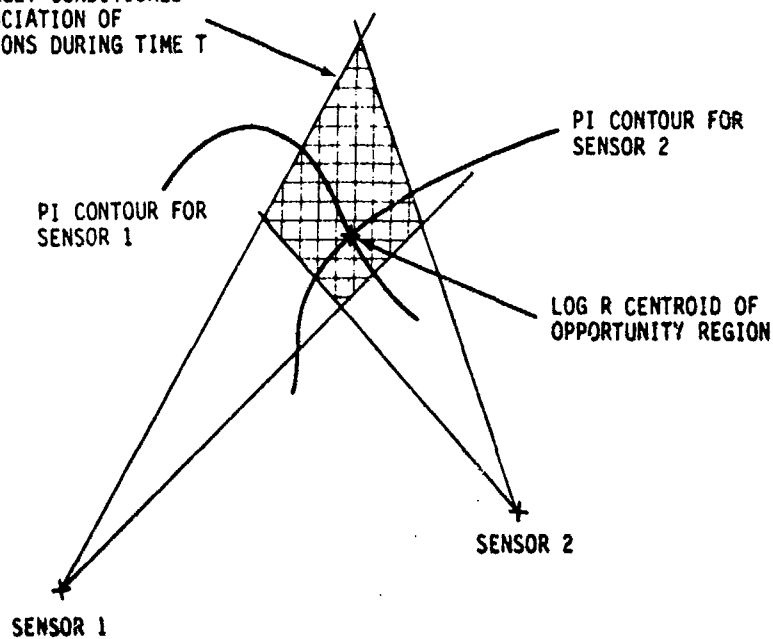


FIG. 4 OPPORTUNITY REGION FOR TWO SENSOR CONTACT DATA ASSOCIATION

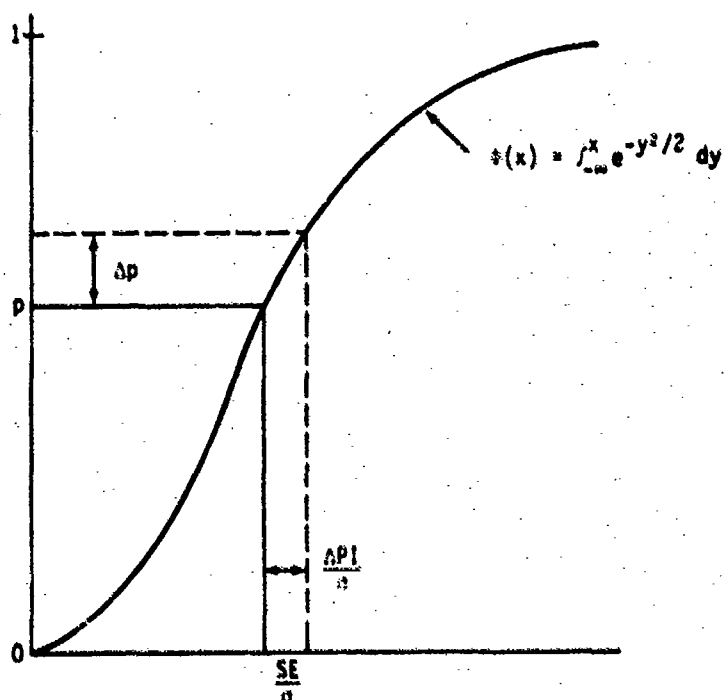


FIG. 5 ESTIMATION OF $\text{Var}[p]$

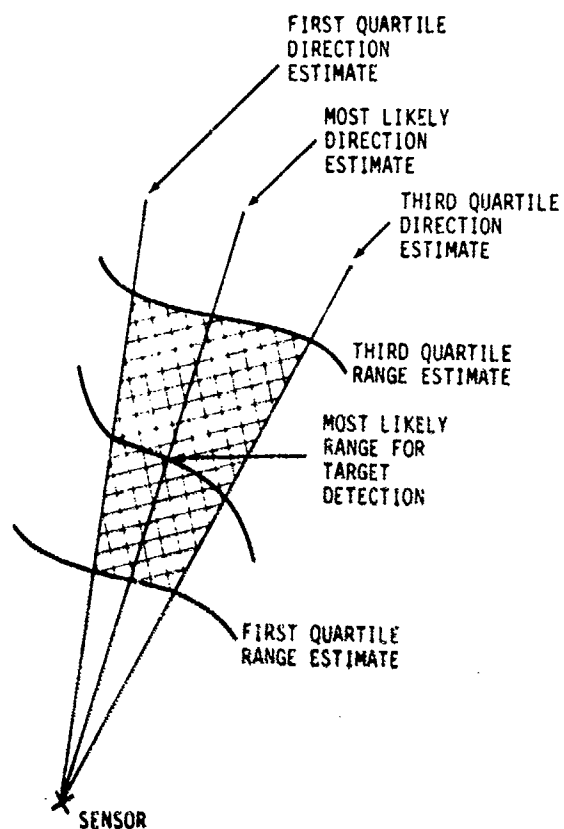


FIG. 6
SINGLE SENSOR RANGE ESTIMATION
USING PREDICTIONS

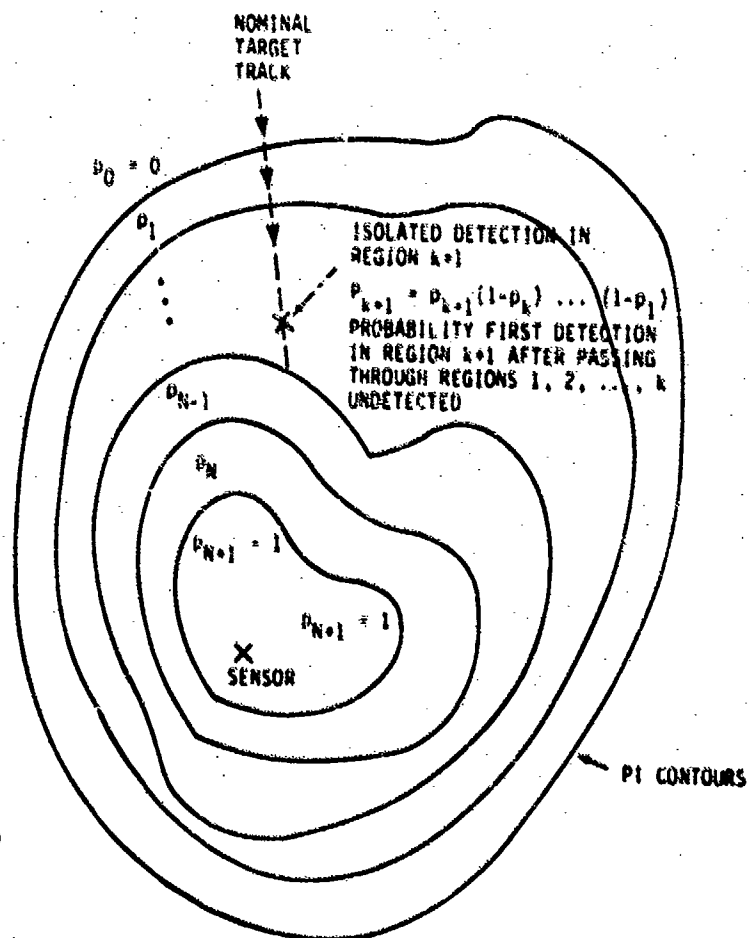


FIG. 7
INITIAL DETECTION SCENARIO

THE PREDICTION OF TEMPORAL STATISTICS OF DIRECTIONAL AMBIENT SHIPPING NOISE

by

Mattheus Groen
 SACLANT ASW Research Centre
 La Spezia, Italy

ABSTRACT

A technique for predicting the probability density function (PDF) of the ambient-noise power received by a narrow-band system in a modelled shipping and wind noise field is described. The densities of the shipping noise are obtained from a mathematical model for spectral-line components. The importance of the probability of occurrence of combinations of spectral-line components in the frequency band of interest is emphasized. It is shown that the uncertainty in receiving a particular combination of lines in the frequency band of interest leads to the definition of the unconditional PDF of the noise. Its prediction consists of the addition of numerically convolved densities in conjunction with the probability of occurrence of a line combination. The results show that the shape of the resulting PDF depends on the processing bandwidth and the statistics of the wind/background noise level. Suggestions are made to extend the technique to use it for closer shipping.

INTRODUCTION

The object of this study is the prediction of the statistics of directional ambient shipping noise with a mathematical-numerical technique. This reported work is an extension of the already existing deterministic model RANDI II <1> to which random theory is added.

The technique for predicting the statistics is based on the statistical model published by Dyer <2> and gives a simple analytical expression for the probability density function (PDF) of the shipping-noise power as a function of a combination of received spectral line components. The total short-time averaged noise power expected to be received in the frequency band of interest depends on the processing bandwidth relative to the assumed distribution of the lines in the noise spectrum. For a "narrow"-band system - narrow in the sense that the bandwidth is smaller than the average line spacing in a single-ship spectrum - the number of lines present in the band will be on the average less than the number of sources. The position of the lines in the spectrum is assumed to be random; consequently the appearance of a combination of lines in the frequency band of interest will be random. As all these combinations are mutually exclusive it can be shown that the unconditional PDF of the noise due to all possible combinations of spectral lines is a weighted sum of the conditional PDFs of the individual combinations; with their probability of occurrence as weighting factors. Results of the prediction of the

statistics of shipping (plus wind noise) from a modelled shipping noise field from RANDI II are presented and discussed. RANDI II and the prediction technique are developed to be used if the beam of a sensor is steered in the direction of a shipping noise field that is kept static during the modelled observation time. This situation may be achieved for distant shipping. Experimental results from closer shipping show a highly variable shipping-noise field due to the moving of shipping in and out of the beam. This is also observed in a simulated shipping-noise field from RANDI II. To solve this problem an extension of the technique is suggested.

Section 1 describes the modelled physical situation and gives typical results using Dyer's Statistical Model. Section 2 proposes a spectral model and describes the uncertainty about the spectral line reception, which is the major reason for defining the unconditional PDF. A block diagram shows how Dyer's Statistical Model, the spectral model, and RANDI II relate to its numerical calculation. Results are presented in Section 3 and Section 4 discusses the moving shipping problem.

1 MODELLED PHYSICAL SITUATION

The medium and system modelled by the prediction system are shown in Fig. 1. The noise due to shipping propagates through multipaths to the sensor. The shipping field in the model is assumed to be static in the sense that the ships do not move during the measurement observation time. The sensor is an array of hydrophones. The signals received in the beams are passed through a band filter. The filter output is squared, short-time-averaged and yields the beam-power output. Figure 1 also shows the most important models used in the prediction system. Dyer's statistics of distant shipping noise <2> models distant shipping noise analytically as phase-random line components arriving from a number of independent sources. The model is applicable for cases where distinct assumptions about the random propagation mechanism <3> and the processing system are satisfied. In order to allow the addition of power intensities in most spectral-line combinations, the averaging time-bandwidth product must be much larger than unity (see App. A).

Dyer's PDFs and mathematical formulas for different spectral line receptions are shown in Fig. 2, in which μ_x is the long-time average intensity of each line and L is the number of lines. The standard deviation (SDEV) of the level of one line is constant, about 5.6 dB. If more lines are combined, the PDF becomes narrower and the standard deviation lower. This is caused by the logarithmic transformation of the power intensities. The prediction technique uses an algorithm that calculates the PDF for a combination of lines with different long-time average intensities (see App. B).

2 THE SPECTRAL MODEL

In the spectral model it is assumed that the radiated noise of merchant ships consists of spectral-line components with a constant line spacing $\langle 2,4 \rangle$. We consider only those pass bandwidths that are smaller than the line spacing (line-spacing/bandwidth ratio greater than 1); no more than one line per ship is expected to be present in the band, as shown in Fig. 3. To characterize the reception of a distinct combination of spectral lines, assuming N merchant ships in the beam of the array, we need to know the probability of receiving this distinct number of lines in the band. If we assume that both the position of the lines in the spectrum and the number of lines in the band of interest are random, we define the conditional probability of ℓ spectral lines given N ships: $P\{\ell/N\}$. As the lines are received from independent sources, we can use the binomial distribution theory to calculate this probability (see App. C).

An indication for the reception of different numbers of spectral lines in the band is obtained by observing the results from SACLANTCEN's towed-array experiments $\langle 4 \rangle$. Figure 4 gives the beam-noise level output as a function of azimuth angle for three adjacent frequency bands with widths of 2.5 Hz. The mean and standard deviation of the noise from 50 data samples are plotted. The centre frequencies of the bands are 148, 151.5 and 153 Hz. Although in general the mean values from the three bands differ little within one beam, the standard deviations differ in some beams by more than 3 dB. Referring to Dyer's PDFs in Fig. 2, this difference is presumably caused by a different combination of spectral-line components in the bands of these beams. Because it is unknown which combination of lines, out of all the possible combinations, will be present in the band, we have defined the unconditional PDF of the noise. The formula is shown in Fig. 5. This PDF is the sum of all the conditional PDFs of every possible combination of lines, weighted by the probabilities of receiving a particular combination of lines in the band. Appendix D proves that the weighted summation of PDFs is allowed because the line combinations, with which the PDFs are connected, occur mutually and exclusively.

The block diagram, Fig. 6, shows the relation of the numerical calculation of the unconditional PDF by means of the different models. Three flows of information are extracted from the RANDI II model and directed to the submodels:

- a) The power intensities of the line arrivals of N ships go to Dyer's statistical model,
- b) The power intensities of the wind/background noise and the processing time-bandwidth product go to the wind statistics model,
- c) The number of ships and processing bandwidth go to the spectral model.

The values of f_{ℓ} corresponding to the PDFs of all combinations of ℓ lines, are summed and normalized. The resulting PDF, f_{ℓ} , is convolved with the PDF of the wind noise f_w ; this gives the PDF, f , which is weighted and summed over all possible numbers of lines.

3 RESULTS FROM THE PREDICTION MODEL

The prediction model has been run with shipping data acquired by maritime patrol aircraft during one of SACLANTCEN's towed-array experiments. The data set is given in Appendix D <4>. A typical result of the unconditional PDF of the noise from the shipping-noise field modelled in RANDI II with the above shipping data is shown in Fig. 7. This figure shows:

- The wind noise level and the noise levels of the 7 spectral lines from 7 ships.
- The conditional probabilities $P\{\ell/7\}$ ($\ell = 0, \dots, 7$)
- The weighted PDF curves for different combinations of lines ℓ . ($\ell = 0, \dots, 7$).
- The unconditional PDF curve.

In this example the shape of the resulting PDF is bimodal. This is because the wind noise (and if the wind is not present, the background noise) is always present in every combination of spectral lines. Every weighted PDF curve is either that of the wind/background noise alone or the result of a convolution of PDFs of wind noise and line noise. It is clear that the influence of the wind/background noise statistics on the unconditional PDF of ambient noise will be substantial, especially for higher frequencies.

Figures 8, 9, 10 and 11 show the results of predicting the unconditional PDF of noise from the modelled shipping noise field for different beam outputs and various time-bandwidth products (TBP) and line-spacing/bandwidth ratios (LBR).

The modelled beam power response level vs azimuth angle and the unconditional PDFs with probabilities of line reception are plotted for some beams. It needs to be emphasized that no conditions are made about the combination of received lines in the band of each beam. It is therefore not possible to compare these results directly with the temporal statistics of real data. The TBP of the processing system influences the statistics of the wind/background noise intensity. A high TBP gives a narrow PDF of the wind noise. For narrow bandwidths the LBR will be high. Figures 8 to 11 demonstrate that the influence of the wind-noise level relative to the total shipping noise level is substantial, especially in beams with few ships. In most of the beams the shape of the PDFs is bimodal. The range of standard deviation is large.

We can draw the following general conclusions from the above results:

- 1) The unconditional PDF of the noise level is non-gaussian for most of the beams.
- 2) In the case of narrow bands the influence of the wind-background noise will be substantial in beams with few ships, because of the high probabilities of receiving no lines in the band.
- 3) Low-level wind-background noise leads to higher standard deviations than high-level wind-background noise.

- 4) Variation of the bandwidth influences the amplitude of the resulting PDF more than its standard deviation.
- 5) Wind-background noise with a narrow PDF dominates the unconditional PDF, particularly for narrow bandwidths.

4 THE MOVING SHIPPING PROBLEM

The above proposed technique is developed to predict the statistics of ambient shipping noise from distant shipping. If the shipping is closer, the influence of moving shipping will have substantial effect on the statistics of the ambient shipping noise. The varying shipping noise field can be observed in the experimental data and can be modelled with RANDI II. Figures 12a and b plot the beam noise level outputs for three series of successive and overlapping noise samples from towed-array measurements. Three values of mean and standard deviations of the noise are plotted against azimuth angle for 150 and 502 Hz. Beam outputs with large variation in the three mean values have, in general, high standard deviations, which might be explained by ships moving in and out of these beams during the measurement period. Another indication for moving shipping is simulated with RANDI II. Figure 13a shows the shipping noise field calculated from the shipping surveillance data (see App. D <4>) collected by maritime patrol aircraft during the measurements shown in Fig. 12. The spikes are shipping-noise levels in one-degree sectors. The curve is the noise field convolved with an unambiguous beam of 5°. Figure 13a shows the field at the start of an observation time period and Fig. 13b shows the field at the end of the period. A highly variable noise field is observed due to moving shipping. The impact on the corresponding modelled beam noise responses is shown in Figs. 14a and b.

In order to handle moving shipping with a prediction technique a dynamic shipping-noise field should be used. The statistics of the noise could be calculated out of noise samples from a varying shipping-noise field. This solution would be beyond the scope of this study, in which an analytical calculation is required. An extension of the prediction technique is suggested with the use of unconditional statistics (Fig. 15). We propose the unconditional PDF of the noise due to all possible combinations of M ships in the beam during the observation time period. This PDF is the weighted sum of the unconditional PDFs due to all possible combinations of spectral lines in the band, given a particular combination of N ships in the beam of the sensor. The weighting factors are the probabilities of occurrence of a particular combination of ships in the beam. With this extension, which is under development, the predicted PDFs are expected to be much wider, with much higher standard deviations. This will be caused by the extra uncertainty about the shipping covered by the beam.

APPENDIX A

JUSTIFICATION OF THE USE OF POWER ADDITION IN
THE PROPOSED PREDICTION TECHNIQUE

If the output of the band-pass filter in Fig. 16 is represented by the signal

$$V(t) = \sum_{k=1}^{\ell} A_k \cos(\omega_k t + \theta_k)$$

as a sum of line signals with amplitude A_k , frequency $f_k = \omega_k/2\pi$, and phase θ_k , it can be shown that the squared and short-time averaged (interval I seconds) signal $v(t)$ becomes:

$$\begin{aligned} P(t) &= \frac{1}{2} \sum_{k=1}^{\ell} \sum_{m=1}^{\ell} \frac{A_k A_m}{I} \int_{t-I/2}^{t+I/2} du \cos[(\omega_k - \omega_m)u + \theta_k - \theta_m] \\ &= \frac{1}{2} \sum_{k=1}^{\ell} A_k^2 + \text{off-diagonal terms} \end{aligned}$$

These off-diagonal terms are ≈ 0 if

$$\min_{k \neq m} |\omega_k - \omega_m| > \frac{2\pi}{I}$$

and $P(t)$ is a sum of line-power intensities.

If we define the minimum relative line spacing Δ as

$$\Delta = \min_{k \neq m} |f_k - f_m| \quad \text{we get the condition } I > 1/\Delta$$

If we use a time-bandwidth product much larger than 1, then

$$IW \gg 1$$

(Eq. A.1)

For a bandwidth that is not too small and a few spectral lines received in the band, it is allowable to use the addition of spectral line power levels if the condition A.1 is fulfilled. If we use a line-spacing/bandwidth ratio of 5 and a maximum possible reception of 7 spectral lines in the pass band, a relative line spacing less than the minimum Δ will have a probability of occurrence of less than 10%.

APPENDIX B

The derivation of the PDF for unequal long-time average intensities is shown in <2>. An analysis of the characteristic functions of PDFs is used. An evaluation by the calculus of residues and transformation to the logarithmic domain yields

$$f(x) = \sum_{m=1}^{\ell} \mu_m^{-1} P_m^{-1} \exp[x - \exp(x/\mu_m)] ,$$

where

$$P_m = \prod_{j \neq m}^{\ell} (1 - \mu_j/\mu_m) ,$$

with μ_m the long-time average intensity of the m^{th} line and ℓ the number

of lines that are combined. The property $\sum_{m=1}^{\ell} P_m^{-1} = 1$ is used in the prediction technique as a quality measure for the numerical calculation.

APPENDIX C

We assume N lines in a spectral line space divided into m bands, where m is the line-spacing/bandwidth ratio. If one line is randomly present in the space, the probability that this line is present in a marked band is $1/m$ and the probability that it is not present in this band is $(m-1)/m$.

Since all the N lines are independent and not labelled, we use the binomial distribution to calculate the probability that ℓ lines out of N are present in the band of interest:

$$P\{\ell/N\} = \binom{N}{\ell} \left(\frac{m-1}{m}\right)^{N-\ell} \left(\frac{1}{m}\right)^{\ell}$$

APPENDIX D

PROOF WEIGHTED SUMMATION OF DENSITIES

Suppose v_i is the event that the value of the random variable (r.v) X is greater than or equal to x_i ; and less than or equal to x_{i+1} , the probability of event v_i is:

$$P\{v_i\} = P\{x_i \leq X \leq x_{i+1}\} = \int_{x_i}^{x_{i+1}} f(x) dx, \quad ,$$

with $f(x)$ being the PDF of r.v. X .

Further, suppose that c_j is the event that the j^{th} combination of spectral lines is received in the band of interest, with probability $P\{c_j\}$.

If v_i is the consequence of c_j , then the probability of event $v_i c_j$ is

$$P\{v_i c_j\} = P\{v_i / c_j\} P\{c_j\} \quad (\text{Eq. D.1})$$

The events in the set $v_i c_1, v_i c_2, \dots, v_i c_{k_T}$ are mutually exclusive because c_1, c_2, \dots, c_{k_T} are mutually exclusive. The subscript k_T is defined as the total number of combinations of lines.

From above and Eq. D.1 we obtain

$$P\{v_i c_1 + v_i c_2 + \dots + v_i c_{k_T}\} = \sum_{j=1}^{k_T} P\{v_i / c_j\} P\{c_j\}$$

or

$$P\{v_i (c_1 + c_2 + \dots + c_{k_T})\} = \sum_{j=1}^{k_T} \int_{x_i}^{x_{i+1}} f_{c_j}(x) dx P\{c_j\}$$

or

$$\int_{x_i}^{x_{i+1}} f_{c_1 + c_2 + \dots + c_{k_T}}(x) dx = \sum_{j=1}^{k_T} \int_{x_i}^{x_{i+1}} f_{c_j}(x) dx P\{c_j\} \quad (\text{Eq. D.2})$$

with $f_{c_j}(x)$ being the probability density of X due to the j^{th} combination

of lines, and $f_{c_1 + c_2 + \dots + c_{k_T}}(x)$ being the probability density of X due to "sum" of all the possible combinations of lines.

In numerical calculations for Δx sufficiently small, we obtain

$$P\{v_i\} = P\{x_i \leq X \leq x_i + \Delta x\} \cong f(x_i) \Delta x$$

From the above and Eq. D.2 we conclude that

$$f_{c_1 + c_2 + \dots + c_{k_T}}(x_i) \Delta x = \sum_{j=1}^{k_T} f_{c_j}(x_i) \Delta x P\{c_j\}$$

or

$$f_{c_1 + c_2 + \dots + c_{k_T}}(x_i) = \sum_{j=1}^{k_T} f_{c_j}(x_i) P\{c_j\} \quad (\text{Eq. D.3})$$

Hence a sample of the total PDF of the noise-power level X is the weighted sum of the PDFs due to all possible combinations of spectral lines with the probability of occurrence of the different combinations of lines as weighting factors.

REFERENCES

1. HAMSON, R.M. and WAGSTAFF, R.A. RANDI II - An undersea ambient noise model that includes coherent hydrophone summation for sonar systems in shallow, intermediate, and deep water. In WAGSTAFF, R.A. and BLUY, O.Z. eds. Undersea Ambient Noise, Proceedings of a Conference held at SACLANTCEN, 11-14 May 1982, SACLANTCEN CP-31, NATO CONFIDENTIAL. La Spezia, Italy, SACLANT ASW Research Centre, 1982.
2. DYER, I. Statistics of distant shipping noise. Journal of the Acoustical Society of America, 53, 1973: 564-570.
3. DYER, I. Statistics of sound propagation in the ocean. Journal of the Acoustical Society of America, 53, 1970: 337-345.
4. URICK, R.J. Principles of Underwater Sound for Engineers. New York, N.Y., McGraw-Hill, 1967.
5. BLUY, O.Z. Underwater ambient noise: Directionality and other statistics. Vol. II: Measurements near Gibraltar, September 1980. SACLANTCEN SR-58, NATO CONFIDENTIAL. La Spezia, Italy, SACLANT ASW Research Centre, 1982.

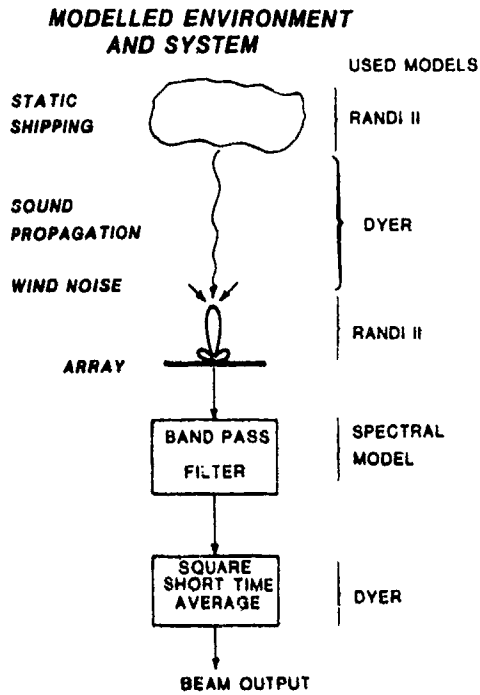


FIG. 1

PDFS FROM DYER MODEL

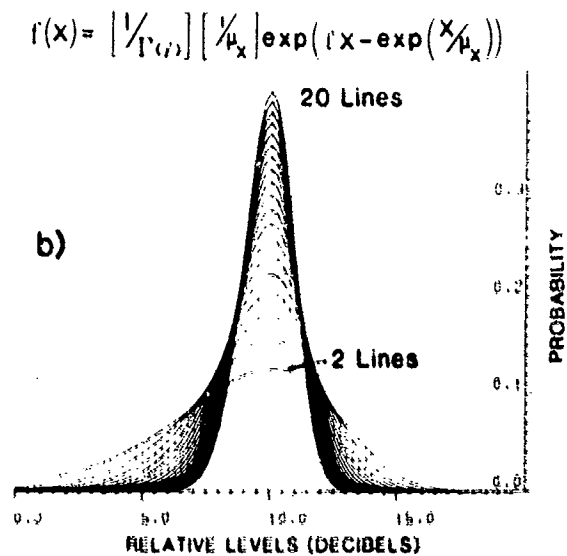
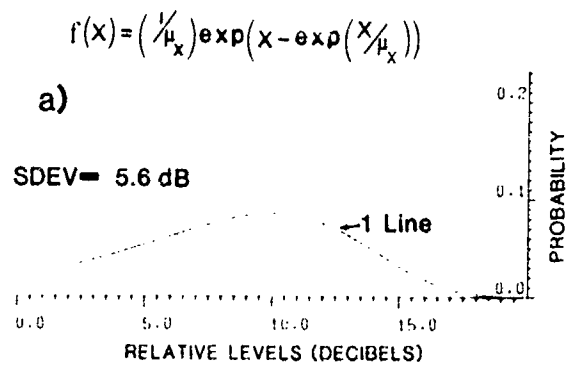


FIG. 2

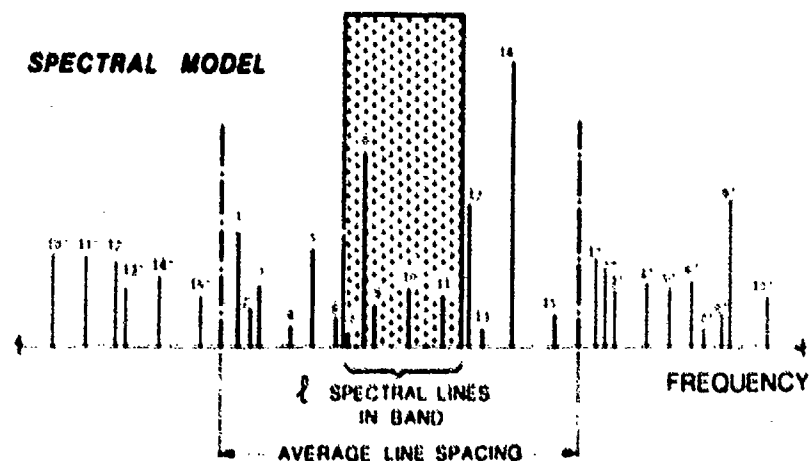


FIG. 3

**BEAM NOISE OUTPUT
FOR THREE FREQUENCY BANDS**

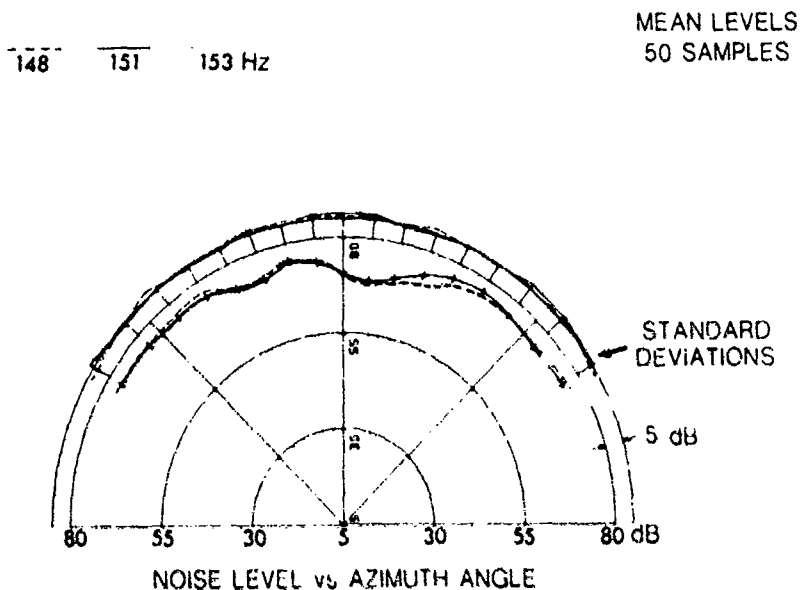


FIG. 4

$P_{1/N}$: PROBABILITY OF l SPECTRAL LINES GIVEN N SOURCES

$K = \binom{N}{l}$: POSSIBLE COMBINATION OF l LINES OUT OF N

$K_T = \sum_{l=0}^N \binom{N}{l}$: ALL POSSIBLE COMBINATIONS OF LINES OUT OF N

$f_T(x)$: PROBABILITY DENSITY DUE TO ALL POSSIBLE COMBINATIONS OF LINES + WIND/BACKGROUND NOISE

$$f_T(x) = \sum_{l=0}^N \frac{P_{1/N}}{K_T} \sum_{i=1}^K f_{l_i}(x)$$

PROBABILITY DENSITY
1st COMBINATION OF l LINES

FIG. 5

CALCULATION OF UNCONDITIONAL PROBABILITY DENSITY FUNCTION

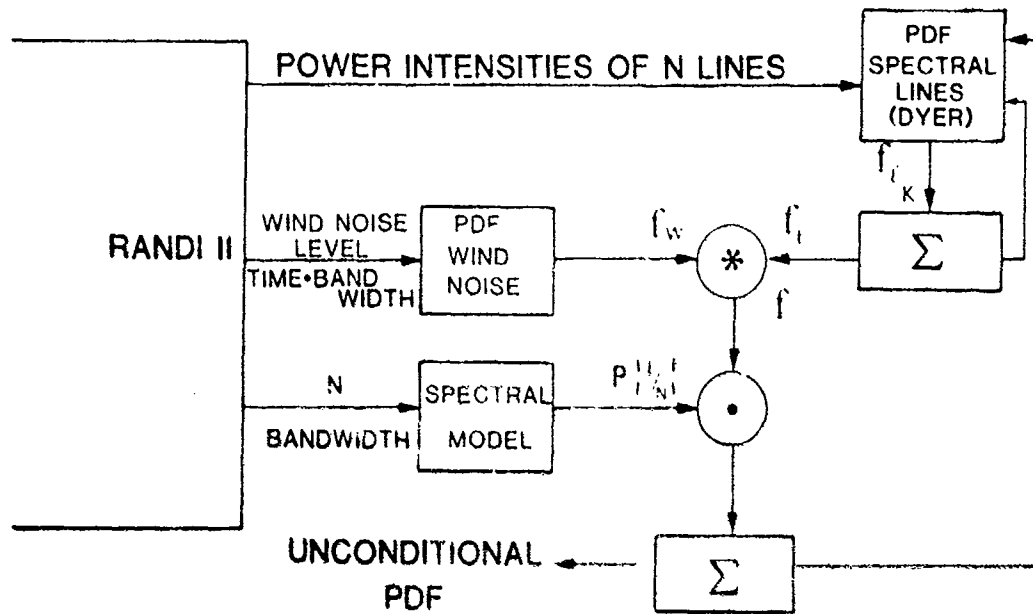


FIG. 6

UNCONDITIONAL PROBABILITY DENSITY FUNCTION OF NOISE POWER OF 7 SHIPS + WIND

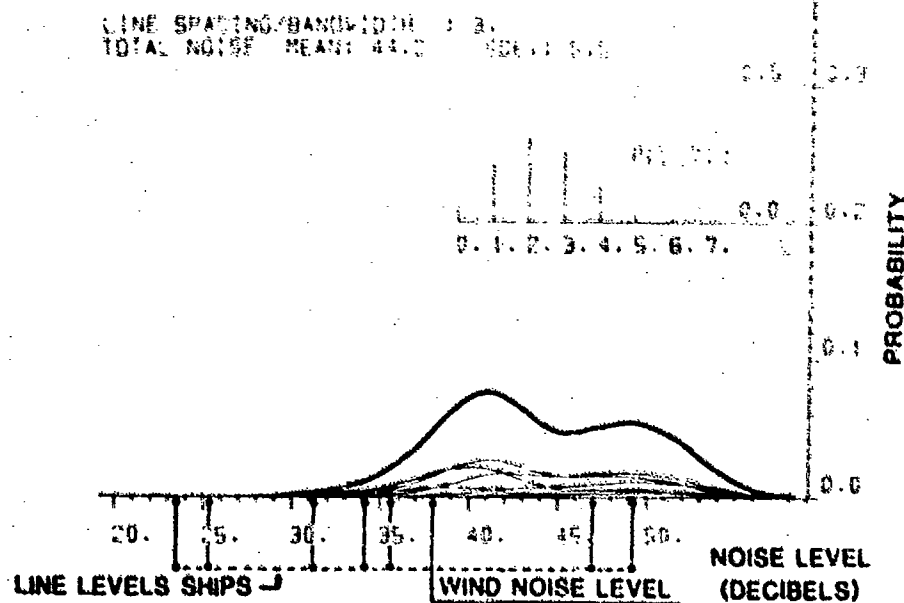


FIG. 7

UNCONDITIONAL PDF's and STATISTICS (dB)

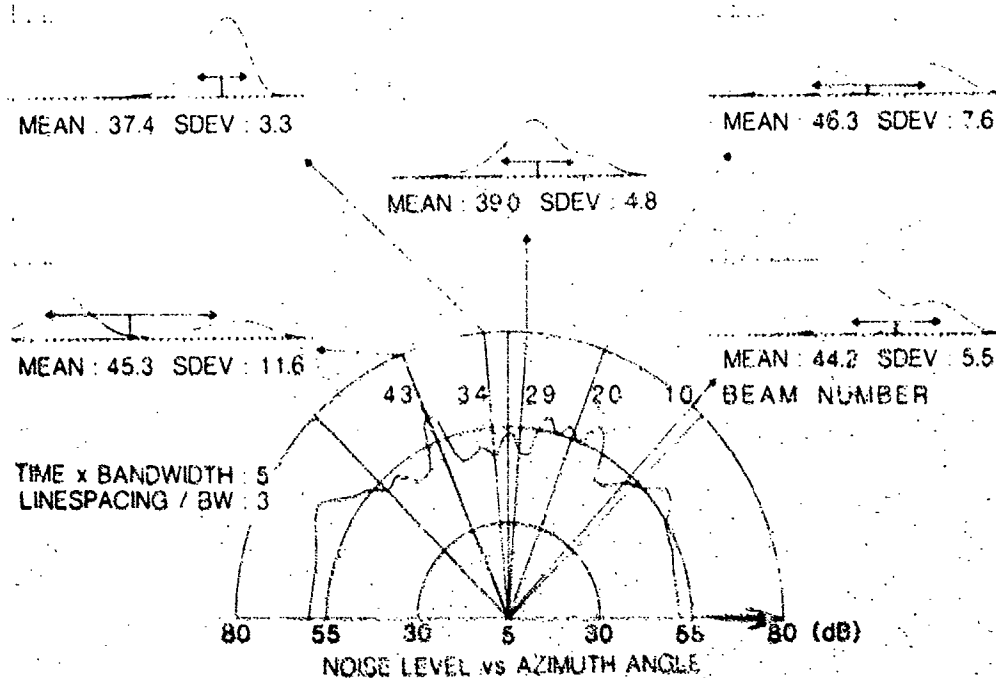


FIG. 8

UNCONDITIONAL PDF's and STATISTICS (dB)

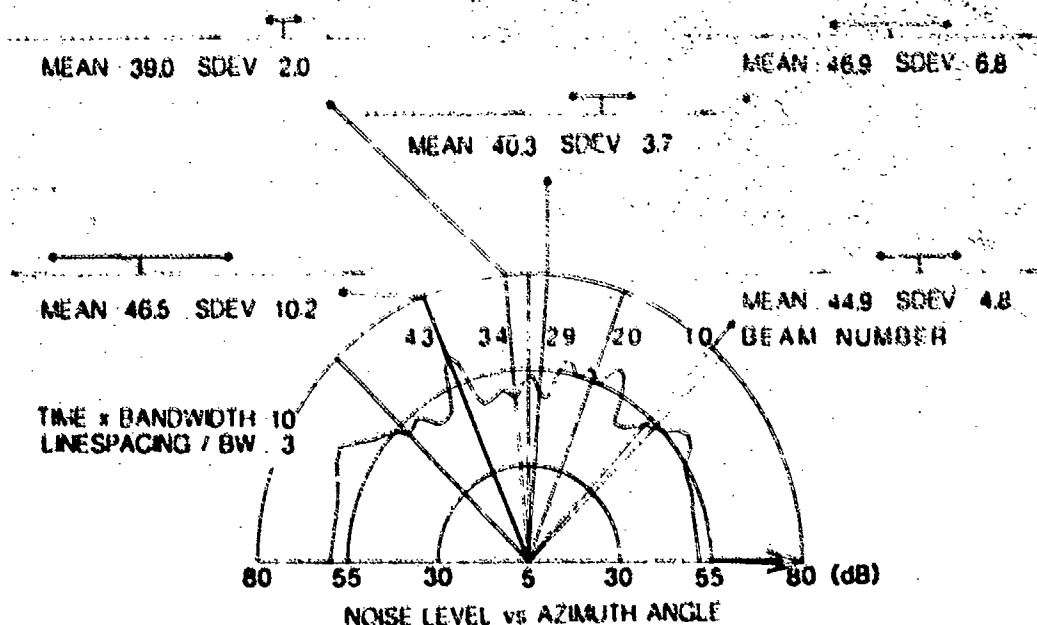


FIG. 9

UNCONDITIONAL PDF's and STATISTICS (dB)

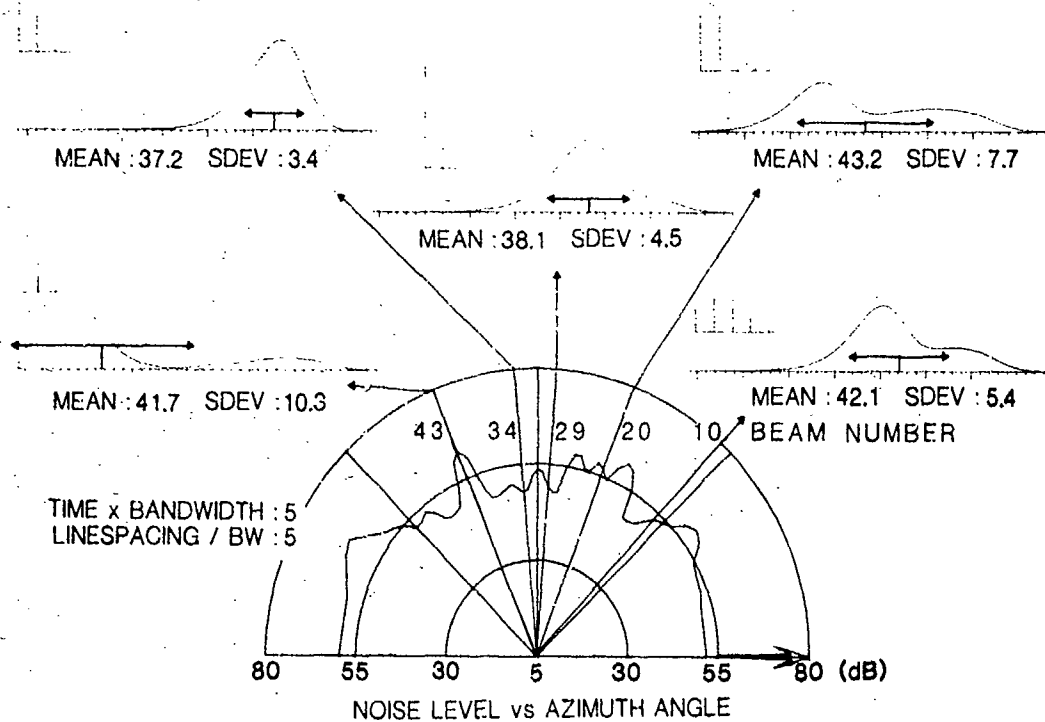


FIG. 10

UNCONDITIONAL PDF's and STATISTICS (dB)

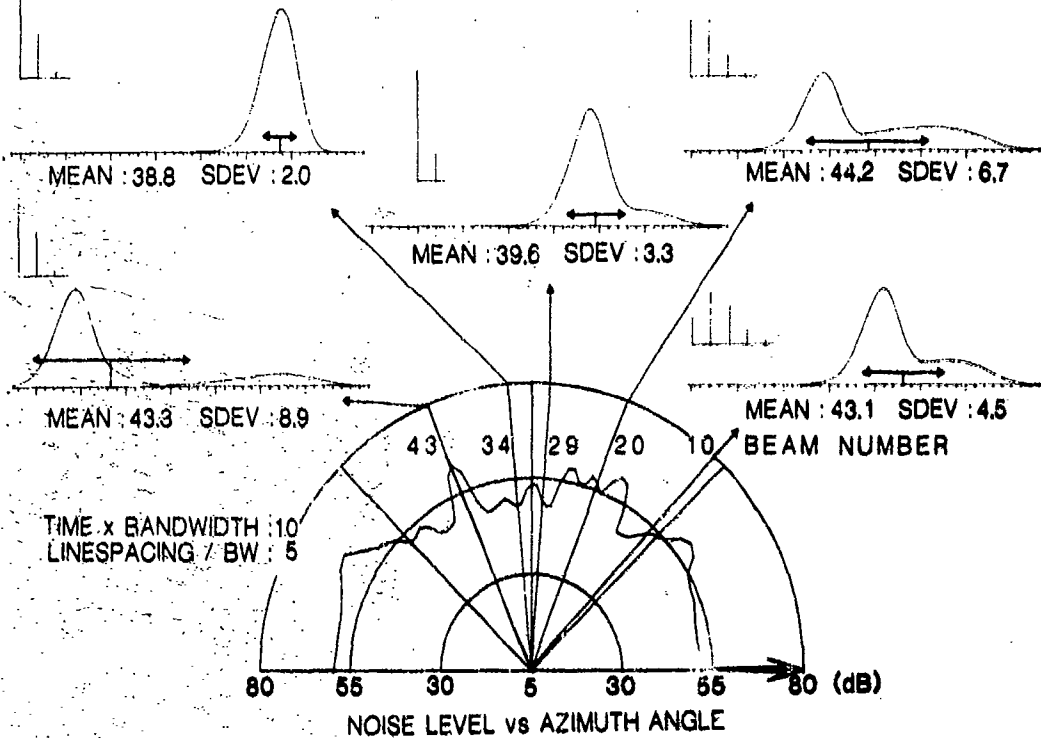


FIG. 11

BEAM NOISE OUTPUT
FOR THREE OVERLAPPING 50 SAMPLE PERIODS

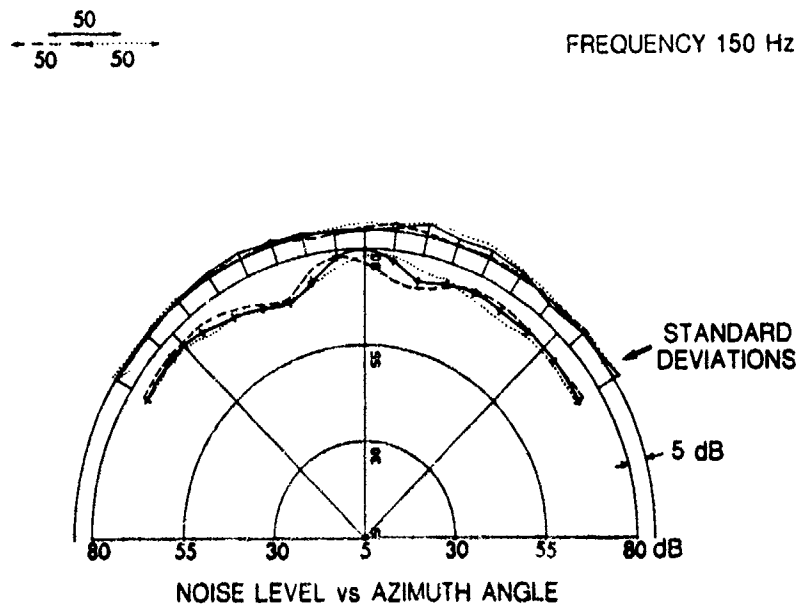


FIG. 12a

BEAM NOISE OUTPUT
FOR THREE OVERLAPPING 50 SAMPLE PERIODS

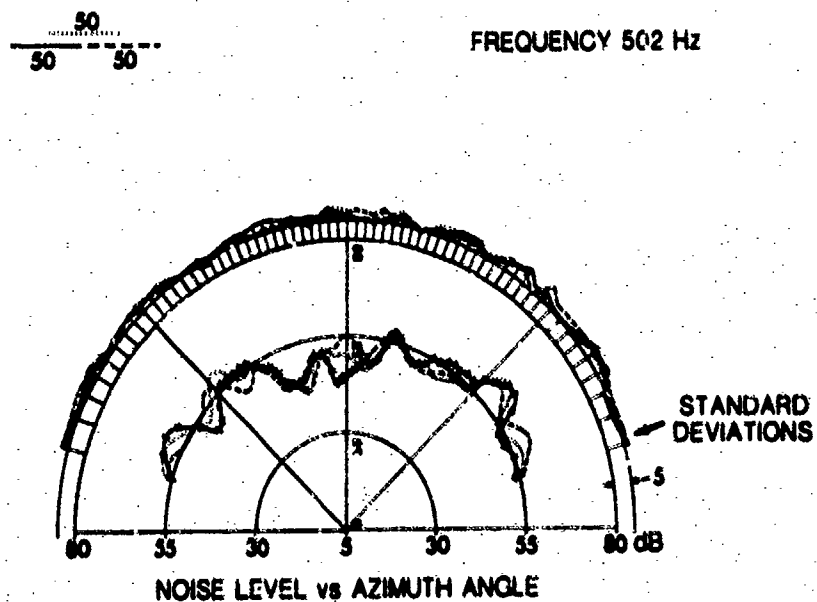


FIG. 12b

MODELLED SHIPPING NOISE FIELD

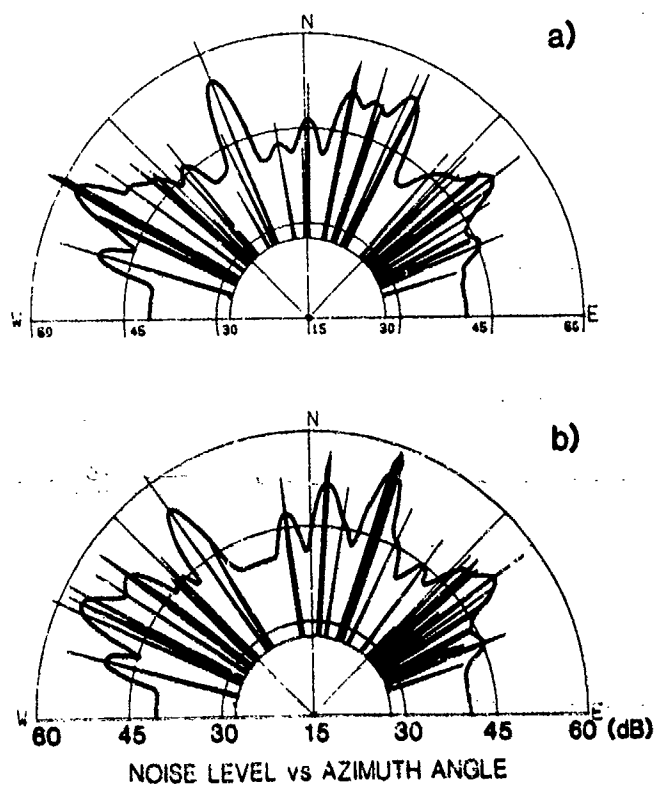


FIG. 13

MODELLED BEAM RESPONSE

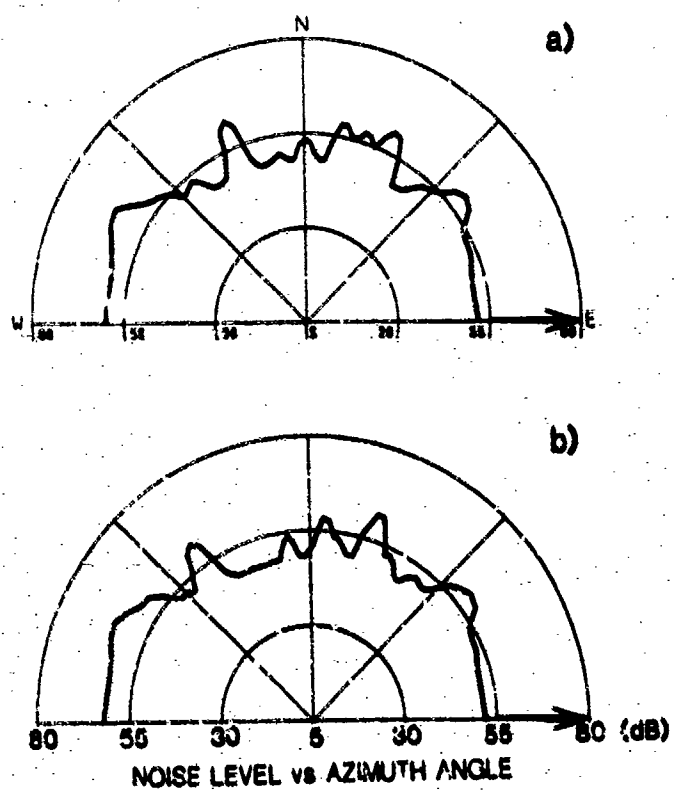


FIG. 14

$P \left\{ \frac{N}{M} \right\}$: PROBABILITY OF N SHIPS GIVEN M POSSIBLE SHIPS
IN BEAM PER OBSERVATION TIME PERIOD

$I = \binom{M}{N}$: POSSIBLE COMBINATION OF N SHIPS OUT OF M

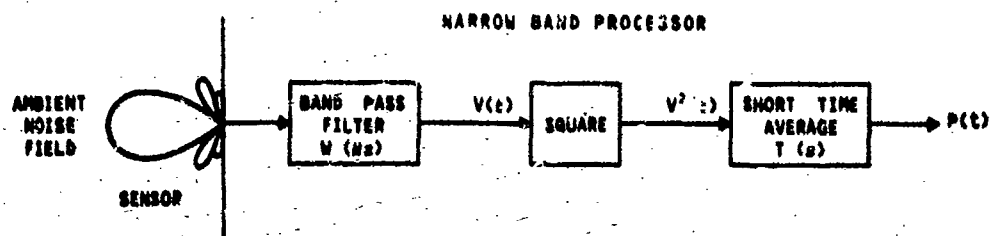
$I_T = \sum_{N=0}^M \binom{M}{N}$: ALL POSSIBLE COMBINATIONS OF SHIPS OUT OF M

$f(x)$: UNCONDITIONAL DENSITY DUE TO ALL POSSIBLE
COMBINATIONS OF SHIPS IN BEAM

$$f(x) = \sum_{N=0}^M \frac{P \left\{ \frac{N}{M} \right\}}{I_T} \sum_{i=1}^I f_{N_i}(x)$$

PROBABILITY DENSITY
ith COMBINATION OF l LINES

FIG. 15



$V(t)$ = BAND PASS FILTER OUTPUT VOLTAGE,
 $P(t)$ = NOISE POWER OUTPUT PROCESSOR.

FIG. 16

SITE AND FREQUENCY DEPENDENCE OF
AMBIENT NOISE IN THE NORTHEASTERN PACIFIC OCEAN

by

Dr. James H. Wilson
Science Applications, Inc.
Canoga Park, Ca., USA

ABSTRACT

One-hour averages of omnidirectional ambient noise measurements at 60 Hz and 165 Hz are analyzed for two nearby, deep ocean sites in the Northeastern Pacific during February and March 1981. Site A is a high noise site and is located near major east-west shipping lanes and near major Pacific storm paths. Site B is a lower noise site and is located approximately 450 n.m. from Site A away from major shipping lanes and Pacific storm paths. The site and frequency dependence of ambient noise is found to be highly variable with shipping noise being totally dominant at 60 Hz at Site A and storm noise being totally dominant at 165 Hz at Site B. Both shipping and storm noise can dominate the 165 Hz Site A or 60 Hz Site B noise levels depending on weather conditions.

Storm noise has a possible indirect effect on shipping noise, since very low noise periods occur in between storms, especially when the storm passes nearby the site. A limited number of WMO ships sampled indicate that ships slow down or stay in port during storms. Average omnidirectional noise levels at 60 Hz at both sites and at 165 Hz at Site A were 3 to 4 dB lower during a stormy week than they were during a relatively calm week.

Array noise gain measurements at Site B indicate that the coherence of noise during stormy periods is much less than it is during calm periods. Generally, this implies that the increase in beam level at 165 Hz, caused by storm noise, will be significantly less than corresponding increase in omnidirectional noise levels. At 60 Hz at Site B, this implies that beam levels will decrease, in general, during storms, especially if the storm system is nearby.

1.0 INTRODUCTION

There are many sources of ambient noise¹ in the ocean and it is shown in this paper that different noise sources (shipping and storms in this case) can dominate the noise characteristics of two nearby sites. For the analysis presented here- it is important to differentiate between short term

(minutes) noise fluctuations and changes in the long term (hours) noise intensity level. The two major factors affecting long term noise intensity levels are the distribution of noise sources relative to the measurement site and transmission loss from each noise source to the measurement site. The data analyzed in this paper illustrate the measurement site dependence and frequency dependence of long term averaged ambient noise. Bottom mounted hydrophone data were collected from two sites and two frequencies in deep water in the Northeastern Pacific Ocean during February and March 1981. The data used in this analysis are averaged over 1 hour at 60 Hz and 165 Hz. Short term noise fluctuations will not be addressed in this paper.

Two dominant sources of noise in the Northeastern Pacific Ocean during the winter are shipping and storms. Site A is located near major Pacific shipping lanes and is in the path of many large Pacific storms. Site B is located approximately 450 miles from Site A and is located well south of major shipping lanes and Pacific storms. Consequently, Site A is much noisier than Site B and the 60 Hz noise levels at Site A were totally dominated by shipping noise. On the other extreme, the 165 Hz levels at Site B were totally dominated by storm noise. The objective of this paper is to show that low frequency ambient noise can be extremely site and frequency dependent and to show the large changes in array noise gain that can occur in a period of 1 day.

To differentiate between storm and nearby shipping events in the ambient noise time series, the following criteria were used: Storm events were defined as increases in noise level lasting from 2 to 7 days at 10 Hz and 165 Hz with little or no change in noise level at 60 Hz. Nearby shipping events, on the other hand, are defined as increases in ambient noise level at all frequencies from 10 Hz to 165 Hz lasting 1 or 2 hours. Distant shipping noise background has a maximum near 60 Hz, and since the shipping spectra is relatively flat, storm events have a greater effect on 10 Hz and 165 Hz noise levels than on 60 Hz levels. The 10 Hz noise levels were used only to define storm events and no analyses of these data are presented in this paper. Every storm event defined in the manner described above was accompanied by a major Pacific storm and it is unlikely, in the author's opinion, that shipping can produce the storm noise characteristics defined above (and vice versa).

A subsequent paper will cover the subjects of distant versus local storm noise and modeling ambient noise based on Wilson's wind source level curves²⁻⁴ and historical shipping densities. This paper covers ambient noise characteristics of Sites A and B, emphasizing the frequency and site dependence of ambient noise.

2.0 AMBIENT NOISE CHARACTERISTICS

The data base for this analysis is 60 Hz and 165 Hz omnidirectional data from two deep water, Northeastern Pacific, bottom mounted hydrophones. A 1-hour (dB) averaging time was used in order to analyze long term changes in ambient noise time series at each site. Wind speed information was taken from the Fleet Numerical Oceanographic Center (FNOC) surface wind analyses

performed every 6 hours (Zulu time). The accuracy of the FNOC surface wind analyses for the mid-latitudes was evaluated in the NORPAC Pole Experiment⁵.

2.1 Site A - The High Noise Site

Figures 1 and 2 show the 60 Hz and 165 Hz omnidirectional ambient noise data at Site A for the month of February 1981. Data points were plotted every 12 hours (Zulu time) except on 12/13 February 1981, when no data were available. Four major Pacific storms passed to the north of Site A during 6 to 8 February, 16 February, 18 to 20 February and 21 to 27 February 1981, while a small local squall passed overhead Site A on 10 February 1981.

Except for the high levels on 10, 18-19 and 24 February 1981, Figure 1 shows little effect of the passage of the Pacific storms at 60 Hz. It can be concluded that the ambient noise at Site A is dominated by shipping the vast majority of the time. The 60 Hz levels of 85 dB/ μ Pa/Hz^{1/2}, shown in Figure 1, are high enough (relative to the 165 Hz levels at Sites A and B) to limit storm effects to 2 to 4 dB increases lasting periods of 1 day or less.

The 5 to 7 dB level increases at 165 Hz shown in Figure 2 during storm periods are much more pronounced with the high levels lasting up to 5 days in duration. The fact that these high levels correlate very well with the presence of large Pacific storms is a direct result of noise produced by storms. The indirect effect of storms is also potentially significant. Figure 2 suggests that very low levels (e.g., 9, 11-12 and 21-22 February 1981) can occur at 165 Hz between storms. Figure 1 shows the same effect at 60 Hz, but to a much lesser extent. The question that arises is "Does the presence of storms reduce shipping noise by causing ships to slow down or change course?"

The author has not done an extensive study of ship course or speed changes during storm periods, but several WMO ships were tracked that were in the Northeastern Pacific during storm periods on 6 to 8 and 10 February 1981. The source of WMO ship position, course and speed data are the WMO ship reports received by FNOC, Monterey. Figure 3 shows the tracks of five WMO ships (with reported speed time series shown in the insert) from 5 to 11 February 1981. These ships were selected because they reported frequently and were located in the east-west shipping lane that crossed the storm center. Although the WMO ship list does not include all ships at sea, several characteristics of WMO ship operations observed during or after storms may be typical of most ships. In examining the WMO ship locations, courses and speeds, the following observations are made:

- o All WMO ships during this time period slowed down within (e.g., JBSP) or near (e.g. H8DE) the major storm system.
- o Not all WMO ships slowed down at the same time, since location relative to storm systems was the major factor in speed changes.
- o WMO ships that did not cross the storm system (e.g., D5HD) tended to maintain constant course and speed.

- o Significant long term changes in WMO ship course were not observed. The preferred method of getting around a storm seems to be slowing down and "waiting" for calm weather.
- o The vast majority of WMO ships during this time period were on easterly courses with very few WMO ships leaving west coast ports on westerly trans-Pacific routes.

The above observations were made on a very limited time period for WMO ships only and, therefore, a much more extensive analysis is needed to say these are typical of ship course and speed changes. However, all the observations imply less ship noise during and between storms. This could be a possible explanation for the low noise levels observed in Figure 2. After a storm has passed, it could take approximately a day for shipping densities and speeds to increase to normal levels.

The week from 5 to 11 February 1981 was a typical storm period for the Northeastern Pacific, with one normal and one small storm during the week. The period from 20 to 27 March 1981 was an extended, unusually calm weather period for the Northeastern Pacific during winter, with one storm beginning on the last day of the week. The period from 20 to 26 March 1981 was shipping-dominated and a comparison of the 1-hour averaged noise statistics between the 2 weeks (5 to 11 February 1981/20 to 27 March 1981) is shown in Figure 4. On the average, noise levels during the calm March week are 3 dB and 4 dB higher at 65 Hz and 165 Hz, respectively, than corresponding noise levels during the stormy February week. Again, the possibility of storms lowering the average noise level between 60 Hz and 165 Hz is suggested for high noise sites like Site A. Certainly, Figure 4 shows there are many more very low noise periods during the stormy week. It is interesting to note the bimodal distribution of noise levels at 165 Hz during the stormy week shown in Figure 4. Physically, this occurs because the noise levels during stormy and calm periods are typically 6 dB apart and there is relatively little time in transition between calm and stormy periods.

Although more intensive analysis of the effect of storms on shipping noise is needed, the data presented here suggests the possibility that, for high noise areas like Site A, storms may produce lower overall noise levels between 60 Hz and 165 Hz by reducing ship noise.

2.2 Site B - The Low Noise Site

As discussed previously, Site B is located approximately 450 n.m. from Site A and is well south of the major east-west shipping lanes and major Pacific storms. Consequently, noise levels at 60 Hz and 165 Hz at Site B are, on the average, approximately 11 dB and 14 dB quieter during calm weather periods than corresponding levels at Site A. Figures 5 and 6 show the omnidirectional levels for Site B during February 1981 at 60 Hz and 165 Hz, respectively. The data are 1-hour averages plotted every 12 hours Zulu time.

In comparing the data in Figures 5 and 6 with the data in Figures 1 and 2, some differences between Sites A and B (other than average level) are evident. The 165 Hz levels at Site B are totally dominated by storm noise with level increases from 9 dB to 13 dB during every February 1981 storm period described previously. During the calm period between storms, the 165 Hz levels at Site B are very low, approaching 59 to 60 dB/ $\mu\text{Pa}/\text{Hz}^{1/2}$ as a "noise floor." At these very low noise levels, shipping noise is not a factor since a 10 or 15 knot local wind^{2,3} is sufficient to dominate these noise floor levels. A large distant storm can raise the noise level above 70 dB/ $\mu\text{Pa}/\text{Hz}^{1/2}$ and Figure 6 shows that the omnidirectional 165 Hz levels at Site B act as a "weather barometer" for Pacific storms. Figure 7 shows the time series at 165 Hz at Site B for the week of 13 to 21 February 1981, which illustrates the major noise sources (local shipping, local storm, distant storm and calm or distant shipping background).

The 60 Hz levels at Site B shown in Figure 5 vary much less (2 to 4 dB) with storm events than the 165 Hz levels. This indicates that the 60 Hz levels are dominated more by shipping noise than storm noise most of the time. However, the 60 Hz levels at Site B have more variability than the 60 Hz levels at Site A (Figure 1) which were totally dominated by shipping.

It appears that the 60 Hz levels at Site B are dominated by relatively nearby ships, since the lowest levels in February 1981 occurred on 11 February 1981, just after the small local storm on 10 February 1981. The other more distant storms in February 1981 did not result in low levels between storms.

Figure 8 shows a comparison of the 1-hour averaged statistics at Site B for the same stormy week (5 to 11 February 1981) and the same calm week (20 to 27 March 1981) used in Figure 4 for Site A. The average 60 Hz levels at Site B increased by approximately 3 dB during the calm week, possibly because shipping densities and speeds increased to normal levels when no storms were present. However, the average 165 Hz levels at Site B decreased by 5 to 6 dB during the calm week due to decreased wind noise. The high noise levels in the bimodal distribution shown in Figure 8 for 165 Hz at Site B during the calm week are due to a storm the last day of that week.

3.0 ARRAY GAIN

Analysis of the omnidirectional data in the previous section illustrated site and frequency variability of ambient noise. However, the coherence of the noise field is an extremely important factor in assessing array performance and omnidirectional data is not impacted by noise coherence. Array noise gain (ANG) measurements were collected for a near broadside beam for both Sites A and B during part of the February/March 1981 data collection period. To eliminate measurement system effects, theoretical array noise gain, ANG_{theo} , was subtracted from measured array noise gain ANG_{meas} as follows:

$$ANG = ANG_{meas} - ANG_{theo} \quad (1)$$

The objective of this section is to illustrate the highly variable noise source dependence of \overline{ANG} by eliminating system gain against an ideal noise field. The results discussed for \overline{ANG} depend on the coherence of the dominant noise source only and apply to any array system.

If the noise field were isotropic and totally incoherent, \overline{ANG} would be zero for all beams and array gain would be constant and equal the theoretical array gain value. For Site A, and especially Site B, \overline{ANG} was highly variable and dependent on the noise source. Physically, \overline{ANG} is expected to be nearly equal to ANG_{theo} when the dominant noise source is a large, distant Pacific storm. Since a typical Pacific storm has a fetch (greater than 20 knot winds) on the order of 2000 n.m. (2/3 the size of the Continental United States), it should appear more incoherent and isotropic than a noise field dominated by nearby surface ships. Figure 9 shows \overline{ANG} at Site B plotted for several weeks in February/March 1981 with the 165 Hz omnidirectional levels at Site B used as an index or "storm barometer." \overline{ANG} at 165 Hz is anticorrelated with the 165 Hz levels probably because distant storm noise is uncorrelated. The noise field during calm periods may be dominated by a relatively few nearby ships and, consequently would be more highly correlated. Since Site B is a low noise site, it is probably not impacted greatly by distant shipping noise. The 60 Hz \overline{ANG} shipping values shown in Figure 9 support this supposition. The storm on 16 to 18 March 1981 passed very close to Site B and the 60 Hz \overline{ANG} values were also anticorrelated with the 165 Hz levels. Other more distant storms did not result in as great a decrease in \overline{ANG} . For example, the 60 Hz \overline{ANG} values did not decrease as much during the distant storm on 1 to 3 April 1981 as it did during the more local storm of 16 to 18 March 1981.

The \overline{ANG} values at 60 Hz and 165 Hz may have different performance implications for an array of elements when the changes in \overline{ANG} plus the omnidirectional level are considered. At 165 Hz, the results imply that beam level increases during storm periods will not be nearly as large as the increases in omnidirectional noise levels. In other words, the coherence of storm noise relative to the coherence of the noise field during calm weather periods results in beam level increases that are much less than the omnidirectional level increases. At 60 Hz, however, the situation is different since the 60 Hz omnidirectional noise levels at Site B remain constant or increase very little during storm periods. Since \overline{ANG} generally decreased more than the omnidirectional level increase, the storm indirectly resulted in lower beam levels at 60 Hz at Site B. Changes in ship speeds and densities are possible explanations for lower beam levels.

REFERENCES

1. Wenz, G. M., "Ambient Noise in the Ocean: Spectra and Sources," J. Acoust. Soc. Am., 48, 1970.
2. Wilson, J. H., "Very Low Frequency (VLF) Wind-Generated Noise Produced by Turbulent Pressure Fluctuations in the Atmosphere Near the Ocean Surface," J. Acoust. Soc. Am., 66 (5), Nov. 1979.
3. Wilson, J. H., "Low Frequency Wind-Generated Noise Produced by the Impact of Spray with the Ocean's Surface," J. Acoust. Soc. Am., 68 (3), Sept. 1980.
4. Wilson, J. H., "Wind-Generated Noise Modeling," Submitted to J. Acoust. Soc. Am. for publication April 1981.
5. Friehe, C. A. and S. E. Pazan, "Performance of an Air-Sea Interaction Buoy," J. App. Met., 17, October 1978.

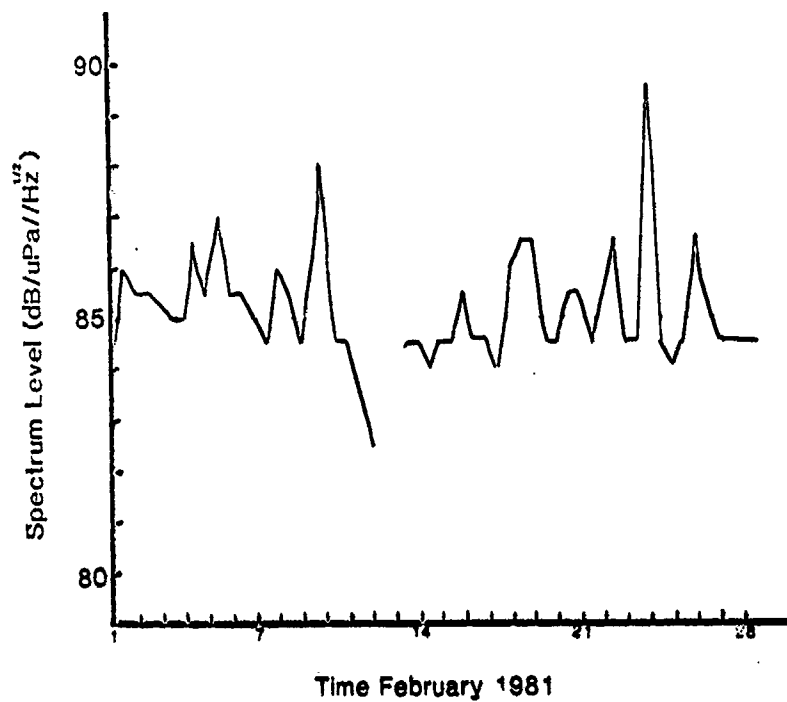


FIG. 1 SITE A - 60 Hz

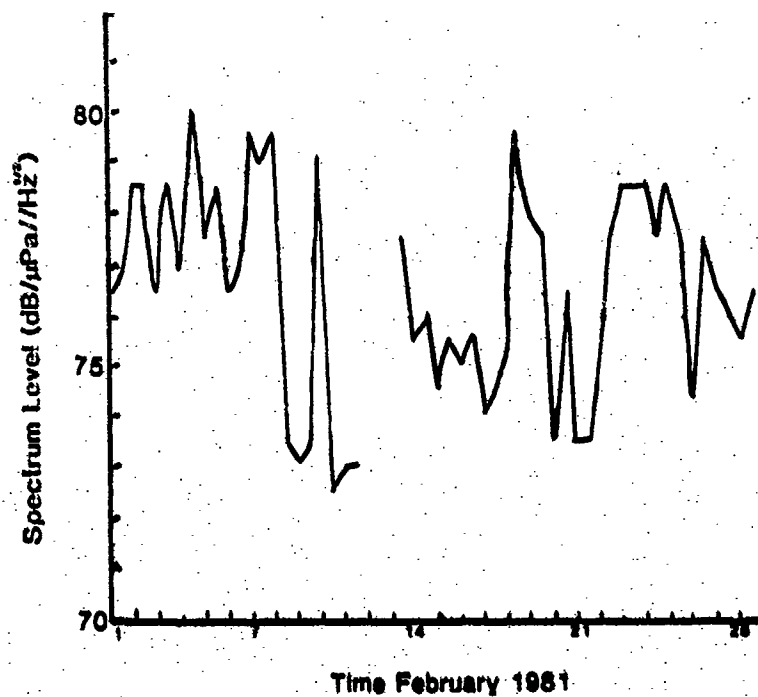


FIG. 2 SITE A - 165 Hz

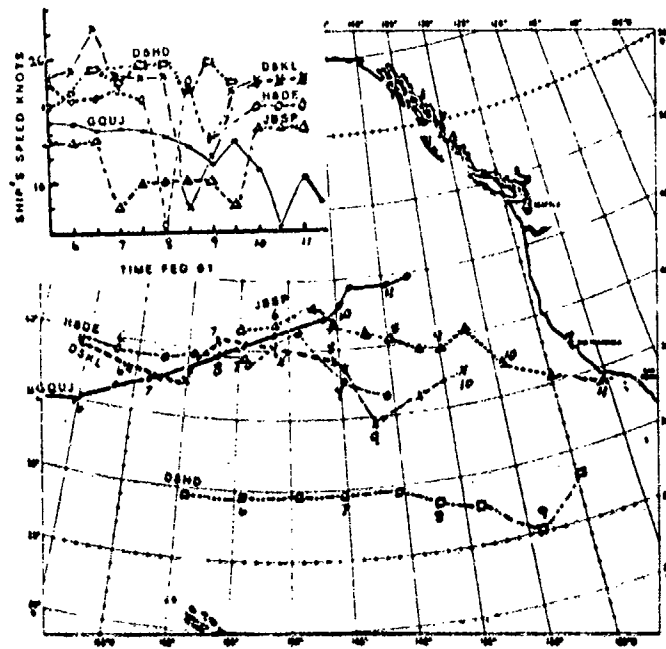


FIG. 3 SELECTED WMO SHIP TRACKS

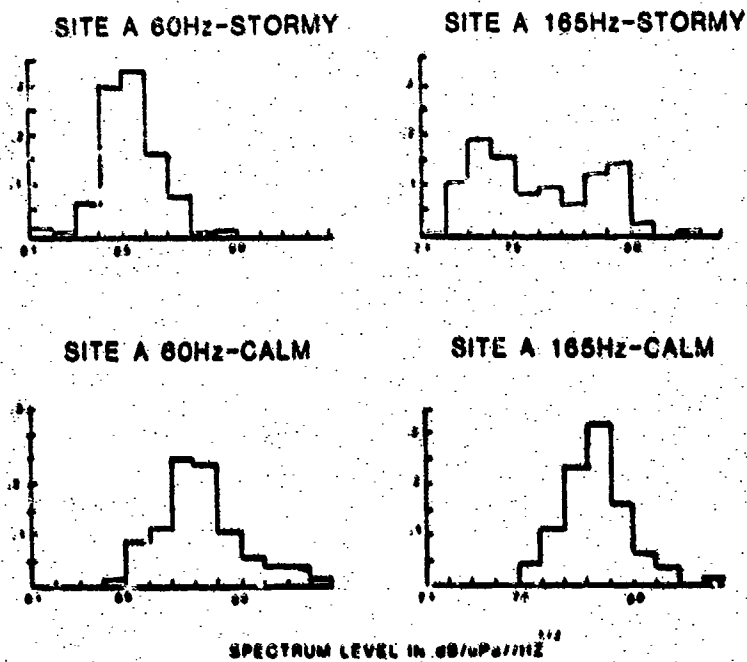


FIG. 4 ONE-HOUR AVERAGE NOISE STATISTICS FOR SITE A FOR A CALM AND STORMY WEEK

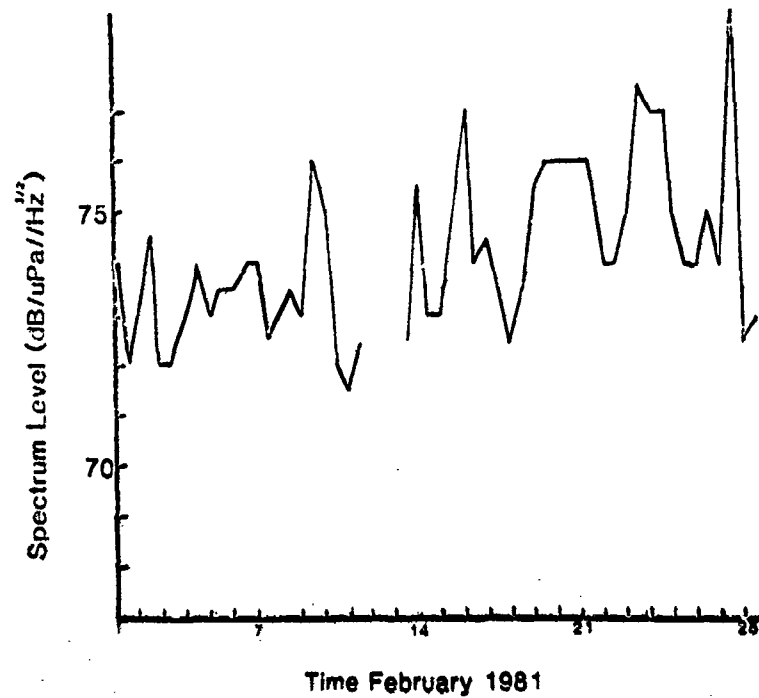


FIG. 5 SITE B - 60 Hz

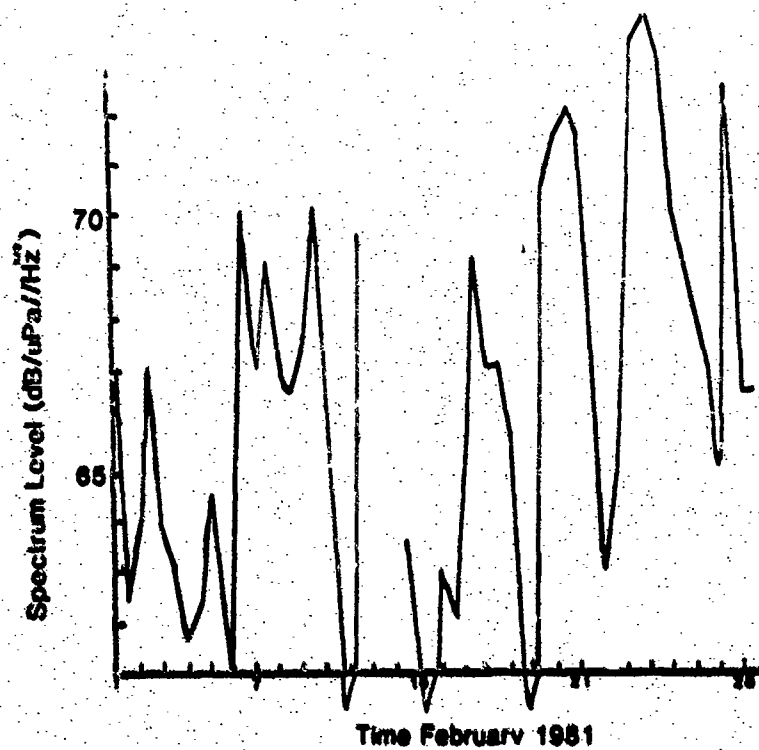


FIG. 6 SITE B - 165 Hz

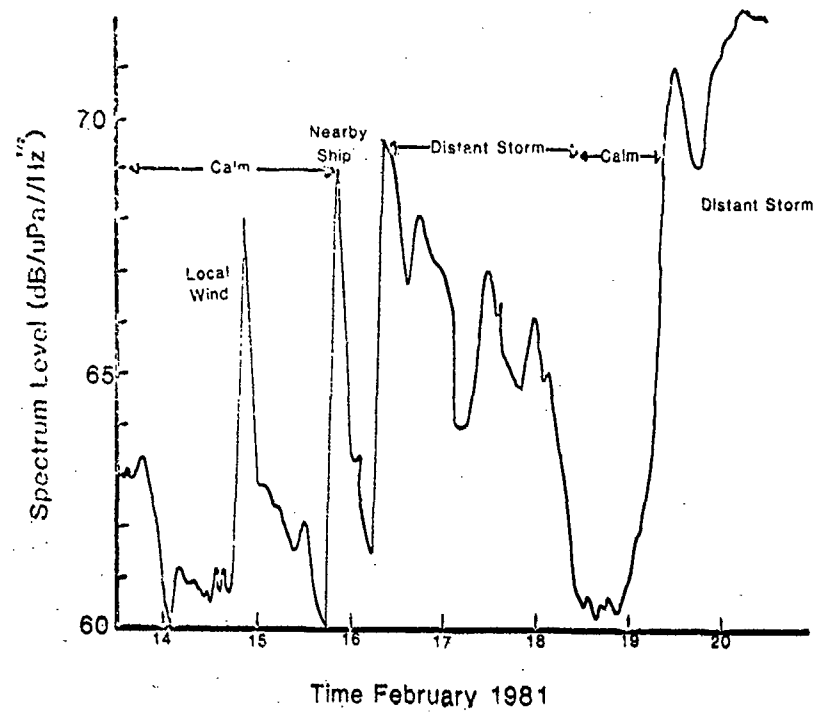


FIG. 7 SITE B - 165 Hz TIME SERIES

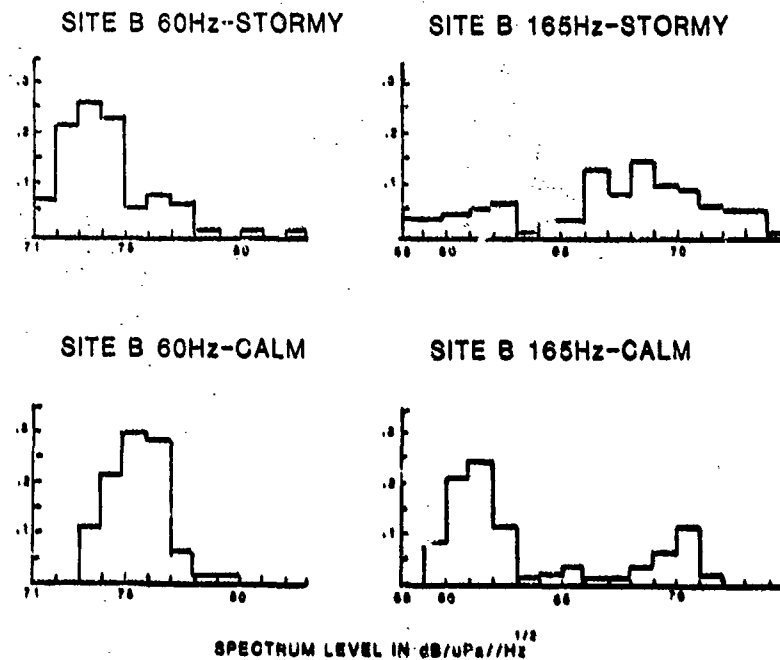


FIG. 8 ONE-HOUR AVERAGE NOISE STATISTICS FOR SITE B FOR A CALM AND STORMY WEEK

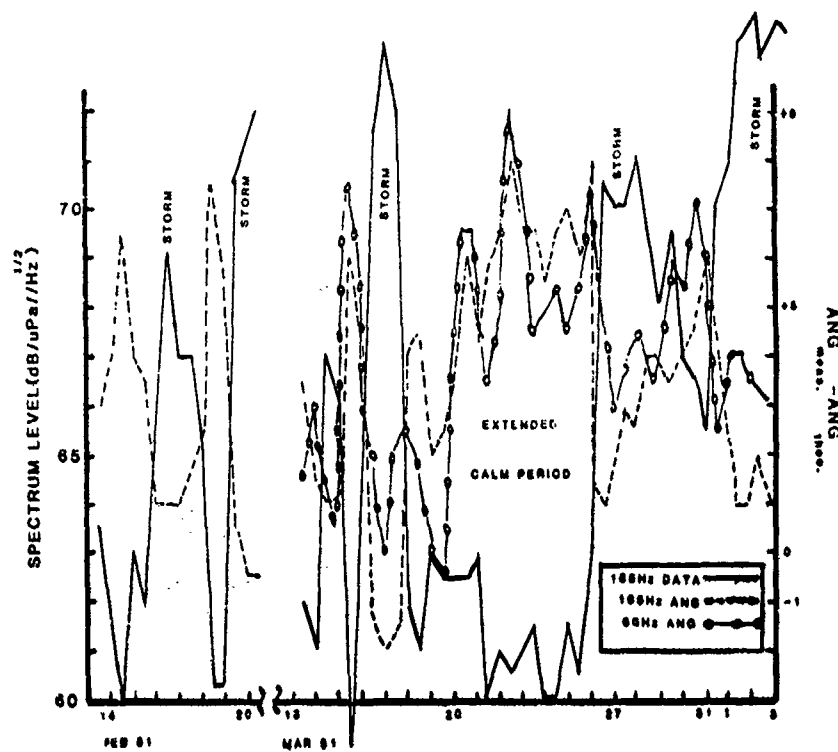


FIG. 9 ARRAY NOISE GAIN AT SITE B AT 60 Hz AND 165 Hz

SITE DEPENDENCE OF WIND-DOMINATED AMBIENT NOISE IN SHALLOW WATER

by

S.N. Wolf and F. Ingenito
Naval Research Laboratory
Washington, D.C. 20375

ABSTRACT

A survey of ambient noise data in shallow water taken under wind-dominated conditions shows substantial differences in spectrum level (often greater than 10 dB) under the same windspeed and sea-state conditions. This area-dependent effect, which is evident even in long-term averaged data, is caused by differences in ocean bottom properties, water depth, and sound-speed profile. Comparisons between those data sets which are accompanied by suitable environmental information and a wind-noise model developed jointly at NRL and SACLANTCEN are shown. The areas in which the data were taken cover a broad range of bottom types, water depths, and sound-speed profiles. Calculated differences in noise level agree well with the measured differences and it is concluded that the model is capable of predicting the effect of the shallow water environment on the spectrum level of wind-dominated ambient noise. We also conclude that commonly used universal ambient noise curves which do not take into account environmental differences are inferior to the model predictions in shallow water.

Introduction

In this paper we present the results of some recent studies of the dependence of wind-driven ambient noise level in shallow water on environmental parameters other than windspeed and sea state. Among these parameters are water depth, sound speed profile and ocean bottom composition. The paper will begin with the presentation of some measurements which suggest that an observable difference in wind-driven ambient noise level exists for different sites under the same windspeed conditions. The model used in the calculation of the effect of the environment on noise level is described. We then present the results of the application of this model to several data sets in order to account for observed level differences.

Shallow water wind driven noise measurements made at a number of locations [1-9] are shown in Figs. 1 and 2. Since the measurements, in general, were not made under exactly the same windspeed conditions, the data are assembled by reported sea state, or by sea state associated with the reported windspeed by using Vine and Volkmann's nomogram [10]. The arbitrary division of a continuum of possible windspeeds into a small number of sea states, the subjective nature of estimating sea states, and the introduction of measurement error are expected to introduce some differences in the measured spectra. The data show spectrum level differences, which in some cases exceed 10 dB. These differences are certainly too large to attribute to usual uncertainty of measurements of acoustic noise level. If we use Piggot's [2] measurements as a guide, we find that a difference of 10 dB in ambient noise level corresponds approximately to a tripling of the windspeed, or a change from sea state 2 to sea state 5. Although the comparison of shallow water ambient noise levels by grouping the data by associated sea state is not "exact", differences in level appear which cannot be explained by usual errors in measurement or sea state estimation.

Another comparison of wind-generated ambient noise [1] is shown in Fig. 3. In this illustration we show noise spectra measured at two sites, one having a sand bottom, the other having a silt bottom along with Piggot's [2] measurements. The present measurements at frequencies above 100 Hz show spectral shapes similar to those obtained by Piggot and were free from lines or other indications of shipping noise, and thus appear to be wind-driven noise. We see that differences in level (~ 5 dB) in the two sets of measurements over the sand bottom, are similar to the differences in Piggot's measurements at the corresponding wind speeds, but the absolute levels made over the sand bottom are somewhat higher. The measurements made over the silt bottom are somewhat lower than those reported by Piggot. In addition, we can see that the measurements made at windspeed 7 m/sec over the silt bottom are 2 dB lower than those made over the sand bottom at windspeed 3-5 m/sec. These data provide further support for the existence of a site-dependence of wind-driven noise. We now turn to the problem of quantitatively accounting for the observed differences in level by examining the ocean environment.

Model Description

The wind-noise model used in this study was developed jointly by NRL and SACLANTCEN and has been described in detail elsewhere [11]. The wind-noise sources are modeled as monopoles distributed over an infinite plane slightly below the surface and parallel to it (see Fig. 4). For the purposes of this study the sources are assumed to be uncorrelated. Because of the pressure release surface the sources are equivalent to dipoles at the surface. The water column has depth-dependent sound-speed and overlies a bottom consisting of a sedimentary layer with depth-dependent sound-speed above a homogeneous fluid or solid half-space. Absorption is present in all three layers. In addition, attenuation due to roughness at the surface and at the interface between the water column and the sedimentary layer is included. When the field of an individual noise source is represented in terms of the normal modes of the system the total intensity at depth z obtained by integrating over the entire source plane is

$$I(z, z') = q^2 \sum_{n,m} \frac{U_n(z') U_n(z) U_m(z') U_m(z)}{k_n^2 - k_m^{*2}} \left[\log_e \left(\frac{k_m^*}{k_n} \right) + i\pi \right]. \quad (1)$$

In Eq. (1) $I(z, z')$ is the intensity at depth z for sources located at depth z' , the u_n 's are the mode amplitude functions, the k_n 's are the complex modal wavenumbers, and q is a source term.

It can be seen from Eq. (1) that the $n = m$ terms dominate the sum. The modal wavenumber, k_n , can be written as

$$k_n = K_n + i \alpha_n \quad (2)$$

where α_n is the mode attenuation coefficient. Neglecting the $n \neq m$ terms and assuming that $\alpha_n \ll K_n$, Eq. (1) reduces to

$$I(z, z') = \frac{\pi q^2}{4} \sum_n \frac{U_n^2(z') U_n^2(z)}{\alpha_n K_n} \quad (3)$$

Since α_n is proportional to the attenuation in the system, Eq. (3) states that the intensity is inversely proportional to the attenuation. Note that α_n is the total mode attenuation coefficient and is the sum of several mode-dependent terms representing the contributions of the various attenuation mechanisms. In most cases absorption in the sediment dominates but loss due to surface roughness and absorption in the water column can be important at higher frequencies.

Results and Discussion

In order to use the wind-noise model described above to calculate environmental effects on the measured noise level it is necessary to have certain accompanying environmental data. These data are sound speed in the water column as a function of depth and the density, sound speed and attenuation coefficient of each bottom layer. A number of sufficiently complete data sets, consisting of noise spectrum levels and environmental data, have been collected [1,5,12,13]. Figures 5 and 6 show measured noise levels at the frequencies 500 Hz and 1000 Hz, respectively, vs windspeed. In most cases the wind showed short-term fluctuations over a range of windspeeds during the course of a noise level measurement so the points are plotted at the mean windspeed. Considerable scatter is observed in the data. Again the scatter is too large to be attributed to inaccuracies in the measurements and uncertainties in the windspeed. The trend of the measurements indicates that the measured noise level varies approximately as the square of the windspeed at both frequencies. Thus the data is consistent with earlier observations reported in the literature [2].

To determine the environmental effects we recast Eq. (1) as follows:

$$10 \log_{10} q^2 = 10 \log_{10} I - 10 \log_{10} \left\{ \sum_{n,m} \frac{U_n(z') U_n(z) U_m(z') U_m(z)}{k_n^2 - k_m^{*2}} \left[\log_e \left(\frac{k_m^*}{k_n} \right) + i\pi \right] \right\}. \quad (4)$$

Here $10 \log I$ is the measured noise level. The second term on the right-hand side of Eq. (4) can be calculated from the model, giving the source level, $10 \log q^2$. Note that the calculated term also depends on windspeed through the attenuation caused by surface roughness. The source level will depend on windspeed but will be independent on the other environmental conditions. The success of the explanation of the scatter of the levels in Figs. 5 and 6 may be inferred from the degree to which the independent determinations of source level produce points which lie on a common curve when plotted vs windspeed.

The source levels for the data of Figs. 5 and 6 are plotted in Figs. 7 and 8. It is immediately evident that the scatter has been reduced considerably by the removal of the environmental effects. We note that because the calculated absorption coefficients depend on surface roughness, and hence on windspeed, the calculated source level depends on a different power of the windspeed than does the noise level. At 500 Hz the source level increases with the fifth power of the windspeed; at 1000 Hz the source level depends on the sixth power of the windspeed.

Conclusion

Measurements of wind-driven ambient noise from a number of sites under similar windspeeds show a site-to-site variability of noise level which can not be readily attributed to errors in acoustic and environmental measurements alone. Some of the measurement sets were accompanied by sufficient water column and ocean bottom information to permit estimates of the effects of the acoustic environment on noise level. These calculated site-dependent terms account for the observed differences among the sites. We conclude that a more accurate prediction of wind-noise level can be made if water column and ocean bottom information is available than can be obtained from "universal" ambient noise-vs-windspeed curves.

Acknowledgments. The authors want to thank David Chapman of the Defense Research Establishment Atlantic in Halifax N.S. for his providing us with acoustic recordings and environmental data for the Scotian Shelf measurements. This work was supported by the Naval Sea Systems Command, Code 63R.

References

1. Scotian Shelf (sand). From recordings supplied to the Naval Research Laboratory by the Defence Research Establishment Atlantic, Dartmouth, N.S.
2. Scotian Shelf (rock and gravel). C. L. Piggot, "Ambient Sea Noise at Low Frequencies in Shallow Water of the Scotian Shelf. J. Acoust. Soc. Am. 36, 2152-2163 (1964).
3. Plantagenet Bank (coral and limestone) 1. A. J. Perrone, "Summary of One-Year Ambient Noise Measurement Program Off Bermuda," Naval Undersea Systems Center Technical Report 4979, 1 April 1976.
4. Plantagenet Bank (coral and limestone) 2. E. M. Arase and T. Arase, "Ambient Sea Noise in the Deep and Shallow Ocean," J. Acoust. Soc. Am. 42, 73-77 (1967).
5. Gulf of Maine (coarse sand and gravel) NRL measurements.
6. Arafura and Timor Seas. D. H. Cato, "Ambient Sea Noise in Waters near Australia," J. Acoust. Soc. Am. 60, 320-328 (1976).
7. G. M. Wenz, "Acoustic Ambient Noise in the Ocean: Spectra and Sources," J. Acoust. Soc. Am. 34, 1936-1956 (1962).
8. Scotian Shelf (silt). See Ref. 1.
9. Gulf of Maine (mud over rock). R. Connaly, Naval Industrial Reserve Plant, South Bristol, Maine - private communication.
10. Vine and Volkmann, Undersea Technology, p. 37, May 1964, reproduced in V. M. Albers, "Underwater Acoustics Handbook-II," p. 351, The Pennsylvania State University Press, University Park, PA (1965).
11. W. A. Kuperman and F. Ingenito, "Spatial Correlation of Surface Generated Noise in a Stratified Ocean," J. Acoust. Soc. Am. 67, 1988-1996 (1980).
12. From NRL measurements in collaboration with SACLANTCEN.
13. E. Murphy, A. Wasiljeff, and F. Jensen, "Frequency-dependent Influence of the Sea Bottom on the Near-surface Sound Field in Shallow Water," SACLANTCEN Memorandum SM-66, 1 May 1975.

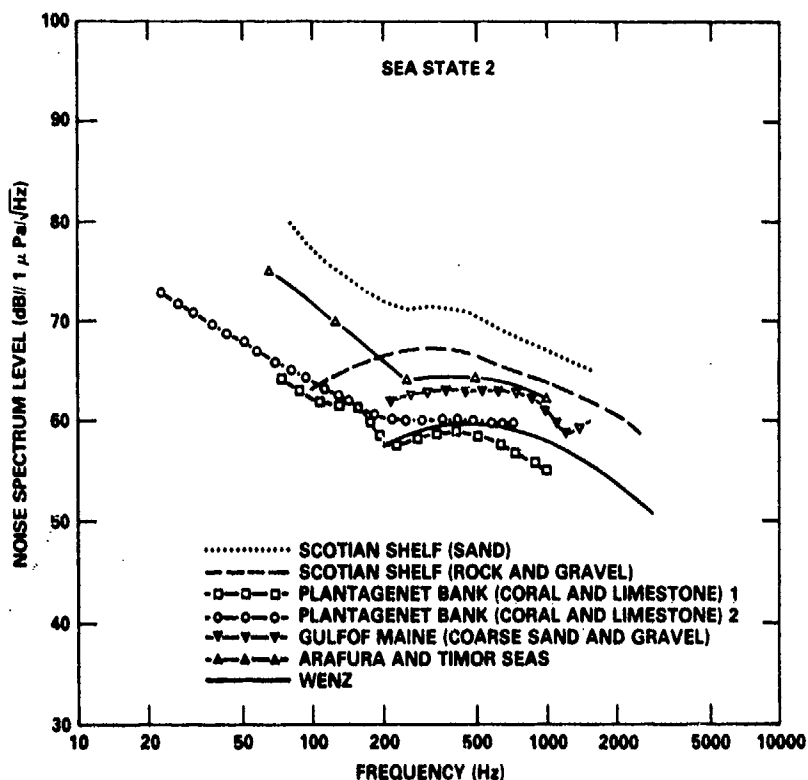


FIG. 1 MEASURED AMBIENT NOISE SPECTRUM LEVELS UNDER SEA STATE 2 CONDITIONS

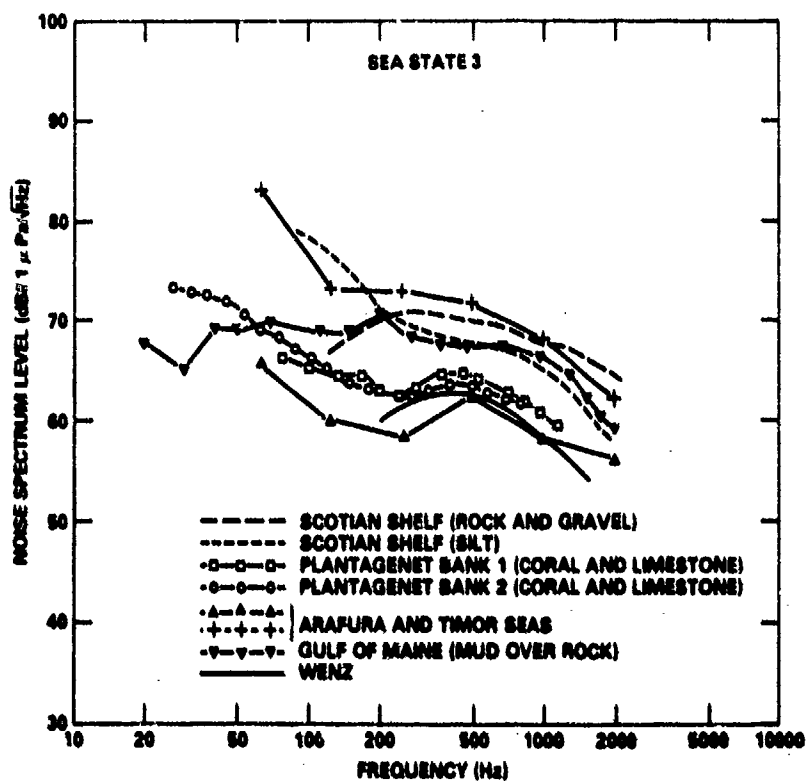


FIG. 2 MEASURED AMBIENT NOISE SPECTRUM LEVELS UNDER SEA STATE 3 CONDITIONS

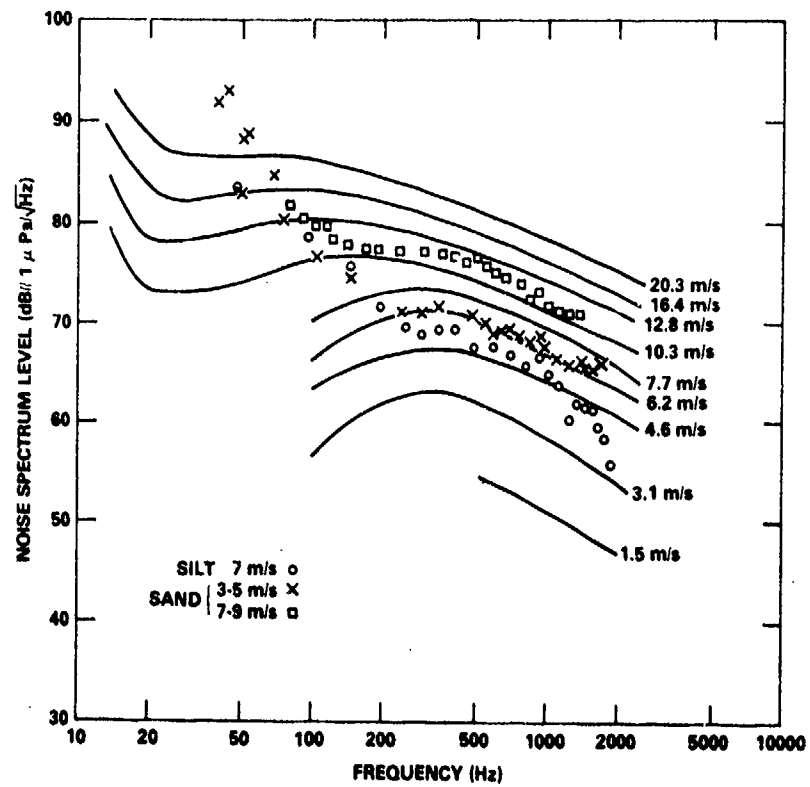


FIG. 3 MEASURED AMBIENT NOISE SPECTRUM LEVELS AT TWO SITES COMPARED WITH PIGGOT'S MEASUREMENTS

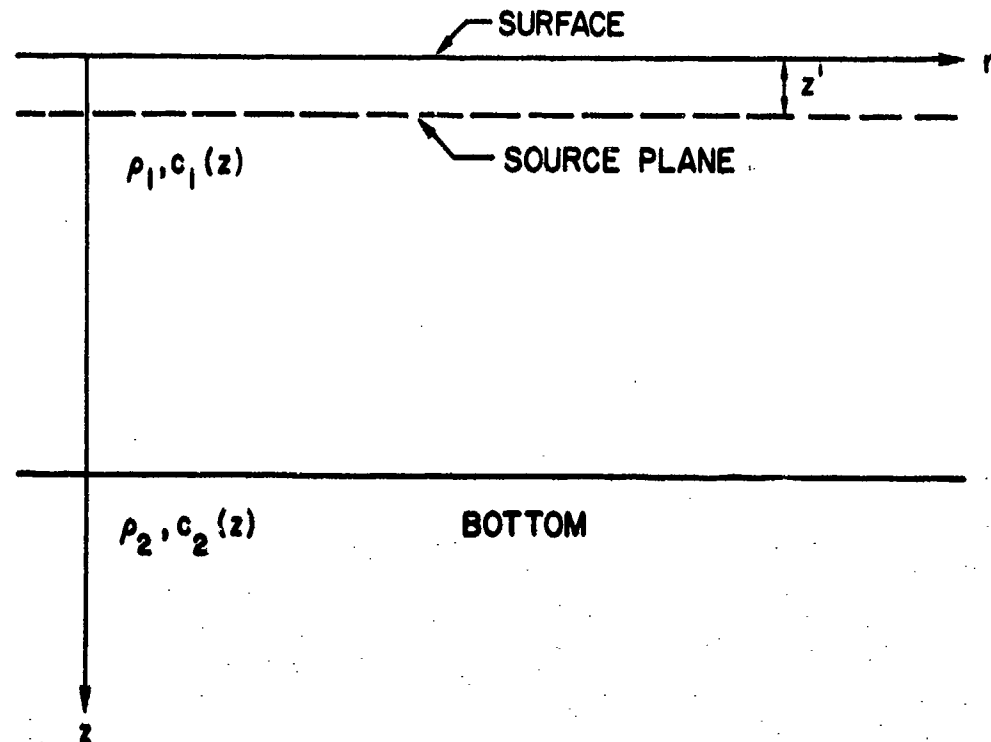


FIG. 4 THE GEOMETRY OF THE WIND-NOISE MODEL

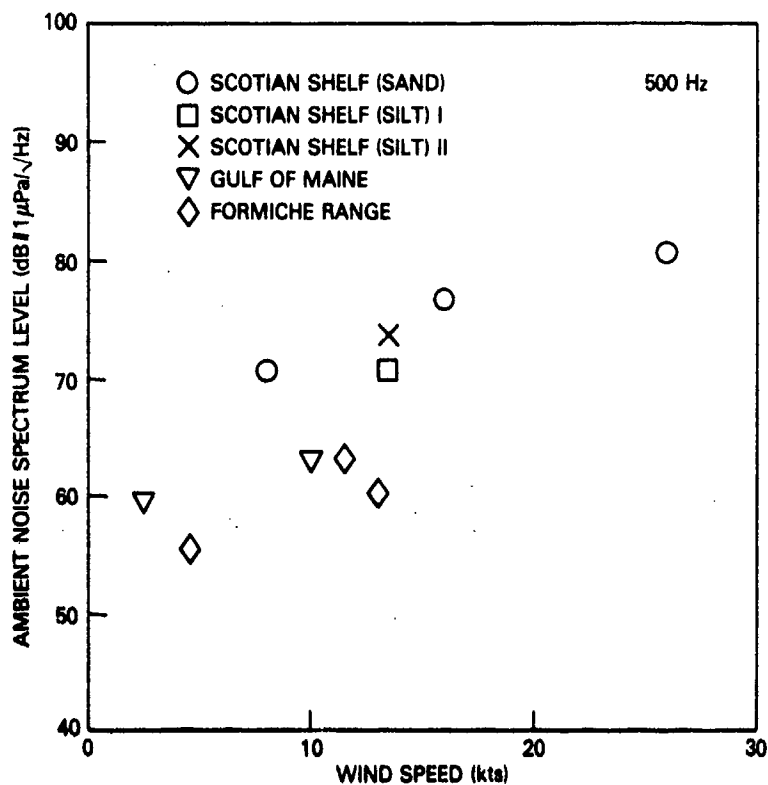


FIG. 5 MEASURED NOISE LEVEL vs WINDSPEED AT 500 Hz

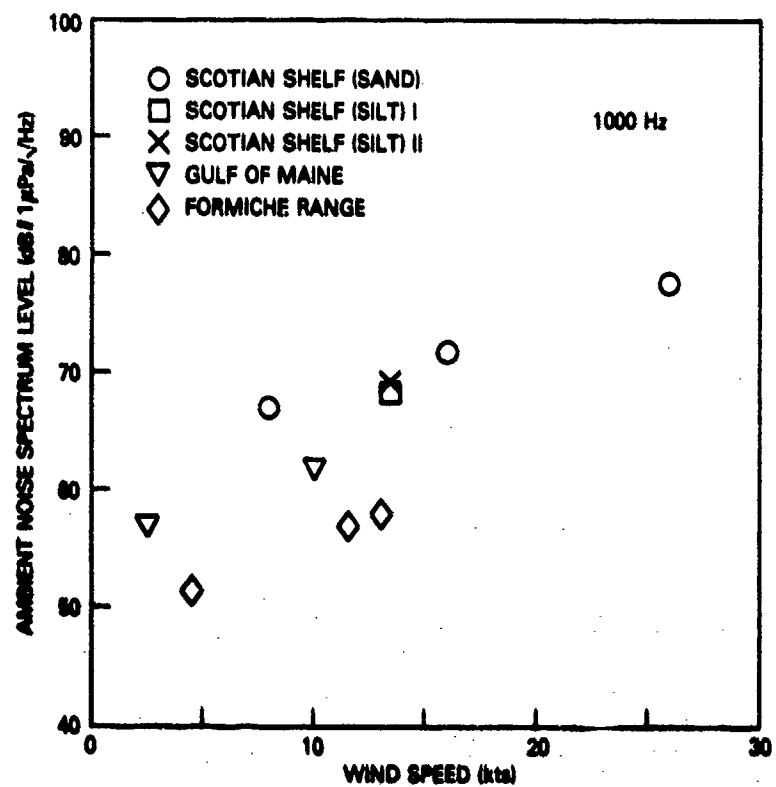


FIG. 6 MEASURED NOISE LEVEL vs WINDSPEED AT 1000 Hz

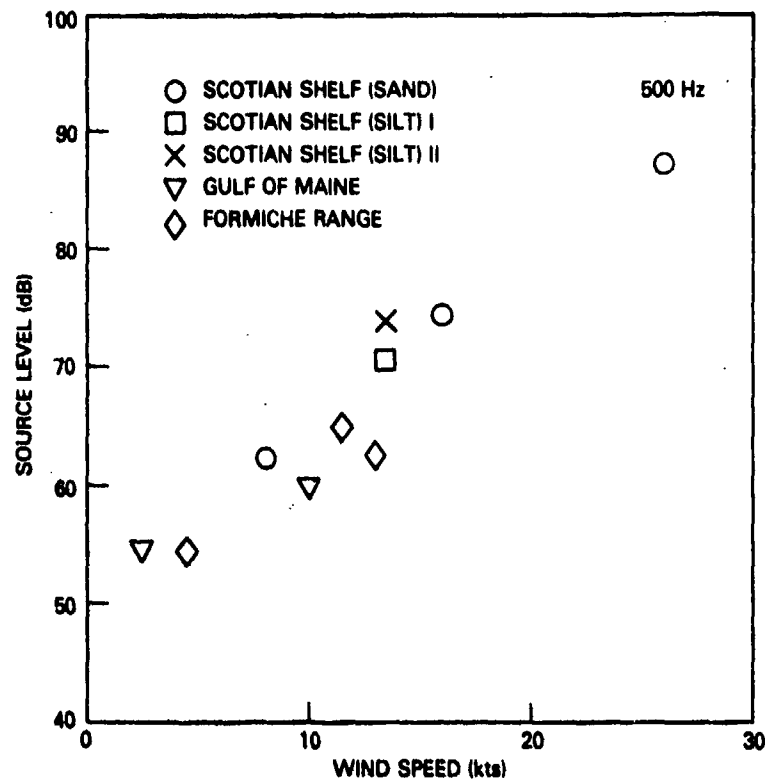


FIG. 7 WIND-NOISE SOURCE LEVELS vs WINDSPEED AT 500 Hz

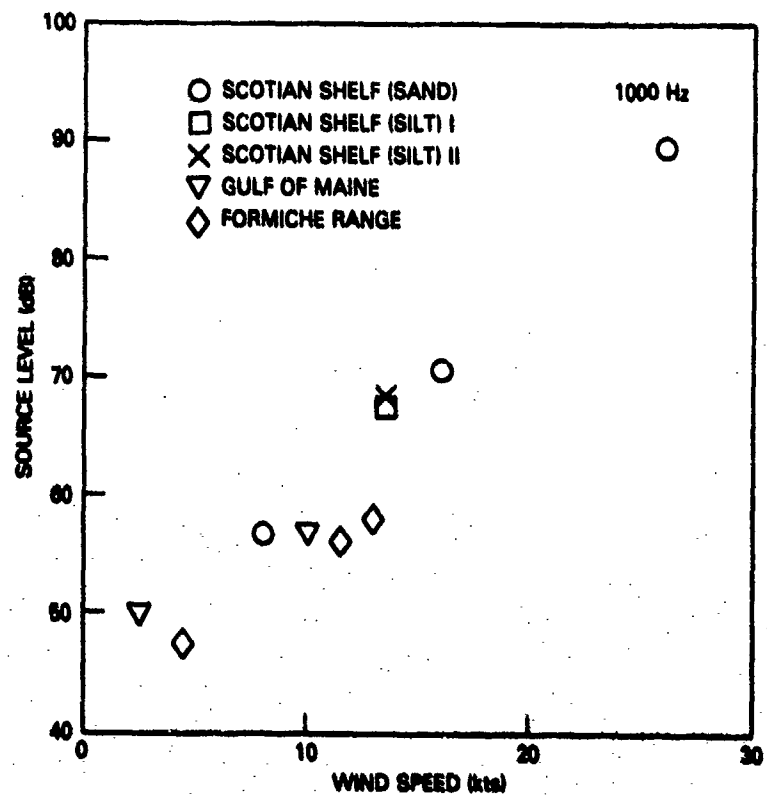


FIG. 8 WIND-NOISE SOURCE LEVELS vs WINDSPEED AT 1000 Hz

EFFECTS OF TOPOGRAPHIC BLOCKAGE AND OCEAN BOUNDARIES
ON LOW FREQUENCY NOISE FIELDS

by

Aubrey Anderson
ONR Detachment, Bay St. Louis, MS
Robert Martin
Samuel Marshall
Naval Ocean Research and Development Activity
NSTL Station, MS

ABSTRACT

Low frequency noise in most ocean areas is dominated by shipping or industrial noise. The composite noise field is the result of radiated energy from each discrete noise source propagating over relatively large distances to the receiving site. The ocean bottom in general, and topographic features in particular, result in vertically directional noise fields in addition to the expected azimuthal directionality. The noise field near the surface displays broadband coherent interaction between the direct and surface image energy, the details of which can be traced in part to the intervening topography. At deeper depths the level versus depth curves also display the impact of the topographic blockage. A measured data set displaying near surface to near bottom low frequency noise levels is analyzed with respect to range dependent environmental factors and shipping densities.

INTRODUCTION

Recently, the depth dependence of the low frequency ocean ambient noise field has been a subject of some interest¹. Depth profiles of ambient noise were obtained from two AUTOBUOY dives to depths of 2800 m which were conducted at widely separated sites under moderate sea conditions as part of the NORLANT '72 experiment². In both cases no ship traffic was observed in the general area of the dive. The deployment vessel, USNS SANDS (T-AGOR-6), was at quiet ship condition during most of each dive (using only its gas turbine on the 02 level to power the ship's facilities) at a distance of 5 nm from the launch point for the first dive on 22 July and 2 nm from the launchpoint for the second dive on 31 July 1972. Aural and graphical monitoring of the recorded data indicated that no obvious nearby ship noise was present. There were, however, waterborne transients occurring at repetition intervals of approximately 10, 18, and 24 seconds. These transients had low frequency characteristics and time durations which indicate that their sources were some distance away and these have been identified as sparkers and air-guns being used for sub-bottom profiling in the Labrador Basin and over the Grand Banks. The effect of these impulses

on the ambient level was eliminated by processing only in the interval between pulses. Thus, the data reported here represent only ambient noise generated by the sea surface and distant shipping.

The resulting data display different noise level versus depth relationships at the two sites. Furthermore, at one site data were acquired to very shallow depths and near-surface interference was observed in the resulting noise versus depth patterns. Two noise models, DANES³ and FANM⁴, were tested against the data to determine their utility in describing the observations. In addition, the range dependent Parabolic Equation⁵ transmission loss model was used to assess the effects of seafloor bathymetry on noise versus depth resulting from distant shipping.

AUTOBUOY DESCRIPTION

AUTOBUOY⁶ is a self-contained, untethered, programmable, free-diving, acoustic data gathering system which is capable of maximum depths to 6,000 m. It is generally programmed to descend quickly to a selected maximum depth, to release a descent weight in order to achieve neutral buoyancy and then to hover sequentially at four shallower depths. At each depth, several types of data are recorded on the seven channel tape recorder located in the instrumentation pressure vessel. These data include calibration signals and the acoustic signals from each of two closely spaced (~10 m) hydrophones together with depth, time, ascent velocity and temperature signals. Depth is controlled during the dive by adjusting the buoyancy around a neutral value in response to depth and velocity error signals. This is accomplished by the alternate valving to sea of light and heavy fluids. While hovering, AUTOBUOY is free to move with the water mass. Thus, no local noise is generated by water flow past the hydrophones. The fluid valving system is operated by solenoids which open valves such that fluid flows out by gravitational force. No noise is detectable from this operation. The depth and velocity signals also determine start times of an analog tape recorder which is preprogrammed for a specific sample size (typically 20 minutes). When recording is completed, the tape is stopped and AUTOBUOY ascends to the next programmed depth. When the last depth station is completed, the system rises to the surface where an attached recovery system, consisting of an rf beacon and a flashing light, is activated.

DIVE DESCRIPTIONS

The dive sites for NORLANT '72² are shown in Figure 1. Dive 1 occurred in the northeastern section of the Labrador Sea between Greenland and the Reykjanes Ridge. Dive 2 occurred in the deeper area of the basin 350 nm due south of the southern tip of Greenland. For each dive, AUTOBUOY was programmed to descend to 2900 m and then to hover at 2300, 1700, 1200 and 600 m depths while recording 20 minutes of ambient noise at each depth. At

the shallowest depth station, recording continued until the tape ran out. Figures 2a and 3a pictorially display the actual dive patterns for each event. During the first dive, hovering was achieved only at the two deepest depths while during the second dive hovering occurred at all but the shallowest depth. When hovering did not occur, ascent rates were approximately 1.2 m/sec (about 0.25 kt). At this slow speed, no observable mechanical or flow noise is introduced into the hydrophones. Failure to hover during a depth station is usually the result of valving too much heavy fluid at the deeper depths and not having sufficient reserve for the shallower depths. Also indicated on Figures 2a and 3a are the ship and wind speed conditions during the dives.

SPECTRAL ESTIMATES AND DEPTH DEPENDENT RESULTS

Figures 2b and 3b show the resulting spectra from the hydrophone acoustic outputs for the two dives. Two hydrophones, vertically separated by ~10 m, yielded virtually identical results. All data were processed in 1/3-octave bands centered at the indicated frequencies. Data were processed twice: once on board the SANDS through log-amplifiers onto a strip chart recorder and later ashore using a digital automatic data processing system (ADP). In both cases all transients (seismics, airguns, etc.) were eliminated from the data. Calibration signals over the entire band were injected at the hydrophone preamplifiers in the laboratory prior to deployment to produce a calibration tape. Also, a broadband calibration signal was automatically injected at the recorder inputs during the dive at the start of each 20 minute segment. The shipboard and ADP results were essentially identical. The principal difference between the spectra for the two dives is their depth dependence. At the deepest depth, the spectrum of the 22 July data has a variation in level with frequency of only 7 dB over the range 25 Hz to 800 Hz. As depth decreases the spectra slowly approach a more familiar shape. The leveling off of the spectra between 200-1000 Hz is a characteristic noted by others^{7,8} and is attributed to the overlap between ship generated noise and wind generated noise. In order for this to be the explanation of the 22 July spectra depth dependence, a significant reduction in ship noise contribution would be required for the deep data.

Figures 2c and 3c show the same data plotted to display the noise depth dependence at the two sites. Each data set represents measurements over approximately 6 hours with depths measured sequentially, rather than concurrently. Nevertheless, in the absence of individual nearby noise sources, the data should be a valid representation of persistent background noise as a function of depth for the measured locations and for the conditions that exist in the summer months. Horizontal noise pattern measurements in the northeast Pacific by R. Wagstaff⁹, for instance, demonstrate repeatable results from year to year for the same season in the shipping noise dominated portion of the spectrum.

Several interesting features of the noise depth dependence can be noted from the data displayed in Figures 2 and 3. The most striking is the strong depth dependence of the low frequency noise below critical depth

(see the sound speed profile on Figure 2c) at the location of Dive 1. This low frequency noise reduction below critical depth is consistent with observations in other ocean basins¹. It results in part because most of the energy from the distant noise sources is carried by low order normal modes of the water column and for these modes the amplitude decays exponentially with depth below the critical depth. The rate of decay of the noise level with depth below critical is determined by the energy distribution among the normal modes. This distribution is governed by several factors including: the distribution of energy among the normal modes of the water column of the source region(s), changes in the distribution of noise energy among modes as the energy travels from sources to receiver through a water column with horizontally changing sound speed versus depth structure (and thus changing normal mode eigenfunctions); varying modal attenuation along the propagation path resulting from several factors including bottom interaction of the modes. We will return to a discussion of some of these factors below when comparisons are made with numerical model noise computations.

Other notable features of the noise depth profiles include the virtually constant level with depth for frequencies above 300 Hz at the site of Dive 1 (Figure 2c) and the much weaker depth dependence throughout the water column at the site of Dive 2 for all frequencies as compared with the low frequencies at the site of Dive 1.

DEPTH DEPENDENCE ANALYSIS

Two computerized ambient noise numerical models were used to produce simulations of the noise fields for the sites of Dives 1 and 2. The models used are DANES³ and FANM⁴. Transmission loss models are useful for analyzing some features of the noise field depth dependence. For this purpose, simulations were run using the Parabolic Equation (PE) computer numerical transmission loss model of Tappert⁵. In this section, the models and model inputs are briefly described. Subsequently, model simulations are compared with the NORLANT '72 AUTOBUOY data and the comparisons are discussed.

The FANM ambient noise model is essentially a computer implementation of the Talham model¹⁰. It treats water column parameters as range independent (single sound speed profile), but allows bottom depth and bottom loss to vary with range; thus, energy from distant ships can be cut off by intervening bathymetric features. DANES utilizes a fully range dependent environment with propagation described by a range averaged transmission loss for 150 resolution tracks. Data base for sound velocity profiles (by season and area), bottom loss provinces, bottom depths and shipping distribution (by month) are accessed by DANES as indicated by input information (site location, time of year, weather). Sources are characterized as a function of frequency, by a source at depth of 6 m; source spectra are modified ROSS-ALVAREZ and ship distribution was obtained from the RMS data base. Similar data bases for bottom depth, bottom loss and shipping distribution were accessed by FANM. Figure 4 summarizes the ship count data base. This data base contains ship counts in 10 by 10

(Lat./Long.) squares. The data are shown in Figure 4 using revised divisions which more clearly indicate the relationship of ship counts, the bottom bathymetry and the measurement sites. Aerial reconnaissance during NORLANT '72² identified only 5 ships in a 50 square area near the measurement sites. No ships were observed from the SANDS during the measurements at the site of Dive 1. The higher density shipping to the south in the region shown in Figure 4 is expected because of shipping lanes in this area.

In Figure 5, the NORLANT data at 25 Hz and 50 Hz are compared with the simulated ambient noise depth profile from the DANES model. DANES was executed with a sound speed profile for the Dive 2 site which was measured during NORLANT '72 and with archival sound speed profiles in other portions of the area. Other data bases needed (ship distribution, bottom type, etc.), were accessed as appropriate to the model. Although the DANES simulated noise levels are reasonably close to the measurements at shallow depths, the details of the depth dependence differ between data and model. FANM simulated results (with similar input parameters) at 25 Hz are also shown on Figure 5. They agree with the data less than the DANES results at shallow depths and exhibit a greater change in level with depth than either the data or the DANES simulations. It has been shown¹¹ that range averaged transmission loss simulations can be valuable in analyzing the depth dependence of ambient noise fields. Such simulations were made using a Parabolic Equation⁵ computer model with a noise source depth assumed to be 6 m and with range varying input parameters for bottom bathymetry and sound speed profiles as shown in Fig 6b. These input parameters are representative of the environment to the south of the Dive 2 site, in the direction of most of the noise sources (ships). Results of these transmission loss simulations, averaged over a source-to-receiver range interval of 500 to 600 nm are also shown in Figure 5. The simulations shown are from a low loss bottom (0.2 dB/nm sediment attenuation). It is significant that, while they differ in terms of the details of the noise level versus depth profile, in general, all of the simulation results agree with the data in describing only a small (at most) dependence of noise level on depth over the sampled depth interval.

A more interesting set of comparisons is shown in Figure 7, wherein NORLANT results for the Dive 1 site are shown in comparison with DANES noise and PE average transmission loss depth profiles at 25 Hz and 50 Hz and with FANM noise depth profiles at 25 Hz. There is clearly significant disagreement between the measurements and all of the simulations. The monotonic decrease of measured noise levels with depth is significantly greater than either noise model simulation and the character of the average transmission loss profile disagrees with the measurements especially in the sharp increase in loss (which would produce a similar decrease in noise level) below about 2000 m. This situation has been analyzed further by a parametric study of the impact of: a) the range dependent nature (horizontal variation) of the sound speed profile in this area; and b) the topographic blockage introduced by the Reykjanes Ridge which is between the receiving site for Dive 1 and most of the ship noise sources (Figure 4). A Parabolic Equation model was used in this study; the basic assumption is that the major contributor to the noise field at the Dive 1 site is distant shipping as local shipping was non-existent. The majority of the distant shipping lies on the far side of the Reykjanes Ridge at distances greater than 300 nm. The Ridge is of varying depth, having a somewhat average

monotonic decline from the surface at Iceland in the northeast to the Labrador Basin in the southwest, ending approximately due south of the southern tip of Greenland. The PE model runs used a source at 6 m depth and were made to a range of 600 nm from the receiver. The water depth at the source was chosen as 4500 m rising to 3300 m at the start of the Reykjanes Ridge, which was chosen as the midway point. The base of the Ridge was assumed to be 200 nm wide with the Ridge plateau rising to selected depths below the surface. The receiver was located 100 nm beyond the far side of the Ridge base (see Figure 6a). All propagation events used here assumed a flat pressure release surface and bottom characteristics as follows: sediment sound speed gradient of 0.1 m along the entire track; 0.2 dB/nm attenuation in the sediment from the source to the Ridge and a fully reflecting bottom at the Ridge and beyond. While this characterization is not realistic, runs performed using a highly absorbing bottom along the entire track differed in transmission loss versus depth characterizations by less than 3 dB overall with near bottom exponential roll-off starting at about 100 m shallower depth. The sound speed was assumed to be range dependent with the profile at the receiving site chosen to be that measured during the exercise and all others chosen from archival data for midsummer in the direction from the receiver to the southeast.

Figure 8 displays transmission loss versus depth profiles averaged over the 500 to 600 nm source-to-receiver range interval. Examining the depth dependence for such a range averaged transmission loss is equivalent to examining the noise field depth dependence for a uniform distribution of noise sources over the 500 to 600 nm range interval. The family of curves shown was obtained by repeating the simulation for a variety of Ridge crest depths (shown in the circle by each curve). Also shown on Figure 8 is the range averaged transmission loss depth profile resulting from a simulation with a single bottom depth (3300 m) and a single sound speed profile (that measured at Site 1 during the acoustic measurements). The first thing to note from Figure 8 is the significant increase in the portion of the water column depth with essentially constant average transmission loss which results from range dependent simulations (for the case of no bathymetric intrusion) as opposed to those from constant environment simulations. Thus, in the absence of the Reykjanes Ridge, one might anticipate a noise field of very nearly constant level with depth down to depths on the order of 3 km. As one would anticipate, the attenuation of energy carried by higher order modes resulting from the bathymetric intrusion by the Ridge results in confinement of the noise energy to shallower portions of the sound channel. Indeed, as the top of the (simulated) intrusion becomes shallower, the resulting distribution of energy (Figure 8) more and more nearly represents a single low order mode of the sound channel at the receiver site. Although none of the profiles of average transmission loss with depth in Figure 8 exactly matches the Site 1 data, the profiles do make the case that the bathymetric intrusion represented by the Ridge will significantly change the depth distribution of energy for noise sources across the Ridge from the receiver. Specifically, the Ridge combined with the local sound speed profile variation will tend to confine more energy to the upper portion of the water column. This tendency, the varying depth of the Ridge along its path between sources and receiving site, and contributions from sources not blocked by the Ridge (including at least a few at shorter range) conspire to produce the observed noise level versus depth profile.

AMBIENT NOISE BOUNDARY EFFECTS NEAR THE SEA SURFACE

During Dive 1 (Figure 2) AUTOBUOY made a slow ascent from approximately 360 m to 20 m below the surface (as indicated by its depth gauge signal) where it hovered for several minutes until it received the command to surface. During this ascent, as AUTOBUOY neared the surface, a radical change in the ambient noise level at low frequency was observed (see Figure 9). The level change during the last 340 m of depth change ranged from 11.5 dB at 25 Hz to 0.5 dB at 200 Hz for the upper hydrophone and from 7 dB at 25 Hz to 0.5 dB at 125 Hz for the deeper hydrophone. These two hydrophones, as mentioned earlier, are approximately 10 m apart so that when the upper hydrophone is at 20 m, the lower hydrophone is at 30 m depth. Assuming a directional noise field, these observations can be interpreted as a manifestation of the Lloyd Mirror Effect which basically states that the resultant output of a hydrophone near a boundary can be described as the algebraic sum of the output of the hydrophone and its image (the reflection of the hydrophone in the boundary taking into account the change in acoustic impedance at the boundary). For the case of a pressure release interface, the boundary effect results in a 180° phase change of the acoustic signal when reflected from the surface. Figure 10 displays effective vertical dipole beam patterns for a receiver at 20 m below the surface for two different frequencies; viz., 31 and 100 Hz. If the receiver were 60 m below the surface, then the 31 Hz pattern would be nearly identical to the 100 Hz pattern for a depth of 20 m. If the noise field were isotropic, integration over these two patterns for a single frequency but different receiver depths (say for 31 Hz at 20 and 60 m) would yield approximately the same value and therefore no significant depth effect would be noted. However, if noise is vertically directional as would be expected if the dominant sources are distant ships, then a significant decrease can be expected as the receiver approaches a boundary. Furthermore, the shape of the receiver dipole pattern is not changed for the horizontal null if the noise is band limited rather than single frequency. Note, in Figure 10, that the dashed curve for 1/3-octave noise is identical to that for a single frequency at the band center for the horizontal null and becomes progressively modified for subsequent nulls.

ANALYSIS OF NEAR SURFACE NOISE DEPTH DEPENDENCE

The pattern function for the dipole receiver, described above, is given by:

$$I = 4I_0 \sin^2(2\pi \frac{d}{\lambda} \sin \theta)$$

where the symbols are defined in Figure 11. The FANM noise model computes the noise energy arriving at a receiver in several vertical arrival angle bins. A special version of FANM was generated to apply the above pattern function separately to each vertical arrival angle bin (using the angle with the horizontal of the center of the bin as θ) and then sum the

resulting energy in the bins for a total (omnidirectional) noise level. This FANM version, producing what is called a coherent sum, was used to simulate the noise versus depth profiles for the upper hydrophone data of Figure 9. In these simulations, sharp decreases in level occurred at low frequency as the surface was approached. This is in contrast to a normal (incoherent) FANM calculation for which noise level either remains constant or actually increases slightly as a function of decreasing depth near the sea surface. In Figure 12, calculations with the new (coherent) FANM model are compared with the NORLANT '72 near surface data. The depth dependence of the data and the FANM simulations is in excellent agreement.

Recall that the FANM model cuts off noise energy which is blocked by bathymetric features. In the earlier discussion of the noise depth profile, it was postulated that the noise field at Site 1 resulted from a combination of noise energy, much of which had undergone varying degrees of bathymetric blockage by the Reykjanes Ridge. This was based in part on the information shown in Figure 8. In addition to a redistribution of energy in the deep portions of the water column, the bathymetric blockage modifies the near surface interference pattern. Figure 13 shows an expanded display of the near surface portion of the parametric, PE transmission loss study of Figure 8. Modification of the details of the near surface interference pattern by the bathymetric feature is evident. One persistent feature of the near surface interference pattern is the final monotonic decrease in noise energy as the receiver approaches the surface. This is a result of the pressure release surface and resulting exponential decay of all modes near the surface¹². Reduction of the interference with increasing Ridge height (decreasing N) is consistent with the earlier description of higher order mode attenuation as the height of the bathymetric intrusion increases. Increased dominance of lower order modes can be interpreted as a reduction of ray angle, with the horizontal, for the interfering energy. From the equation of Figure 11, as the height of the bathymetric intrusion increases, the attendant decrease of should result in a shift to greater depth of various features of the interference pattern, such as the depth of occurrence of peaks and nulls. Just this behavior is exhibited by the results shown in Figure 13. For example, the first minimum in transmission loss (maximum of noise energy) occurs at its shallowest depth with no bathymetric interference and monotonically increases in depth as the Ridge height increases. The near surface features of the NORLANT '72 data are consistent with an interpretation of the field as a result of noise energy which has undergone varying degrees of bathymetric blockage by the Reykjanes Ridge. Note that the depth of the second (and higher order) nulls in the patterns of Figure 13 would be filled in by the 1/3-octave processing of the NORLANT data, although the first, near surface null would be unaffected (recall Figure 10). This and the reduction of the interference null by sea surface roughness are probable explanations for the absence of second and higher order nulls in the measured surface noise field.

CONCLUSION

In the NORLANT '72 data, both the near surface interference pattern and the depth profile of the noise field for the deeper portion of the water column

have been shown to be consistent with a postulated description of the noise field as a combination of noise energy fields from distant sources which have experienced varying degrees of blockage by the Reykjanes Ridge. Numerically simulated range averaged transmission loss has been shown to be a useful tool for analyzing the depth dependence of ambient noise fields. Such simulations have illustrated the impact of bathymetric blockage on both the noise versus depth profile in the deep portion of the water column and on the near surface interference pattern. Although they exhibited reasonable success in simulating the noise depth profile in the simpler region of the NORLANT '72 Dive 2, neither the DANES nor the FANM model was successful in reproducing the noise depth profile of more complicated origin at the Dive 1 site.

REFERENCES

1. Morris, G.B., August 1978. "Depth Dependence of Ambient Noise in the Northeastern Pacific Ocean," JASA 64(2), 581-590.
2. Martin, R.L., May 1978. "NORLANT 72 Exercise Summary Report (U)," LRAPP Report S78-022, Naval Ocean Research and Development Activity, NSTL, MS.(SECRET)
3. Osborne, K.R., 1979. "DANES - A Directional Ambient Noise Prediction Model for FLENUMOCEANCEN," Report for Naval Ocean Research and Development Activity, Ocean Data Systems, Inc., San Diego, CA.
4. Cavanagh, R.C., 1974. "Fast Ambient Noise Model I (FANM I)," Acoustic Environmental Support Detachment, Office of Naval Research, Washington, D.C.
5. Tappert, F.D., 1977. "The Parabolic Approximation Method," in Wave Propagation and Underwater Acoustics, J.B. Keller and J.S. Papadakis, Eds., Lecture Notes in Physics, 70, 224-287, Springer-Verlag, New York.
6. Gozzo, R.S. and R.L. Martin, June 1973. "Autobuoys: Present Capabilities and Planned Modifications," NUSC TR 4505, Naval Underwater Systems Center, New London, CN.
7. Wenz, G.M., December 1962. "Acoustic Ambient Noise in the Ocean: Spectra and Sources," JASA 34(12), 1936-1956.
8. Perrone, A.J., September 1969. "Deep-Ocean Ambient-Noise Spectra in the Northwest Atlantic," JASA 46(3), 762-770.
9. Wagstaff, R.A., July 1977. "An Ambient Noise Model for the Northeast Pacific Ocean Basin (U)," JUA 27(3), 525-540. (CONFIDENTIAL)
10. Talham, R.J., August 1964. "Ambient-Sea-Noise-Model," JASA 36(8), 1541-1544.

11. Anderson, A.L. and K.C. Focke, April 1978. "Model Sensitivity Studies: Ambient Noise Depth Dependence Related to Propagation Loss (U)," JUA 28(2), 219-228 (CONFIDENTIAL)

12. Pedersen, M.A., D.F. Gordon, and D. White, September 1975. "Low-Frequency Propagation Effects for Sources or Receivers Near the Ocean Surface," NUC TR 488, Naval Ocean Systems Center, San Diego, CA.

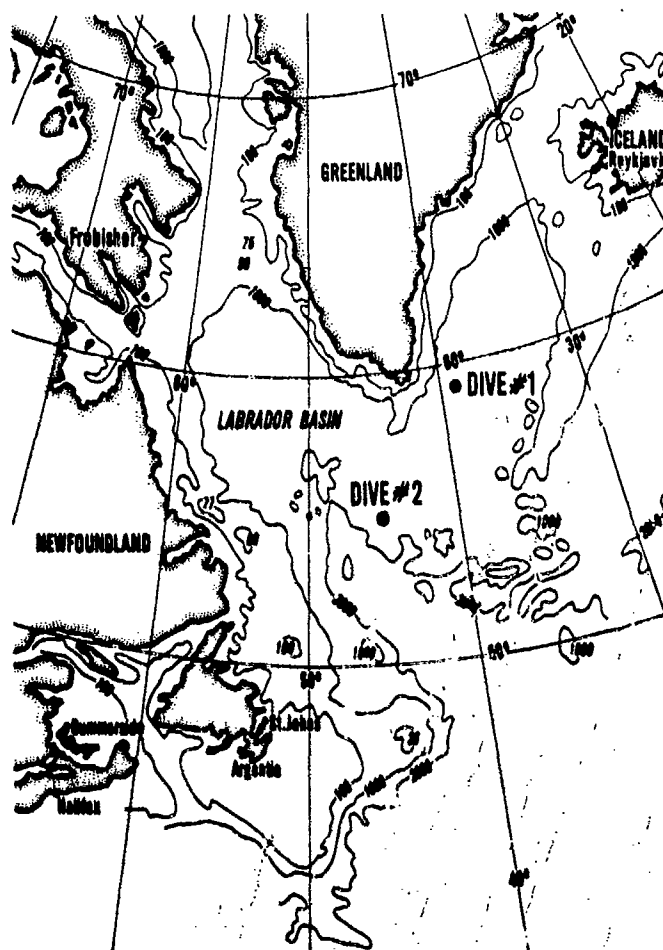


FIG. 1 LABRADOR SEA LOCATIONS

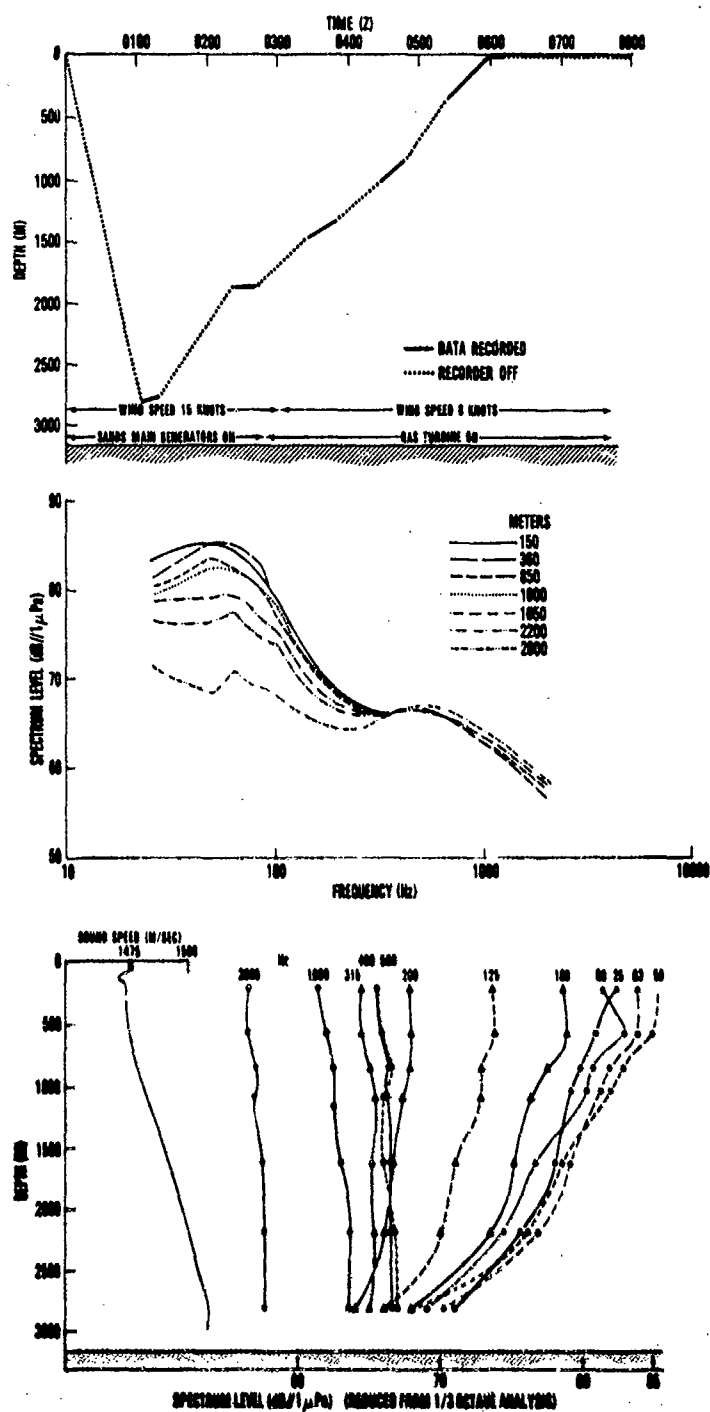


FIG. 2 DIVE 1: DIVE PATTERN; MEDIAN AMBIENT NOISE SPECTRUM; AMBIENT NOISE vs DEPTH

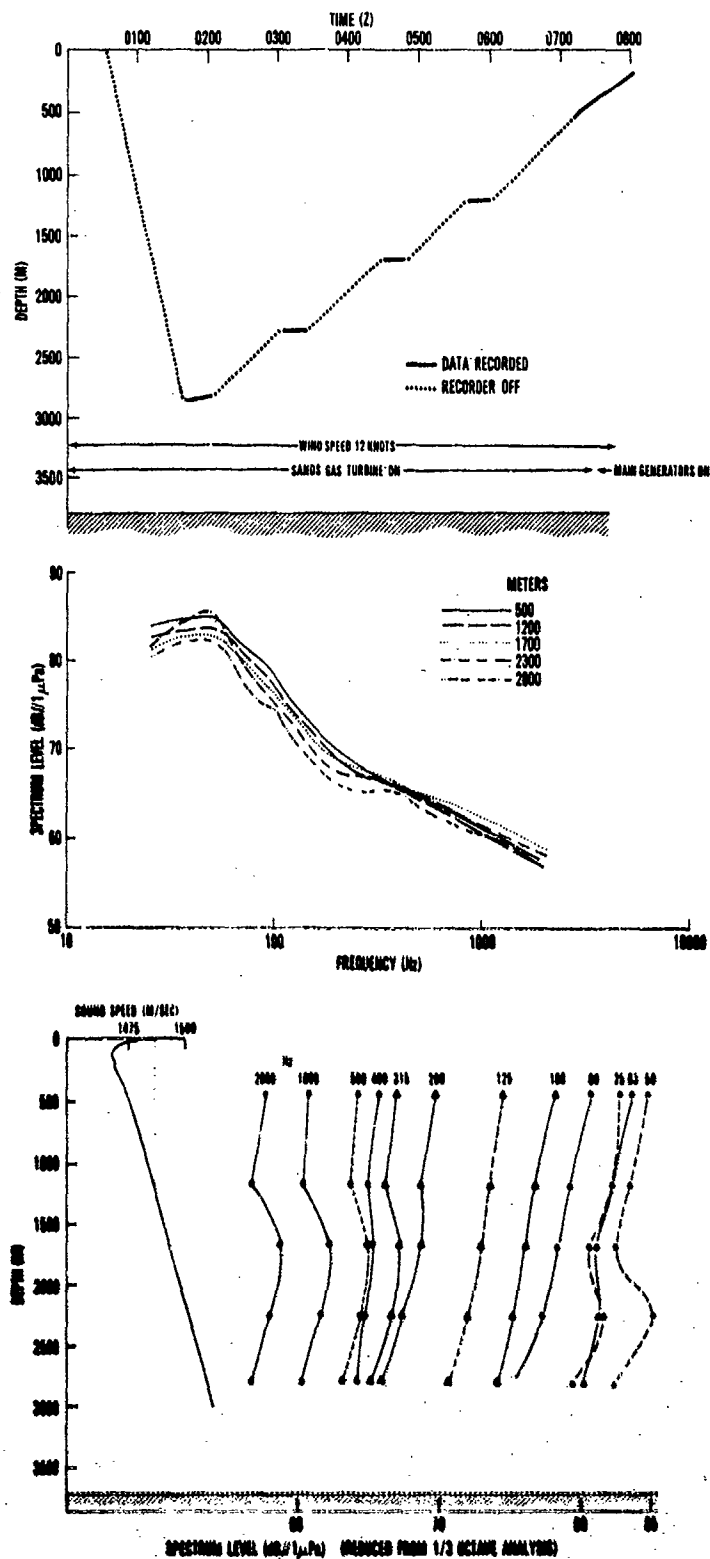


FIG. 3 DIVE 2: DIVE PATTERN; MEDIAN AMBIENT NOISE SPECTRUM; AMBIENT NOISE vs DEPTH

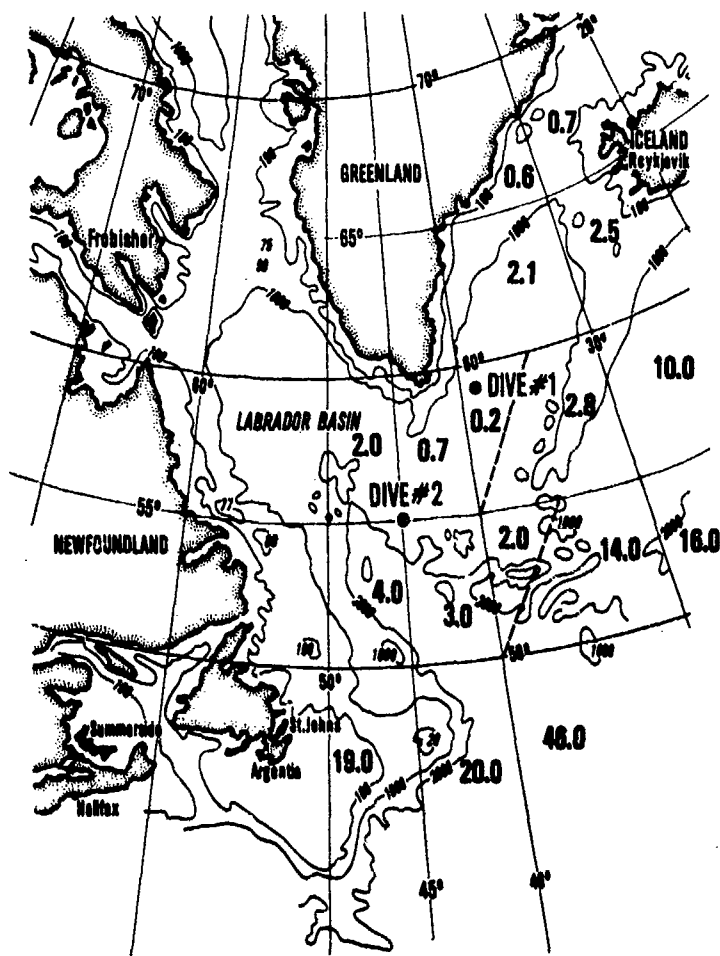


FIG. 4 SHIP COUNT, DAILY AVERAGE

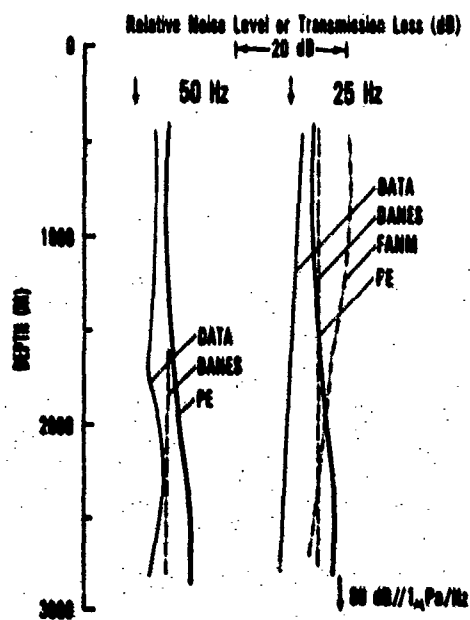


FIG. 5 DIVE 2: DATA MODEL COMPARISON

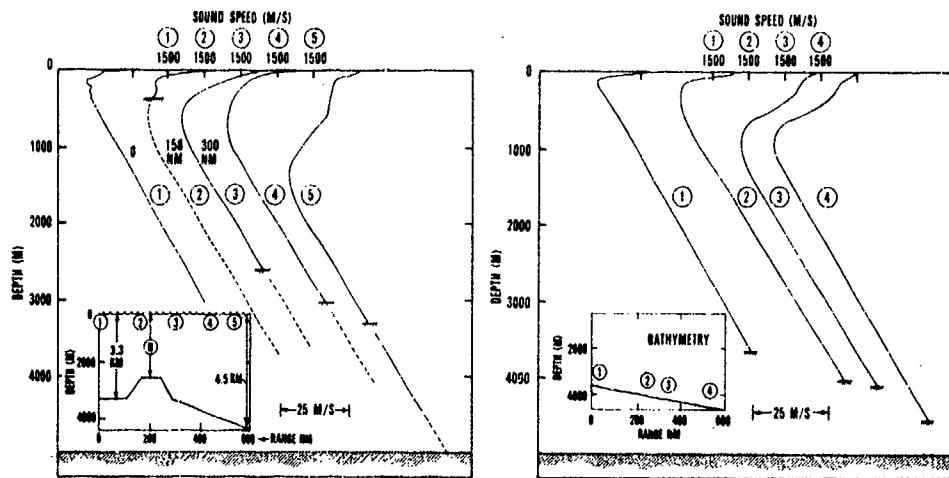


FIG. 6 ENVIRONMENTS FOR MODEL RUNS, DIVES 1 and 2

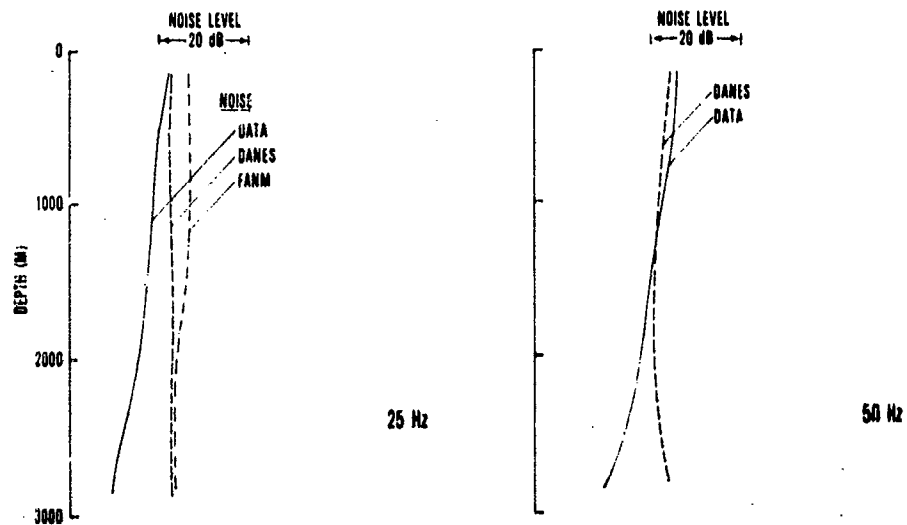


FIG. 7 DIVE 1: DATA MODEL COMPARISON

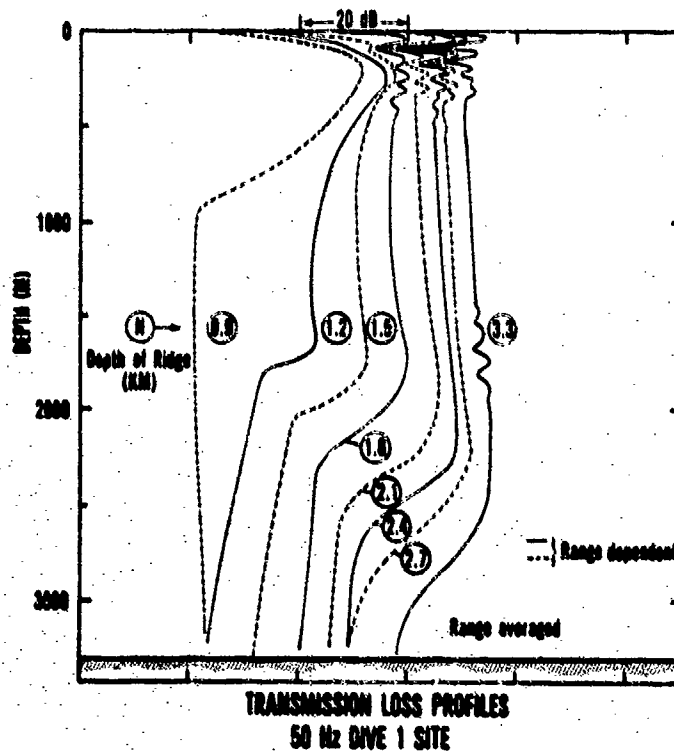


FIG. 8
DIVE 1: PARAMETRIC PE STUDY

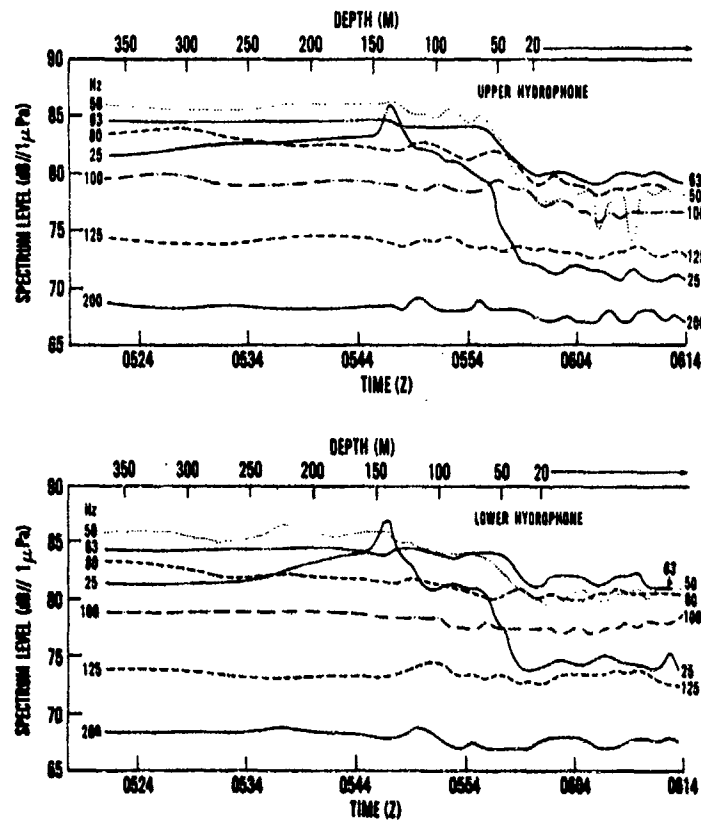


FIG. 9 DIVE 1: NEAR SURFACE AMBIENT NOISE DATA

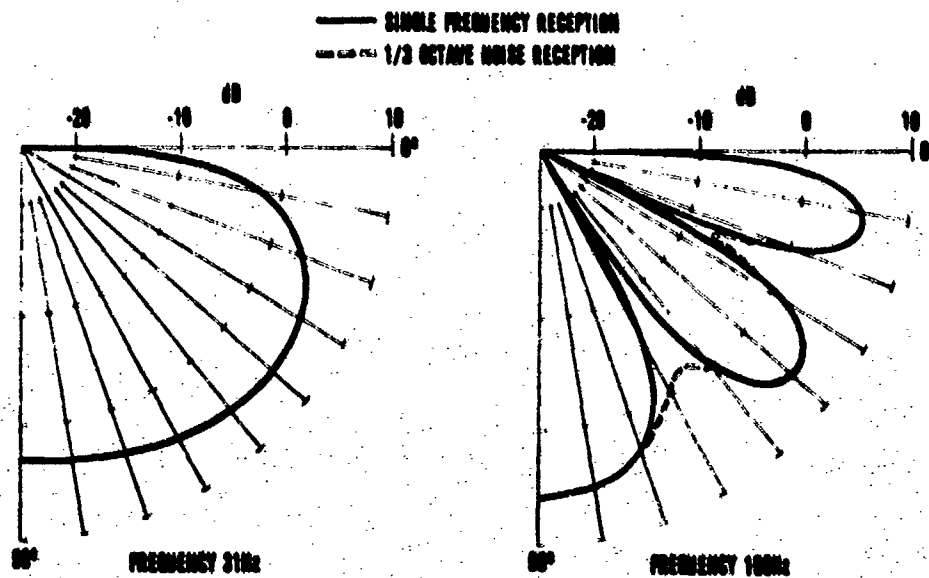


FIG. 10 VERTICAL DIPOLE BEAM PATTERN

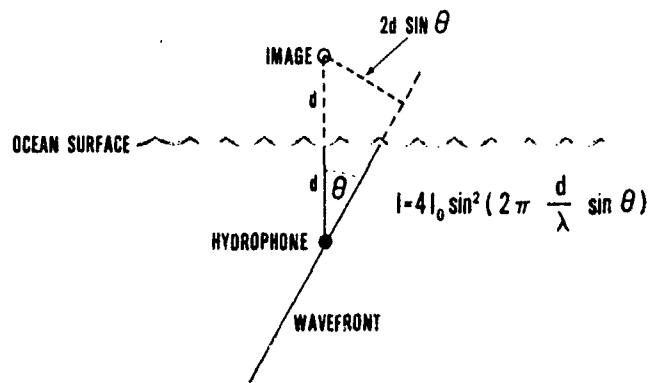
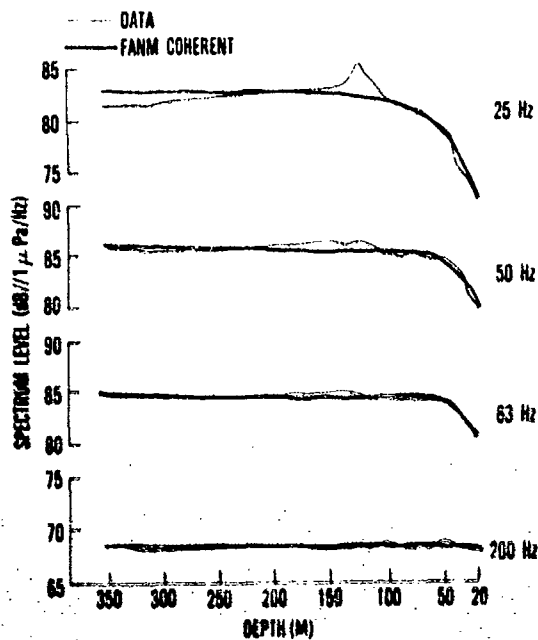


FIG. 11 GEOMETRY FOR VERTICAL DIPOLE BEAM PATTERN



COMPARISON OF FANM AND DATA

FIG. 12

DIVE 1:

NEAR SURFACE DATA MODEL COMPARISON

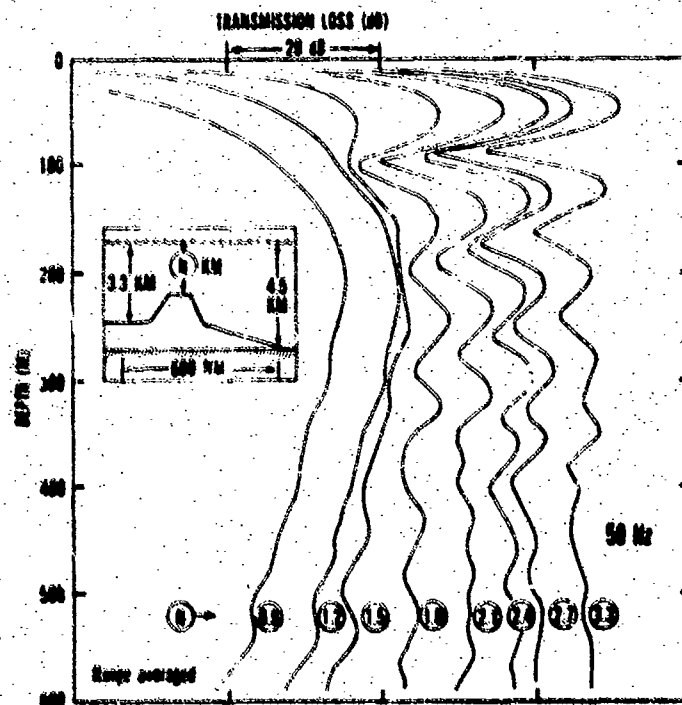


FIG. 13

DIVE 1:

NEAR SURFACE PARAMETRIC PE STUDY

THE SEAMOUNT AS A NOISE BARRIER

by

Herman Medwin, Emily Childs* and Edgar A. Jordan**
 Physics Department, Naval Postgraduate School, Monterey, CA 93940, U.S.A.

ABSTRACT

When the path from a localized noise source is intercepted by a seamount the shielded noise consists of a diffracted component and, if the seamount is close to a sufficiently smooth ocean surface, a multiply-reflected component as well. The magnitude and frequency filtering of the blockage caused by the seamount is here determined by using the impulse solution of diffraction by a rigid wedge as a module for the computer calculation of multiple diffraction at gross changes of slope along the seamount and at its crest line. These computer calculations are validated by comparison with laboratory measurements using a scale model of DICKENS Seamount which has previously been shown to be an effective technique for the calculation of topographical diffraction at sea.

BACKGROUND

The ambient noise measured at any location depends on the noise source and the transmission path. A factor that may significantly affect the propagation loss is the interception of the noise path by a seamount; shadowing losses of 15 to 20 dB are commonly measured.

One successful technique for the prediction of shadowing losses by a seamount is the use of a 2M x 2M laboratory scale model¹ (Figs. 1,2); the scaled frequency-dependent diffraction losses at the seamount are added to the losses in the body of the sea which are calculated by a computer model such as FACT. There is good agreement with ocean data (Figs. 3,4). The seamount is assumed to be rigid; no other assumptions are needed. The increase of shadowing loss with frequency^{1/2} has since been observed in several ocean experiments by different laboratories². Whether this diffraction component is dominant depends on the distance between the seamount and the sea surface as well as the roughness of the sea surface³.

*Ocean Acoustics Associates

**LT, U.S. Navy

In the example studied, DICKENS Seamount with a slope of about 14° culminating in a crest approximately 500M from the surface, a 35 knot wind resulted in an ocean surface of rms height 1.6M calculated from the Pierson-Moskowitz wind wave spectrum. In this case, the model studies show that not only was the diffraction component the first, it was also the largest component; multiple reflections between the seamount and the wind blown sea produced a much weaker signal. Note signal after 203 μ s in Fig. 5

The physical basis for the interpretation of the diffraction is the fact that the diffracted energy comes principally from a region near the sound ray track. The crestline of the seamount at the sound track may be approximately most simply by the apex of a flat wedge; the rigorous closed form impulse solution of a rigid wedge is given by⁴ eqs. (1)-(3),

$$p(t) = (-Spc/4\pi\theta_w)\{\beta\}[rr_0 \sinh y]^{-1} \exp(-\pi y/\theta_w), \quad (1)$$

where

$$\beta = \frac{\sin[(\pi/\theta_w)(\pi \pm \theta \pm \theta_0)]}{1 - 2 \exp(-\pi y/\theta_w) \cos[(\pi/\theta_w)(\pi \pm \theta \pm \theta_0)] + \exp(-2\pi y/\theta_w)}, \quad (2)$$

$$y = \text{arc cosh} \frac{c^2 t^2 - (r^2 + r_0^2 + Z^2)}{2rr_0} \quad (3)$$

The term $(\pi \pm \theta \pm \theta_0)$ is written for simplicity; the curly bracket consists of the sum of four terms obtained by using the four possible combinations of the angles, $\pm\theta$ and $\pm\theta_0$.

Source coordinates are $(r_0, \theta_0, 0)$, receiver coordinates are (r, θ, Z) . The angle of the wedge measured in the fluid region is called θ_w .

The sound diverges spherically from the point source and cylindrically from the crestal line scatterer. The earliest, strongest, pressure arrivals vary as $(\text{time})^{-1/2}$, and the frequency dependence of the scatter goes as $f^{1/2}$. For these reasons, the appropriate model scaling parameter is the far field diffraction strength, DS, given by

$$DS = 20 \log_{10} [(P_D/P_0)(r_0/R_0)(r/\lambda)^{1/2}] \quad (4)$$

where

- P_D = diffracted pressure
- P_0 = reference pressure at range R_0
- R_0 = reference range (=1 M)
- λ = wave length
- r_0 = range, source to diffracting edge
- r = range, diffracting edge to receiver

The far field diffraction strength is a function of wedge angle, angle of incidence, elevation and azimuthal scatter angles.

The concept of diffraction strength is used throughout this work. To convert to diffraction loss DL in dB one uses

$$DL = 20 \log_{10} [(r_0/R_D)(r/\lambda)^{1/2}] - DS \quad (5)$$

where R_D is the direct range from source to receiver.

The equivalence of DS in the laboratory, where dimensions are measured in centimeters and frequencies go to 100kHz, and in the ocean with ranges in Km and frequencies in hundreds of Hertz, is shown in Fig. 6.

The asymptotic approach to the far field diffraction strength is presented as a function of r/λ in Fig. 7. It will be noted that the plane 14° wedge, the simplest approximation to the seamount, has a DS some 10dB too high; and the "contour wedge" which is contoured to the seamount profile along the sound track, and which is the physical realization of the two dimensional parabolic equation solution, is also several dB too high.

METHOD

The purpose of this paper is to demonstrate the extent to which the diffraction strength of the seamount may be determined by simple computer models based on plane wedge diffraction. The degree of validity of each computer model is measured by its ability to match the results of the laboratory scale model, whose effectiveness has already been proven by comparison with ocean experiments. Three types of computer models are considered: (1) a double wedge interpretation of the two-dimensional contour of a seamount; (2) a segmented plane wedge idealization of the crest of the three-dimensional seamount; (3) a multiple wedge representation of the three-dimensional seamount.

Model 1:

Impulse calculations of double diffraction 6,7 have been used to describe the noise shadowing by a thick barrier. An example of the success of this technique for a thick plate is shown in Fig. 8. The two-dimensional double diffraction technique is now used to approximate the seamount as a wide barrier with two changes of slope; diffraction at the first edge is interpreted as due to a line of properly-timed secondary sources which reradiate over the second edge. Fig. 9 presents the two-dimensional Track 6 ray path contour of DICKENS seamount and two different approximations for the double diffraction calculations. In approximation one, plane surfaces are assumed from the source to position a where the sound diffracts through angle $\theta_w = 186^\circ$, from a to position c where the diffraction angle is $\theta_w = 210^\circ$, and from c to the receiver. In approximation two, the assumed plane surfaces are from source to b, b to d, and d to receiver; the two wedges thereby defined have $\theta_w = 212^\circ$ and 186° at b and d, respectively. The comparison of the double diffraction computer calculation with laboratory experiment shows good to excellent agreement.

Model 2:

A naïve assumption will now be evaluated, namely that the crest of the three-dimensional seamount is where most of the major changes of slope occur, and that this may be approximated by crestal line segments of finite length, Fig. 10. Each segment produces a response that is a truncation⁵ of the temporal response given by eq. (1), due to the limited time of interaction with the finite segment. The diffraction at the crest is then comprised of the sum of the plane wedge impulse responses. When this sum of the segmental responses for DICKENS Seamount is transformed to the frequency domain one obtains the DS shown in Fig. 10. Only the lowest frequencies are seen to be in agreement with experiment, as one should expect for this plane wedge model which ignores changes of slope along the slopes of the seamount. The DS of this crestal segment model is 1 or 2 dB better than that of the simple plane wedge, $Q_w = 208^\circ$, but it is still about 10 dB too large, compared with laboratory measurements.

Model 3:

The correct calculation should consider the multiple diffraction at all significant changes of slope at, and adjacent to, the ray path. The simplifying assumption is now made that we can visually identify the major changes of slope near TRACK 6 and use these for an adequate calculation of DS. Several wedge identifications have been made at regions of large change of slope. Fig. 11 shows these wedge approximations drawn on a photograph of the critical part of the seamount model. We find (Fig. 12) that computer calculations for four such approximations are within 2, 3 dB of each other and about 2 or 3 dB too high compared to the scale model experiment. The identification of larger numbers of changes of slope would be needed to improve the accuracy of the shadowing prediction.

CONCLUSIONS

Using topographical data that show the lines of significant changes of slope, the double diffraction technique permits accurate computer calculations of the diffraction loss of noise in the shadow of a two-dimensional seamount, and approximate predictions for the three-dimensional body.

ACKNOWLEDGEMENT

The comparison of our predictions with the results of ocean experiments was made possible by the generous cooperation of Gordon Ebbeson, N. Ross Chapman and the Defense Research Establishment Pacific, Victoria, B.C., Canada. This work was supported by the U.S. Office of Naval Research.

REFERENCES

1. H. Medwin and R.P. Spaulding, Jr., "The seamount as a diffracting body" in Bottom-Interacting Ocean Acoustics, W.A. Kuperman and F.B. Jensen eds., Plenum Press, New York, 1980.
2. H. Medwin, Chairman "Panel discussion of topographical effects on ocean propagation". J. Acoust. Soc. Am. 69, Suppl 1, S60 (Spring 1981).
3. E.A. Jordan and H. Medwin, "Scale model studies of scattering and diffraction at a seamount", J. Acoust. Soc. Am. 69, Suppl. 1, S59(1981).
4. M.A. Biot and I. Tolstoy, "Formulation of wave propagation in infinite media by normal coordinates with an application to diffraction", J. Acoust. Soc. Am. 29, 381-391 (1957). See also, I. Tolstoy, Wave Propagation (McGraw-Hill, New York, 1973).
5. H. Medwin, "Shadowing by finite barriers", J. Acoust. Soc., 9, 1060-1064 (1981).
6. H. Medwin, "Impulse studies of scattering by finite barriers", J. Acoust. Soc. Am. 71, Suppl. 1, S35(1982).
7. H. Medwin, E. Childs and G.M. Jebsen, "Impulse studies of double diffraction: a discrete Huygens interpretation", in press.

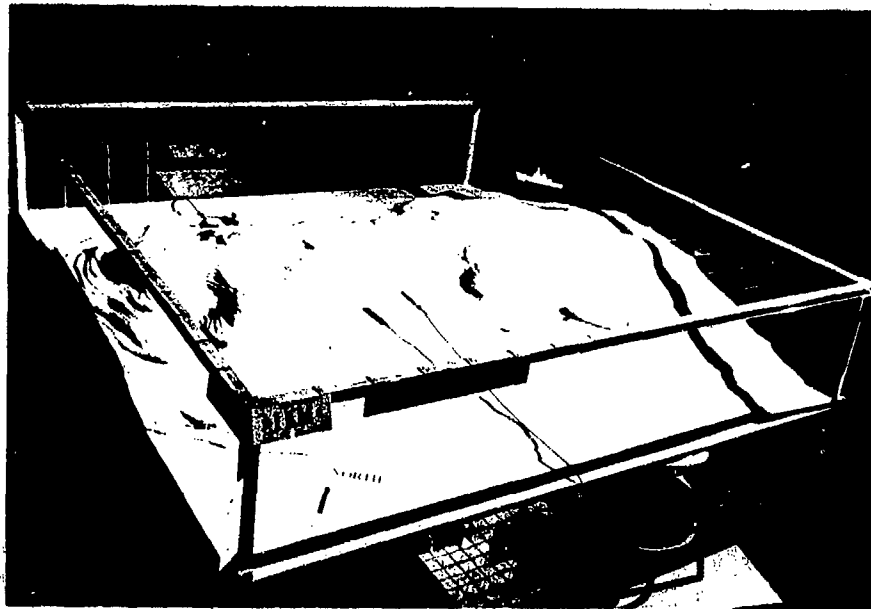


FIG. 1 LABORATORY MODEL OF DICKENS SEAMOUNT TO SCALE 1 km = 5 inches

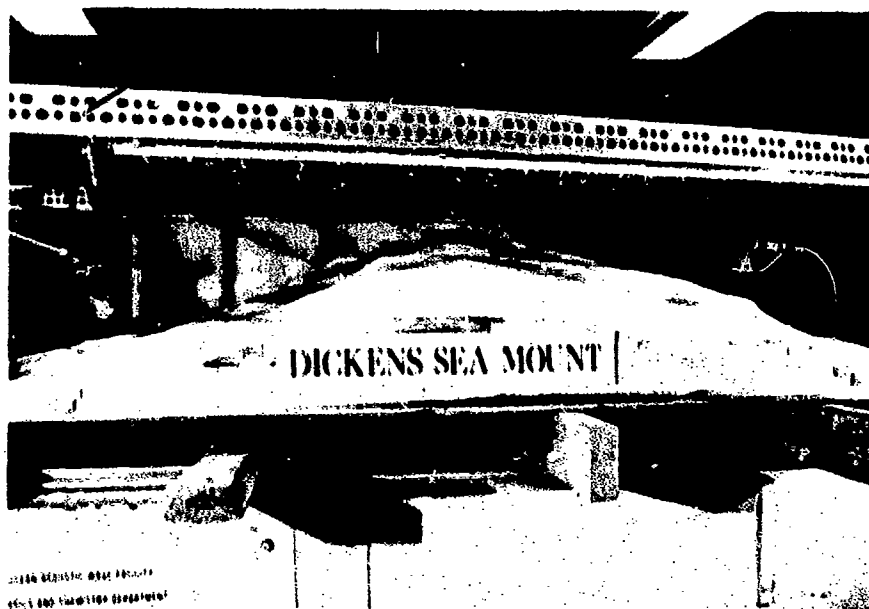


FIG. 2 LABORATORY MODEL OF DICKENS SEAMOUNT WITH SCALED MODEL OCEAN REPRESENTING 35 kn WIND CALCULATED FROM PIERSON-MOSKOWITZ WIND WAVE SPECTRUM

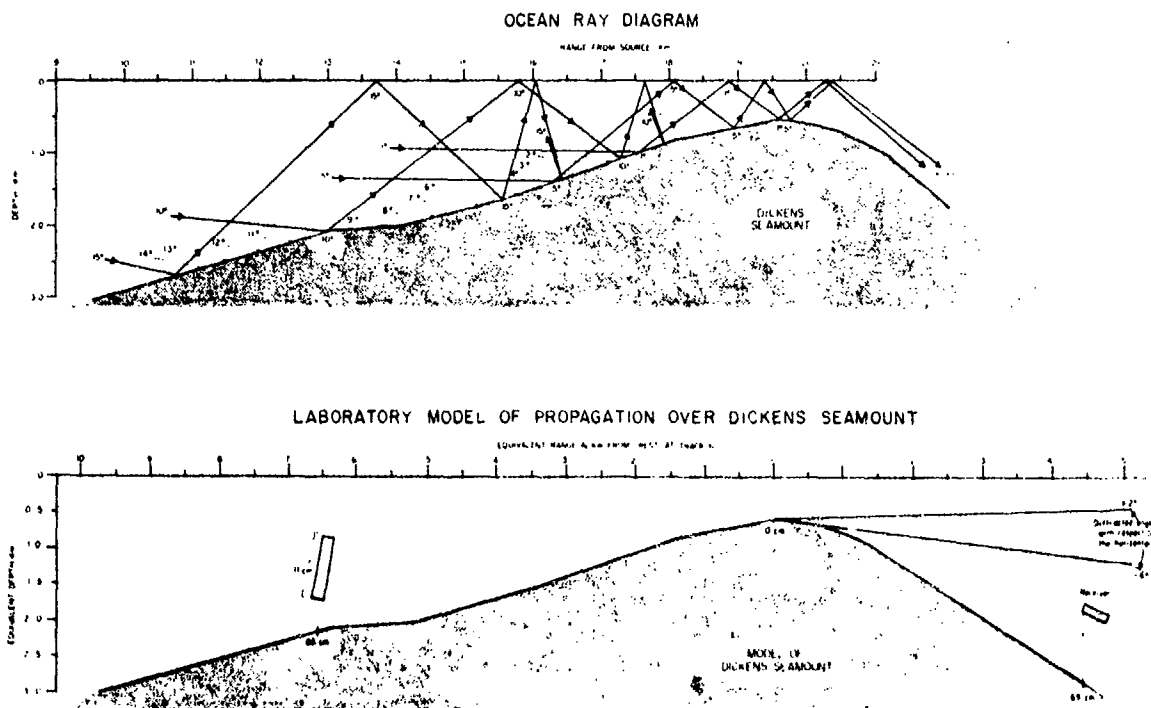


FIG. 3 RAY DIAGRAM OF FORWARD SCATTER AND DIFFRACTION BY DICKENS SEAMOUNT ALONG TRACK 6 OF THE OCEAN EXPERIMENT

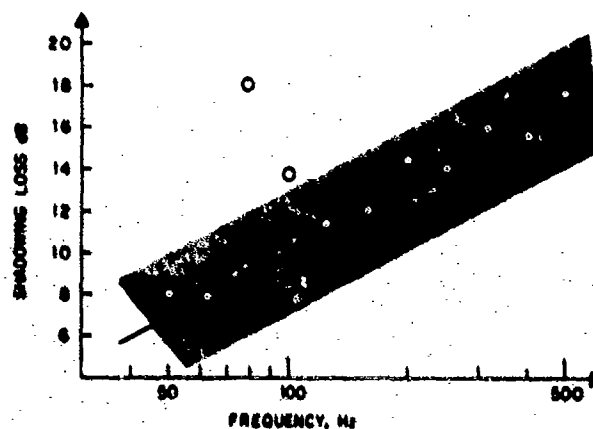


FIG. 4 PREDICTED SHADOWING LOSS CAUSED BY DICKENS SEAMOUNT FOR SOURCE-RECEIVER CASE SHOWN IN FIG. 3. Shaded area shows error bounds of scale model calculation. Circles are ocean data provided by N.R. Chapman and G.R. Ebbeson, Defense Research Establishment, Pacific, Victoria B.C., Canada. The theoretical slope, solid line, is 3 dB/octave

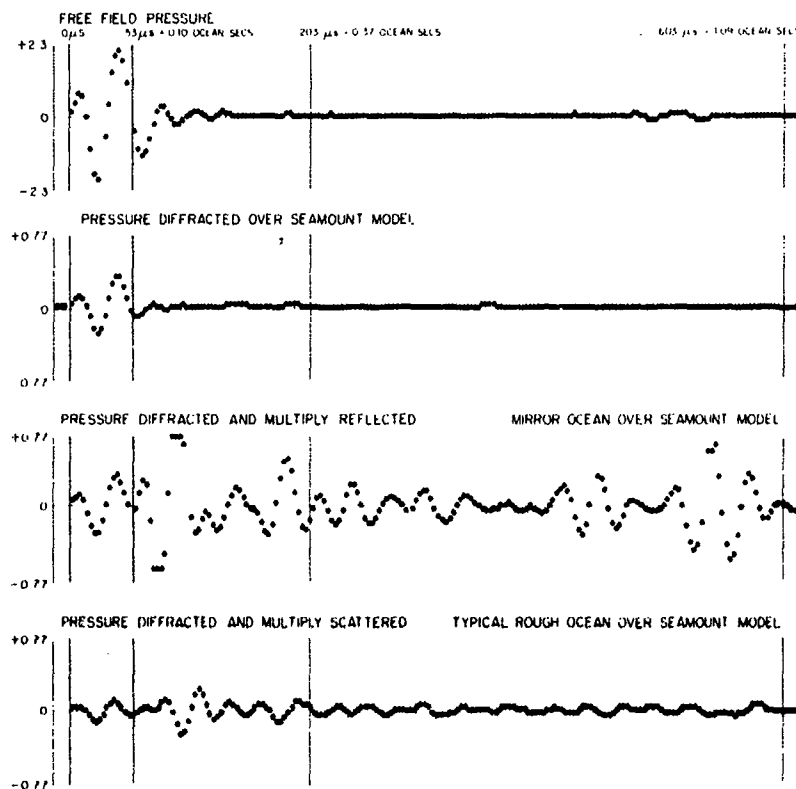


FIG. 5 LABORATORY STUDY OF IMPULSE DIFFRACTION AND MULTIPLE REFLECTION AT DICKENS SEAMOUNT. Top, free field pressure of source; second graph, pressure diffracted over seamount model; third graph, pressure diffracted and multiply reflected by a mirror smooth ocean surface; bottom graph, pressure diffracted and multiply reflected at a model sea surface for a 35 kn wind. The first 50 microseconds is the diffracted signal; from 50 to 203 μ sec is scale model reflection scatter that does not occur at sea; from 203 μ sec the signal is multiple scatter that represents the ocean situation

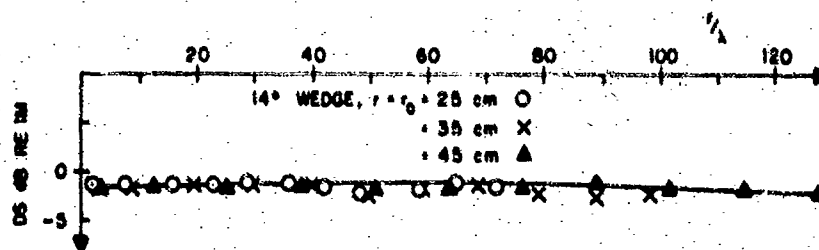


FIG. 6 DIFFRACTION STRENGTH, DS, FOR A SYMMETRICAL PLANE RIGID WEDGE WITH $\theta_w = 208^\circ$ and $z = 0'$. The solid line gives the theoretical value for $r = r_0 = 3.5$ km in water; data points are for a laboratory model experiment in air at three ranges, 25, 35 and 45 cm

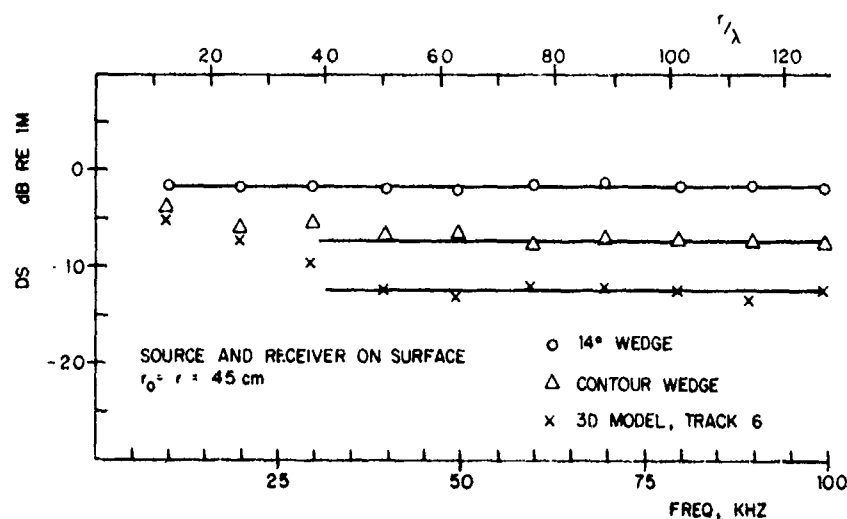


FIG. 7 DIFFRACTION STRENGTHS FOR THREE MODELS OF DICKENS SEAMOUNT. Solid lines from top to bottom are: theory for plane wedge of $\theta_w = 208^\circ$; asymptote for the two-dimensional contour wedge along the sound track; asymptote for the three-dimensional model along the sound track. Experimental data given by circles, triangles and crosses, respectively.

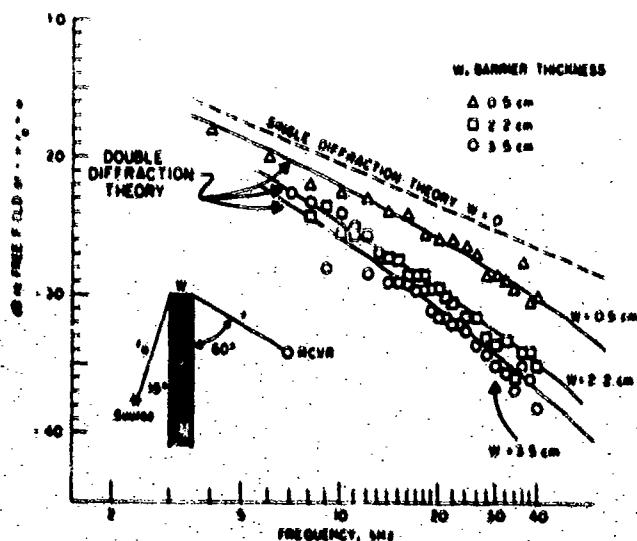


FIG. 8 SHADOWING LOSSES BY DOUBLE DIFFRACTION CALCULATIONS, SOLID LINES, COMPARED WITH EXPERIMENTAL MEASUREMENTS FOR THICK PLATES. The ranges are $r = r_0 = 25$ cm

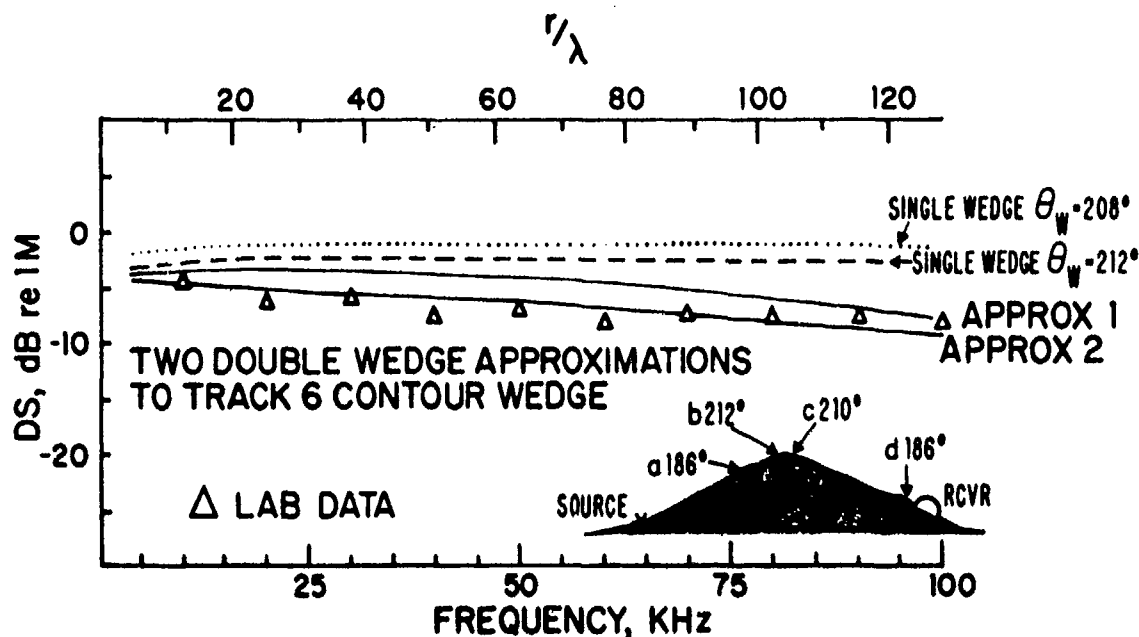


FIG. 9 TWO DOUBLE DIFFRACTION COMPUTER CALCULATIONS OF DIFFRACTION STRENGTH COMPARED WITH LABORATORY EXPERIMENTAL MEASUREMENTS OF THE TWO-DIMENSIONAL "CONTOUR MODEL" OF SOUND TRACK 6 OVER DICKENS SEAMOUNT. The double diffraction barriers are plane surface fittings to the true contour (inset). Single plane wedge theory for $\theta_w = 208^\circ$ (14° slopes) and $\theta_{ww} = 212^\circ$ (16° slopes) are shown for comparison

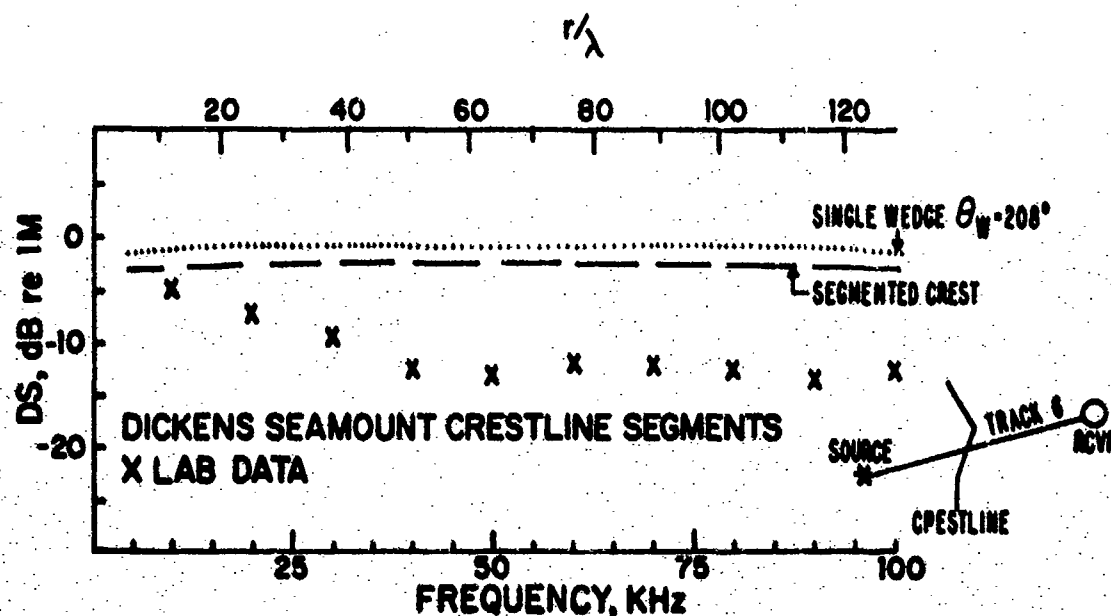


FIG. 10 PREDICTED DS FOR CRESTLINE SEGMENTAL WEDGES AS SHOWN IN INSET. Laboratory measurements for DS for scale model of DICKENS seamount shown by crosses. The dotted line is the solution for a single plane wedge $\theta_w = 208^\circ$.

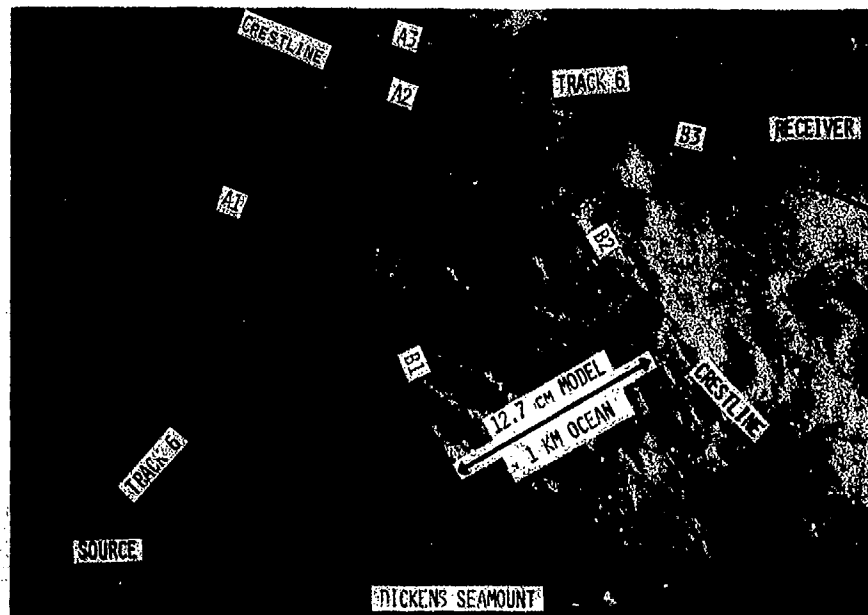


FIG. 11 PHOTOGRAPH OF THE DICKENS SEAMOUNT MODEL WITH IDENTIFICATION OF WEDGE CRESTS USED FOR THE DOUBLE DIFFRACTION CALCULATIONS NEAR SOUND TRACK 6

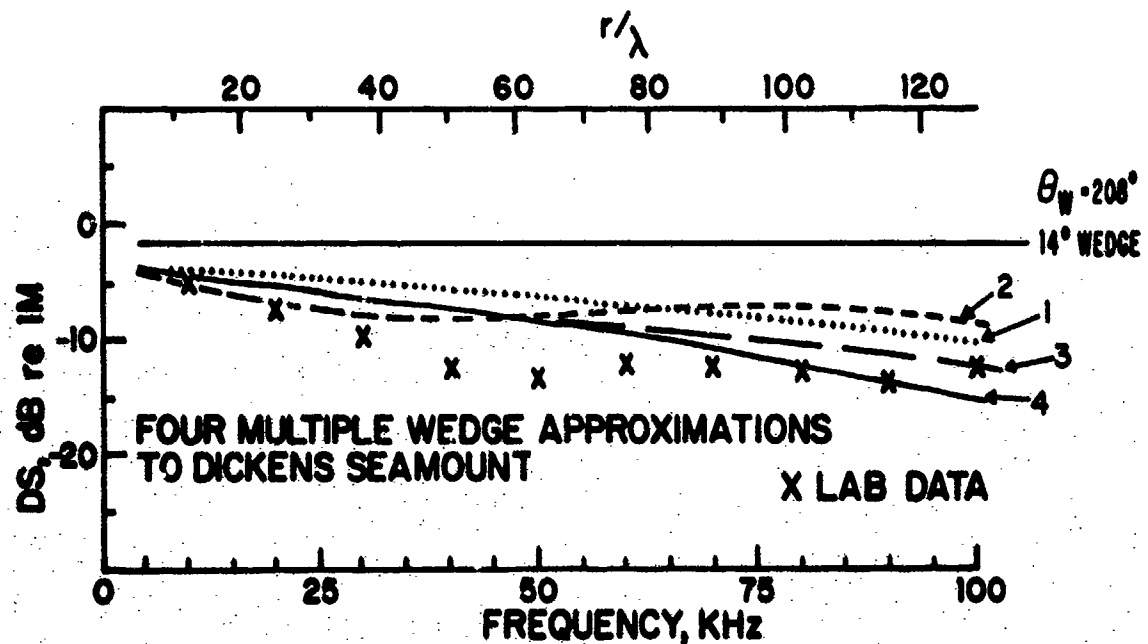


FIG. 12 MULTIPLE DIFFRACTION CALCULATIONS OF DS FOR WEDGES THAT ADJOIN THE PRINCIPAL RAY PATH CONTOUR (TRACK 6) COMPARED WITH LABORATORY MEASUREMENTS FROM THE THREE DIMENSIONAL SCALE MODEL OF DICKENS SEAMOUNT. Referring to Fig. 11, approximation 1 consists of segments A1 and B1 and a wedge between A2 and A3 and between B2 and B3. Approximation 2 is comprised of the double wedge A1, A2 and double wedge B1, B2. Approximation 3 uses a wedge between A2, A3 and B2, B3 and a second (unmarked) wedge closer to the receiver. Approximation 4 is a triple diffraction which is composed of wedges A1, B1 and A2, B2 and A3, B3

INITIAL DISTRIBUTION

	Copies		Copies
<u>MINISTRIES OF DEFENCE</u>		<u>SCNR FOR SACLANTCEN</u>	
MOD Belgium	2	SCNR Belgium	1
DND Canada	10	SCNR Canada	1
CHOD Denmark	8	SCNR Denmark	1
MOD France	8	SCNR Germany	1
MOD Germany	15	SCNR Greece	1
MOD Greece	11	SCNR Italy	1
MOD Italy	10	SCNR Netherlands	1
MOD Netherlands	12	SCNR Norway	1
CHOD Norway	10	SCNR Portugal	1
MOD Portugal	5	SCNR Turkey	1
MOD Turkey	5	SCNR U.K.	1
MOD U.K.	16	SCNR U.S.	2
SECDEF U.S.	55	French Delegate	1
		SECGEN Rep. SCNR	1
		NAMILCOM Rep. SCNR	1
<u>NATO AUTHORITIES</u>		<u>NATIONAL LIAISON OFFICERS</u>	
Defence Planning Committee	3	NLO Canada	1
NAMILCOM	2	NLO Denmark	1
SACLANT	10	NLO Germany	1
SACLANTREPEUR	1	NLO Italy	1
CINWESTLANT/COMOCEANLANT	1	NLO U.K.	1
COMIBERLANT	1	NLO U.S.	1
CINCEASTLANT	1		
COMSUBACLANT	1	<u>NLR TO SACLANT</u>	
COMMAIREASTLANT	1	NLR Belgium	1
SACEUR	2	NLR Canada	1
CINCNORTH	1	NLR Denmark	1
CINC SOUTH	1	NLR Germany	1
COMNAVSOUTH	1	NLR Greece	1
COMSTRIMFORSOUTH	1	NLR Italy	1
COMEDCENT	1	NLR Netherlands	1
COMMAIRMED	1	NLR Norway	1
CINCHAN	1	NLR Portugal	1
		NLR Turkey	1
		NLR UK	1
		NLR US	1
		ATTENDEES	100
		Total initial distribution	231
		SACLANTCEN Library	10
		Stock	19
		Total number of copies	360